THE ROLE OF TUMOR DESMOPLASIA IN NANOPARTICLE DELIVERY OF DRUGS AND GENES

Lei Miao

A dissertation submitted to the faculty at the University of North Carolina at Chapel Hill in partial fulfillment of the requirements for the degree of Doctor of Philosophy in Division of Molecular Pharmaceutics in the Eshelman School of Pharmacy

Chapel Hill
2016

Approved by:

Leaf Huang

Philip C. Smith

Elena V. Batrakova

Xiao Xiao

William Y. Kim

ABSTRACT

Lei Miao: The Role of Tumor Desmoplasia in Nanoparticle Delivery of Drugs and Genes
(Under the direction of Leaf Huang)

In desmoplastic tumors, stroma cells capture nanoparticles (NPs), preventing them from reaching tumor cells, resulting in compromised anti-tumor efficacy. This dissertation focuses on understanding the basis role of tumor associated fibroblasts (TAFs), one of the major stroma cells constituting desmoplasia, in NP delivery and tumor resistance, as well as proposing strategies to overcome the TAF-elicited barriers and improve efficacy.

While the capture of therapeutic NPs in TAFs interferes tumor-stroma crosstalk and inhibits tumor progression, we found that the chronic exposure of NPs paradoxically induced the secretion of survival factors (e.g., Wnt16) from the damaged TAFs, facilitating tumor proliferation and metastasis. Therefore, we proposed the delivery of siRNA against Wnt16 to TAFs via the off-target capture, to downregulate this survival factor. The priming of damaged fibroblasts could synergize with a nanoformulation of cisplatin, and benefit the treatment of a desmoplastic bladder cancer xenograft (UMUC3/3T3). Since the off-target delivery of NPs have been verified, we further utilized the same rationale to generate a group of tumor-suppressive TAFs through transfecting TAFs with a plasmid encoding highly secretable TNF-related apoptosis-inducing ligand (sTRAIL). The production of sTRAIL from TAFs bypassed the stroma barrier and resulted in efficient killing of tumor cells.

Furthermore, we also proposed a stroma depletion method via combination therapy of cisplatin NPs and gemcitabine NPs. This combination was not only detrimental to tumor cells, but induced superior apoptosis in TAFs of the UMUC3/3T3 model. To ensure the sufficient synergy, we further designed a nano-formulation with ratiometric co-loading and co-delivery of these two regimens. The design of converting these two drugs with totally different physicochemical properties

into nano-cores with similar hydrophobic surface and particle size, allows for their simultaneously and ratiometric loading in a single PLGA NPs. This combinatory NPs showed potent anti-cancer efficacy compared to each regimens in separate NPs.

In summary, the stroma modulating strategies proposed in the current dissertation provide new paradigms for the treatment of desmoplastic tumors. Combined with cancer immunology, a more prolonged and efficient outcome can be anticipated. The ratiometric combination nano-platform also provides a promising approach for encapsulating agents with different physicochemical properties.

To my parents Xingwang Miao and Guihua Huang

ACKNOWLEDGEMENTS

First of all, I would like to express my utmost gratitude and appreciation to my supervisor, Dr. Leaf Huang who offered me this great educational opportunity in his lab as a graduate student. In the past few years, he provided me constant support, priceless guidance and extraordinary wisdom throughout my PhD journey. He is a remarkable and exceptional mentor I am so blessed to have. I will be forever thankful to his mentorship, inspiration and sense of humor. I would also like to thank my committee members, Dr. Elena Batrakova, Dr. Xiao Xiao, Dr. William Kim and Dr. Philip Smith for their precious guidance throughout the years. They advised me through the obstacles in completion of my research work and reviewed all my progress and dissertation. In addition, I would like to extend my special appreciation to Dr. Gregory Forest, Dr. Samuel Lai, Dr. Shawn Hingtgen, Dr. Shutao Guo, Dr. Yuhua Wang and Dr. Jing Zhang for their collaboration and as my external advisors.

Moreover, I want to express my gratitude to UNC Eshelman School of Pharmacy for allowing me pursuing higher education. I also like to acknowledge my colleagues and friends, C. Michael Lin, Lu Zhang, Yao Lu, Yi Zhao, Qi Liu, Ning Cheng, Xiaomeng Wan, Qiaoxi Li, Andrew Satterlee, Matt Haynes, Tyler Goodwin, Yang Xiong, Lina Liu, and all past and present members of the Huang Laboratory for their sincere friendship and kindly help throughout my graduate study. Particularly, I will never forget the happiness, frustration, jokes, and parties we had in addition to the inspiring scientific conversations. I would like to acknowledge BRIC imaging core facility, Flow Cytometry core facility, Animal Pathology core facility, ICP-MS core facility, CHANL for their assistance especially Dr. Hong Yuan, Dr. Wallace Ambrose, Nazar Filonov, and Charlene Santos.

I would particularly thank my parents, my brothers and sisters for their unconditional support and love all along the journey. I cannot go this far without their understanding, patience, standing by my side, faith and love.

TABLE OF CONTENTS

LIST OF TABLES

LIST OF FIGURES

LIST OF ABBREVATIONS AND SYMBOLS

AA	anisamide
ALT	alanine aminotransferase
αSMA	alpha smooth muscle actin
AST	aspartate aminotransferase
BM	basement membrane
BSB	Binding Site Barrier
BUN	blood urea nitrogen
D_{eff}	diffusion coefficients
DMMA	2,3-dimethylmaleic anhydride
DOPA	dioleoylphosphatydic acid
DOTAP	1,2-dioleoyl-3-trimethylammonium-propane chloride salt
DOX	doxorubicin
DSPE-PEG	1,2-distearoryl-sn-glycero-3-phosphoethanolamine-N-[methoxy (polyethyleneglycol-2000) ammonium salt
ECM	extracellular matrix
EDS	energy dispersive microscopy
EPR	enhanced permeation and retention
FAPα	fibroblasts activation protein alpha
FRET	intermolecular Főrster resonance energy transfer
GAG	glycosaminoglycans
GFP	green fluorescence protein
HA	hyaluronan
HCT	hematocrit
HIF	hypoxia-inducible factor

HGB	hemoglobin
HSV	herpes simplex virus
ICP-MS	inductively coupled plasma mass spectrometry
IF	immunofluorescent staining
IFP	interstitial fluid pressure
IHC	immunohistochemistry staining
IRES	internal ribosomal entry site
ITZ	isoleucine zipper
LCP NPs	lipid coated calcium phosphate nanoparticles
LOX	lysyl oxidase
LPD	lipid-coated polycation DNA complexes
NER	nucleotide excision repair
NPs	nanoparticles
NSCLC	non-small cell lung cancer
PAI-1	plasminogen activator inhibitor type 1
PDAC	pancreatic ductal adenocarcinoma
PSC	pancreatic stellate cells
PNIPAM	poly(N-isopropylacrylamide)
PVC	poly(vinyl chloride)
SHH	sonic hedgehog
Sigma R	sigma receptor
TAFs	tumor associated fibroblasts
TAMs	tumor associated macrophages
TUNEL	terminal deoxynecluotidyl transferase dUTP nick end labeling
FGF	fibroblast growth factor

TME	tumor microenvironment
RBC	red blood cell
RFP	red fluorescence protein
sTRAIL	secretable TNF-related apoptosis inducing ligand
TGF-β	transforming growth factor beta
TNFα	tumor necrosis factor alpha
VDR	vitamin D receptor
VEGF	vascular endothelial growth factor
WBC	white blood cell
Wnt	Wingless-type MMTV integration site

CHAPTER 1: STROMAL BARRIERS AND STRATEGIES FOR THE DELIVERY OF NANOMEDICINE TO DESMOPLASTIC TUMORS[1]

1.1 Summary

Nanoparticles (NPs) based delivery formulations have become a leading delivery strategy for cancer imaging and therapy. The success of NP-based therapy relies heavily on their ability to utilize the enhanced permeability and retention (EPR) effect and active targeting moieties to their advantage. However, these methods often fail to enable a uniform NP distribution across the tumor, and lead to insufficient local concentrations of drugs. Oftentimes, this heterogeneous drug distribution is one of the primary reasons for suboptimal treatment efficacy in NPs delivery platforms. Herein, we seek to examine the biophysical causes of heterogeneous NPs distribution in stroma-rich desmoplastic tumors; namely the abnormal tumor vasculature, deregulated extracellular matrix and high interstitial hypertension associated with these tumors, and also the off-target depletion of NPs in non-tumor stroma cells. It is suggested that these factors help explain the discrepancy between promising outlooks for many NPs formulations in preclinical studies, but suboptimal clinical outcomes for most FDA approved nanoformulations. Furthermore, examination into the role of the physicochemical properties of NPs on successful drug delivery was conducted in this chapter. In light of the many formidable barriers against successful NP drug delivery, we provided possible approaches to mitigate delivery issues from the perspective of stromal remodeling and NPs design.

---

[1]This chapter previously appeared as a review article in Journal of Controlled Release. The original citation is as follows: Lei Miao, C. Michael Lin, Leaf Huang, Stromal barriers and strategies for the delivery of nanomedicine to desmoplastic tumors, Journal of Controlled Release, 2015, 219 (10):192-204.

In all, this chapter seeks to provide guidelines for optimizing nanoparticle-based cancer drug delivery through both modified nanoparticle design and alleviation of biological barriers to successful therapy.

1.2 Introduction

The field of nanomedicine has recently attracted tremendous attention, particularly for applications in cancer drug delivery. Owing to the advancements in material science and new manufacturing methods, NP-mediated drug delivery platforms can now be fabricated to an almost unlimited number of configurations with respect to size, shape, and payload, allowing for versatile applications for the detection, prevention and treatment in oncology. Nanotherapeutics such as liposomes, polymeric micelles and inorganic NPs possess a distinct functional advantage over conventional small molecule chemotherapy regimens by overcoming severe systemic toxicities that limit the clinical application of most chemotherapy drugs [1]. Furthermore, NP drug delivery platforms permit significantly prolonged circulation when compared to small molecule drugs alone. Most importantly, the leakiness of vessels established during angiogenesis and the impairment of lymphatic drainage, constituting the so called *EPR effect*, provides the primary driving force for the extravasation of NPs, improving the intratumoral accumulation and distribution and resulting in enhanced therapeutic outcome [2]. Examples of applications include both the preclinically investigated nanoformulation (i.e. liposomes, polymeric micelles) and FDA approved NPs of liposomal doxorubicin (Doxil®) and albumin-bound paclitaxel (Abraxane®). Despite demonstrating outstanding antitumor efficacy in preclinical studies and promising outlooks for multifunctional use in clinical trials, nanoparticulate anti-cancer therapeutics have only provided modest survival benefits overall [3]. Factors such as the fundamental design of the NPs, abnormal tumor microenvironment, and the heterogeneity across tumors can compromise the EPR effect. This serves to explain the discrepancies between the promising results obtained from preclinical studies, and the subpar performance in clinical trials. The tortuous tumor vasculature and abnormal basement membrane limit

both the trans-vascular and interstitial transport of NPs. Furthermore, the high level of extracellular molecules, increased solid stress and high interstitial pressure act as another set of barriers to successful NPs extravasation. Consequently, the limited NPs perfusion directly inhibits the therapeutic efficacy of the nanocarriers. The heterogeneity of the tumor stroma microenvironment underlines the importance of intratumoral off-target distribution of NPs to non-tumor stroma cells, since their disparate response towards treatment may be another major mechanisms behind chemotherapeutic resistance and compromised clinical outcomes [4].

Herein, we first present mathematical models for intratumoral NPs transport to achieve a better understanding of this complex process. We then discuss the key physiological barriers for NPs transport, and analyze the design of NPs for enhanced intratumoral transport. Finally, we summarize the strategies to overcome delivery barriers through remodeling the tumor microenvironment and designing the tumor microenvironment-responsive NPs.

1.3 Mathematical Modeling and *In Vitro* Models of NP Intratumoral Distribution

The intratumoral delivery of macromolecules and NPs requires several steps in transport, including vascular transport, transvascular transport, interstitial transport, cellular binding, internalization and metabolism (**Figure 1.1**) [1]. All these steps are generally limited by pathophysiology of tumors. To better understand the biophysical underpinnings of these transport barriers, Jain and his colleagues have developed several mathematical models to simulate the intratumoral behaviors of NPs [5-7].

For the modeling of vessel and trans-vasculature transport, the tumor vasculature was represented by a two-dimensional percolation network with one inlet and one outlet that resembles the vascular structure and function of tumors [8]. Vessel transport is mainly dominated by convection (flow rate governed by pressure gradient) and is quantified based on the perfusion rate of blood flow (Q). Poiseuilles's law was used to simulate vessel transport, suggesting that blood flow is proportional to the vascular pressure gradient and blood viscosity [8]. The transvascular flow was set

proportional to hydraulic conductivity of the vessel wall, the surface area of the vessel and also the influence of interstitial fluid pressure. All parameters can be measured using standard intravital microscopy, multiphoton microscopy and optical frequency domain imaging [1, 9-12]. This modeling formula emphasizes the potential influence of blood vessel area, pore size and interstitial fluid pressure (IFP) on NPs transport.

Interstitial transport, mainly indicating the diffusion of NPs through the extracellular matrix (ECM) toward tumor cell targets, is another significant step in determining NPs diffusion and penetration. Interstitial transport follows the Darcy's theory, which requires calculation of the diffusion coefficients (D_{eff}) of NPs in the ECM [8, 13]. Diffusivity of NPs in the ECM was modeled *in vitro* using matrigel or collagen confined diffusion chamber models. Diffusion coefficients were determined using these *in vitro* ECM models by non-linear fits of intensity gradients to a diffusion model (e.g. Fickian model) [3, 13, 14]. Diffusion coefficients of macromolecules and liposomes can also be quantified *in vivo* using either single-photon fluorescence recovery after photobleaching or two photon fluorescence correlation microscopy. These measurements are more clinically relevant, but limited by equipment requirements and cost [14, 15].

For the majority of the aforementioned short time scale transvascular transport models or long-term NPs penetration models, neither the binding of NPs to cancer cells, nor cell uptake was included [16]. However, these two factors play a substantial role in the process of NPs transport. In light of this, Mok et al. are credited for the development of mathematical models considering rapid cell surface binding, internalization and degradation through an intratumorally infused Herpes Simplex Virus (HSV). In addition to diffusion coefficient, second-order binding rate constants, first-order dissociation constants and internalization constants were included in the differential equation to distinguish the free interstitial virus, bound virus and internalized virus respectively [16, 17]. Using a similar mathematical model, Kim et al discriminated the interstitial diffusion, cellular uptake and intracellular release of fluorescein-labelled gold NPs (6 nm overall with ligand) on a three-dimensional multicellular tumor cylindroid model [18]. The intracellular release kinetics of

fluorescein from NPs were further included into the differential equation. However, these mathematical equations are all confined to *in vitro* 3D tumor models or intratumoral injection of NPs, and do not consider the effect of vascular transport and plasma clearance. In another study, Schmidt et al. modeled the cellular binding affinity of the targeted molecules along with the dynamic plasma clearance of macromolecules into the mechanistic compartmental model, and avidly studied the effect of molecular size and binding affinity on tumor targeting [19].

Although, most of the mathematical and *in vitro* models are based on assumptions and limitations, the overall modeling of intratumoral transport of NPs still provides a semi-quantitative method for the extrapolation of parameters such as NPs physicochemical properties and tumoral barriers on NPs transport. This can then be extended so as to predict dynamics of NPs transport and the therapeutic outcomes of NPs delivering chemotherapy and gene therapy.

1.4 Enhanced Permeability and Retention Effect and Anti-cancer NPs in the Clinical Trials

The mathematical models discussed in the previous section emphasize the importance of the tumor vasculature on vascular and transvasculature transport of NPs. New vessels formed during angiogenesis are known to have a leaky and tortuous morphology, permitting NPs extravasation [20]. On a different note, rapid unconstrained proliferation is coupled to an IFP and solid stress, which results in the compression of lymphatic vessels and impairs NPs clearance [21]. Together, these characteristics comprise the EPR effect. The EPR effect describes how the leaky vasculature of tumors permits enhanced NPs permeability, while the lack of a functioning lymphatic network promotes NPs retention in the tumor. The EPR effect states perhaps one of the most fundamental advantages for NPs-based drug delivery. Clinically, NPs have been applied to treat a broad range of cancers. Abraxane is an albumin-stabilized NPs designed for the delivery of paclitaxel [22]. Along with other platforms such as a PEGylated liposome based doxorubicin delivery system (Doxil®), both share the ability to exhibit enhanced tumor localization through the EPR effect.

1.5 Tumor Microenvironment Barriers for Intratumoral NPs Diffusion and Distribution

Ironically enough, the mechanistic basis for the EPR effect also comprises one of the primary barriers to NPs delivery. Namely, the elevated IFP [23] and increased solid stress act to inhibit successful NPs extravasation into the tumor. This paradoxical observation explains the discrepancy between promising preclinical research and the subpar clinical outcomes for NPs application. Therefore, successful NPs drug delivery relies heavily on the balance of these two competing aims (**Table 1.1**).

1.5.1 Abnormal Tumor Vasculature Plays Paradoxical Roles in NPs-based Delivery

When compared with non-cancerous tissues, tumor vessels are known to be heterogeneous, leaky and dilated, leaving avascular spaces of various sizes. In addition, abnormal vessel-wall structures with heterogeneous basement membranes, wide inter-endothelial junctions and large pore sizes contribute to the irregularity of the tumor vasculature [2, 24-27]. These factors therefore compromise NPs transport and undermines the efficacy of therapeutic agents.

Genetic and epigenetic changes drive tumor and mesenchymal cells to produce pro-angiogenic factors, such as vascular endothelial growth factor (VEGF) [28]. Due to over-activation of these pro-angiogenic pathways, tumor vessels become tortuous and leaky. As mentioned in the previous section, leaky vasculature then facilitates transient NPs extravasation through the EPR effect. However, the mechanistic basis behind the EPR effect also contributes to excessive fluid extravasation, inducing increased IFP, fluid viscosity and therefore impairs NPs vascular transport [29]. The tortuous nature of tumor vessels further contributes to these elevated geometric resistance through decreased blood flow [20, 30]. Meanwhile, solid stress resulting from unconstrained tumor growth and an abnormal ECM, further compresses vessels, blocking blood flow and leading to vessel collapse [20]. The decrease in blood flow, in turn, has a great effect on the viscous resistance of the blood. Slow blood-flow rates and high blood viscosities govern the vascular and transvascular transport of small molecules, macromolecules and NPs. Furthermore, unlike normal tissues, blood

velocity in tumors is independent of vessel diameter and unevenly distributed. The poorly perfused or even unperfused blood supply leads to hypoxia and acidic conditions, which bolsters drug resistance and further limits NPs diffusion [2]. Aside from blood vessel constriction, the lymphatic vessels in the tumor are also compressed by proliferating cancer cells, causing collapse. The inefficient drainage of fluid from the tumor center coupled with fluid leakage from tumor vessels contributes to interstitial hypertension, which further limits NPs perfusion deep into the tumor core [4].

1.5.2 Acidic and Hypoxia Limit Nanotherapeutic Approaches to Necrotic Areas

Acidic and hypoxic conditions are distinctive features of most solid tumors. Acidification of tumor microenvironments primarily arises from the Warburg effect, which describes the tumor's shift in energy metabolism from pyruvate oxidation to glycolysis. The excess lactic acid produced through this pathway remains in the tumor due to poor lymphatic drainage as described previously, a characteristic of most solid tumors [31]. Acidic conditions lead to the ionization of weakly basic drugs and compounds, limiting their ability to diffuse in the ECM [32]. On the other hand, hypoxic conditions primarily arise due to unconstrained cell proliferation that outgrows the blood supply in the tumor. As a result, it is well documented that hypoxic regions most commonly surround the necrotic center of the tumor [33]. Due to the altered blood-flow in hypoxic regions, particles often fail to localize in regions of hypoxia [34]. Even if delivery of NPs is successful to hypoxic regions, cells deficient of oxygen show surprising resilience to chemotherapy. As hypoxia reduces cell proliferation, chemotherapy drugs targeting rapidly proliferating cells are rendered useless in these regions [35]. Furthermore, hypoxic regions are hotspots of hypoxia-inducible factor (HIF) production. The stabilization of HIF-1A, a normally labile transcription factor, is known to induce drug resistance through up-regulation of genes such as MDR1 [35] [36]. Therefore, hypoxic and acidic environments are a barrier to nanoparticle-based chemotherapy options from both a delivery and therapeutic standpoint. However, many novel treatment regimens seek hypoxic and acidic environments as a

tumor drug target. Specifically, some treatments use the acidic environment to induce drug release from polymeric nanoparticles [37].

1.5.3 High Interstitial Fluid Pressure Limits NPs Convection and Accumulation

Another notable contradiction that arises when discussing the mechanism behind the EPR effect is the elevated IFP. The balance between elevated IFP and the increased NPs uptake via EPR effect influences successful NPs delivery. High IFP is known to be the result of a variety of factors. Firstly, the dense surrounding collagen matrix of the tumor microenvironment is rich in tumor associated fibroblasts (TAFs), which contract and tighten the collagen network by secreting ECM associated molecules and integrin dependent binding [23, 38]. This first barrier physically limits the expansion of the tumor cavity in response to growth. Continuous unregulated tumor proliferation in this enclosed space then compresses blood and lymphatic vessels due to growth induced solid stress, which in turn prevents the efficient discharge both NPs and interstitial fluid from the tumor [20, 39, 40]. An elevated IFP is known to be particularly detrimental for large molecule/nanoparticle delivery, which rely primarily on convection for their extravasation [26]. High IFP acts against convection and force NPs to enter via passive diffusion, a kinetically slower process. Furthermore, IFP induced vessel constriction has been shown to cause tumor hypoxia, where the increased precedent of angiogenic and growth factors contribute to lymph node metastasis and drug resistance. These secreted factors are then relocated from the tumor periphery toward the outer invasive front due to the IFP gradient where they communicate with fibroblasts to induce resistance and metastasis [41-43]. A high IFP therefore obstructs the therapeutic efficacy of NPs and leads to heterogeneous drug distribution in the tumor stroma.

1.5.4 Abnormal Extracellular Matrix Interferes with NP-based Drug Delivery

The tumor extracellular matrix (ECM) is a key element for regulation of cell proliferation and differentiation [43]. Particularly, the high cellularity of tumors compresses the interconnected collagen network and space-filling hydrogel-like glycosaminoglycans (GAG) of the ECM. The

compressed network in turn results in the accumulation of solid stress and dictates interstitial transport [44]. At the cellular level, ECM is localized at two different intratumoral sites, the basement membrane (BM) and the interstitial matrix.

The BM functions as a scaffold for endothelial and mural cells. In particular, the matrix of the BM contains highly compact, sheet-like dispositions formed from fibronectin, laminin and type IV collagen, linked via nidogen and heparin sulfates [45, 46]. More than 99% of non-cancerous blood vessels are covered by a thin layer of BM, which regulates vessel development through paracrine secretion of pro-inflammatory and pro-angiogenic cytokines. Specifically, cytokines such as transforming growth factor beta (TGF-β) and tumor necrosis factor alpha (TNFα) support the homogenic architecture of the blood vessels; whereas the BM of tumor microvessels are primarily continuous but conspicuously abnormal [47]. Heterogeneous BM morphologies were observed in different tumors or different regions of the same tumor. MCa-IV breast carcinomas and 4T1 breast cancer are characterized by a lesser amount of collagen in the vessel wall, which are loosely associated with the underlying endothelia [48]. Separately, breast cancer 3LLL and pancreatic cancer BXPC3 are characterized by a second type of BM, with a distribution of brighter collagen nodules are more condensed and overlapped with the capillary. The BM does not induce the elevation of IFP, yet functions as a sieve to modulate extravasation of free drug and NP from capillaries into the tumor microenvironment. Free DOX, FITC-tagged dextran and 80 nm PEGylated, DOX loaded liposomes were used as tracers to evaluate the extravasation of small molecules and large NPs into the tumor microenvironment. Yokoi et al's study showed that the extravasation pattern of small molecules in the type I BM model 3LLL and type II BM Model 4T1 were comparable [48]. However, the extravasation of NPs from the same two tumor types was very different, as suggested by their *in vivo* NPs diffusion model and *in vitro* collagen-sleeve model. Diffusion based transport of NPs was severely hindered by the thickness of collagen fibers, fiber mesh pore size and fiber density. Moreover, the BM is not static, but dynamic as angiogenesis of blood vessels requires degradation of collagen IV by matrix metalloproteases MMP2 and MMP9 [49, 50]. Therefore, degradation of

collagen IV provides a transient niche with leaky tumor vasculature, low and thin BM, a very beneficial window for NPs delivery. Besides the collagen meshwork, some earlier works also proposed that the extensively charged heparin sulfate chain, which is attached to the laminin/collagen IV network, is essential for the microscopic filtering of positive charged particles. Simultaneously, the nidogen molecules and the protein core of the perlecan complex geometrically hinder the negatively charged particles [51]. Overall, BM characteristics such as the matrix density, presence of proteoglycans and angiogenesis mediated BM remodeling limit the extravasation of NPs from blood vessels into the interstitium of tumors.

While the interstitium is also rich with ECM, it limits NPs penetration differently from the BM in three ways. Firstly, high stromal fraction and large matrix molecules are restricted to a limited interstitial volume, compressing the matrix into a dense network with increased IFP; limiting convection of NPs. Secondly, fibrillar structure, mesh size and collagen thickness directly limit the diffusion of NPs. Since the molecular components of interstitial ECM are more confluent than BM, the interactions between these parameters are both more pronounced and more complicated. The tortuous nature of the interstitial space is the third primary barrier for NPs since it elongates the diffusion path of both NPs and macromolecules from blood vessels to target cells. In tumors with a lower amount of interstitial matrix, such as melanoma and colorectal cancers, NPs can easily diffuse across the interstitial barrier, access tumor cells and therefore induce growth inhibition [52]. However, this process proves more difficult for tumors with a thick interstitial matrix. Collagen content is the major determinant of interstitial transport [2]. Unlike BM, collagen I rather than collagen V is the major component of the collagen matrix [53]. Fibril or collagen orientation can also influence particle diffusion rates. During cancer development, collagen-remodeling enzymes convert the orientation of collagen scaffolds from thin and relaxed collagens (curly fibrils) to thick, aligned fibrils. Stylianopoulos et al. established a mathematical model to evaluate particle diffusion across collagen fibers with varying degrees of alignments, suggesting that alignment of the collagen matrix stiffens the ECM, which thereafter not only elicits diverse effects on cellular migration and differentiation,

but also [54]narrows the inter-fiber spacing, retarding the movement of particles [55]. The collagen organization pattern also causes disparate NPs diffusion. Crosslinking of collagen via lysyl oxidase (LOX), regulated by fibronectin and organized by SPARC (secreted protein acidic and rich in cysteine), resulted in the stiffness of collagen fibers [55, 56]. These molecules are therefore used as interesting target candidates to inhibit stromal stiffness. With this aim, Kanapathipillai et al. designed a PLGA loaded LOX inhibitory antibodies to decrease collagen crosslinking and improve therapy [57].

The contribution of GAGs toward macromolecular diffusion is controversial. As one of the major non-sulfated GAG, hyaluronan is a linear polysaccharide with repeating disaccharide units of β-d-glucuronic acid and N-acetyl-β-D-glucosamine [54]. In most cases, the elimination of hyaluronan negatively affected nanoparticle transport, opposite to the effect of eliminating collagen [15]. The polymerization of HA has been shown to partition the collagen matrix into aqueous and viscous compartments. Hyaluronidase treatment increased the proportion of slow-diffusing compartments and shifted the slow diffusion coefficient to smaller values [58, 59]. On the other hand, for certain tumors such as pancreatic cancer, in which more than 70% ECM consists of HA, the degradation of HA resulted in increased drug diffusion [60]. The sulfated glycosaminoglycan, similar to that in the BM, carries a highly negative charge, which can inhibit the transport of macromolecules or NPs by forming aggregates [2, 61].

1.5.5 Stromal Cells Regulate the Interstitial Distribution of NPs

In contrast to features of the non-cancerous ECM, tumor stroma contains modified ECM attached to multifaceted stromal cells, including fibroblasts/myofibroblasts (carcinoma-associated fibroblasts), mesenchymal cells such as pericytes/mural cells, endothelial cells and immune cells [4, 20]. The high cellularity of tumors works in two distinct ways to limit NPs penetration and internalization. Firstly, solid stress induced by unconstrained proliferation of stromal and tumor cells compress the matrix into a disorganized network. Secondly, the stromal cells nonspecifically deplete

NPs, which extravasate from adjacent microvessels, compromising the internalization of therapeutic NPs in cancer cells and in turn, the overall therapeutic effect.

In the modified tumor ECM, pericytes play an important role, as they are a ubiquitous part of the tumor microenvironment. Pericytes are primarily characterized as periendothelial mesenchymal cells embedded within the vascular basement membrane[62], which can be identified by pericyte markers such as alpha smooth muscle actin (αSMA), PDGFR-β, NG2, RGS5 and XlacZ4 [63]. The establishment of pericytes starts with recruitment, which is primarily mediated by endothelial cells through PDGF-β /PDGFR-β signaling during physiological angiogenesis [62]. On the other hand, VEGF-α acts as a negative regulator of pericyte function and vessel maturation [64, 65]. The structure of newly established pericytes is loosely associated with the endothelial cells, and has cytoplasmic processes that penetrate deep into the tumor parenchyma. However, heterogeneity of tumors determines the spatial arrangement pericytes. Work by Kano et al recently classified cancers into two categories based on pericytes coverage: those with less coverage of tumor neovasculature (e.g. colon cancer, CT26) by pericytes and those with more (e.g. pancreatic cancer and diffuse-type gastric cancer) [66]. Pericytes regulate blood flow and control the stabilization and maturation of tumor vasculature. Neither leaky, immature blood vessels with little coverage, nor over-matured vessels with abundant pericyte coverage are suitable for NPs delivery and should be optimized for better NPs perfusion [67]. For example, NPs extravasation was severely impeded in the high pericyte coverage (BxPC3) model. Yet, treatment by TGF-β inhibitors or PDGF-β inhibitors could slow down pericyte recruitment, inhibit endothelial pericyte associations and therefore, improve NPs extravasation. While the low pericyte subtype showed better NPs perfusion, modulation of the pericytes still offered an improvement in NPs perfusion with respect to the unmodified group. Specifically, through diminishing non-functional microvessels with low pericyte coverage while increasing pericyte coverage in the normalized tumor vasculature [67]. For example, the VEGF inhibitor, Sorafenib, which negatively controls the regulations of pericytes, increased extravasation of 2 MDa dextran in the CT26 model [68].

TAFs are another major player of tumor fibrosis. TAFs inhibit the interstitial transport of NPs via the secretion of ECM, construction and stiffening the fibrillar structure and also secretion of paracrine growth factors for tumor resistance and metastasis. For example, lysyl oxidase (LOX) synthesized by TAFs could be stimulated via the TGF-β signaling pathway and contributed to increased stromal stiffness through crosslinked collagen fibers [69]. As a major stromal cellular component, TAFs also nonspecifically internalize therapeutic NPs and compromise NPs' association with tumor cells; resulting in sub-optimal clinical outcomes [70]. The ratio of off-target NPs distribution into fibroblasts is regulated by the spatial distribution of blood vessels in relation to tumor cells and other stromal components (i.e. fibroblasts) [71]. Two dominant phenotypes based on tumor stromal architecture delineate tumor types into either a tumor vessel phenotype (with vessels embedded throughout tumor cells) or a stromal vessel phenotype (vessels distributed in proximity to fibroblasts). While the tumor vessel phenotype is commonly applied in xenograft models, the stroma vessels are more clinically relevant and seen in orthotopic tumors (4T1 breast cancer or pancreatic cancer) and other primary cancers. Off-target distribution of NPs into TAFs is in fact, more prominent in the stromal vessel type. This was demonstrated in an experiment with 120 nm Docetaxel-conjugated NPs could distribute to fibroblasts in 4T1 and MDA-MB-231 orthotopic breast cancer and deplete TAFs content by 70% [72]. Given that the tumor-fibroblast transition is one major source of TAFs, surface receptors that are highly expressed in tumor cells are not surprisingly also found on respective fibroblasts [73]. Because of the increased binding affinity between fibroblasts and targeted NPs, the binding site barrier of TAFs is stronger for the targeted NPs, rendering off-target distribution more likely. Although therapeutic NPs that were delivered off-target to fibroblasts could deplete fibroblasts, and synergize with chemotherapy in some tumor models [74], the therapeutic effect of anti-cancer therapies are also likely to significantly deviate from initial predictions in TAFs, due to the different sensitivities and resistance mechanisms of benign fibroblasts and tumor cells [71]. For example, TAFs attacked with chemotherapy could secrete survival factors such as Wnt16 that

induced the formation of resistant phenotypes of prostate cancer [70]. Overall, the off-target delivery of NPs in TAF severely hinders NPs penetration and induced convoluted anti-tumor efficacy.

Immune cells, including B cells, T cells, granulocytes, dendritic cells, myeloid derived suppressor cells and macrophages, are indispensable constituents of the tumor microenvironment that modulate the intra-tumoral immune response [75, 76]. Owing to the partial peri-vasculature localization of infiltrated immune cells (other immune cells are likely to distribute in inflammatory hypoxia and necrosis area) [77] and phagocytic properties of some of the immune cells (e.g. macrophages) [78], off-target internalization of NPs is inevitable. Using an orthotopic model of melanoma and fluorescently labeled PRINT nanoparticles, Roode et al demonstrated that association between tumor-associated macrophages (TAM) and NPs were 4-fold greater than that of cancer cells despite TAM constituting only 1% of all cells in tumors [79]. In another study, the correlation between increased delivery and release of CKD-602 from S-CKD602 liposomes, and increased expression of CD11c-positive dendritic cells in a SKOV3 ovarian xenograft suggested that the NPs disposition may be associated with the phagocytic cells (i.e. DC and TAM) [80, 81]. Although, the off-target association of NPs in leukocytes and the general immune compartment may modulate the immune pathway (i.e. Stat-3, ERK) and modify the suppressive tumor microenvironment to synergistically improve cancer vaccines (data not shown), direct phagocytosis of NPs by phagocytic cells may deplete the NPs and limits accumulation into the tumor. Overall, the cellular components of the tumor stroma deplete NPs through multiple mechanisms and interfere with the therapeutic outcome of anti-cancer agents.

1.6 Physicochemical Properties of NPs influences NPs transport in Stroma-rich Tumors

Though the biophysical properties of tumors present prominent barriers for successful NPs delivery, the physicochemical properties of NPs govern the extent and limitations of such barriers. Steric small particles (with size <50 nm), such as PEGylated NPs (i.e. polymeric micelles, gold nanoparticles or quantum dots), can penetrate poorly permeable hypovascular tumors such as BxPC3,

better than the larger NPs (> 50 nm) [52]. The inverse relationship between diffusion rate and NPs size was also observed *in vitro* on the multicellular spheroid models [82]. One potential explanation is that the vascular pore size and the cross-linked collagen fiber mesh form pores that are in between the size of the large and small particles. Therefore, both transvascular and interstitial transport of smaller NPs occur rapidly [83]. However, one should note that NPs smaller than 10 nm are likely to be excreted from the kidney, at least partially. Therefore, NPs below the 10 nm limit exhibit compromised pharmacokinetic profiles and an increase in collateral damage toward normal organs. Increasing the size of NPs will provide selectivity, but at the cost of limiting extravasation and diffusion.

Aside from particle size, surface charge also affects intratumoral transport by regulating NPs' diffusive mobility in the ECM. Both PEGylated NPs and neutrally charged liposomes exhibit quasi-free diffusive motion in ECM hydrogel and have the advantage of deep penetration into tumors. Cationic NPs (e.g. DOTAP liposomes), on the other hand, were entrapped in the hydrogel [51]. However, cationic NPs have been shown to exhibit optimized transvascular transport by preferential targeting to the tumor endothelial cells and electrostatic attraction with the negatively-charged vessel pores [84, 85]. Furthermore, positively charged NPs are more likely to be taken up by proliferating cells (e.g. tumor cells) compared to neutral and negatively charged NPs, which is an additional advantage for effective drug delivery [18].

As far as the shape of NPs is concerned, research has shown that NPs or macromolecules with linear, rod-like semi-flexible configurations diffuse and penetrate more efficiently into the interstitial matrix compared with solid spherical particles of similar size. The shape of therapeutic NPs also affects their circulation time in the blood stream. For example, rod-shaped micelles have a circulation lifetime ten times longer than their spherical counterparts [2, 5, 86].

Surface modification of NPs with targeting ligands is another concern for enhancing NPs intra-tumoral transport. High binding affinities between NPs and the target site are generally seen as an advantage by increasing the internalization of NPs. However, the use of targeted NPs with high

binding affinity may elicit a binding site barrier. This regards a phenomenon where NPs binding to target cells paradoxically reduces diffusion deep into tumors. The binding site barrier was first observed during antibody delivery into tumors and later found to be present for NPs based delivery as well. High avidity may also comprise the selectivity, since particles may also inadvertently bind to non-tumor cells expressing low levels of tumor specific determinant and depleted accordingly. After all, targeting ligands exclusive to tumor cells are unlikely to exist [87, 88].

Though surface charges and targeting moieties modulated intra-tumoral NPs distribution, growing evidence suggested that nanomaterials that interact with biological fluids (e.g. plasma) are likely to adopt a "new" identity through acquiring a surface corona of biomolecules (such as lipid and proteins), a phenomenon that, in turn, may comprise the influence of surface properties and dictate the *in vivo* biodistribution of NPs. The composition of this corona is dynamic, reflects the nanomaterial-intrinsic properties, e.g., size, surface curvature and hydrophobicity. Among the identified compositions, opsonins (including immunoglubin (IgG), complementary factors and fibrinogen) were reported to promote receptor mediated phagocytosis, leading to rapid clearance and limited tumor accumulation of NPs. The attachment of antifouling polymers, in particular PEGylation, has widely been used to prevent protein binding, and consequently module the pharmacokinetic profiles of NPs. On the other hand, strongly bound monolayer bio-corona could be taken advantage of to prolong the NPs circulation. For example, albumin was said to complex with negative charged NPs and promote prolonged circulation times. Abraxane™, the FDA approved albumin-bound form of paclitaxel, is a good example of using albumin as a drug carrier for efficient anti-tumor therapy. Furthermore, one may consider exploit the bio-corona phenomenon for targeting purposes. Kim et al found that preadsorption of apolipoprotein E (ApoE) onto PEG-polyhexadecylcyanoacrylate NPs shown efficient delivery across the BBB into the brain. Other examples include specific adsorption of transferrin onto NPs for targeting purposes. Above study focused on bio-corona formed in plasma and discussed the pros and cons of this bio-corona for NPs delivery. However, considering the ultimate fate of NPs as to approach tumor cells through dense stroma, therefore, how the bio-corona coated

NPs interact with stroma, or whether the covered biomolecules will exchange with stroma and dynamically reform a new bio-corona are also influential for NPs disposition and need more detailed investigation.

Overall, the physiological properties of NPs greatly influence the pharmacokinetics, transvascular transport, intratumoral penetration and cellular internalization in paradoxical manners. This helps to explain the inconsistency between preclinical animal studies and clinical outcomes and therefore, physicochemical properties of NPs need to be optimized for each tumor.

1.7 Strategies to Improve NPs extravasation and Penetration

Examination of the barriers that hinder NPs delivery has opened doors for new treatment regimens that seek to mediate these factors. Generally, these approaches involve restoring the abnormal tumor vasculature and interstitial stress towards that of normal tissue, and modifying NPs with environmentally responsive modifications to enhance delivery (**Table 1.1**).

1.7.1 Normalization of Tumor Vasculature Benefits NPs Extravasation

To counter the detrimental effects of abnormal tumor vasculature on NPs transport, strategies to restore normal vasculature have been proposed [66, 88]. Since irregular BM and pericyte coverage hinders the maturation of tumor vasculatures, promoting BM and pericyte recruitment has been proposed to normalize blood vessels [66] Collagen IV, the major constituent of BM, have been shown to be degraded by MMPs. Therefore, the application of MMP inhibitors such as the peptide inhibitor TIMP-1, or a non-peptide inhibitor, AG3340, could inhibit BM remodeling and is considered a promising method for vessel normalization [89]. Another method involves the knockdown of the VEGF signaling pathway. VEGF receptor-2 blocking antibody DC101 can prune immature vessels and recruit pericytes. Proangiogenic molecules, including VEGF, fibroblast growth factor (FGF) and PDGF are overexpressed in tumors and favor angiogenesis [2]. Therefore, VEGF inhibitors can also be applied as an anti-angiogenic agent to revert the vasculature toward a more normal phenotype. A

variety of monoclonal antibodies (mAb) against VEGF and other angiogenic signaling factors have been designed. For example, bevacizumab (Avastin), the first approved anti-angiogenic mAb, and its derivative, ranibizumab have been applied in the treatment of metastatic colorectal cancer. Furthermore, the inhibition of heparanase, which plays a major role in angiogenesis, has also been considered as a promising tumor priming strategy [90]. The resulting modifications reduced size of pores in the vessel walls and decreased IFP, allowing NPs extravasation to occur through convection rather than diffusion, a much faster process for free molecules and small NPs (<12 nm) [8].

Despite these improvements, the smaller vessel pores established through normalization may compromise the advantages gained from enhanced convection for large NPs, since the increased steric and hydrodynamic hindrance inhibit the extravasation process [6, 8]. As an additional consideration, the anticancer agents should be administered during the window of normalization to obtain improved delivery, since vascular normalization is a transient process. Furthermore, this strategy may not lead to desirable results against cancer with compressed and less permeable tumors as seen in the case of pancreatic tumor BXPC3 and breast cancer 4T1. Owing to the thick pericyte coverage that limits diffusion of NPs in these compressed hypovasculature tumor models, strategies to inhibit angiogenesis may lead to diminished NPs accumulation. While somewhat counterintuitive, tumors of the hypovasculature phenotype should be remodeled to improve the leakiness of blood vessels by decreasing pericyte coverage and BM thickness. TGF-β receptor antagonists are the most frequently used therapeutic agents, since low dose TGF-β inhibitor inhibits pericyte recruitment without affecting the function of tumor cells and endothelial cells. Consistent with this finding, various types of TGF-β inhibitors, including small kinase inhibitor and its nano-formulation in addition to siRNA and antibodies, have been used to improve the intratumoral penetration of sub-100 nm NPs, such as liposomes, polymeric micelles and PEI-PEG-coated MSNPs in hypovasculature tumor models [67, 91, 92]. Another approach to improve NPs penetration in the hypovascular models involves the administration of vasoactive agents such as thrombin, lipopolysaccharide endoxin, to initiate a cascade of cellular events that lead to the disruption of endothelial cell junction and increase

vascular permeability. Transiently raising the systemic pressure by infusing vasoconstrictors (e.g., angiotensin II) can also increase the vascular permeability and consequently increase NPs extravasation. A combined treatment might also beneficial for hypovasculature model, with one treatment to alleviate solid stress through depletion of stromal cells or extracellular matrix, and a subsequent or concurrent vascular normalization treatment to improve perfusion [93]. Overall, the approaches for remodeling tumor vasculatures to improve NPs delivery vary with regards to vasculature contents and abnormalities, as well as the size of the therapeutic NPs. One should be cautious when choosing strategies and agents since the efficacy of treatment depends largely on the nature of each specific tumor [67].

1.7.2 Normalization of the Extracellular Matrix Improves NPs Penetration

Apart from activation of chemical signaling, interstitial stromal barriers in desmoplastic tumors physically restrict diffusion of macromolecules and nanotherapeutics within the tumor parenchyma. Attesting to this, Dellian et al observed heterogeneous distribution of stealth liposomal-clusters in the perivascular ECM of a xenograft tumor, indicating the role of ECM in limiting the particle diffusion [94]. In another study, Eikenes et al. showed that the degradation of the structural collagen network is more important than the degradation of the GAG and hyaluronan when attempting to increase diffusion of NPs and macromolecules [58]. Jain and his colleagues further confirmed this finding [15, 95, 96]. Based on these findings, numerous studies have focused on the subsequent or concurrent delivery of collagenase alongside nanotherapeutics to enhance the intratumoral transport of NPs. For example, co-intratumoral injection of oncolytic HSV vector along with bacterial collagenase increased the viral vector distribution by nearly a 3-fold difference in a human melanoma xenograft [97]. In another example, intravenous injection of collagenase-I resulted in higher gene expression of lipoplex in xenograft tumors, further confirming the usefulness of collagen degradation in improving NPs distribution [98]. Enhanced diffusion after modification of collagen production was also demonstrated by the use of hormone relaxin, which was reported to both

stimulate collagenase synthesis and down-regulate collagen production [99, 100]. Additionally, relaxin is safer compared with bacterial collagenase for *in vivo* application and proposed for long term use [20].

Similar to collagen, GAG are also key matrix element that induces vascular collapse; among which, hyaluronan (HA) is a major component [96]. HA polymerizes into cage-like structures, partitioning the interstitial space into aqueous and viscous compartments as previously investigated. The use of hyaluronidase to improve the tumor permeability is controversial. High doses of hyaluronidase collapse the HA-based water swelling cage, increase the ECM viscosity and thereby reduces the diffusion coefficient of NPs [101]. Notably, elevated expression of tumor-derived hyaluronidase has been used as a diagnostic cue for high-grade bladder cancer and limited perfusion, suggesting the negative outcome of combining hyaluronidase with therapeutic NPs [59, 102]. However, in pancreatic ductal carcinoma (PDAC), with HA overpowering collagen and constituting 70% of the ECM, the opposite is observed [54]. In a genetically engineered mouse model of PDAC, PEG-PH20, a PEGylated recombinant human PH20 hyaluronidase, can effectively improve vascular perfusion of doxorubicin and gemcitabine [54]. Intratumoral administration of bovine hyaluronidases has also shown promise in several xenograft models [103, 104]. A recent study in a human osteosarcoma xenograft model indicated that hyaluronidase induced a 4-fold increase in the distribution of liposomal doxorubicin [60]. Therefore, the application of HA is not limited to small molecules and can also be a promising combinatory component to improve the delivery of NPs with larger particle size [54].

However, the aforementioned ECM modifiers may produce collateral damage in healthy tissues (e.g., bacterial collagenase) or increase the risk of tumor progression (e.g., relaxin, matrix metalloproteinases, and hyaluronidase) [105]. Therefore, rather than systemic delivery of these modifiers, site-specific degradation of ECM was preferred and conducted by coating NPs with specific ECM enzymes [106, 107]. Goodman et al indicated that collagenase coated 100 nm gold NPs showed a 4-fold increase in the number of particles delivered to the spheroid core compared with

normal stealth particles [106]. The major concern for enzyme coated NPs is maintaining the enzymatic activity during, and after conjugation with the NPs. Also, the pharmacokinetic profile of the coated NPs proves important as well. Recent work by Ji et al examined these major concerns with enzyme coated NPs platforms and confirmed the applicability of the design for improved NPs diffusion [108].

1.7.3 Disruption of Stromal Cells Improves the Intratumoral NPs Delivery

In addition to high ECM concentrations, desmoplastic tumors are usually characterized with high levels of stromal cell density. This abundance of stromal cells synthesizes and secretes interstitial matrix molecules (i.e. collagen, fibronectin, etc.) that constituent the high interstitial solid stress. Simultaneously, they act as strong binding site barriers for interstitial NPs delivery. TAFs have been considered to be the major component of tumor stroma. The dense ECM associated with TAFs also obstructs the intratumoral vasculature, preventing small molecule and NPs delivery. These findings suggest that TAF represents a potential target for both therapeutic efficacy and NPs delivery. Directly eliminating fibroblasts from the tumor can increase the interstitial transport and distribution of nanotherapeutics by decreasing the tortuosity of the interstitium. For example, off-target distribution of therapeutic NPs through platforms such as cisplatin NPs and Docetaxel conjugates greatly improved the outcome of stroma rich bladder and breast cancer models through depletion of fibroblasts [72, 74]. To improve the therapeutic outcome, targeted depletion of fibroblasts was investigated in detail. One example is the oral DNA vaccine that targets fibroblast activation protein (FAP), which is commonly overexpressed on TAFs [109]. The DNA vaccine specifically depleted fibroblasts and improved the delivery of the therapeutic agents [109]. Later on, TAF-targeted NPs, such as FAP antibody conjugated immuno-liposomes and FAP substrate conjugated drugs, were designed to specifically deplete TAFs [110, 111]. Though depletion of TAFs undoubtedly induced an increased vessel perfusion and enhanced NPs diffusion, two recent studies also suggest that eliminating stroma by targeted deletion of fibroblasts results in undifferentiated progression of

aggressive pancreatic cancer, suggesting the paradoxical effect of TAF depletion [112]. One explanation for the paradox is that these depletion strategies run the risk of eliminating key stromal components needed for tissue homeostasis. Furthermore, the off-target distribution of chemotherapy in fibroblasts may induce senescence in TAFs, a procedure that will induce the growth and resistance of neighboring tumor cells and ultimately stiffen ECM, limiting NPs perfusion in the long run [113]. To prevent this paradox, alternative approaches were adopted to remodel fibroblasts and ECM. Note that resting fibroblasts (normal fibroblasts) can be transdifferentiated into TAFs in response to cytokines (i.e. TGF-β, PDGF and sonic hedgehog (SHH) [114-116]), growth factors, oxidative or metabolic stress, and synthesize abundant ECM proteins to support tumor proliferation. Therefore, the pharmacological means to reprogram TAFs back to this quiescent state would be a promising strategy to inhibit tumor growth and improve NPs delivery [117, 118]. Recent studies by Diop-Frimpong et al indicated the downregulation of TGF-β signaling in TAFs by an angiotensin receptor inhibitor, Losartan, could reprogram and reduce the activity of TAFs, decreasing the synthesis of collagen I and thus improving the intratumoral penetration of NPs [105]. Success from this formulation has led to a phase II clinical trial of Losartan along with FOLFIRINOX in patients [88, 119]. Vitamin D Receptor (VDR) has also been shown to be overexpressed in the pancreatic stellate cells (PSC), an activated form of TAFs in PDAC. Sherman et al suggested that the VDR ligand acts as a master transcriptional regulator of PSC to reprise the quiescent stroma, reduce the fibrotic content and increase intratumoral vasculatures; which is promising for enhancing NPs delivery [117]. Evidence presented above emphasizes the advantages of stromal cell reprogramming over depletion. Despite diluting the ECM components for increased NPs perfusion in the reprogramming strategy, high cell densities still act as a *binding site barrier* for NPs with high cell binding affinity, which limits the outcome of this strategy. Considering the spatial intratumoral distribution of TAFs and blood vessels as discussed in the earlier sections, fibroblasts are a more likely target for NPs and regarded as a therapeutic target. Instead of depletion and transdifferentiation back to noncancerous fibroblasts, TAFs can be reprogrammed into killer cells that secrete toxins or other factors that inhibit the proliferation of

neighboring tumor cells. Fibroblasts can be engineered into macrophage like cells, providing us hope for *in situ* engineering using NPs delivered agents to convert fibroblasts into natural killers [120].

1.7.4 Design of Extracellular Matrix Targeted NPs

Specific characteristics of the TME can either be utilized, or modified for improving NPs drug delivery (**Table 1.2**). Both strategies can be divided into two categories. These methods are primarily based on the notion that the EPR effect allows improves NPs accumulation in tumors over free drugs. In terms of the first strategy, stimuli-responsive NPs can be designed to release the free drug in the tumor interstitium. This method is advantageous as it overcomes the limitation of barriers in the ECM for large sized NPs. Stable hydrophobic drugs with membrane permeability could be used as candidate drugs, for example, doxorubicin (DOX). The hydrophobic drug could be directly conjugated to a hydrophilic polymer through an ECM cleavable linkage, or the segments of block copolymers could be connected by stimuli-cleavable linkers and further assembled into micellar NPs [121]. Another strategy is based on the premise that the *binding site barrier* hindered NPs distribution. To improve the penetration, stealth materials, such as PEG, were linked to the NPs with stimuli-responsive linkers as a shielding layer. The degradation and cleavage of this shield triggered by the TME resulted in the exposure of targeting ligands, which lead to the efficient internalization by neighboring cells [122]. The aforementioned ECM stimuli, distinct from intracellular stimuli, are usually referred to as extracellular stimuli, including temperature, acidic pH and enzymes. When designing the responsive structure, the structure should be smart enough to distinguish the extracellular signals from intracellular signals, and thus achieve the original designed purposes.

Temperature Responsive NPs. Temperature is originally considered as an external stimuli (e.g. magnetic field), generated by using external forces [123]. Temperature responsive materials was first found during hyperthermia treatment of tumors, dated back to 1970s, and lately became a major constituent of chemotherapy and used as a complementary strategy for hyperthermia treatment [123, 124]. However, in early 1990s, studies revealed that the core temperature of breast cancer was higher

than the peripheral tissues, suggesting that temperature is not only applied as an external force but also an internal physicochemical feature of the ECM [125]. Abnormal temperature gradients were also observed later in brain tumors and melanoma [126, 127]. It is suspected that the elevated temperature in tumor regions is due to glycolysis degradation and reaction, energy exhaustion [128]. Temperature dependent response is usually governed by a sharp nonlinear change in the conformation and physicochemical properties of at least one component of the nanoformulations across their phase transition temperature. The sharp response triggers the release of free drugs from the cargos. Ideally, materials exhibiting relatively sharp thermal phase transitions around body temperature would be utilized to form the thermo-response NPs [123]. The commonly used chemicals are summarized in figure, among which the thermo-responsive polymer, including poly(N-isopropylacrylamide) (PNIPAM), poly(vinyl chloride) (PVC) and their derivatives were most widely investigated. Thermo-responsive NPs were designed according to the aforementioned two strategies. Besides polymer micelles, liposome and peptide conjugates were also designed with thermal responsive components [129]. For liposomes, temperature responsiveness usually arises from a phase transition of the constituent lipids and the associated conformational variations in the lipid bilayers [123]. However, since the tumor temperature is hard to detect, most of the studies in this field focus on the *in vitro* characterization.

Tumor acidity Due to the production of lactic acid converted from glucose during the aerobic glycolysis (also known as the Warburg effect, the hallmark of tumors), the extracellular pH of most tumor tissues is mildly acidic in the range of 6.5-6.8, which is in between that of blood (7.4) and lysosome pH (6.4) [130, 131]. pH variations between pathological situations and the normal tissues have been exploited to trigger the release of therapeutic drugs and imaging agents [121]. Notably, pH-dependent delivery systems designed on the basis of this subtle pH difference require that the systems possesses ultrasensitive pH-responsiveness [132]. In the past decades, pH sensitive polymers that are synthesized to meet the requirement include tertiary amine-containing methacrylate copolymers, poly(β-amino ester) (PAE) and poly(sulfadimethoxine) (PSD), as well as those containing pH-

sensitive chemical bonds (e.g., imidazole functionality of histidine, 2,3-dimethylmaleic anhydride (DMMA) modified amine moieties) [121]. Accordingly, designs of nanoformulations can be classified into two categories. One is the use of polyacids or polybase with ionizable groups that undergo conformational changes in response to environmental pH variations; the other is the design of polymeric systems with acid-sensitive bounds whose cleavage enables the release of molecules anchored at the polymer backbone. For example, a series of micellar NPs possessing ultrasensitive pH-activatable fluorescence emission were formulated by Gao's group [132, 133]. The pH-activatable nano-probe was composed of a PEG conjugated poly(2-(hexamethyleneimino)ethyl methacrylate) copolymer and showed a micellization-disintegration transition within a narrow pH range of 0.25 units. The release of fluorescent dye from micelles in response to extracellular pH can nonlinearly amplify tumor microenvironment specific signals for imaging purposes [132].

Extracellular Enzymes In the tumor tissue microenvironment, specific enzymes, including MMPs, phospholipases, glycosidases and esterases, etc., are present with high concentrations and abnormally high activity [121]. Therefore, they have been extensively exploited to modulate targeted drug delivery and release. The first approach is the direct conjugation of lipophilic drugs to a hydrophilic polymer via enzyme cleavable linkage, and further self-assembled into micelles for both anti-tumor drug delivery and tumor imaging. One such linker is the MMPs specific cleavable peptide Gly-Pro-Leu-Gly-Val (GPLGV) [134]. The PEG-peptide-DOX micelle formulation improves the release and delivery of DOX both *in vitro* and *in vivo* [134, 135]. The second approach is to use the enzyme-cleavable linkers to link segments of polymers or to use enzyme-degradable materials to loaded chemotherapeutic drugs or imaging agents and release them via enzyme degradation. Enzyme-cleavable linkers crosslinked with hydrogel is among one of the most commonly used formulations. For example, cisplatin was loaded in PEG-diacrylate hydrogel wafers linked with an MMP substrate. The controlled release of cisplatin from the hydrogel upon MMP degradation improved the therapeutic outcome for the treatment of Glioblastoma multiform (GBM) [136, 137]. Gelatin is another frequently used nanocarrier that can be degraded by MMP-2, which is overexpressed in the

ECM. A recent study by Wong et al. indicated that a multistage NPs composed of 100 nm gelatin core covered with 10 nm quantum dots showed deep tumor diffusion. The triggered release of smaller NPs upon MMP degradation lowered the diffusional hindrance in the interstitial matrix compared to larger NPs. In the meantime, the lymphatic clearance rate for 10 nm NPs was significantly lower in comparison with free small molecular drugs [3, 16].

1.8 Conclusions and Future Perspectives

The treatment of tumors requires efficient delivery of therapeutic agents to the target cells through a series of transport steps, including vascular transport, transvascular transport and interstitial transport. The dense ECM structure and aberrant tumor vasculature constitute the physiological barriers that hinder the transport of NPs through these steps, and subsequently limit therapeutic outcome. In this review, we summarized the barriers and provided strategies to overcome these barriers for improved NPs delivery. However, penetration alone is not the only criteria to evaluate therapeutic response. Firstly, the approaches to remodel the TME for enhanced NPs transport may controversially promote tumor cells migration and metastasis, compromising or even reversing the therapeutic effects. As seen, degradation of collagen improves the NPs diffusion, but also increases the risk of tumor cell migration by eliminating barriers that usually prevent it. Using cell-based delivery systems such as stem cells with homing properties, may overcome the delivery barriers without adversely changing the TME. Secondly, heterogeneous distribution of NPs in the interstitium and disparate internalization of NPs to stromal cells may result in acquired resistance from TME and eventually lead to the treatment failure. Therefore, the current challenge is to design multifunctional NPs to target both tumor and stroma cells, blocking the resistant tumor-stroma crosstalk [138]. The heterogeneity of the TME also differs across different cancers or even individuals. So the optimal design of NPs is likely to be specific to each case. This is a formidable task, especially considering the differences between one type of tumor and another. However, this review emphasizes the heterogeneity as a potential reason for the discrepancy between the successes of many formulations in

preclinical studies but later failure in clinical trials. Further, we hope to provide guidance for the possibility of individual therapy.

Thirdly, in addition to delivering therapeutic and diagnostic NPs to solid tumors, the delivery of NPs to metastatic sites for cancer therapy is even more difficult considering the difference in TME between primary tumors and the metastatic niche. Recently, Swami et al. approached this challenge by formulating NPs to target myeloma and the bone metastatic microenvironments [139]. Furthermore, a recent study on the relationship of melanoma-derived exosomes, which induce vascular leakiness at pre-metastatic sites, may provide a means of passively targeting NPs to metastatic sites [140]. More systemic cancer treatments may require the combination of immune therapy, and other methods.

Overall, the advancement of NPs mediated cancer drug delivery has been fueled by discoveries in material science. These advances allow the development of nanotherapeutics that can cater to a seemingly endless number of situations. As examined, this versatility is crucial considering the differences between each tumor and across different patients. As each specific case demands its own specific treatment approach, the diversity of investigated and available nanotherapeutics proves promising to the advancement of cancer treatment.

Table 1.1 Summary of stromal barriers and strategies

Major Barriers	*Type*	*Barriers Constituent*	*Barriers Mechanism*	*Strategy Mechanisms*	*Strategy Agents*	*Applied Tumor Models*	*Ref*
Vasculature		Angiogenesis; Tortuosity; Low blood flow; High viscosity	IFP increase; Solid stress Increase; *EPR effect* decrease	Normalization	DC101 (VEGF-R mAb); bevacizumab, ranibizumab (VEGF mAb); SST0001 (Heparanase inhibitor); Trastuzumab (HER2-R mAb)	Hypervasculature: colon carcinoma, myeloma, melanoma	[2, 20, 67, 90]
				Leakiness Improvement	Imatinib (PDGF antagonist); LY364947 (TGF-β inhibitor); Thrombin (vasoactive agents) Angiotensin II (transient vessels pressure raising agent)	Hypovasculature: pancreatic, lung and breast carcinoma	[52, 67, 68]
Stroma	**BM**	Collagen IV	Thickness, mesh size, orientation, and density limit NP penetration	Degradation	Collagenase; MMPs	Lung and breast carcinoma	[48]
		Nidogen	Crosslinking Collagen Network, and hinder the anionic NP	-	Modulating the surface charge and antifouling effect of NP	-	[2, 51, 58]
		Perlecan					
		GAG	Trap the cationic NP	-		-	
	ECM	Collagen I	Same as Collagen IV	Degradation	Collagenase; Relaxin	Lung carcinoma, melanoma	[97-99]
		HA	Partitioning collagen matrix into aqueous and viscous compartments	Degradation (Paradox)	Hyaluronidase; PEGPH20	Osteosarcoma, PDAC	[54, 60]
Stromal Cells	**TAFs**		Secrete ECM molecules, stiffen ECM	Reprogram to Normal Fibroblasts	Losartan (inhibit collagen synthesis); VDR inhibitor (inhibit TAFs activation)	Breast carcinoma, PDAC	[105, 117]

			Off target depletion NP	TAF Depletion (Paradox)	cisplatin NP and Doxectaxel conjugates; pFAP (anti-FAP vaccine); FAP substrate-drug Conjugates; FAP targeted liposomes	Stroma Rich Bladder Cancer; 4T1 breast cancer; colon	[72, 74, 110, 111]
	Pericytes		Regulate vasculature maturation and limit NP penetration		TGF beta inhibitors PDGF-β inhibitors VEGF inhibitors	Pancreatic and breast carcinoma	[66, 68, 92]

Table 1.2 Design of ECM targeted NP[2]

Stimuli Factors	Major Stimuli Structure	Formulation	Materials	Stimuli Criteria	Disease Model (Cell line)	Drug	*In Vitro*& *In Vivo*	Ref.
Thermo Sensitive	**PNIPAAm**	Polymeric Micelle	PNIPAAm-*b*-PLA	LCST 36°~40°	-	Dox	*in vitro*	[141]
			P(NIPAAm-*co*-NDAPM)-*b*-PCL	LCST 36.5°	-	Prednisone Acetate	*in vitro*	[142]
			PNAS-*b*-PNIPAAm-*b*-PCL	LCST 36.5°	Hela	Dox	*in vitro*	[143]
			DHBCS, PEG-*b*-PNIPAM	LCST 32.0°	PKH26	Dox	*in vitro*	[121]
	PNVCL		Chitosan-*g*-PNVCL	LCST 38.0°	L929, MCF7, PC3, KB	Curcumin	*in vitro*	[144, 145]
			P(mNVCL)-*co*-PNVCL	LCST1 20~24°; LCST2 30~42°	B16-F10 melanoma	Dox	*in vitro*	[146]
	DPPC, DSPC	Liposome	DPPC, DSPC, CHOL, DSPE-PEG2000	Tm 41°	SK-BR-3,MDA-MB-435 breast cancer; U87-MG glioma; B16F10	Dox	*in vivo & in vitro (external)*	[147, 148]
	Leucine Zipper Peptide	Lipid-peptide NP	Leucine zipper peptide;DPPC, DSPC,MSPC, HSPC	Tm 40°	B16F10, SW480	Dox	*in vivo & in vitro*	[149]
	Elastin & Elastin mimetic	NP	Elastin/DNA aggregation	Tm 50-60°	-	-	-	[150]
pH Sensitive	**PHis**	Micelle	PEG-PHis-PLL or PLL-*b*-PEG and PHis-*b*-PEG Mixed	pKa ~6.5; dissembling	4T1 breast cancer	Dox	*in vivo*	[142, 151, 152]
			PHEMA-*b*-		HCT116	Dox	*in vivo*	[15

[2]PNIPAAm, poly(N-isopropylacrylamide); NDAPM, N-(3-(dimethylamino)propyl)methacrylamide; PNAS, poly(N-acroyloxysuccinimide); PNVCL, poly(N-vinylcaprolactam); DPPC, 1,2-dipalmitoyl-sn-glycero-3-phosphocholine; DSPC, 1. 1,2-distearoyl-sn-glycero-3-phosphocholine; PAE, polyacrylic ester; PSD, polysulfonamide

			PHis		human colon		*& in vitro*	3]
	PAE		PEG-*b*-(PLA-*co*-PAE)	pKa ~7.0	HepG2	Dox	*in vitro*	[154]
			PEG-PAE		BT-20, B16F10 melanoma	Paclitaxel	*in vitro*	[155]
	PC7A		PEG-b-PC7A	pKa ~6.9	A549	Fluorescence	*in vivo*	[132, 133, 156]
	PSD	Polyplex	PEG-PSD/PEI NP	pKa ~7.0	A2780, human ovarian carcinoma	Gene	*in vitro*	[157]
	Chitosan	NP	Chitosan-silica nanospheres	pKa~6.3; swelling	MCF-7 Breast cancer	TNFα	*in vitro & in vivo*	[158]
Enzyme Sensitive	**MMP2-cleavable octapeptide**	liposome	PEG-MMP cleavable peptide-PE (Gly-Pro-Leu-Gly-Ile-Ala-Gly-Gln)	MMP	4T1 breast cancer	Fluorescent probes	*in vitro & in vivo*	[159]
	gelatin	NP	gelatin-gold/quantum dots fabricated multistage NP		C6 glioma cells	Gold NP, quantum dots	*in vitro & in vivo*	[3, 160]
	GPA peptide sequence	Drug Conjugate	Peptide-FAP cleavable substrate-promelittin protoxin	FAP	MCF7 breast cancer	promelittin protoxin	*in vitro & in vivo*	[110]

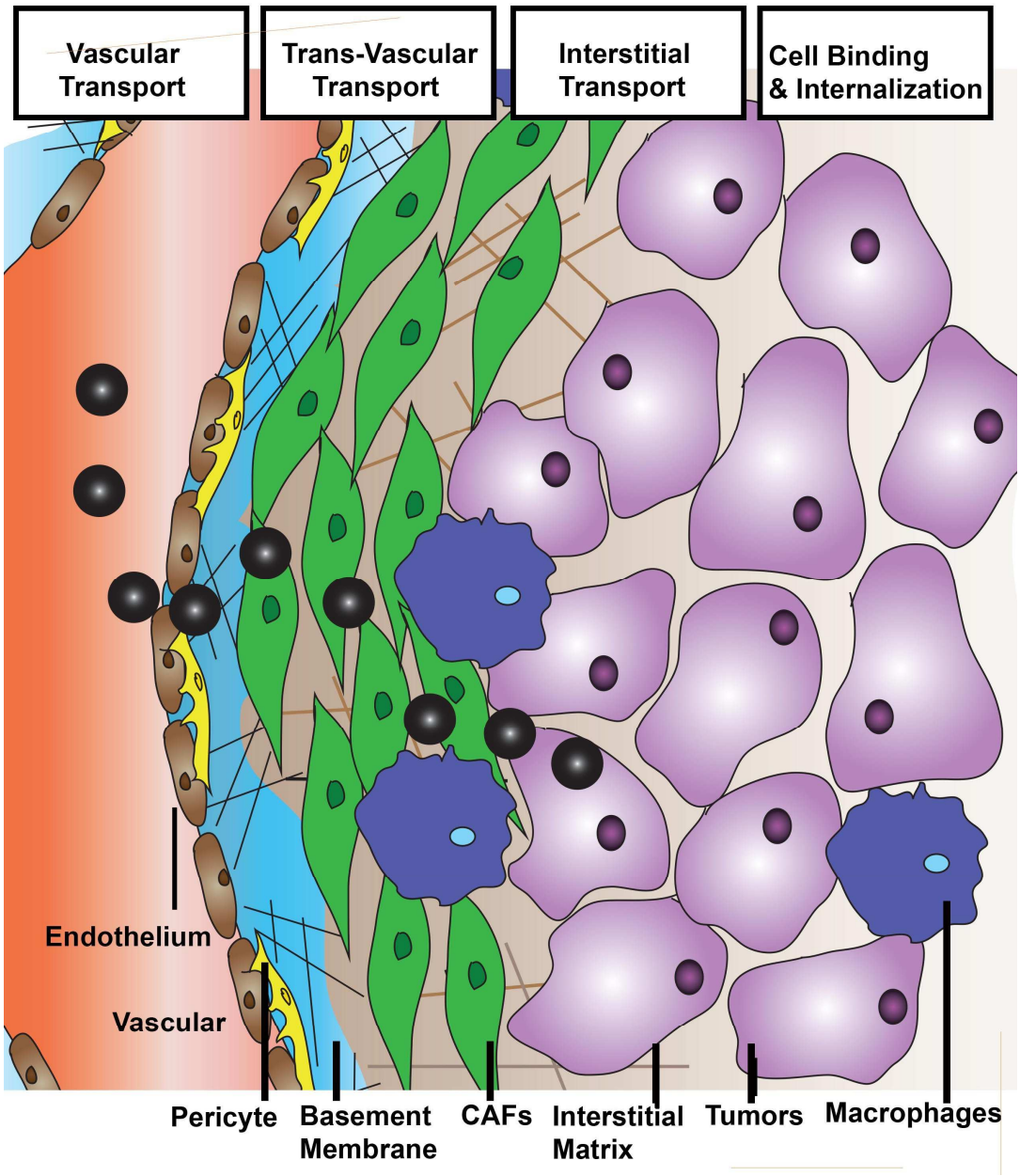

Figure 1.1 Scheme of desmoplastic tumors

CHAPTER 2: THE BINDING SITE BARRIER ELICITED BY THE TUMOR ASSOCIATED FIBROBLASTS INTERFERES DISPOSITION OF NANOPARTICLES IN THE STROMA-VESSEL TYPE DESMOPLASTIC3

2.1 Summary

The binding site barrier (BSB) was originally described decades ago that binding of antibody to cells near the vessel prevents it from deep penetration into the tumor. It is revisited herein with respect to the intratumoral cellular disposition of nanoparticles (NPs). Specifically, BSB limits NP diffusion and results in unintended internalizations of NPs by stroma cells localized near the blood vessels. This not only limits the therapeutic outcome, but also poses the danger of off-target adverse effects. In the current study, we showed that tumor associated fibroblasts (TAFs) are the major component of the BSB, particularly in desmoplastic tumors with a *stroma-vessel* architecture where TAFs align with the blood vessels. Specifically, TAFs' distance to blood vessels, expression of receptor proteins, and binding affinity affect the intensity of BSB. The physical barrier elicited by extracellular matrix also prolongs the retention of NPs in stroma, potentially contributing to BSB. The influence of particle sizes on the BSB was also investigated. The highest BSB was found with small (~18 nm) NPs targeted with the anisamide ligand. The uptake of these NPs by TAFs was about 7-fold higher than that of the other cells 16 h post intravenous injection. This was because TAFs also expressed the sigma receptor under the influence of TGF-β secreted by the tumor cells. Overall, the current study underscores the importance of BSB in the delivery of nanotherapeutics and provide rationale of exploiting BSB to target TAFs.

---

[3]This chapter previously appeared as a manuscript soon to be submitted

2.2 Introduction

The BSB hypothesis was originally proposed by Weinstein to explain the non-uniform distribution of monoclonal antibodies in tumor nodules [161, 162]. Specifically, he proposed that cell populations localized near the blood vessels with high antigen density and binding affinity are likely to elicit strong BSB [161, 162]. Beyond affecting antibodies, the BSB may be extended to the intratumoral dispositions of NPs [87]. Unintended binding of NPs to cells in vicinity of the blood vessels may significantly decrease the number NPs available for penetration into the tumor matrix [73]. Considering the heterogeneous stromal cell populations around the blood vessels, unintended uptake of NPs into these cells constitutes the basis of the off-target effect [81, 87].

Stromal desmoplasia, in conjunction with tumor associated fibroblasts (TAFs), localize near blood vessels in multiple solid tumor systems such as pancreatic adenocarcinoma (PDAC), non-small cell lung cancer (NSCLC), aggressive urothelial carcinoma and breast cancer, suggesting TAF's potential as major component of the BSB [68, 71, 163-166]. Previous studies conclude that TAFs can enhance cancer cell proliferation, invasion, and contribute to immune suppression [167]. Resultantly, destruction of TAFs through off-target distribution of therapeutic NPs has emerged as a promising therapeutic approach. The depletion of fibroblasts then decreases the synthesis of ECM proteins, downplaying mechanical barriers and facilitating targeting to tumor cells [72, 74]. However, recent studies paradoxically indicated the role that TAFs play in constraining tumor growth. Specifically, the transgenic depletion of FAP positive fibroblasts facilitated tumor growth and metastasis in a PDAC model [112, 168]. Furthermore, off-targeted distribution of therapeutic agents to TAFs may elicit paracrine secretion of survival factors such as Wnt16, promoting neighboring tumor cells' drug resistance [169]. Moreover, the response of tumor cells and TAFs toward therapeutic agents is inconsistent across different models, leading to discrepancy in treatment outcomes [71]. Collectively, the investigation of fibroblasts as BSB is of great significance in understanding and solving off-target effects for the dilemma at hand.

Herein, the function of fibroblasts as BSB for NPs uptake was quantitatively investigated using lipid coated calcium phosphate nanoparticles (LCP NPs). LCP NPs possessed a steric surface with brush PEG coating and cationic lipid shell for enhanced uptake and release. In addition, LCP NPs demonstrated stable delivery of several modalities including macro-biomolecules and small phosphorylated drugs [170, 171]. Therefore, LCP NPs were used to evaluate tumor perfusion and predict therapeutic outcomes. By tuning the surfactant ratio, LCP NPs could also be prepared with variable sizes [172]. The influence of particle sizes on the BSB uptake was also investigated. Anisamide (AA), a model targeting ligand, was added on the surface of LCP NPs to evaluate the role of targeting ligands in dictating intratumoral cellular association of NPs [173]. To investigate fibroblasts' role on BSB, their distance to blood vessels, expression of receptor proteins, and binding affinity were quantified. An *in vitro* tumor spheroid model was also established to evaluate the BSB. Based on the spheroid model, a mathematical model was created to assay the influence of each independent parameter. Overall, this study emphasizes the role of the BSB in dictating NPs delivery. Considering the large population of stromal cells, this study also investigates a platform to quantitatively evaluate the effect of the BSB on other stromal cell populations, providing guidance for NP-mediated treatment of desmoplastic tumors.

2.3 Methods and Materials

2.3.1 Materials

Dioleoylphosphatydic acid (DOPA) and 1,2-dioleoyl-3-trimethylammonium-propane chloride salt (DOTAP) were purchased from Avanti Polar Lipids, Inc. (Alabaster, AL). 1,2-distearoryl-sn-glycero-3-phosphoethanolamine-N-[methoxy (polyethyleneglycol-2000) ammonium salt (DSPE-PEG2000) and 1,2-distearoryl-sn-glycero-3-phosphoethanolamine-N-[amine (polyethyleneglycol-2000) ammonium salt (DSPE-PEG2000) were obtained from NOF America Corporation. The hydrophobic dye, 1,1'-Dioctadecyl-3,3,3',3'-tetramethylindocarbocyanine perchlorate (DiI) was purchased from Thermo Fisher Scientific, Inc. (Carlsbad, CA). Double-strand

oligo DNA (sense sequence, 5'-CAAGGGACTGGAAGGCTGGG-3') and Texas-Red labeled sense-strand oligo DNA (sequence: 5'-[TxRd]CAAGGGACTGGAAGGCTGGG-3') were both synthesized by Sigma Aldrich (St. Louis, MO). Cholesterol, 4-methoxybenzoyl chloride, 2-bromoethylamine hydrobromide, N,N-diisopropylethylamine (DIPEA) , dichloromethane, triton X-100, Igepal CO-520 and cyclohexane were purchased from Sigma-Aldrich (St Louis, MO) without further purification.

2.3.2 Cell Culture and Animals

The human bladder transitional cell line (UMUC3) was provided by Dr. William Kim (University of North Carolina at Chapel Hill, NC). The mouse melanoma cell line D4M was a gift from Dr. Constance E. Brinckerhoff (Geisel School of Medicine at Dartmouth, NH). The mouse embryonic fibroblast cell line (NIH3T3), mouse breast cancer 4T1, human melanoma cell line A375lu, and human non-small cell lung cancer H460 were obtained from UNC Tissue Culture Facility. These cell lines were cultured in Dulbecco's Modified Eagle's Media (DMEM) (Invitrogen, Carlsbad, CA) (for UMUC3, A375lu, H460), Advanced MEM Media (For D4M), RMPI1640 (For 4T1) supplemented with streptomycin (100 μg/ mL) (Invitrogen), penicillin (100 U/mL), and 10% fetal bovine serum (Sigma, St. Louis, MO) respectively. NIH3T3 was cultured in DMEM supplemented with 10% Bovine calf serum (Hyclone, Logan, Utah). Cells were cultured in a humidified incubator at 37 °C with 5% CO_2.

Female athymic nude mice used in all studies weighed between 22–28 g and were 6–8 weeks of age. They were provided by the University of North Carolina animal facility. Animals were cared for in the Center for Experimental Animals (an AAALAC accredited experimental animal facility) at the University of North Carolina. Experimental animal handling procedures were performed following the protocols conformed to the Guide for the Care and Use of Laboratory Animals and approved by the University of North Carolina Institutional Animal Care and Use Committee.

2.3.3 Synthesis of DSPE-PEG$_{2000}$-AA

The synthesis was performed according to the previous synthetic protocol with some modifications [173]. Firstly, an aqueous solution of 2-bromoethylamine hydrobromide (1.32g, 6.4 mmol) was mixed with 4-methyoxybenzoyl chloride (1g, 5.8 mmol) in 50 mL of warm benzene to synthesize the N-(2-bromoethyl)-4-methoxy-benzamide. The mixture was shaken and cooled under running water. At the meantime, a 5% aqueous solution of sodium hydroxide was added dropwise to the mixed emulsion. The precipitate was solidified out of the reaction mixture within a few minutes to form an amorphous mass. The mixture was continued stirred for 1h. And then, the sold amide was filtered with suction and washed once with benzene and air dried for 2-3h [174]. Then, the synthesized N-(2-bromoethyl)-4-methoxy-benzamide (100 mg, 0.4 mmol) was reacted with DSPE-PEG-NH_2 (100 mg, 23.3 μmol) in acetonitrile (5 mL) in the presence of DIPEA (30 μL, 0.2 mmol) at 65-70 °C for 16h. After removing the solvent by rotary evaporation, 5 mL of methanol was added to dissolve the pellet followed by precipitating with excess ether (50 ml). The mixture was then kept at -80 °C overnight. Afterwards, the precipitate was collected by centrifugation and recrystallized twice. The overall yield was 70%. The product was characterized by NMR and TLC as reported elsewhere [173].

2.3.4 Preparation of LCP NPs with Tunable Size

Briefly, one hundred μL of 500 mM $CaCl_2$ was dispersed in 8 mL of oil phase containing Igepal CO-520/cyclohexane (29:71, V:V). The other emulsion was prepared by adding 100 μL of 100 mM pH9.0 Na_2HPO_3 into a separate oil phase. Another 185 μL of 37.5 mM DOPA was added to the phosphate phase before mixing of the two separate emulsions. The mixed emulsion was then stirred for 45min, and 16 mL of ethanol was added and the mixture, which was centrifuged at 10,000 g for 15 min to remove the surfactants and cyclohexane. After being washed with ethanol twice, the pellets were re-dispersed in 250 μL of chloroform for storage. To label the LCP core, 16 μL of 2 mg/mL Texas Red labeled oligonucleotide was added to the $CaCl_2$ phase and the LCP core was prepared with

the same method as mentioned above. To tune the LCP core size, a Trition surfactant system (cyclohexane/hexanol/Trion X-100=75/0/15, v/v/v) was mixed with the original Igepal surfactant system. As the portion of the Triton surfactant system increased (from 1:0, to 1:7, as Igepal:Triton surfactant), the size of LCP core could be enlarged from 8~10 nm to ~50 nm. To create the outer leaflet coating, 100 μL of 20 mM DOTAP, 100 μL of 20 mM cholesterol and 50 μL of 20 mM of DSPE-PEG_{2000} (all in chloroform) were mixed with the LCP cores. After the removal of chloroform, the precipitate was suspended in a small volume of pre-warmed THF and ethanol, and then dispersed in water. As expected, when the cores size increased to 50nm, the final LCP enlarged to around 65nm in diameter. To create the AA targeted LCP NPs, 20 μL of 20mM DSPE-PEG_{2000}-AA was mixed with 30 μL of 20mM DSPE-PEG_{2000} and added to the outer leaflet lipid mixture followed by the same preparation method.

Particle size and zeta potential of purified LCP NPs were measured using a Malvern ZetaSizer Nano series (Westborough, MA). The morphology of LCP cores and LCP NPs were determined by TEM microscopy (JEOL 100 CS II). The final LCP NPs were negatively stained with 2% uranyl acetate.

2.3.5 Preparation of Fluorescence-labeled LCP NPs

The LCP NPs was prepared using a previously described method with some adjustments. Additional details of NPs manipulation are provided in the *Supplementary Methods*. To label the final LCP NPs, 0.5% DiI (mole/mole) was mixed with the outer leaflet lipid solution before the solvent was removed. Sucrose gradient centrifugation was performed to remove the excess lipid. Briefly, LCP NPs were loaded into a tube containing a sucrose density gradient ranging from 0% to 60% (w/w). After ultra-centrifugation at 40,000 g for 3 h, excess lipids in the upper part of the gradient were separated from the dense LCP, which formed a sharp band around the 10~30% layer in the gradient. The morphology from each layer was confirmed by TEM.

2.3.6 GFP/RFP Lentivirus Transduction in NIH3T3 Fibroblast and UMUC3

Lentiviral agents with RFP and GFP were generously provided by Dr Shawn Hingtgen (University of North Carolina at Chapel Hill, NC). The virus particles were assembled via transfecting 293FT packaging cells. The virus-containing culture medium was harvested and filtered through 0.45-μm syringe filters 48 to 96 hours post-transfection. NIH3T3 fibroblasts and UMUC3 cells were then infected by exposure to virus-containing medium for 48 hours, maintained in the complete medium, followed by selection in puromycin.

2.3.7 Sigma Receptor Silencing with Small Hairpin RNA (shRNA) in NIH3T3 Cell Lines

Sigma R shRNA lentivirus particles and control shRNA lentiviral particles were purchased from Santa Cruz. The transduction process were performed followed the protocols provided by the manufacturer. In brief, the NIH3T3 and GFP transfected NIH3T3 cells were infected by exposure to virus-containing medium for 12 to 16h, maintained in the NIH3T3 complete medium, followed by selection in puromycin. The interference of Sigma R was confirmed by western blot with pretreating the cells with TGFβ (10 ng/mL, 24h).

2.3.8 Preparation of Tumor Models

Female nude mice (18~22 g) were inoculated subcutaneously with a combination of NIH3T3 (2.5×10^6 cells) and UMUC3 (5×10^6 cells), or with H460 (5×10^6 cells, 100 μL) to form the stroma-vessel phenotype tumor model, or with A375lu (5×10^6 cells, 100 μL) to form the tumor vessel phenotype tumor model. The 4T1 cells (5×10^5 cells, 50 μL) were orthotopically inoculated into the breast fat pads of the BALb/c mice and the D4M. 7A cells were injected intradermally (3×10^5 cells, 50 μL) into C57/B6 mice to form the stroma-vessel and tumor-vessel type models, respectively, in the syngeneic host.

2.3.9 Plasma Clearance

Tumors were allowed to grow until reaching a diameter of 4–8 mm (2–3 weeks post-inoculation) for *in vivo* pharmacokinetics and biodistribution studies. Mice were injected intravenously via the tail vein with 3H labeled LCP NPs with similar 3H levels. At 5 min, 15 min, 30 min, 1, 2, 4, 8, 12, 24, 48, and 72 h post-injection, blood samples were collected from the saphenous vein using a heparinized capillary tube. The amounts of radioactivity in the blood and tissue samples were determined by liquid scintillation.

2.3.10 Intratumoral Distribution of LCP NPs.

^{3}H (^{3}H-chesterolester) -labeled LCP NPs were intravenously administered into nude mice bearing UMUC3/3T3 GFP (300 mm^3) (n = 4). At determined time points, mice were euthanized. Tumor tissues were transferred to a dish and dissociated with tumor cell digestion solution (1 mg/ml collagenase A, 0.1 mg/mL HAse, 0.2 mg/mL DNAse), followed by incubation at 37°C for 40 min. Dissociated tumor cells were then collected by centrifugation. Extracellular radioactivity was collected from the supernatant. This method was validated previously to produce highly pure cytoplasmic fractions. Dissociation of the tissue samples likely leads to a certain degree of cell rupture: therefore, the amount of ^{3}H-LCP NPs measured in the intracellular fractions may be an underestimate. However, it should be noted that all tumors harvested from each treatment groups were homogenized in the same manner. In this way, the data afforded relative comparisons with no preferential bias towards mice treated with either method.

2.3.11 Measurement of Binding Affinity of L-LCP NPs for UMUC3 and Activated NIH3T3.

A modification of the method reported by Zhou et al. (2007) was performed to determine the binding affinity of LCP NPs to Sigma R expressing cells. Briefly, 2×10^5 UMUC3 cells, NIH3T3 cells (activated with TGF-β 10ng/mL, overnight), or GFP-positive fibroblasts sorted from the tumor tissues were incubated with various dilutions of DiI labeled L-LCP NPs (+/- AA) at 4 °C for 40min (concentration of NPs ranges from 0.31-2.5 nM) in FACs buffer. Considering the similar surface

properties of LCP to liposomes, the concentration of LCP NPs was roughly converted from the concentration of phospholipid on the basis of the approximate number of phospholipid molecules per 120 nm liposome (80,000). Then the reaction was stopped by washing twice with FACs buffer. Afterwards, the amount of cell-bound NPs was quantified by flow cytometry in BD FACs Machine. Kd values were determined by the following equation:

$$\mathrm{MFI} = \mathrm{MFImin} + \mathrm{MFImax}\left(\frac{[NP]}{Kd+[NP]}\right),$$

where MFI=mean fluorescence intensity, MFImin=background fluorescence, MFImax was calculated from the plot. The term [NP] has been substituted for [NP-NP_{bound}], the unbound NP concentration, based on the assumption that the concentration of bound NPs is much less than total NPs.

2.3.12 Flow Cytometry Analysis.

To study the kinetics of the intratumoral cell populations that took up NPs, DiI-labeled LCP NPs (S/L, +/- AA) at a dose of 300 μg/kg DiI were intravenously administered into nude mice bearing UMUC3/GFP-3T3 xenograft (tumor volume, 400~600 mm^3, n=3~6 for each group). The mice were euthanized at determined time points and tumor tissues were collected. Fresh tumor tissues were dissociated with the digestion solution to generate a single cell suspension. After red blood cell lysis, cells were washed with PBS and subjected to flow cytometry analysis. To study the non-target LCPs NP (S/L) dispositions in 4T1, H460, D4M, A375Lu at early time point, the same dose of DiI-LCP NPs was intravenously injected into mice bearing different tumors. Mice were sacrificed 8 h post injection and subjected to the same treatment as mentioned above. After obtaining single cell suspensions, cells were fixed with 2 % paraformaldehyde. For the staining of fibroblasts with PDGFRα, the fixed cells ($5*10^6$ cells/mL) were stained with APC anti-mouse PDGFRa antibody (BD bioscience, San Jose, CA) and processed following the manufacturer's instruction. For the staining of intracellular fibroblasts marker, αSMA, the cells from the tissues were penetrated with penetration buffer (BD, Franklin Lakes, NJ) following the manufacturer's instructions. The anti-mouse αSMA (Abcam, Cambridge, MA) and isotype control were then applied, followed by extensive washing and

Fluor 647 conjugated anti-rabbit secondary (Abcam, Cambridge, MA) staining. All staining procedures were carefully compensated by flow cytometry. To analyze the expression of Sigma R in tumor cells and fibroblasts, and to evaluate how the expression levels correlated with the DiI-LCP NPs' distribution, cells were stained with an anti-Sigma R antibody (Santa Cruz biotechnology, Inc.) following the same staining protocol. The UMUC3 cells were pre-transfected with red fluorescence protein (RFP) and fibroblasts were pre-transfected with green fluorescence protein (GFP) to define the cell populations (n=3~6). The flow cytometry data were analyzed using FlowJo 7.6.1 (FLOWJO, Ashland, OR). The % of DiI-positive cells per cell population was calculated according to the following equation:

$$\%\ \text{of DiI positive cells per cell population} = \frac{\%\ \text{of } (DiI^{+} Cell\ population^{+}) \text{ of the parent cells}}{\%\ \text{of } (DiI^{+}\ Cell\ poplulation^{+} + DiI^{-} Cell\ population^{\mp}) \text{of the parent cells}}$$

Cell population indicates either GFP-3T3, RFP-UMUC3, Sigma R^{+} or $CD45^{+}$ cell populations.

2.3.13 *In vitro* NP Penetration in a Core-Shell Tumor Spheroid Model.

For evaluating the effects of the binding site barrier elicited by fibroblasts in vitro, an ex vivo multicellular Core-Shell 3D tumor spheroids mimicking the single tumor nest surrounded by fibroblasts were developed using the lipid overlay system with some adjustments. This models was used to study the penetration behavior of LCP NP after extravagating from the blood vessel. In brief, 1×104 UMUC3 cells were seeded into each well (using complete medium) of the ultra-low attachment round bottom 96 well plates (Costar, Corning, NY), followed by slight centrifugation at 900 rpm for 2min to cluster the cells to the bottom of the wells, and incubated at 37°C for 4 days. The culture medium was changed every 2 days. On the fourth days, 1×104 GFP-NIH3T3 cells were added into each well, followed by continuous gentle rotation (200 rpm, 37°C) for 6h. And then the formed core-shell tumor spheroid was incubated overnight. The structure of the core-shell spheroid was confirmed using a Zeiss LSM700 confocal microscope. Briefly, the spheroid was carefully transferred to a chambered coverslips and scanned from the bottom. Each scanning layer was 15 mm in thickness,

and the total scanning was 90 mm in depth. Only the ones with uniform and compact core-shell structure were selected for the follow-up studies (approximatedly 20 out of the 96 well-plate). For the time-lapse assay, fluorescent images were acquired at fixed focus at determined time points. Radial fluorescence intensity profiles in the spheroids were generated using a customized script in ImageJ. Average fluorescence intensity were determined for two annular regions; the tumor region (non-fluorescence) and the fibroblast region (fluorescence region). The treated spheroids were also washed with PBS, and dissociated with collagenase and trpsinase. The DiI positive cell populations in both fibroblasts and tumor cells were quantified by Flow Cytometry.

2.3.14 Mathematical Modeling of the 3D spheroid

We model the tumor spheroids as perfect spheres (radius $R = 500\mu m$) with radially symmetric NP concentrations (parameters shown in **Table** 2.2). The Stokes-Einstein diffusion coefficient in water for a particle of radius $18nm$ is $D_W = 4.9 \times 10^4 \mu m^2/\text{hour}$. We expect the effective diffusion coefficient of NPs within the spheroid to be less than the Stokes-Einstein diffusion coefficient due to the porous ECM. We also consider that the diffusion coefficient within the fibroblast layer may be less than regions of the spheroid containing tumor cells. The equation for the extracellular concentration of NPs within the spheroid is

$$\frac{\partial c}{\partial t} = D\nabla^2 c(r,t) - kc(r,t), \quad 0 < r < R,$$

where k is the NP absorption rate. Initially, there are no NPs within the spheroid, so we set

$$c(r,0) = 0, \quad 0 < r < R.$$

Each spheroid is in a solution with a fixed concentration C_{EV} of NPs. Covering each sphere is a permeable barrier, possibly due to ECM, restricting the diffusive flux of NPs into the spheroid. This is modeled by imposing a boundary condition at the spheroid edge:

$$D\frac{\partial}{\partial r}c(R,t) = \frac{R\kappa}{3}[C_{EV} - c(R,t)],$$

where κ is the rate at which NPs enter the spheroid. Based on NP distribution within the spheroids, we find that $C_{EV}\kappa = 2.34 \pm 0.097$, which did not vary significantly between spheroids or between targeted and non-targeted NPs. The averaged concentration absorbed into cells is

$$C_{\text{absorbed}}(t) = \frac{3k}{R^3}\int_0^R r^2\, c(r,t)dr.$$

The total concentration of NPs (both absorbed and extracellular) within the spheroid is

$$c_T(r,t) = c(r,t) + k\int_0^t c(r,s)ds.$$

To determine the diffusivity and the NP absorption rate, we first examine the data set for the S-LCP spheroid. We define the diffusion time $\tau_D = R^2/(4D)$ as the time it takes for a concentration starting at the spheroid edge to diffuse inward so that the concentration at the center is roughly 80% of the value at the edge. Because the concentration is distributed relatively evenly within the tumor, we can conclude that NPs have time to diffuse throughout the spheroid before they get absorbed; in other words $\tau_D < 1/k$. We find that $D = 3.1 \times 10^4 \mu m^2/\text{hour}$ and $k = 0.25(\text{hour}^{-1})$ provides a reasonable match between the model and the data.

We next examine how the NP distribution within the UMUC3-only spheroid changes for AA S-LCP NPs. Because the AA S-LCP NPs have roughly the same hydrodynamic radius as the S-LCP NPs, we assume they have the same diffusion coefficient. The AA S-LCP NPs have a higher uptake rate than the S-LCP NPs. The distribution of NPs within the UMUC3-only spheroid is shifted toward the edge because more NPs are absorbed before they have time to diffuse very far into the spheroid. We find that a four-fold increase in the uptake rate for AA-S LCP provides a reasonable match between our model and the data.

In the UMUC3-3T3 spheroid, the outer layer is comprised of fibroblasts. Based on **Figure 2.9C** and **D**), we assume that the uptake rate by fibroblasts is the same as tumor cells. Because the ECM excreted by fibroblasts has smaller average pore size, the diffusion coefficient in the outer

stroma layer is reduced. The model prediction of the NP distribution with a 65% reduction of the diffusion coefficient in the stroma matches well with experimental data.

The mathematical model provides qualitative guidance and reasonable quantitative accuracy. Improved accuracy can be achieved by expanding the model to account for non spherical shape of tumor spheroids, heterogeneity within the spheroid, and variations in the diffusivity due to ECM and cell density. However, based on the qualitative behavior and observed timescales of absorption and diffusion, we conclude that an increased absorption rate acts as a barrier to NP penetration into the spheroid center when the average absorption time becomes less than the diffusion time (i.e., $1/k < \tau_D$), and that this effect is amplified when the diffusion coefficient is reduced in the fibroblast layer at the edge of the tumor.

2.3.15 Western-blot Analysis

For the analysis of Sigma Receptor expression levels in different cell lines. Cultured UMUC3, activated NIH3T3 (treated with 10 ng/mL TGF-β for 0, 24, 48h respectively), and other normal fibroblast cell lines including MRC5, PA319, WI-38, were collected and lysed using radioimmunoprecipitation assay (RIPA) buffer (Sigma). After incubation on ice for 30 min, the concentration of total protein in each cell lysates was quantified using bicinchoninic acid (BCA) protein assay reagent following the manufacturer's instruction (Thermo, Rockford, IL). Then, identical amounts of protein samples were diluted with 4×sample buffer containing a reducing agent and heated at 95 ºC for 5 min, 40 μg of protein per lane was separated by 4–12% SDS-PAGE electrophoresis (Invitrogen, Grand Island, NY). After gel separation, the proteins were transferred to polyvinylidene difluoride (PVDF) membranes (Millipore, Billerica, MA). The protein loaded membranes were blocked with 5% skim milk for 1 h and incubated overnight at 4 ºC with anti-Sigma Receptor primary antibody and the loading control GAPDH antibody (1:4000 dilution; Santa Cruz biotechnology, Inc.), respectively. On the second day, the membranes were washed three times and then incubated in horseradish peroxidase-conjugated secondary antibodies (1:4000 dilution; Santa

Cruz biotechnology, Inc.) at room temperature for 1 h. Finally, the membranes were washed four times and detected using the Pierce ECL Western Blotting Substrate following the manufacturer's instructions (Thermo Fisher Scientific).

2.3.16 Immunofluorescence Staining

For the frozen tissue sections, mice bearing different tumors, were intravenously injected with DiI-labeled LCP NP, or Texas Red labeled LCP NPs, at determined time points, mice were sacrificed and tumor tissues were collected. Tissues were fixed with 4% paraformaldehyde overnight, and dehydrated with sucrose gradient. Then, fixed tissues were frozen in OCT (Tissue-Tek, Dublin, OH) on dry ice. After the generation of 5 μm thick cryosections, the tissue sections were then mounted on Superfrost Plus slides (Fisher Scientific Co., Houston, TX). After the brief rinse with PBS, some of the tissue sections were mounted with ProLong Gold antifade reagent with DAPI (Invitrogen). Other slides were blocked with 1% bovne serum albumin at room temperature for 1h, followed by anti-CD31 (Abcam, Cambridge, MA) primary antibody staining overnight at 4C. On the second day, after being washed three times, tissue sections were stained with Fluor 647 conjugated anti-rabbit secondary antibody (Abcam, Cambridge, MA), and then mounted with mounting solution containing DAPI. For paraffin embedded sections, paraffin embedded tissues were prepared by the UNC Tissue Procurement Core and the slices were deparaffinized, antigen retrieved, permeabilized and fixed if necessary and blocked with 1% BSA at room temperature for 1h. Cell markers (including αSMA, Sigma Receptor, CD31) were detected with primary antibodies followed by visualization using Fluoro conjugated secondary antibodies. All antibodies were diluted after optimization. Images were taken using fluorescence microscope (Nikon, Tokyo, Japan). Three randomly selected microscopic fields were quantitatively analyzed using Image J software.

2.3.17 Cellular Uptake Study in single cell layers

UMUC3 cells and pre-activated fibroblasts were seeded into a 48-well plate (1.5×10^5 cells/well) containing 1 ml of media. Twenty-four hours later, 500 μL of DiI labeled LCP NPs were

incubated with cells in a serum-free medium. At determined time points, cells were dissociated, the mean DiI intensity in each cell line was analyzed by flow cytometry.

2.3.18 Statistical Analysis.

Data are presented as Mean ± SD (standard deviation). A two-tailed Student's t-test or a one-way analysis of variance (ANOVA) were performed when comparing two groups or larger than two groups, respectively. Statistical significance was defined as the *P* value less than 0.05. Statistical analysis was performed using Prism Software.

2.4 Results

2.4.1 Characterization of LCP NPs

LCP NPs were prepared according to established protocols [172]. By adjusting the composition of the surfactant system, LCP core sizes could be tuned between 6 to ~50 nm. The hydrophobic DOPA-cores were further self-assembled with outer leaflet lipids to form the asymmetric lipid-bilayer NPs (**Figure 2.1A-D**). Sucrose-gradient centrifugation was used to purify LCP NPs. Approximately 0.5% DiI was incorporated into the outer leaflet to monitor the purification process. LCP NPs containing dense CaP cores localized at the interface between the 10% and 20% sucrose layers. TEM imaging confirmed successful purification of LCP NPs (data not shown). Particle size and surface modifications had minimal effect on purification efficacy as approximately 85% of DiI labeled NPs were consistently recovered (**Table 2.1**).

Large LCP NPs (diameter ~65 nm and PDI ~ 0.3) are termed L-LCP NPs. Smaller LCP NPs (diameter ~18 nm and PDI ~ 0.2) are termed S-LCP NPs (**Table 2.1**). All NPs demonstrated a clear core/membrane structure as determined by TEM and presented similar positive zeta potentials ranging from 18~20 mV due to cationic DOTAP (**Figure 2.1** and **Table 2.1**). Structure and zeta potential were independent of particle size and particles maintained their diameters over 96 h (**Figure 2.1E**). NPs showed similar plasma clearance rates independent of size or the presence of targeting ligands (**Figure 2.1F**), consistent with studies using other NPs of different sizes and targeting motifs

[52, 175]. To confirm that outer leaflet lipids containing DiI served as a feasible tracker, the integrity of NPs before cellular internalization was determined *in vivo*. A hydrophilic Texas Red oligo was encapsulated into the CaP core along with hydrophobic DiI in the outer leaflet of L-LCP NPs. The fluorescence intensity of each dye remained similar when loaded alone or simultaneously into the NPs, suggesting low to no intermolecular Fŏrster resonance energy transfer (FRET) between two fluorophores interfering with the fluorescence measurement (**Figure 2.2**). Therefore, co-expression of Texas Oligo and DiI in an individual tumor cell after systemic circulation is an indication of NP integrity. Flow cytometry analysis indicated that ~15% of cells in the tumor tissue co-expressed the aforementioned two fluorophores within 16 h after injection of the double labeled NPs (**Figure 2.1G**), accounting for ~70 % of all the fluorescence positive cells. Dissociated single-dye positive cells were observed 28 h post injection, probably due to dissociation of NPs trapped in the extracellular matrix (ECM) or intracellular degradation of released fluorophores. Data herein suggests that DiI localized in the outer leaflet remains associated with the inner core within 16 h during systemic delivery. The co-localization of these two fluorophores was also visualized by confocal microscopy (**Figure 2.1H**). Majority of these dyes were distributed in the GFP positive stromal area, only a small portion was observed in other cells. Thus, size tunable DiI-labeled LCP NPs were suitable for the evaluation of NP size or surface properties on intra-tumoral cellular distribution.

2.4.2 Binding Site Featured by TAFs within the *Stroma-vessel* Type Tumors Affects the Intratumoral Dispositions of Non-targeted NPs at Early Time Point

The role of stromal patterns on the intratumoral distribution of NP was investigated. According to the criteria proposed by Smith et al., malignant solid tumors are categorized into two phenotypes based on the stromal architecture [71]. In *stroma-vessel* phenotype tumors, e.g. breast cancer 4T1 and NSCLC H460, immunofluorescence (IF) indicated the formation of tumor nests surrounded by well-developed stroma structures containing the majority of CD31-positive vessels and αSMA-positive fibroblasts. Whereas, in melanoma tumors such as D4M and A375lu, the tumor vessels are embedded throughout the tumor cell mass, revealing a *tumor-vessel* phenotype,

represented in **Figure 2.3A**. The influence of stromal architecture on NP dispositions would be best visualized in animals bearing two tumor phenotypes and treated with highly permeable NPs with minimal selective cellular binding. Further, the difference should be magnified at earlier time points [162]. Therefore, D4M and H460 were used as model tumors in animals treated with non-targeted S-LCP NPs and examined 8 h after injection. The representative images are shown in **Figure 2.3B**. Since these two tumors vary in blood vessel perfusions and interstitial fluid pressures (IFP), the results should be interpreted with caution. Yet, the percolation of S-LCP NPs from blood vessels into both αSMA positive stroma and the negative area was observed in the *tumor-vessel* phenotype tumor, D4M. Meanwhile, the majority of DiI-positive S-LCP NPs were trapped in the stroma of H460, a *stroma-vessel* type tumor. Therefore, proximity of stromal components to blood vessels likely dictates the distribution of non-targeted NPs in regions of dense stroma in *stroma-vessel* type tumors.

Mechanical barriers such as tight junctions, ECM or elevated IFP can trap non-targeted NPs in the non-cellular stroma [161]. The binding and internalization of NPs in the cellular compartment of the stroma (BSB) also depletes the NPs. To examine role of BSB in stromal cells, the association of DiI-labeled NPs with major stromal cells (fibroblasts) was investigated. Individual cells were collected after tumor tissue digestion and labeled with anti –αSMA, commonly used for TAFs [176]. After staining, samples were studied with flow cytometry and results were shown in **Figure 2.3C**. In *stroma-vessel* type tumors (both H460 and 4T1), association of DiI NPs (S/L) with αSMA positive was ~2- to 3-fold higher than those delivered to the tumor nests. Stroma densities vary among tumors (i.e., 4T1 has higher amount of stroma than H460), but the preferential distribution of NPs in stroma remains constant. Consistent with previous findings, smaller NPs demonstrated higher association with total cells, but the association ratio between fibroblasts and other cells (mainly tumor cells) was independent of size. However, the trend was reversed in the tumor vessel models (D4M and A375lu) where tumor cells favored DiI NPs' accumulation. The data suggests that the binding site characteristic of fibroblasts was independent of particle size and stroma density, but was strongly dependent on whether the blood vessels are associated with the stroma.

To minimize the interference of heterogeneity in fibroblasts and the non-specific staining using antibodies, a xenograft model consisting of the GFP transfected NIH3T3 fibroblasts (GFP-3T3) and human bladder cancer UMUC3 was established. It was found that this bladder tumor mainly adopted a *tumor-vessel* structure when smaller than 200 mm^3. The tumor then transitioned to a *stroma-vessel* structure when larger than 400 mm^3 (**Figure 2.4A**). Consistent with the previous results, NPs specifically favor fibroblasts in large tumors, independent of the size of the NPs tested (**Figure 2.4B**). This observation was also paralleled in a patient derived xenograft bladder cancer model (**Figure 2.4C**), suggesting the artificial UMUC3/3T3 model can recapitulate the NP disposition features in the patient tumors. All data herein demonstrates that the binding site characteristics of fibroblasts in *stroma-vessel* tumors affect the initial distribution of non-targeted NPs. Since *stroma-vessel* tumors often indicate poor patient prognosis, further studies on these tumor subtypes were conducted using UMUC3/3T3 (> 400 mm^3, ~30% fibroblasts) as a standard model.

2.4.3 Fibroblast induced BSB was Intensified and Prolonged for Targeted NPs in the *Stroma-vessel* Type Tumor Models

AA has been exploited for targeted delivery of NPs to many epithelial cancers over-expressing the sigma receptor (Sigma R) [170, 173, 177]. To assess whether AA could increase binding affinity of LCP NPs to tumor cells and overcome the fibroblast-mediated BSB, the intratumoral dispositions of NPs (+/-AA) were examined. Eight % of AA (40 % of total DSPE-PEG) was coated onto the surface of NPs to ensure enhanced cellular uptake while maintaining the same physicochemical properties (**Figure 2.1**and **Table 2.1**). The time-dependent disposition of NPs in GFP positive fibroblasts and other cell populations were further measured by flow cytometry and compared. As expected, non-targeted NPs gradually extravasated from the stromal layer for binding and internalization by tumor cells, despite the presence of BSB. Consistent with other studies, S-LCP NPs were preferentially internalized by tumor cells over L-LCP NPs. Sixteen h after injection, over 40 % of cells containing S-LCP NPs were tumor cells and over 30 % of tumor cells were DiI-positive.

Surprisingly, the addition of AA did not increase the ratio of DiI-positive tumor cells. Rather, the initial association ratio of NPs (S/L) with fibroblasts increased almost two-fold over non-targeted NPs and was plateaued over 16 h (**Figure 2.5A**). The preferential association of NP with stroma was further confirmed by fluorescence imaging (**Figure 2.5B**). After 4 h, NPs were localized within the GFP-positive stroma. The S-LCP NPs demonstrated a disperse distribution pattern compared to L-LCP NPs. Perhaps, either uneven blood vessel permeabilization or differences in ECM composition may have limited the distribution of large NPs. However, at 16 h post injection, non-targeted S-LCP NPs in particular, expanded across the stroma and penetrated deeper into the tumor core (arrows in **Figure 2.5B**). In contrast, the stromal matrix was populated with targeted NPs, leaving minimal distribution in the GFP negative area (**Figure 2.5B**). Therefore, the fibroblast-mediated BSB was intensified and prolonged when NPs were modified with AA.

2.4.4 Increased Expression of Sigma Receptor in TAFs Resulted in the Enhanced BSB for Targeted NPs

The distribution of Sigma R was then evaluated by co-immunostaining Sigma R with GFP-positive fibroblasts, CD31 or αSMA. Results in **Figure 2.6A** demonstrate a heterogeneous Sigma R distribution. Tumor cell-rich areas were primarily Sigma R-positive, whereas, CD31-positive endothelial cells were not. However, the distribution of Sigma R was uneven among GFP-fibroblasts (**Figure 2.6C**). Primarily, the expression of Sigma R was greater in αSMA-positive fibroblasts than αSMA-low fibroblasts (**Figure 2.6B and C**). Consistently, other tumor models, 4T1, A375lu and H460 (**Figure 2.6D-F**) expressed different levels of Sigma R in the αSMA-positive activated fibroblasts, suggesting that the expression of Sigma R positive fibroblasts was not unique to the mixed bladder cancer xenografts. Furthermore, western blot analysis indicated that under normal conditions, the expression level of Sigma R in fibroblasts (e.g., NIH3T3, MRC5, WI-38) was constantly low compared to tumor cells, which was consistent with previous findings (**Figure 2.6G**). This was actually the rationale of utilizing AA coated NP for specific tumor targeting. However, fibroblasts activated by TGF-β (TAFs) showed increased both αSMA and Sigma R expressions with

time (**Figure 2.6H**), and consistently a higher uptake efficiency for the targeted, but not the untargeted NPs compared to un-activated fibroblasts (data not shown). Therefore, activated TAFs expressing higher levels of Sigma R induced enhanced uptake of NPs and led to an intensified BSB.

To confirm the aforementioned hypothesis, individual cells in tumor tissues were collected 8 h post NP injection for Sigma R staining and flow cytometry. To exclude interference from other stromal cells, the tumor cells were pre-transfected with fluorescent RFP. As shown in **Figure 2.7A-E**, the association of NPs with cells increased with the expression of Sigma R. Consistent with previous findings, the fibroblasts were categorized based on the expression level of Sigma R, into Sigma R (-), Sigma R low (L) and Sigma R high (H) (**Figure 2.7C and Figure 2.8**). Next, a fibroblast cell strain expressing shRNA specific to Sigma R to block induction of Sigma R expression was generated (**Figure 2.7F**). NIH3T3-GFP (shRNA Sigma R) cells were mixed with UMUC3 and inoculated, low to no level of Sigma R expression of fibroblasts in the knockout model was confirmed (data not shown). As expected, the disposition of IV administered AA-targeted NPs in Sigma R knockout fibroblasts was significantly decreased, while association of NPs with tumor cells increased compared to standard NIH3T3/UMUC3 model (**Figure 2.7G**). Thus, specific AA-Sigma R interactions facilitated BSB in fibroblasts for targeted NPs.

2.4.5 High Binding Affinity Explains the Intensified BSB for Targeted NPs

The binding affinity of NPs to fibroblasts and tumors is a direct indicator of the BSB strength. As described above, fibroblasts possess a heterogeneous expression of Sigma R *in vivo*. Thereby, to relate the NPs binding properties in activated NIH3T3 *in vitro* with the average behavior of the *in vivo* TAFs, GFP-positive fibroblasts were sorted from the tumor tissue by MoXlo Flow. The binding affinity of AA LCP NPs was determined with these sorted fibroblasts, and was identical to NIH3T3 activated with TGFβ for 24 h *in vitro* (**Figure 2.9A**). The binding constant (K_D) of both non-targeted and targeted NPs were then compared *in vitro* on this activated NIH3T3 and UMUC3 cells. As shown in **Figure 2.9B**, both UMUC3 and NIH3T3 did not bind with any non-targeted NPs. Yet, AA-

modified NPs bound strongly with both UMUC3 and activated NIH3T3 at low concentrations. Binding plateaued as the particle number increased. The apparent K_D of AA L-LCP NPs for UMUC3 and activated NIH3T3 was 11.13 and 10.11 nM, respectively. Low and comparable dissociation constants suggested strong and similar binding affinities for both types of cells. The binding capacity of UMUC3, indicated by the surface saturation level, was higher compared to activated NIH3T3. This finding is consistent with the fact that higher levels of Sigma R are present on UMUC3 over majority of the activated fibroblasts even though the sigma receptor was upregulated in TAFs (**Figure 2.9B**).

In most cases, NPs entered the cells following binding to the cell surface. Thereby, the uptake process including adhesion and internalization was further evaluated on both fibroblasts and tumors. To mimic the unsaturated conditions *in vivo*, approximately 0.1 nM NP were given to a single layer of cells. As expected, the targeted NPs entered cells more rapidly regardless of size compared to non-targeted NPs, most likely due to the facilitated ligand-receptor interaction process. Consistent with the previous hypothesis of involving a wrapping time of the membrane, larger NPs with required stronger driving forces and additional energy for successful cellular internalization [178, 179]. Therefore, cellular uptake quantities of NPs decreased with increasing particle size. Additionally, similar linear uptake profiles were observed between the two cell types (**Figure 2.9C** and **D**). The uptake rates for the targeted NPs in these two cell lines were almost identical. While, for the non-targeted NP, the uptake rate was slightly higher in UMUC3 than in the activated fibroblasts (**Figure 2.9D**). Altogether, observations herein demonstrated that targeted NPs with high avidity can bind rapidly to and be taken up by non-tumor cells expressing lower levels of Sigma R. Subsequently uptake is sufficient to elicit a BSB.

2.4.6 *In vitro* Tumor Spheroid Modeling of the BSB

To quantify the BSB *in vitro*, a spheroid model was generated in which tumor cells (UMUC3) were enclosed by fibroblasts (GFP-NIH3T3) to simulate the *in vivo* condition. The core-shell structure was confirmed by confocal Z-stack scanning from the bottom to the center of the spheroid

with each layer measuring 15 μm in thickness (**Figure 2.10A**). Images indicated that the overall diameter and the fibroblast-shell thickness increased as the amount of added fibroblasts increased (**Figure 2.10C**). The core-shell 3D model (35% fibroblasts) closely mimicked the *in vivo* condition of the UMUC3/3T3 model where a single tumor nest was surrounded by a thin layer of stroma cells (**Figure 2.10B**). Thereby, this model was used to analyze the real-time disposition of NP into tumor nests after their extravasation from blood vessels.

An excess of DiI labeled LCP NPs (S/L, +/- AA) was incubated with the 3D spheroids in 37°C under frequent stirring. The spheroids were imaged at determined time points approximately 150 μm from the bottom of the spheroid (**Figure 2.11A**). Background fluorescence was corrected by subtracting the fluorescence at 0 h. Consistent with the *in vivo* study, the use of targeting ligands had a pronounced effect on the penetration of NPs in the spheroid. DiI labeled AA S-LCP NPs and L-LCP NPs bound rapidly to the surface of fibroblasts within 30 min after incubation. Upon binding, the fluorescence intensity of targeted NPs in the fibroblast region increased with time. However, penetration into the tumor nest required nearly 6 h post incubation before a notable amount was observed. On the other hand, non-targeted NPs required longer incubations before initial binding. Yet, fluorescence penetrated rapidly into the tumor nest upon binding, resulting in the illumination of the entire nest soon afterwards. These dynamics were further observed by averaging the intensities in the fibroblast (**Figure 2.11B and C**, grey bar) and tumor cell regions. For targeted NPs, the fluorescence intensity in the fibroblast region was approximately 4 times higher than that in the tumor region, demonstrating lower penetration of targeted NPs. Time dependent accumulation of non-targeted NPs in the fibroblasts region of the spheroid was notably similar to targeted NP except for the delayed binding. However, the behavior was different in the tumor region, in which the fluorescence intensity increased monotonically and eventually matched to the intensity in the fibroblasts region. Together, these observations are consistent with the *in vivo* observation and demonstrate that the fibroblasts served as the primary barrier for NPs penetration, especially for targeted NPs. The distribution of

large NPs was similar to the small NPs but significantly smaller in signal strength, suggesting the role of particle size in tumor penetration.

2.4.7 Mathematical Model: Mechanical Barrier Strengthen the BSB

A descriptive mathematical model was developed to examine the coupled effects of extracellular diffusion and cellular uptake on the distribution of AA S-LCP NPs in the aforementioned 3D spheroid model. For simplicity, several assumptions were made. Firstly, tumor spheroids were modeled as perfect spheres with radius R = 500 μm and NP distribution was assumed to possess radial symmetry. The thickness of the fibroblast shell was estimated as 80 μm based on the measurement of ex-vivo 3D spheroids and the volume fraction of fibroblasts in the UMUC3/3T3 xenografts. Furthermore, the diffusion of NPs in the ECM was assumed to follow the Stokes-Einstein relationship, similar to the proposed movement of NPs in the gel-like cervicovaginal mucus (CVM) [180, 181]. Lastly, no pressure-mediated convection was considered in the scope of the current study [83]. The diffusivity (D) and uptake rate (k) for non-targeted S-LCP NPs were derived from a spheroid model of only UMUC3 cells (UMUC3 only spheroid). UMUC3-GFP constitutes the spheroid shell, with the same thickness to the UMUC3/3T3-GFP spheroid model (**Figure 2.12**). Assuming the D is constant within this single-cell-population spheroid, modeling results fit the experimental data when $D=3.1\times10^{4}$ $\mu m^2/h$ and $k=0.25$ h^{-1}(**Figure 2.14A** and **Table 2.2**). The calculated D and k are comparable with those of 10 nm cationic quantum dots or 15 nm PEGylated polymeric NPs reported elsewhere [18, 83]. This match was therefore considered reasonable. Both the modeling results and experimental images demonstrate the diffusion time of S LCP NPs as evidently faster than the uptake rate. Therefore, small NPs have ample time to diffuse throughout the spheroid before absorption. To illustrate the impact of the uptake rate of NPs on the distribution pattern, the distribution of AA S-LCP NPs in the same UMUC3 only spheroid was examined. We assumed the D of AA S-LCP NPs is consistent with that of the non-targeted NPs, since both NPs possess identical size, surface charges and PK profiles. In contrast to the uniform distribution of S-LCP NPs, the

localization of AA S-LCP NPs was shifted toward the GFP-edge. A 4-fold increase in the uptake rate for AA-S LCP NPs was predicted by the model, which was only slightly higher than the measured values *in vitro* on a single layer of UMUC3 (**Figure 2.9C and D**). Results therefore demonstrate a reasonable match between modeling and experimental data wherein cells with high affinity for NPs hinder the penetration of targeted NPs.

However, this NP distribution shift was intensified and pronounced in UMUC3/NIH3T3 spheroids when treated with AA S-LCP NPs. Preliminary studies suggest that the fibroblasts' expression of Sigma R was consistent to that quantified *in vivo* over the course of measurement (data not shown). Therefore, the NP uptake rate for fibroblasts mirrored the uptake rate for UMUC3 as confirmed *in vitro* on a single cell level (**Figure 2.9C**). So, decreased diffusivity was proposed to fit the experimental data (**Figure 2.14C**). The cellular association of NPs was then examined based on the modeling data (**Figure 2.14E and F**). The ratio of cell associated NPs in the fibroblast shell versus the tumor core was found to be higher in the UMUC/3T3-GFP spheroid as opposed to the UMUC3 spheroid. Therefore, the increased retention of NPs in the fibroblast shell is likely due to decreased diffusivity, which further enhanced the cellular uptake of NPs and intensified the BSB. This prediction was confirmed by examining the ratio between the MFI of DiI in fibroblast layer and tumor layer of the two spheroid models using flow cytometry (**Figure 2.13**).

The modeling results accurately replicate a number of characteristics for NPs distribution and provide valuable insight into the parameters responsible for limiting NP uptake. Firstly, the uptake rate of AA S-LCP NPs overshadowed the rate of diffusion as opposed to S-LCP NPs, retarding the penetration NPs. Furthermore, the decreased diffusivity in the stromal layer intensified the BSB elicited by fibroblasts when compared to tumor cells with less secretion of ECM proteins.

2.5 Discussion

In summary, a detailed investigation into the BSB elicited by TAFs and the subsequent effects on intratumoral deposition of sub-100 nm NPs in a *stroma-vessel* tumor model was conducted.

Results herein focus on characterization of the TAF-elicited BSB through three major qualities defining the BSB: the proximity of the TAFs to blood vessels, the number of Sigma R and binding affinity [161].

Firstly, the close proximity of fibroblasts to blood vessels in *stroma-vessel* type tumors contributed to TAFs' role as a binding site for NPs. Data herein suggested that NPs preferentially distributed to fibroblasts initially, regardless of size and targeting ligands, resulting in depletion of NPs available for tumor uptake. While the biological mechanism for the formation of this *stroma-vessel* architecture is unknown, it is conceivable that fibroblasts infiltrate during desmoplasia and envelop the neoplasm, subsequently influencing the architecture [163]. Although blood vessels are sometimes observed in the tumor nests, the intra-nest NP extravasation is still retarded due to the malfunction of these intra-nest blood vessels [52].

The number of receptors characterizes a second feature of the BSB. Overexpression of Sigma R is reported in several fast growing cancer cell lines. Since TAFs are highly metabolic active compared to the quiescent fibroblasts, increased expression of Sigma R is reasonably consistent with previous investigations demonstrating the up-regulation of Sigma R in rapidly dividing normal tissues [167, 182]. Consistently, both the up-regulation of Sigma R and its heterogeneous distribution could be correlated with αSMA expression and triggered by TGF-β. The overexpression of Sigma R on TAFs was also observed in several patient bladder cancer samples, unveiling the clinical-relevancy of this finding. As expected, we found that AA (ligand of Sigma R) targeting paradoxically strengthened the BSB elicited by fibroblasts for NPs. This off-target binding of NPs to stroma cells was not the only challenge for AA coupled NPs. Other targeting receptors whose expression correlates with metabolic rate (e.g. folate and transferrin receptors) also exist in non-tumor cells and are likely prone to unspecific targeting [87, 183, 184]. Since these ligands are commonly used for tumor-targeted therapy, evaluation of off-target distribution would be of significance for therapeutic guidance.

While the induced expression of Sigma R in TAFs is still somewhat lower than in cancer cells, a strong binding affinity of NPs to TAFs constitutes the third parameter of the BSB. Notably, the high avidity of targeted NPs to receptors compromise the selectivity based on the number of receptors per cells, as NPs can bind rapidly with fibroblasts expressing lower levels of receptors.

Mathematical modeling simulations based on the *in vitro* spheroid model parallel the aforementioned experimental findings that enhanced binding and uptake in TAFs subsequently enhanced the BSB. It should be noted that the BSB is not a feature unique to TAFs and can be extended to various types of cells (including tumor cells) with strong binding affinity to NPs and near the NP pool. However, the reduced diffusivity of NPs in stroma herein tuned the balance of NP accumulation towards the edge of the spheroid, which mainly consist of TAFs. This observation was confirmed both experimentally and with mathematical modeling. Factors such as the highly packed extracellular proteins secreted from TAFs, the spindle shape of TAFs, the presence of tight junction and the raised IFP could also contribute to the decreased diffusivity in TAFs. These mechanical barriers contribute to the TAF-specific BSB by prolonging the retention of NPs in the stroma layer.

Consistent with other studies, this study suggested that non-targeted NPs demonstrated favorable tumor penetration over targeted NPs. The association of non-targeted NPs to tumor cells was actually higher than for targeted NPs over time, opposing the dogma that non-targeted NPs have greater penetration but lower cellular uptake. Compared to other studies using anionic NPs, cationic PEGylated NPs were studied herein. Previous studies demonstrated that shedding of the PEG layer on DOTAP coated NPs causes a subsequent shift in the PEG confirmation from brush to mushroom. This shift exposes cationic charges and enhances cellular uptake, offering a potential explanation for the observations made in the current study [185]. Since infiltrating leukocytes also constitute the TME, their contribution to off target effects was also investigated. Flow cytometry analysis shown that NP association with CD45-positive leukocytes on the tested tumor models was relatively low compared to that in TAFs (**Figure 2.15**). No significant trend was observed in terms of different

phenotypes and targeting ligands. This finding highlights the rule that TAFs possess as the primary BSB in the selected models.

What then, is the significance of studying the TAF-elicited BSB? The TAF-elicited BSB depletes the number of NPs available to tumor cells, compromising therapeutic efficacy. At the meantime, it further induces adverse effects due to resistance of stromal cells to tumor-specific therapy. Examples of adverse effects can be found in a previous study, where TAF's internalization of cisplatin NPs induced the secretion of Wnt16 (a survival factor) and paradoxically promotes tumor growth and metastasis. Despite certain limitations and assumptions, this study demonstrates the mechanistic basis of these off-target effects from the aspect of NP-delivery, and offers guidance for the development of nano-therapeutics against *stroma-vessel* desmoplastic type tumors. Separately, these findings explore the rationale of intentionally targeting fibroblasts through the BSB. This feature can be utilized to exploit TAFs as an *in situ* cytokine or cytotoxic protein producing reservoir, overcoming the tumor-specific delivery barrier, orchestrating the suppressive tumor microenvironment and improving the currently marginal anti-tumor outcome of desmoplastic tumors.

Table 2.1 LCP NPs characterization

NP	Diameter (nm)	PDI	Zeta Potential (mV)	DiI Encapsulation (%)
S-LCP	18.2±3.4	0.21±0.04	21.9±2.3	82.9±2.6
AA S-LCP	18.5±2.2	0.28±0.06	20.8±1.8	85.4±3.5
L-LCP	67.8±8.6	0.32±0.08	19.9±3.3	80.1±4.1
AA L-LCP	71.3±4.5	0.27±0.12	18.7±2.6	84.6±3.6

Table 2.2 Parameters in the mathematical modeling

Parameter	Symbol	Model	Value	Unit	Note
radius of tumor nests	**r**	**3D tumor spheroid**	**~500**	**μm**	**measured**
		UMUC3/3T3	~300	μm	Fig.3A
		H460	~650	μm	Fig.2A
		4T1	~200	μm	Fig.2A
		BXPC3	~200	μm	[68]
thickness of fibroblasts	**d**	**3D tumor spheroid**	**~80**	**μm**	**measured**
		UMUC3/3T3	~60	μm	Fig.3A
		H460	~30	μm	Fig.2A
		4T1	~40	μm	Fig.2A
		BXPC3	~50	μm	[68]
particle diffuson coefficient	**D**	**18 nm S LCP NP (+/-AA)**	**3.0×10^{4}**	**$\mu m^2/h$**	**measured**
		11 nm quantum dots (anionic)	5.0×10^{4}	$\mu m^2/h$	[83]
		11 nm quantum dots (cationic)	4.0×10^{4}	$\mu m^2/h$	[83]
		20 nm polymeric NP	2.5×10^{4}	$\mu m^2/h$	[186, 187]
		10 nm polymeric NP	20×10^{4}	$\mu m^2/h$	[186, 187]
cell uptake rate constant	**k**	**18 nm S LCP NP (+/-AA)**	**7×10^{-5}**	**/S**	**measured**
		20 nm polymeric NP	5×10^{-5}	/S	[93, 187]

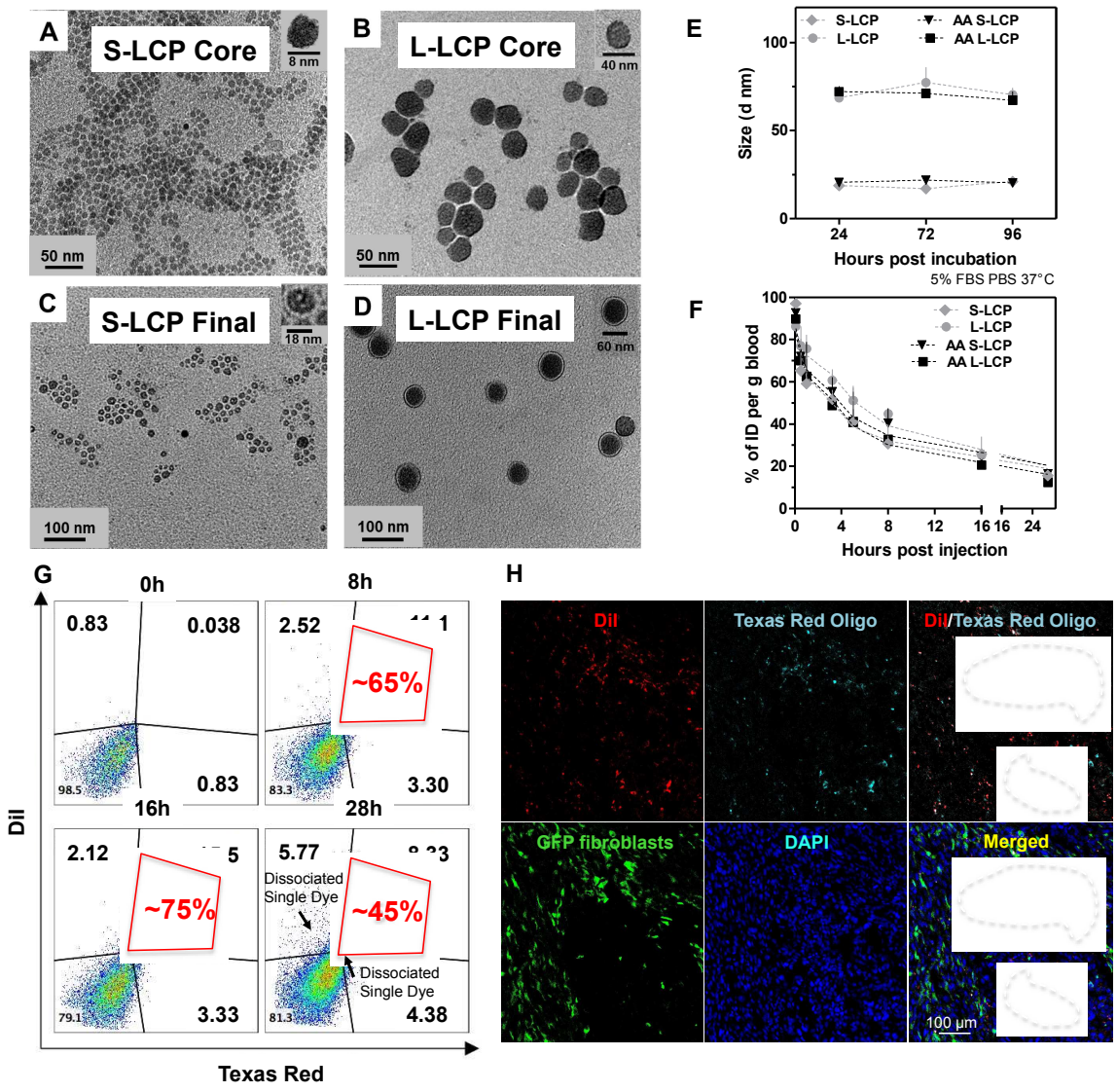

Figure 2.1 Characterization of LCP NPs.

A-B, representative TEM images of LCP cores (S/L). C-D, TEM images of final LCP NPs (S/L). E, in vitro stability of LCP NPs (S/L, +/- AA) in 5 % FBS, 37 ºC, over 96 h. F, PK profiles of LCP NP (S/L, +/-AA). G, co-association of DiI and Texas Red Oligo in the same cells within the UMUC3/3T3-GFP tumor models 8, 16 and 28 h after NPs injection. Data were analyzed by flow cytometry and the fluorescence was compensated. The red-marked population indicates the % of double positive cells in all fluorescence positive cells. H. Fluorescence images of DiI/ Texas Red Oligo labeled LCP NPs in the GFP positive fibroblasts 8 h post injection of the UMUC3/3T3-GFP tumors. The circled population indicates the double fluorescence (DiI and Texas Red) positive GFP-fibroblasts (cryosection).

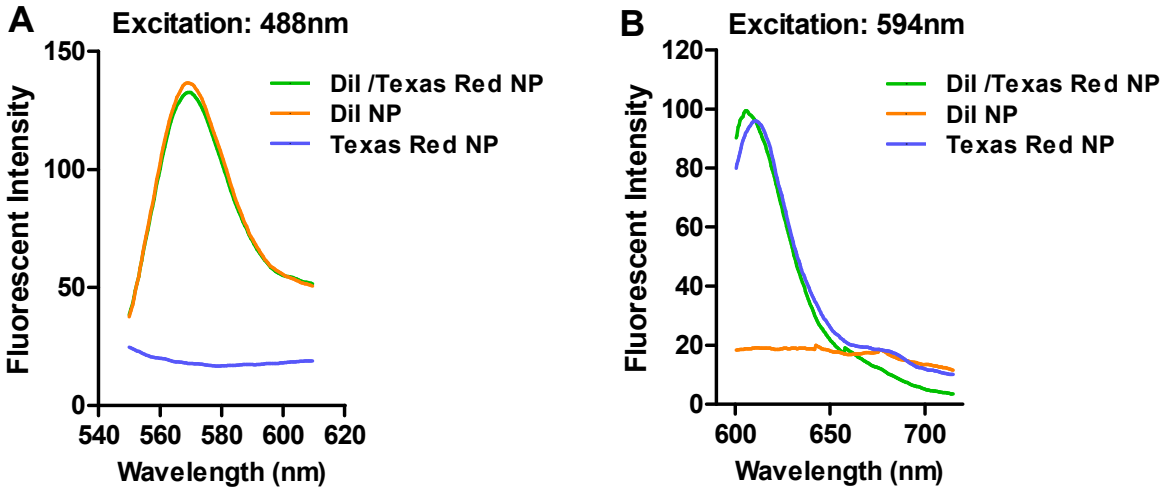

Figure 2.2 Fluorescence Intensity of DiI/Texas Red Oligo labeled NPs, in comparison with only DiI labeled NPs and only Texas Red Oligo labeled NPs.

A, excitation was fixed at 488nm, B, excitation was fixed at 594 nm.

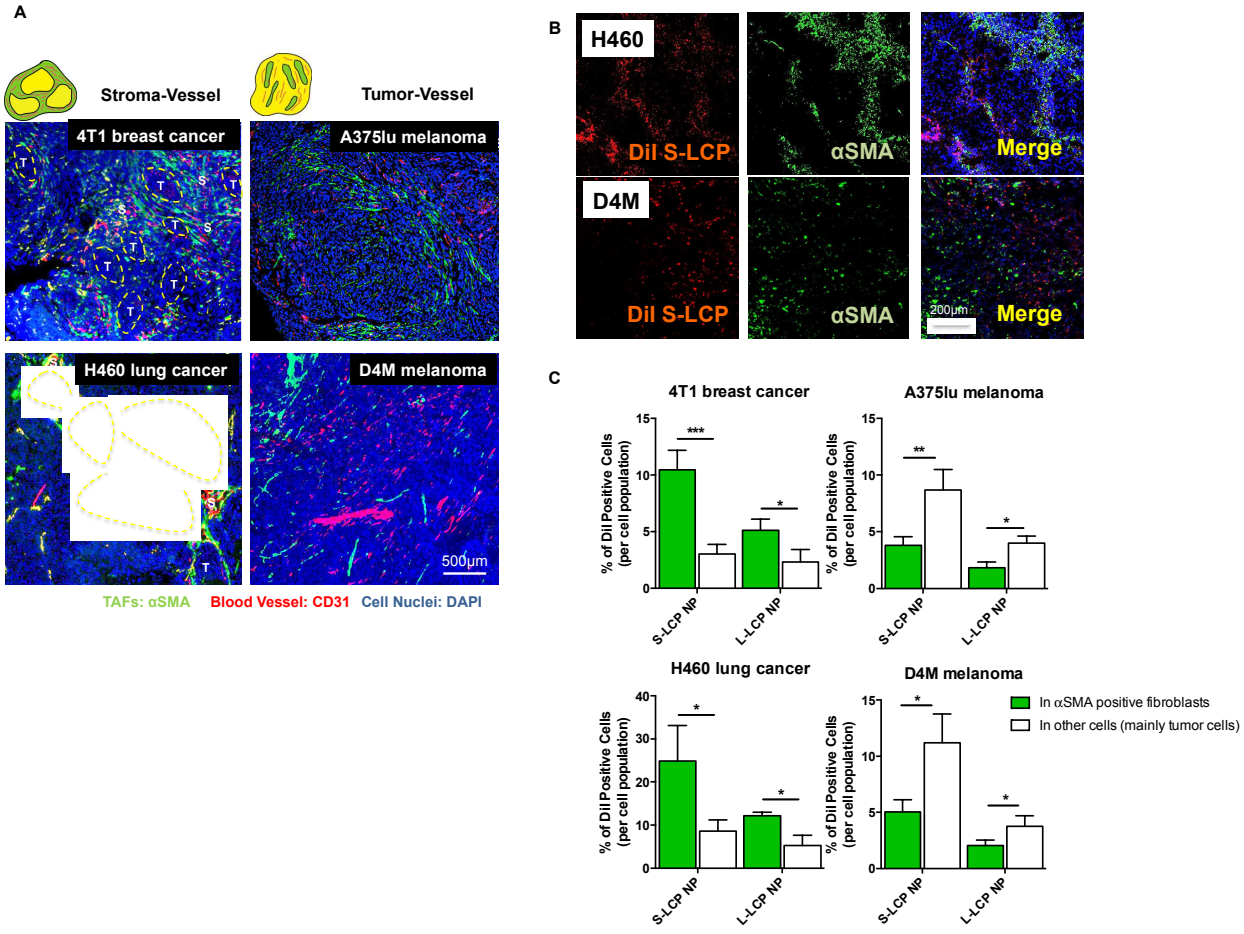

Figure 2.3 Stroma-vessel architecture affects the intratumoral distribution of non-targeted NPs.

A. Immunostaining of CD31 (red, stained for blood vessel) and αSMA (green, stained for fibroblasts) in subcutaneous tumor models (paraffin sections) with different tumor-stroma architectures. 4T1 and H460 belong to the *stroma-vessel* phenotype. Tumor nests (T) are highlighted in the images. D4M and A375lu belong to *tumor-vessel* phenotype. B. Confocal images of DiI-labeled NP distribution in D4M and H460 8 h post injection (Cryosections). The fibroblasts were visualized by staining with αSMA. C. Flow cytometry analysis of the association of non-targeted DiI-labeled NPs with either αSMA-positive fibroblasts or other non-labeled cells 8 h post injection in the four different tumors (n = 3, * $P < 0.05$, ** $P < 0.01$, *** $P < 0.001$).

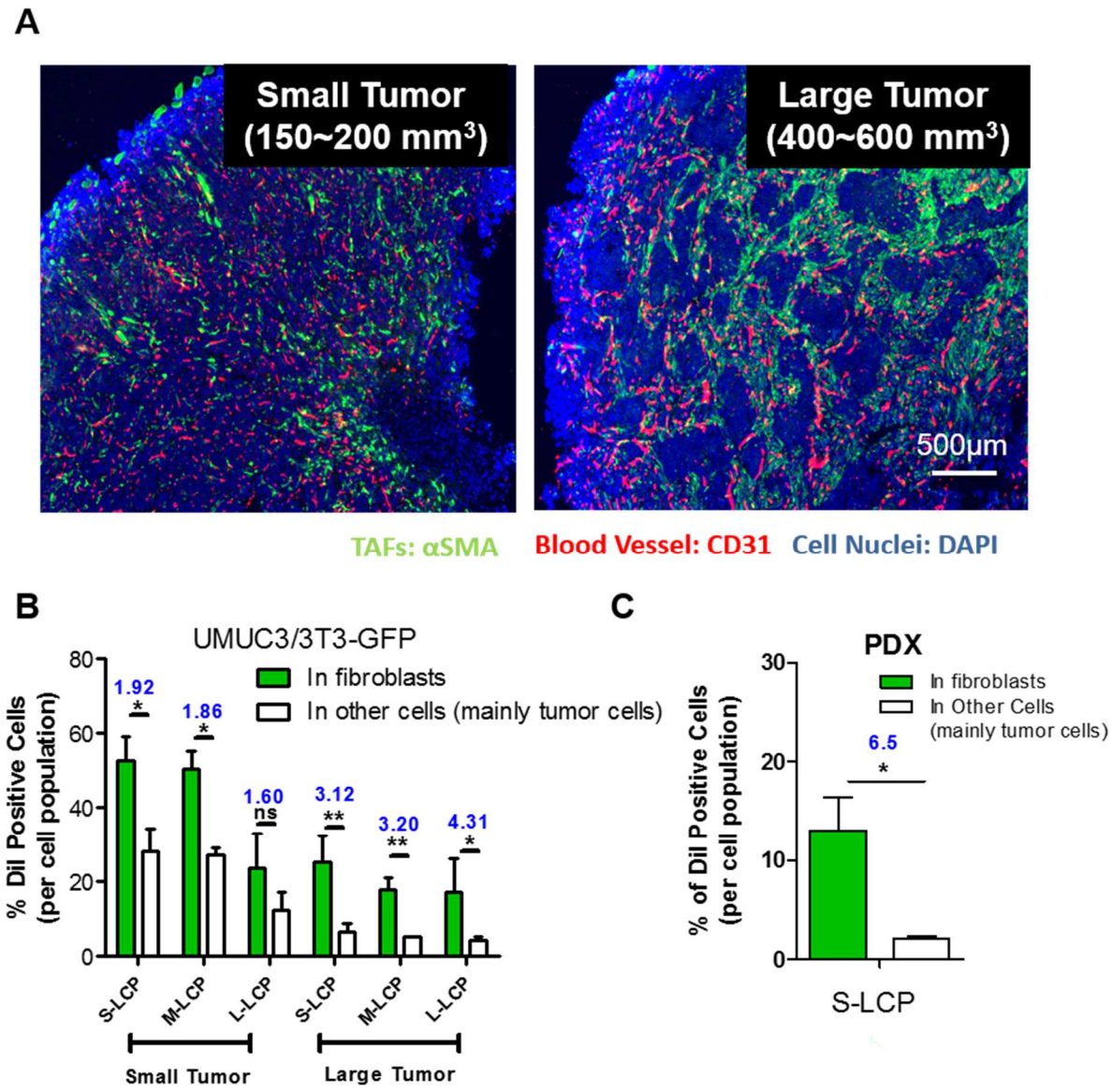

Figure 2.4 UMUC3/3T3 recapitulates NPs distribution pattern in the desmoplastic tumors.

A tumor model established by co-inoculating UMUC3 with GFP-transfected fibroblasts NIH3T3. When the tumor was small, it adopted a *tumor-vessel* phenotype in most area. As the tumor grew, it adopted a *stroma-vessel* phenotype. B. Flow cytometry analysis of the cellular distribution of non-targeted NPs (S-LCP NP, 18 nm; M-LCP NP, 35 nm (Characterization not shown); L-LCP NP, 75 nm), the ratio of DiI-positive fibroblasts and other cells are calculated and shown in blue (n = 6). F. Flow cytometry analysis of the association of S-LCP NPs in a bladder cancer patient derived xenograft (PDX) model 8 h post injection (* $P < 0.05$, ** $P < 0.01$, n = 3).

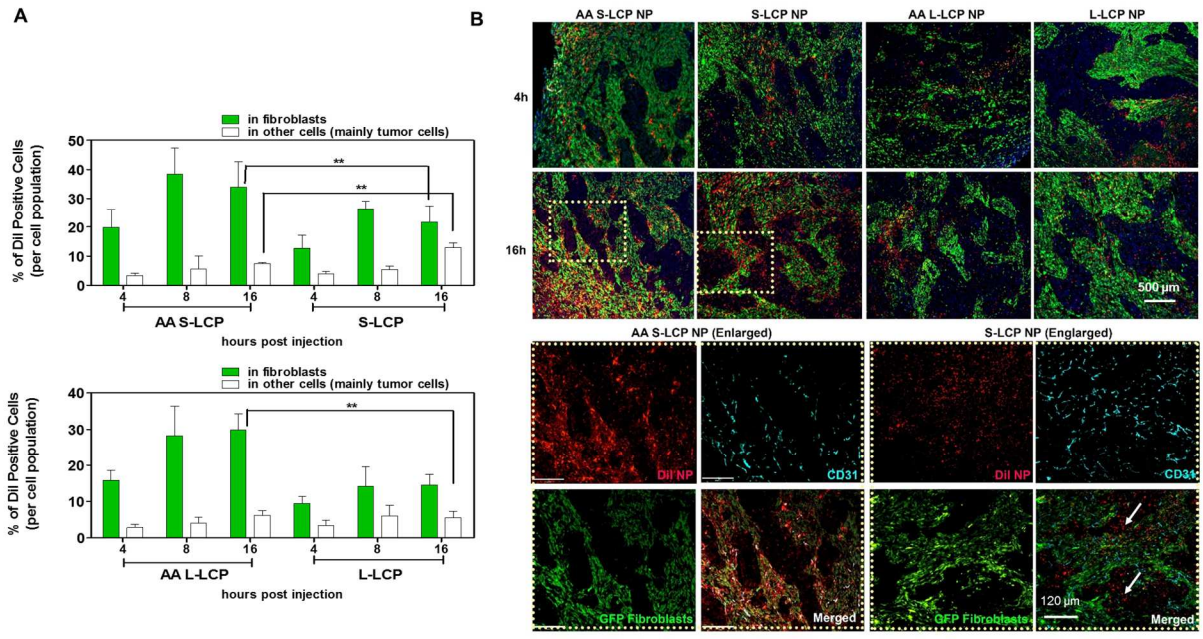

Figure 2.5 Time dependent association of non-targeted and targeted NPs in fibroblasts and other cells (tumor cells).

A. Flow cytometry analysis of the time dependent cellular distribution of NPs (S/L, +/-AA). B. Confocal images of the DiI NPs distribution in the tumor sections at 4 or 16 h post injection. Boxed areas in 16 h images are also shown as enlarged images below. Green: GFP-NIH3T3, cyan: blood vessel, red: DiI NPs. n = 6, **, $P < 0.01$.

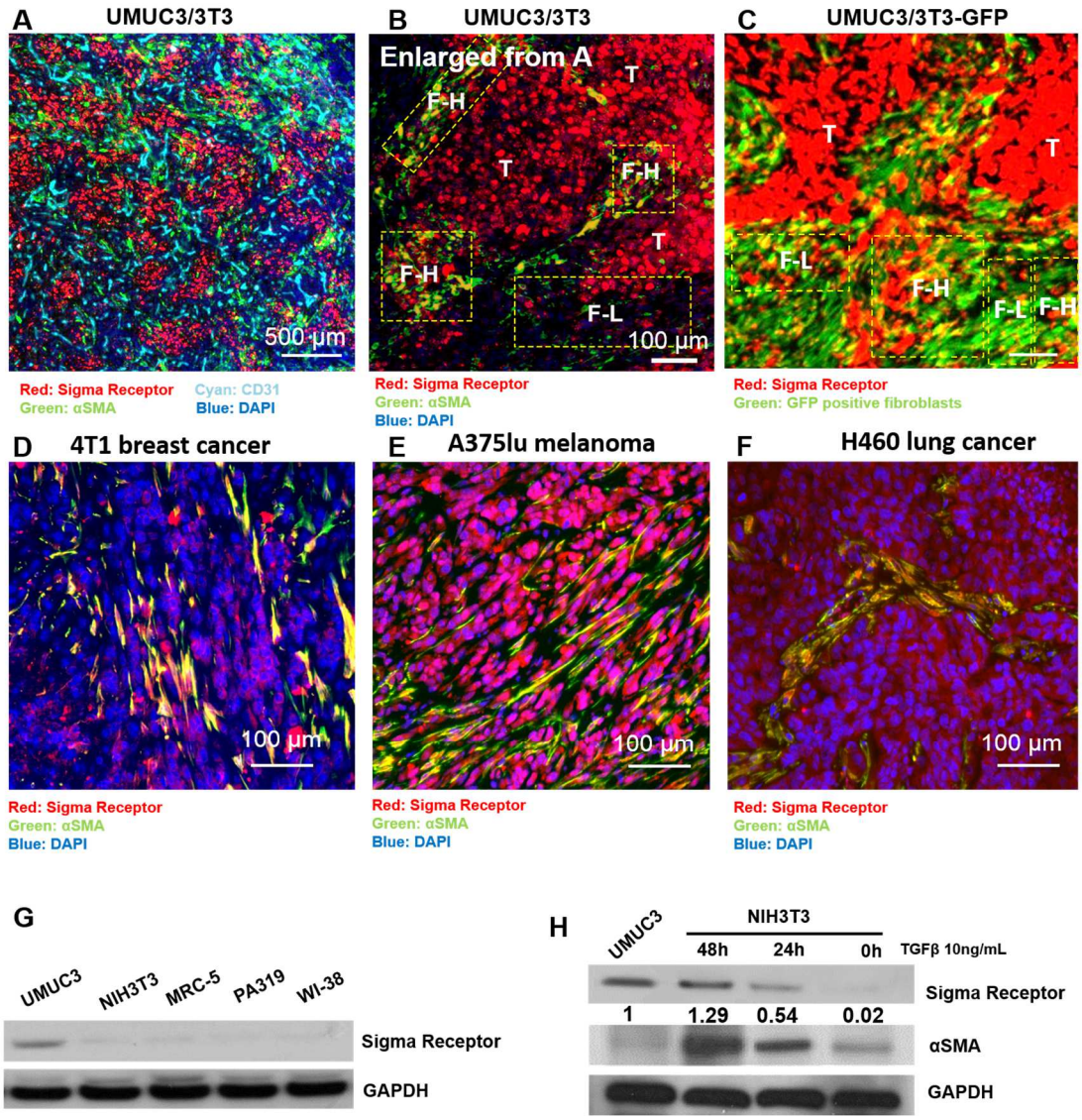

Figure 2.6 Sigma Receptor is expressed in αSMA positive TAFs.

A. IF staining of paraffin embedded tumor section from UMUC3/NIH3T3 model. Red: Sigma R; Green: αSMA; Cyan: CD31. Co-localization was observed partially between Sigma R and αSMA, appeared as orange or yellow. B. Higher magnification of the UMUC3/NIH3T3 model stained with Sigma R and αSMA. The sigma receptor High and Low regions in fibroblasts were marked as F-H and F-L. Tumor nest (T) was highly positive for Sigma R. C. Cryosection of UMUC3/NIH3T3. Green indicates all the GFP-positive fibroblasts. Red indicates Sigma R. D-F: co-staining of Sigma R (red) and αSMA (green) in 4T1, A375lu and H460. G and H. Western blot analysis of sigma receptor expression *in vitro* on different cell lines (including tumor cells UMUC3, and other mouse or human fibroblasts). Note that, activation of NIH3T3 with TGFβ enhances the expression of Sigma R.

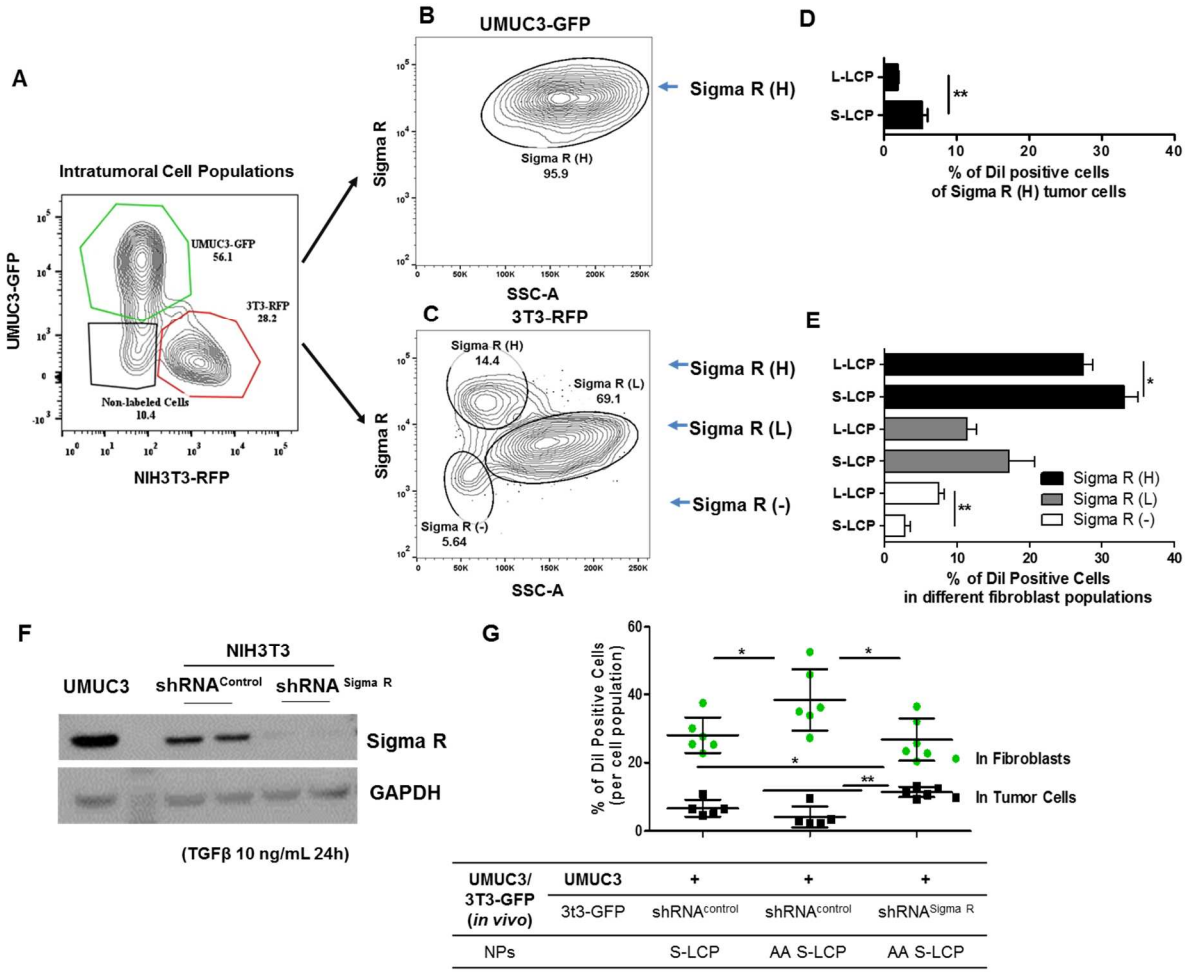

Figure 2.7 The correlation between Sigma R level and distribution of targeted NP.

A. Gating of UMUC3-GFP and 3T3-RFP in the dissociated tumor tissues. B and C. Gating of Sigma R positive populations in tumor cells and fibroblasts. Isotype controls were shown in supplementary figures. Most of tumor cells have high and coherent Sigma R expressions. Whereas, fibroblasts can be classified into Sigma R (H), Sigma R (L) and Sigma R (-) groups based on the expression of Sigma R levels. D and E. Quantitative flow analysis of the distribution of DiI NPs in different groups (different Sigma R level) of cells. F. Western blot confirmation of the shRNA knockout of Sigma R in the NIH3T3 fibroblasts *in vitro*. G. % of DiI positive cells in tumor cells and fibroblasts 8 h after injection of DiI NPs in the normal UMUC3/NIH3T3-GFP model or UMUC3/NIH3T3-GFP Sigma R knockout model (n = 6). * $P < 0.05$; ** $P < 0.001$.

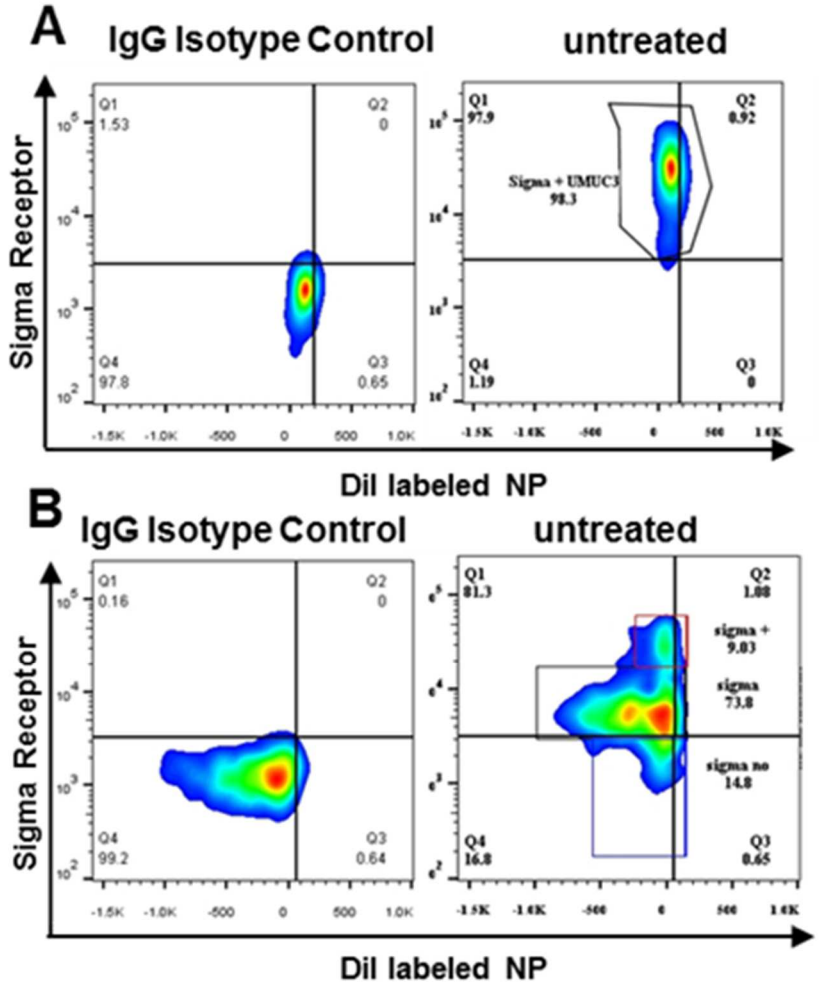

Figure 2.8 Flow Cytometry analysis of Sigma R

A. Gating of UMUC3-GFP and 3T3-RFP in the dissociated tumor tissues. **B.** Flow cytometry analysis of the DiI NPs distribution in Sigma R labeled cells (n=4). The upper row is the Sigma R and DiI distribution in the UMUC3-GFP cells. The lower row is the Sigma R and DiI distribution in the NIH3T3-RFP cells. The fibroblasts can be classified into Sigma R (H), Sigma R (L) and Sigma R (-) groups based on the expression of Sigma R levels.

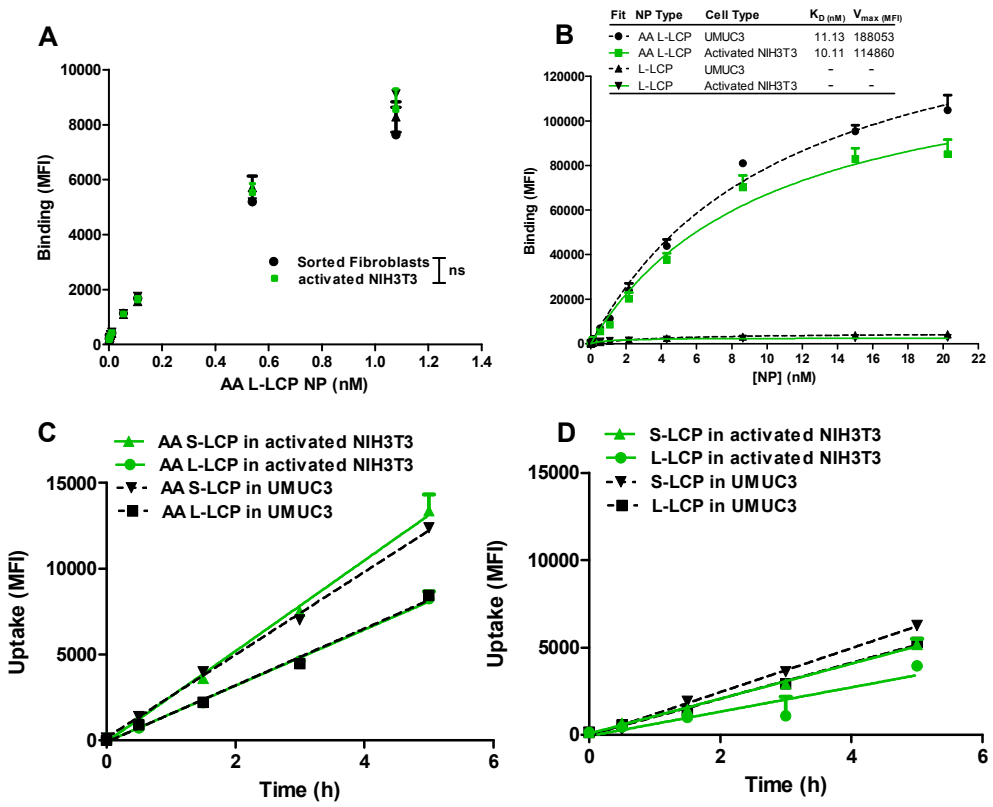

Figure 2.9 Binding affinity and uptake rate of LCP NPs (S/L, +/-AA) in UMUC3 and activated fibroblasts.

A. Binding curve of AA L-LCP NPs for activated NIH3T3 and sorted GFP-fibroblasts from the stroma-rich bladder tumor models. B. Binding affinity of LCP NPs (S/L, +/- AA) in UMUC3 and activated NIH3T3. The data points were fitted to Michaels-Menten curve, KD and Vmax were calculated and shown in the inserted chart. Time dependent uptake of 1 nM LCP NP (S/L, +/-AA) in activated NIH3T3 and UMUC3 was shown in C and D (n = 3).

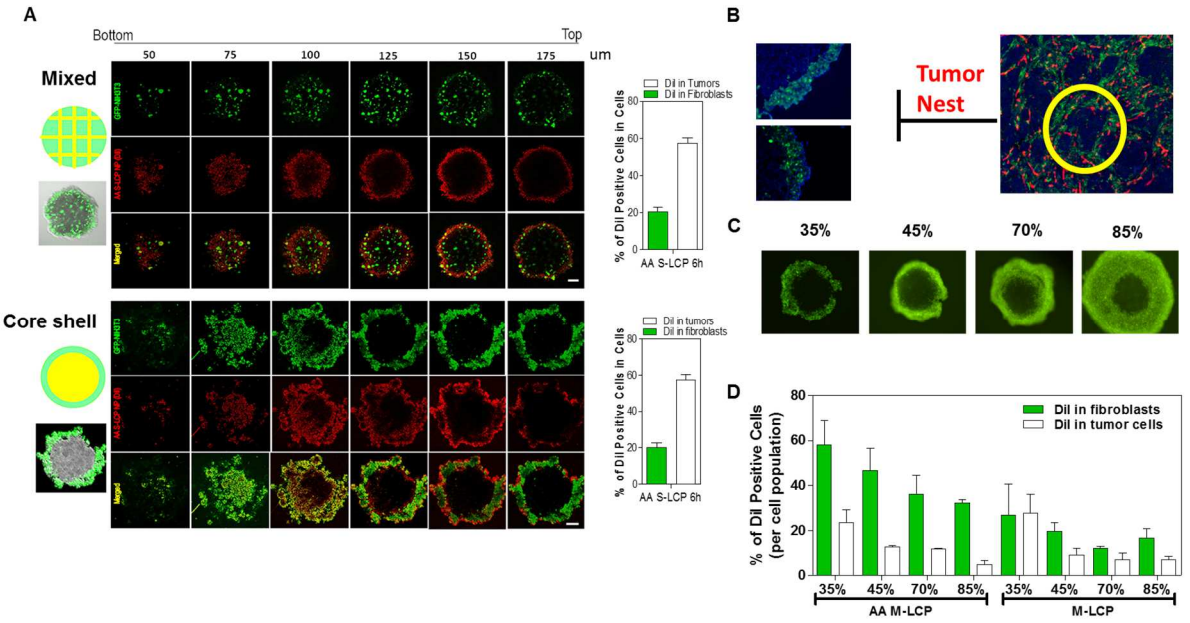

Figure 2.10 Establishment and Characterization of the "Core-Shell" exvivo tumor spheroid model.

A. Confocal Z-stack Scanning of a mixed spheroid model (mixture of 35% GFP-3T3 and 65% UMUC3) and the "core-shell" spheroid model. AA S-LCP NP were incubated with the spheroid, the penetration of DiI labeled NP were shown 4h after incubation in A. And the association of NP with cells were analyzed by flow cytometry and shown on right. B. The "core-shell" spheroid closely mimicked the tumor nest in the stroma-vessel tumor model. C. The morphology change of the spheroid when increasing amount of fibroblasts were added. D. The association of DII Labeled 35nm AA-LCP NP with spheroid with different amount of fibroblasts. The association fibroblasts with NP increased when the fibroblasts ratio increased.

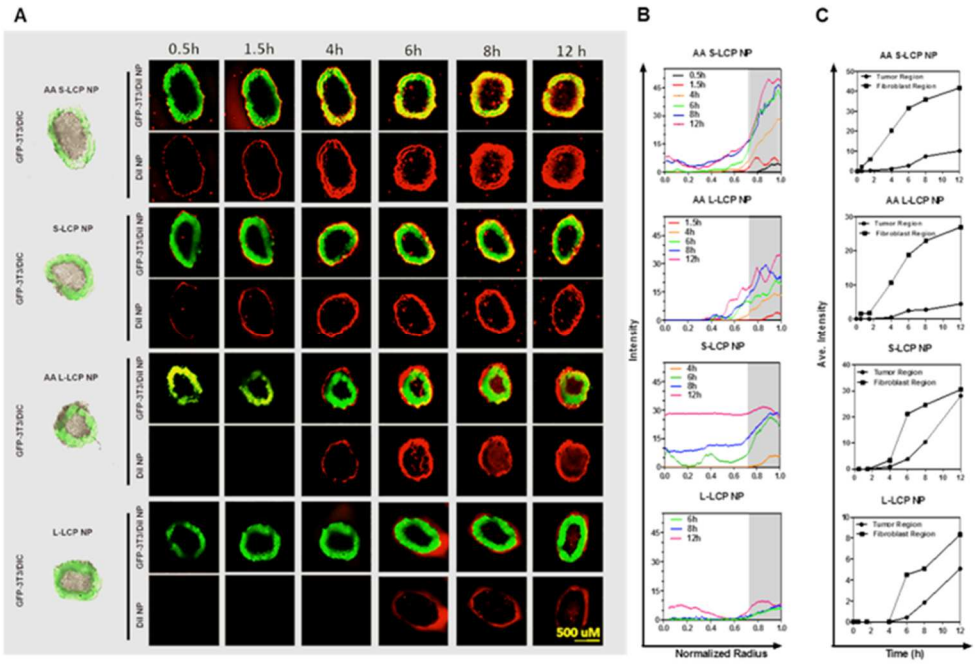

Figure 2.11 Penetration, binding and internalization kinetics of LCP NP (L/S, +/- AA) in a" Core-Shell" ex-vivo spheroid model.

The "Core-Shell" spheroid model was established by coating the UMUC3 spheroid with GFP-3T3 fibroblasts. Fluorescence images were acquired after incubation with DiI labeled LCP NP for determined time points and shown in A. Scale bar, 500 um. The corresponding fluorescence intensity profiles are shown at determined time points in B. The grey rectangle indicates the position of fibroblasts. Change of average fluorescence intensities overtime in the tumor region and the fibroblasts region after incubation with DiI labeled LCP NP are shown in C. Mean value was presented (n = 3).

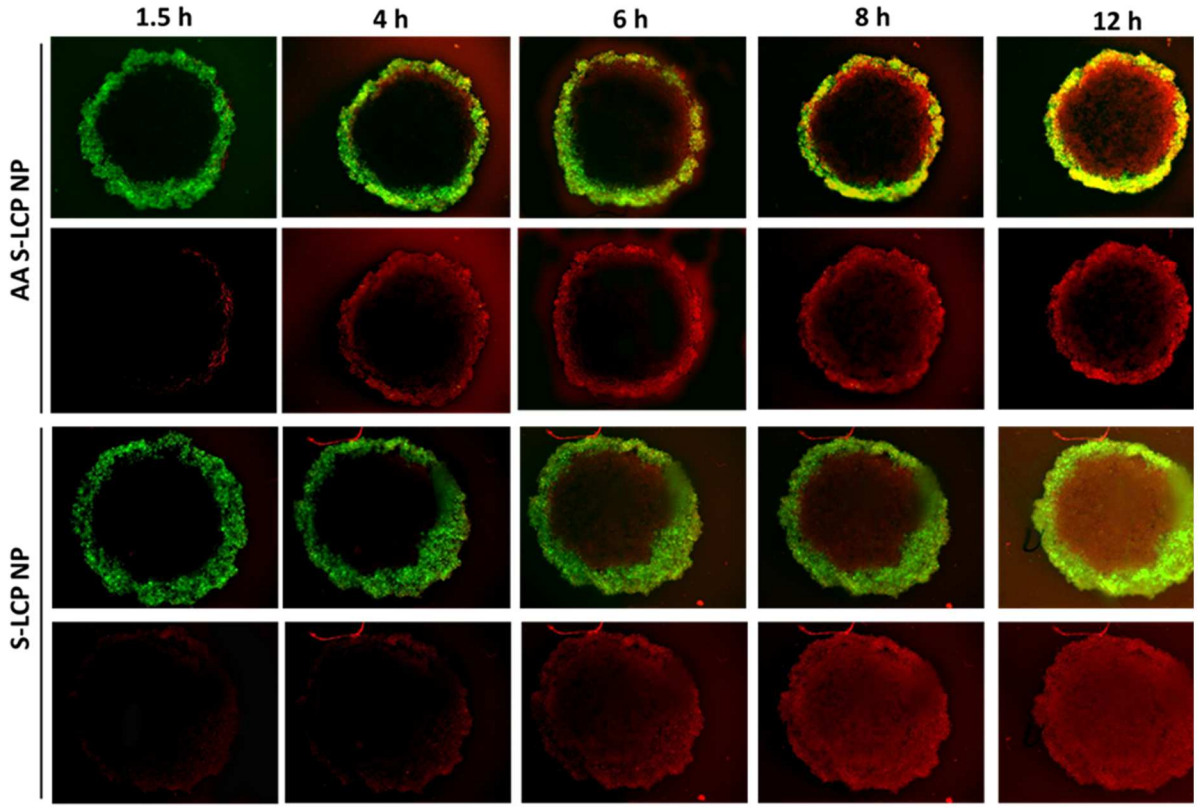

Figure 2.12 Time-dependent penetration of DiI labeled S-LCP NPs (+/-AA) in UMUC3 only spheroid.

UMUC3-GFP constitutes the shell of the spheroid, with the similar thickness as compared to the UMUC3/3T3 spheroid. Upper two lanes are the AA-S-LCP NPs, bottom two lanes are the S LCP NPs.

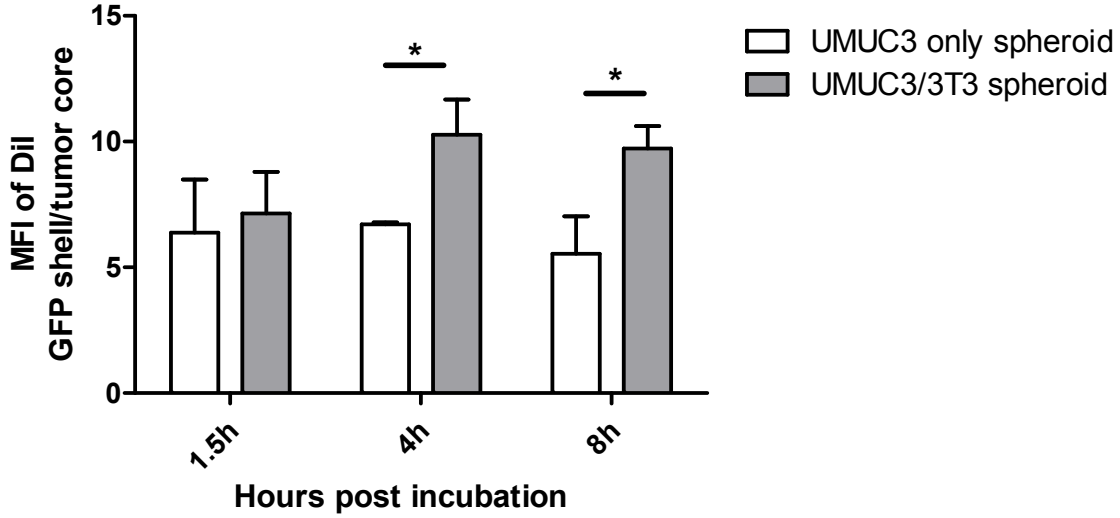

Figure 2.13 The ratio of mean fluorescence intensity (MFI) between the GFP shell and tumor core at different time points.

AA S-LCP NPs were dosed. UMUC3 only and UMUC3/3T3 spheroids were compared (n = 3, * $P < 0.05$).

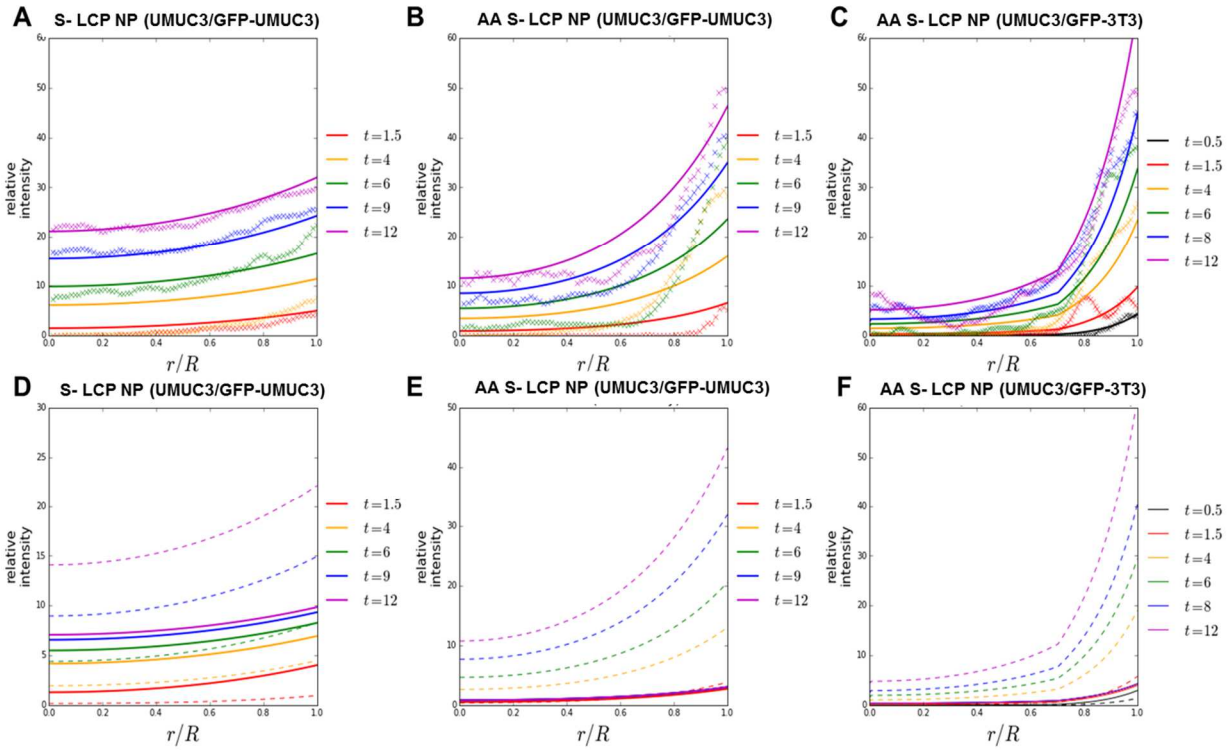

Figure 2.14 Mathematical modeling of S-LCP NPs (+/-AA) distribution in the core-shell spheroid and predictions of cellular uptake of S-LCP NPs (+/-AA)

A, B, C Fluorescence intensity profiles measured in fluorescence images of core-shell 3D spheroids (symbols), and those predicted by the mathematical model (solid lines). D, E, F Predictions of cellular associated NPs (dashed lines) and acellular NPs (solid lines).

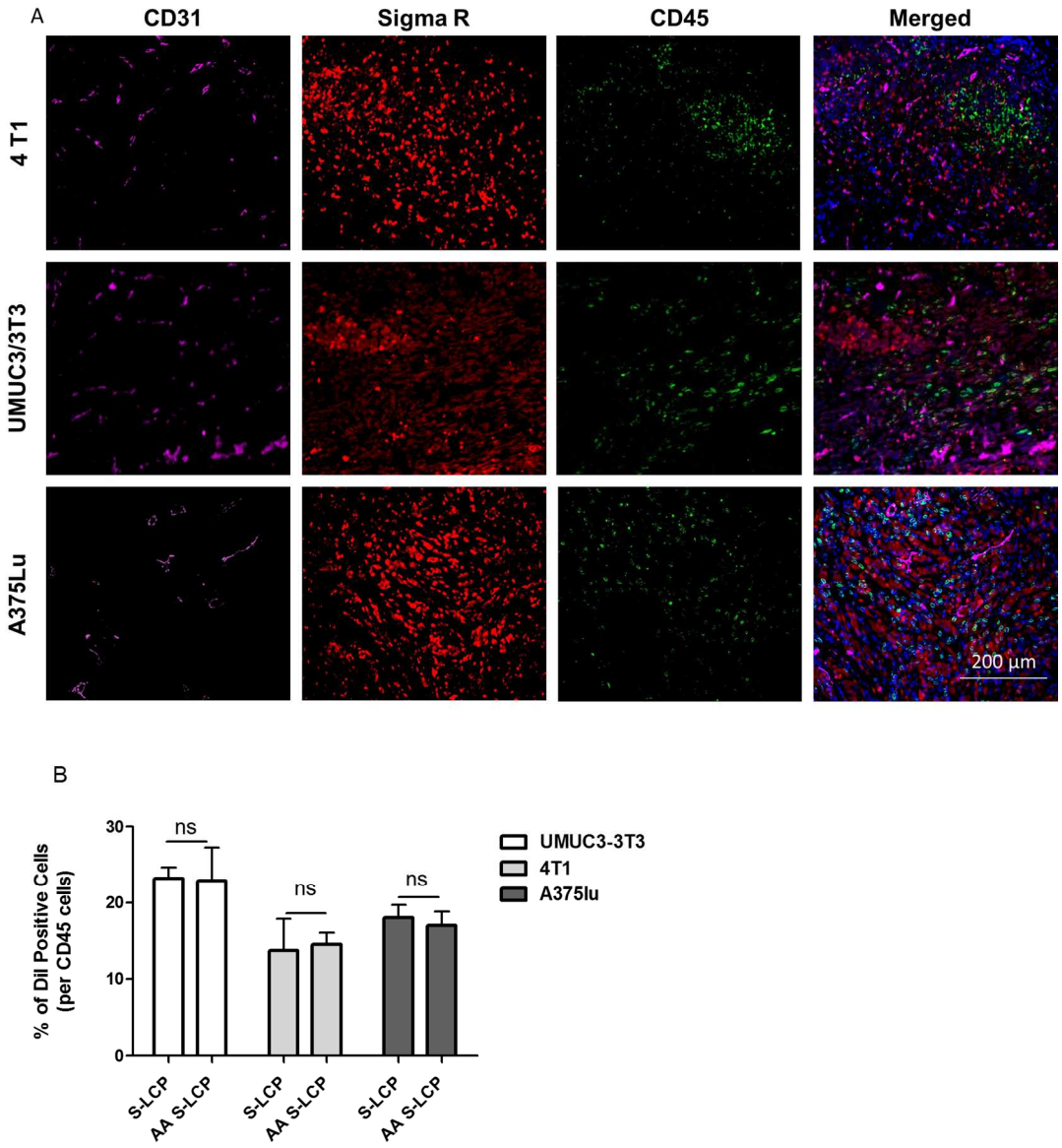

Figure 2.15 Off-target distribution of NPs in infiltrating leucocytes of the desmoplastic UMUC3 xenografts.

A. IF staining of blood vessel (CD31, shown as cyan), Sigma R (shown as red) and CD45 (shown as green) positive leucocytes in the stroma vessel type tumors (4T1 and UMUC3/3T3) and tumor vessel type tumors (A375lu). Results indicated the CD45 positive cells were not localized near blood vessel in either types of tumors and most of them were not Sigma R positive. B. Flow cytometry analysis of the distribution of DiI S-LCP NPs (+/- AA) in CD45 positive cells 8 h after intravenous injection (n = 3). The ratio of DiI-positive CD45 positive cells in all CD45 positive cells was lower compared to that in fibroblasts. And the % was independent of the presence of targeting ligands.

CHAPTER 3: PRIMING OF THE DAMAGED TUMOR ASSOCIATED FIBROBLASTS ENHANCES THERAPEUTIC EFFICACY OF CISPLATIN NANOPARTICLES FOR DESMOPLASTIC BLADDER CANCER TREATMENT[4]

3.1 Summary

The tumor microenvironment (TME) serves as a multidrug resistant center for tumors under the assault of chemotherapy and a physiological barrier against the penetration of therapeutic NPs. Previous studies have shown that TAFs, as the major stroma cells, create a binding site barrier (BSB) that trap almost 60% of NPs. Though, the off-target distribution of therapeutic NPs to TAFs can partially suppress stroma cells, contributing to improved therapeutic outcomes, a drug resistant phenotype gradually arises after repeated doses of chemotherapeutic NPs. Herein, the acquisition of drug resistant phenotypes in the TME after repeated cisplatin NPs treatment was examined. Particularly, this study was aimed at investigating the effects of NP-damaged TAFs on neighboring cells and the alterations of stromal structure after cisplatin treatment. Findings suggested that while off-targeted NPs damaged TAFs and inhibited tumor growth after an initial dose, chronic exposure to cisplatin NPs led to elevated secretion of Wnt16 in TAFs. Wnt16 upregulation was then attributed to heightened tumor cell resistance and stroma reconstruction. Results attest to the efficacy of Wnt16 knockdown using siRNA against Wnt16 in damaged TAFs as a promising combinatory strategy to improve efficacy of cisplatin NPs in a desmoplastic bladder cancer xenograft (UMUC3/3T3).

[4]This chapter previously appeared as a research article in Journal of Controlled Release. The original citation is as follows: Lei Miao, Yuhua Wang, C. Michael Lin, Yang Xiong, Naihan Chen, Lu Zhang, William Y. Kim and Leaf Huang, nanoparticle modulation of the tumor microenvironment enhances therapeutic efficacy of cisplatin, Journal of Controlled Release, 2015, 217 (10):27-41.

3.2 Introduction

Cisplatin, a front line DNA alkylating agent, is a chemotherapeutic regime used to treat basal type muscle invasive bladder cancer [188]. Clinical application of cisplatin is limited by adverse effects including neuro- and nephrotoxicity [177, 189, 190]. Herein, NPs have been designed to improve the pharmacokinetics, facilitate the intratumoral accumulation and subsequently reduce adverse effects of cisplatin-based treatment [191-193]. In previous work we developed a novel cisplatin nanoformulation consisting of hydrophobic solid cisplatin cores surrounded by PEGylated cationic lipid corona for the delivery of cisplatin (cisplatin LPC NPs, shorted as cisplatin NPs) [194, 195]. Anisamide (AA), a ligand for the sigma receptor (Sigma R) overexpressed on the surface of cancerous epithelial cells and TAFs, was coated on the NPs to enhance receptor mediated endocytosis [173, 177, 194]. Previous results proved this novel cisplatin NPs exhibited enhanced anticancer activity for the treatment of aggressive bladder cancer at low doses (cisplatin 1mg/kg) compared to free cisplatin, which was completely ineffective at the same dose level [74].

Despite encouraging antitumor efficacy after initial treatment, drug resistant eventually contributes to ultimate treatment failure [74, 196]. Efforts have been focused on combining cisplatin NPs with another nanoformulated therapeutic regimen to inhibit DNA repair enzymes, cisplatin export and subsequently reverse tumor cell autonomous resistance [195, 197, 198]. However, inconsistencies between the *ex vivo* prediction of combinatory NPs sensitivity and the *in vivo* therapeutic outcome suggests that stroma cells in the TME also play a key role in the *innate* resistance [70, 199-201]. Stromal cells in the TME, including TAFs, macrophage and endothelial cells build a physical barrier within tumors by crosslinking the ECM to inhibit penetration of the therapeutic NPs [92, 105]. They also mediate tumor cell-resistance by secreting growth inducing cytokines and growth factors [201-204]. Yet, the *innate* resistance from TME still fails to explain progressions from high treatment sensitivity in early stages to late stage therapeutic failure [70]. Findings suggest acquired resistance in stromal cells may contribute to the long-term treatment failure [70]. DNA damage

induced secretion of extracellular molecules was likely to explain the acquired resistance [205, 206]. In agreement with this theory, recent research indicates that damaged stromal cells secrete damage response program (DRP) molecules to promote the survival and growth of neighboring cells [70], and thus paracrinely influence treatment outcome [207, 208].

Stromal cell populations damaged by cisplatin uptake control the secretion of DRP molecules. Therefore, intratumoral disposition, in particular the off-target distribution of NPs in stroma cells was hypothesized to regulate drug resistance through secretion of DRP molecules. To reverse the cisplatin NPs induced drug resistance, the blockade of DRP production and secretion was proposed in combination with cisplatin NPs as a proof of concept strategy.

DRP molecules mainly consist of proteases and mitogenic growth factors [70, 207, 209]. Wingless-type MMTV integration site (Wnt) family molecules are considered one of the major mitogenic growth factors that constituent DRP molecules [210]. Though little information has linked Wnt signaling to cisplatin induced resistance, abnormal Wnt signal activation promotes tumorigenesis, stemness and resistance in various tumors [211, 212]. In addition, previous studies correlated Wnt16 expression and chemotherapy-induced DNA damage in prostate and breast cancer fibroblasts [70, 213]. So, Wnt16 plays a potentially significant role in regulating the crosstalk between neighboring cells during DNA damage. Herein, Wnt16 is investigated as a potential DRP molecule for cisplatin mediated resistance and knockdown of Wnt16 was therefore proposed to overcome cisplatin induced resistance. Several studies have demonstrated functional blocking of Wnt-canonical β-catenin pathway using monoclonal antibodies or small molecule inhibitors [214]. However, undesired off-target effects have led to safety concerns in this approach [215, 216]. RNA interference provides an alternative way to maintain the aforementioned specificity while also improving safety. Liposome-protamine-hyaluronic acid NPs (LPH-NPs) was used to encapsulate siRNA and was shown to be an effective delivery tool in various tumor models [217]. Therefore, based on previous claims, a combination therapy of cisplatin NPs and LPH-NPs delivered siRNA against Wnt16 (siWnt NPs) was proposed to be the optimal treatment for of aggressive bladder cancer.

In the current study, a desmoplastic bladder cancer xenograft (UMUC3/3T3) was established, similarly to the one described in the previous chapter, by co-inoculating human basal type bladder tumor UMUC3 with mouse NIH3T3 fibroblasts. This model resembles bladder tumor patient samples in the components and in the morphology of the TME [74]. In the desmoplastic UMUC3/3T3 model, we investigated the off-target effect of cisplatin NPs on TAF-damage, the Wnt16 secretion level and antitumor efficacy. We also studied the role of cytokines, such as Wnt16 in the regulation of crosstalk between tumor cells and the TME. We conclude that targeting tumor-stroma regulatory cytokines in the TME along with NPs-delivered chemotherapy could potentially overcome intratumoral off-target effects and improve treatment responses.

3.3 Materials and Methods

3.3.1 Materials

1,2-distearoyl-sn-glycero-3-phosphoethanolamine-N-(methoxy(polyethyleneglycol)-2000) ammonium salt (DSPE-PEG2000), 1,2-dioleoyl-3-trimethylammonium-propane chloride salt (DOTAP), dioleoyl phosphatidic acid (DOPA) were obtained from Avanti Polar Lipids (Alabaster, AL). Cholesterol, hyaluronic acid (HA), protamine sulfate (fraction ×from salmon), hexanol, triton-100, cyclohexane were obtained from Sigma-Aldrich (St Louis, MO). Cisplatin was purchased from Acros Organics (Fair Lawn, NJ). All the other chemicals were purchased from Sigma-Aldrich unless otherwise mentioned. DSPE-PEG-AA was synthesized based on the previous established protocols [173]. The mouse Wnt16 siRNA with sequence 5'-CCAACUACUGCGUGGAGAA-3', the human Wnt16 siRNA with sequence of 5'-CCAACUACUGUGUAGAAGA-3' and the control siRNA with sequence 5' AATCTCCGAACGTGTCACGT-3' were purchased from Sigma-Aldrich.

3.3.2 Cell lines and Animals

The human bladder transitional cell line UMUC3 was provided by Dr. William Kim (University of North Carolina at Chapel Hill, NC). The mouse embryonic fibroblast cell line NIH3T3 and the human umbilical vein endothelial cells (HUVEC) were purchased from UNC Tissue Culture

Facility. UMUC3 and NIH3T3 were maintained in Dulbecco's Modified Eagle's Media (Invitrogen, Carlsbad, CA), supplemented with 10% feta bovine serum (Sigma, St. Louis MO) or 10% bovine calf serum (Hyclone, Logan, Utah), penicillin (100 U/mL) (Invitrogen) and streptomycin (100 μg/mL) (Invitrogen). HUVECs were cultured in HuMEC basal medium (Invitrogen, Carlsbad, CA), supplemented with 10% fetal bovine serum (sigma, St. Louis, MO), bovine pituitary extract (Invitrogen, Carlsbad, CA) and HuMEC Supplement (Invitrogen, Carlsbad, CA). Female athymic Balb/C nude mice of 6–8 weeks old were provided by the University of North Carolina animal facility. All animal protocols were approved by the University of North Carolina at Chapel Hill's Institutional Animal Care and Use Committee. Antibodies used for western-blot analysis and immunostaining are listed in **Error! Reference source not found.**

3.3.3 Preparation and Characterization of Cisplatin NPs

Cisplatin NPs were formulated as previously described [41, 74, 154]. Briefly, 300 μL of 200 mM cis-$[Pt(NH_3)_2(H_2O)_2](NO_3)_2$ and 300 μL of 800 mM KCl aqueous solution were separately dispersed in a mixed oil solution cyclohexane/triton-X100/hexanol (75:15:10, V:V:V) and cyclohexane/Igepal CO-520 (71:29, V:V) to form a well-dispersed reversed micro-emulsion. Then, 500 μL of DOPA (20 mM) was added to the cisplatin precursor emulsion and the mixture were stirred for 20 min. Afterwards, the two emulsions were mixed and reacted for another 20 min. Forty mL of ethanol was then added to break the micro-emulsion and particles were collected by centrifuge at 10,000 g for at least 15 min. The pellets were washed with ethanol twice to completely remove the surfactants and cyclohexane, and then re-dispersed in 2.0 mL of chloroform for storage. Finally, the preparation of cisplatin NPss consisted of mixing 1 mL of cisplatin nanocores with 200 μL of 20 mM DOTAP/Cholesterol (1:1), with 20 μL of 20 mM DSPE-PEG-2000 or 20 μL of 20 mM DSPE-PEG-2000/DSPE-PEG-AA (4:1). After evaporating the chloroform, the residual lipid was dispersed in 100 μL of 5% glucose. The particle size of cisplatin NPs was confirmed using a Malvern ZetaSizer Nano series (Westborough, MA). TEM images of LPC NPs were acquired using a JEOL 100 CX II TEM

(JEOL, Japan). Cisplatin NPs were negatively stained with 2% uranyl acetate. The drug-loading capacity and platinum content were measured using Inductively Coupled Plasma-Mass Spectroscopy (ICP-MS, NexlONTM 300, Perkin Elmer Inc). Samples were digested in 60% HNO3 and diluted in water to a final acid content of 2%. Platinum concentration was determined using the 195Pt isotope.

3.3.4 Preparation and Characterization of siWnt NPs

siWnt NPs were prepared through a stepwise self-assembly process based on a previously well-established protocol [217]. Briefly, cholesterol and DOTAP (1:1, mol/mol) were dissolved in chloroform and solvent was removed by rotary evaporator. The lipid film was then hydrated with distilled water to make the final concentration of 10 mmol/l cholesterol and DOTAP. Then, the liposome was sequentially extruded through 400 nm, 200 nm, 100 nm, and 50 nm polycarbonate membranes (Millipore, Billerica, MA) to form 70–100 nm unilamellar liposomes. The siWnt NPs polyplexes core were formulated by mixing 140 μl of 36 μg protamine in 5% glucose with equal volume 24 μg siRNA and 24 μg HA in 5% glucose. The mixture solution was incubated at room temperature for 10 minutes and then 60 μl cholesterol/ DOTAP liposome (10 mmol/l each) was added. Post insertion of 15% DSPE-PEG and DSPE-PEG-AA were further performed at 50 °C for 15 minutes. The size and surface charge of the NPs were determined by Malvern ZetaSizer Nano series (Westborough, MA). TEM images were acquired using a JEOL 100 CX II TEM (JEOL, Japan). Particles were negatively stained.

3.3.5 GFP Lentivirus Transduction in NIH3T3 Fibroblast

Please refer to **Section 2.3.6**

3.3.6 Establishment and Evaluation of Patient Derived Xenograft (PDX) Model

PDX tumors were obtained from human bladder cancer patients. Excess bladder tumors were taken at the time of the transurethral resection of the bladder tumor (TURBT). Further pathologic examination confirmed that the tumor was a high grade, urothelial carcinoma of the bladder. The

primary tumor was first processed for implantation and then sectioned. Tumor fragments were stored in a urine cup on ice for transport and storage. Prior to implantation, tumor fragments were washed in 5x Pen-Strep in PBS and dipped in aliquots of Matrigel. Fragments were then surgically implanted into NOD-NSG-SCID mice on the flank of the animal. Typically, tumor fragment sizes were approximately 2 mm^3. Once an appropriate size was reached, tumors were resected and passaged into additional mice. Passages were conducted until passage three was reached. At this point, passage three mice were administered a total of five doses of LPC NPs via IV every other day.

3.3.7 Collection of Conditioned Medium

Conditioned medium was collected as described elsewhere [207, 218]. NIH3T3 cells were activated by 10 ng/mL TGF beta 2h before experiments. The activated NIH3T3 cells were treated with siCont NPs, siWnt NPs respectively with Opti-MEM medium for 4h. Post transfection, cells were further treated with free cisplatin and cisplatin NPs for another 3h. After treatments, the cells were rinsed thrice with PBS and left overnight (in total 2 days including the treatment) in DMEM medium with 5% BCS. Culture medium was then collected and centrifuged at 900 rpm for 5 min, and then supernatant was filtered through 0.45 μm filter and collected as conditioned medium for further study.

3.3.8 Cell Treatments with Cisplatin

NIH3T3 cells were pre-activated with 10 ng/mL TGF-β and treated with10 μM free cisplatin or cisplatin NPs for 3h before replacing into fresh full medium, and then left overnight (in total 2 days). After treatment, the conditioned medium (CM) was collected (Supplementary Methods) and cells were rinsed 3x with PBS. Both CM and cells were used for western-blot assay (Supplementary Methods) and ELISA assay (Supplementary Methods) to detect the expression levels of Wnt16.

3.3.9 *In vitro* Transfection of siWnt NPs

UMUC3 cells or activated NIH3T3 cells were grown until 80% confluent in six-well plates. Then LPH NPs loaded with siRNA against mouse Wnt16 (siWnt NPs), human Wnt16 or control siRNA (siCont NPs) were added to each well in the presence of OptiMEM medium with final concentration of 250 nmol/L. Medium was refreshed 4h post transfection. The remaining cells were treated for another 3h with 10 μM cisplatin to boost the expression of Wnt16, then washed and left overnight. The knockdown efficiency and specificity of Wnt16 by siRNA were determined by western-blot analysis with GAPDH as a loading control.

3.3.10 Non-contact Co-culture Model for Mechanistic Study

Non-contact co-culture transwell system was established according to a previous protocol with little adjustment (**Figure 3.1**)[218]. Briefly, activated NIH3T3 were seeded into a transwell filter (polycarbonate membrane insert, 0.45 μm pore, Corning Inc.). Before co-culture, transwell insert received different types of treatments, including solo siCont NPs or siWnt NPs treatment, or LPH NPs (containing either siCont or siWnt) transfection followed by cisplatin (NPs) assault (namely siCont NPs/cisplatin (NPs) or siWnt NPs/cisplatin (NPs)). Immediately after extensive washing of the insert cells with PBS, the co-culture start by setting the insert in to the lower chambers pre-seeded with UMUC cells, HUVEC cells or naïve NIH3T3 for different experimental purpose. After determined time of co-culture, bottom cells were collected for western-blot analysis, β-catenin nucleus translocation assay, tube formation and other immunofluorescence assay (Supplementary Method). **β-catenin nucleus translocation assay.** β-catenin assay was carried out in the lower chamber UMUC3 cells, as a mechanistic study to determine the canonical Wnt pathway activation in the neighboring UMUC3 cells by Wnt16 secreted from damaged fibroblast [219]. Lower chamber UMUC3 cells were seeded on a coverslip (Fishier Scientific), and co-cultured with upper chamber NIH3T3 cells subjected to the aforementioned treatments. At indicated time points, coverslips were taken out, fixed, permeabilized, blocked and probed with anti-β-catenin antibody. Cells were further

incubated with FITC-labelled secondary antibody and then counterstained with Hoechest 33342 (Invitrogen). Co-localization of β-catenin with cell nuclei was visualized using a confocal microscope (Laser Scanning. Zeiss 510 Meta). **Scratch assay.** The spreading and migration capabilities of UMUC3 cells affected by Wnt16 secreted from neighboring fibroblasts were also assessed in the lower chamber UMUC3 using a scratch assay [220, 221]. Upon co-culturing with treatment assaulted NIH3T3, a linear wound was scratched into the monolayer of UMUC3 with a sterile 200 μl pipette tip. The width of the wound was measured under a microscope at 0 and 20h after co-culture to assess the migration ability of the cells. The data were performed in duplicate and analyzed using Image J. **Lentiviral luciferase reporter assay.** The activation of Wnt pathway in the neighboring naïve fibroblast by damaged fibroblast was evaluated using TCF/LEF reporter assay [222]. To produce stable Wnt-reporter cell lines, NIH3T3 cells were transduced with the Cignal Lenti TCF/LEF Reporter (luc) kit for 48h. Following transduction, the cells were cultured under puromycin selection to generate a homogenous population of transduced cells. Activated NIH3T3 and Wnt-reporter cell lines were seeded on to the upper chamber and lower chamber of the non-contact co-culture system respectively. Four h post co-culture, bottom cells were collected and luciferase assays were performed using a Luciferase Assay Kit (Promega, Inc.) according to the manufacturer's instruction. Tube formation assay. Paracrine secretion of Wnt16 in inducing angiogenesis was evaluated by tube formation assay [223, 224]. The non-contact co-culture system was established with the upper chamber of activated NIH3T3 receiving different treatments and bottom chamber of HUVEC in a 24-well plate. For the formation of capillary-like structures, 24-well plate were pre-coated using growth factor-reduced matrigel (BD biosciences, San Jose, CA, USA). HUVECs (4×10^4 cells/well) were plated on top of matrigel (280 μL/well). Four h after co-culture, HUVECs were stained by calcein AM (Invitrogen) and visualized under a fluorescence microscope. The number of tubes was quantified using Image J from 5 randomly selected microscopic fields.

3.3.11 *In vitro* Analysis of Cell Proliferation and Chemotherapy Resistance

To assess the role of Wnt16 in inducing cisplatin resistance of cancer cells, two sets of experiments were designed. First, UMUC3 cells were cultured with recombinant Wnt16 protein (R&D systems) at different concentrations (0.03, 0.3, 3, 6, 12 μg/mL) 6 h prior to cisplatin treatment. Then, cisplatin at a range of concentrations bracketing cell line's IC_{50} was added to the medium and incubated for 48 h. Cell viability was assayed by 3-(4,5-Dimethylthiazol-2-yl)-2,5-Diphenyltetrazolium Bromide (MTT) to address the extent of resistance. Non-linear regression curves were plotted using GraphPad Prism. Second, chemo-resistance of bladder cancer was evaluated by culturing the UMUC3 with CM (Details of CM generation was described in Supplementary Method) generated from activated fibroblasts under different types of treatments, including siCont NPs, siWnt NPs, siCont NPs/cisplatin (NPs), siWnt NPs/ cisplatin (NPs)). The CM treated cells further received cisplatin (10 μM) for 2 days. Cell viability was then assayed, and the percentage of viable cells was calculated by comparing each experiment to UMUC3 treated with CM of normal activated NIH3T3 cells. For short-term proliferation assay of fibroblast to cisplatin and siRNA treatment without considering the neighboring effect, 96-well plates were seeded with activated NIH3T3 of 80% confluence. To evaluate the pro-apoptotic property of siWnt NPs, cells were transfected with siWnt NPs or siCont NPs at different concentrations. To study the combo effects, free cisplatin within the range of concentration bracketing its IC50 were combined with fixed concentration, 250 nM, of either control siRNA or siRNA against Wnt16. Forty-eight h later, cells were subject to MTT assay described elsewhere.

3.3.12 Tumor Growth Inhibition

Desmoplastic UMUC3/3T3 model was established as described in the previous chapter [74, 195]. In brief, UMUC3 (5×10^6) and NIH3T3 (2.5×10^6) were subcutaneously co-inoculated into the right flank of mice with Matrigel (BD biosciences, CA) at a ratio of 1:1 (V/V). Small tumor treatments were initiated on the 9 th day when tumor sizes reached 150~200 mm^3. Mice were then

randomized into 5 groups (n = 5~7 per group) as follows: Untreated group (PBS), siCont NPs, siWnt NPs, cisplatin NPs, siWnt NPs/ cisplatin NPs. Dosing and dose schedule of cisplatin NPs and siWnt NPs were optimized on mice bearing desmoplastic UMUC3/3T3 tumors. After optimization, IV injections were performed every other day for a total of 5 injections with siRNA dose of 0.6 mg/kg (equivalent to 12 μg siRNA per mice) and cisplatin dose of 1.0 mg/kg. Tumor volume was measured every day with a digital caliper (Thermo Fisher Scientific, Pittsburg PA) and body weight was also recorded. Tumor volume was calculated as (1/2*length*length*width). To monitor the dynamic intratumoral Wnt16 and cisplatin level, Mice were sacrificed 1 day after dosing, in total five doses. The tumor tissues were collected for further analysis. To compare the TME remodeling after single and multiple doses (4 doses), the collected tumor tissues 2 days after single and multiple treatments were subjected for western-blot analysis, immunofluorescence staining, Masson trichrome staining for Wnt16 and other extracellular matrix components. To analysis the TME remodeling of NPs penetration, DiI labeled NPs were IV injected 1 day before sacrificing (refer to flow cytometry analysis for details). To evaluate the combinatory efficacy on the large tumor, treatments were initiated 14 days post inoculating, when tumor volume reached ~700 mm^3 in size. Mice were then randomized into 4 groups (n = 5) subjected to the following treatments: PBS, siWnt NPs, cisplatin NPs and siWnt NPs/cisplatin NPs respectively. IV injections were performed every day (siRNA 0.6 mg/kg and cisplatin 1.0 mg/kg) with total 4 treatments. Tumor volume and body weight were continuously monitored for another week post last injection to determine combination effect on tumor regression and resistance.

3.3.13 Flow Cytometry Analysis

To study the cell population that took up NPs in tumors, mice were administrated with DiI labeled cisplatin NPs at a dose of 0.1 mg/kg DiI and were sacrificed 8h post IV injection. Fresh tumor tissues were dissociated with 1 mg/mL collagenase Type IV (Invitrogen), 1 mg/mL hyaluronidase (Sigma) and 200 μg/mL DNAase I (Invitrogen) in DMEM/ 2% FBS for 40 min to generate a single

cell suspension (1×10^6 cells/mL). The UMUC3 cells were pre-transfected with red fluorescence protein (RFP), fibroblasts were pre-transfected with green fluorescence protein (GFP). RFP and GFP were used to define tumors and fibroblasts, respectively. Leukocytes portion were stained with APC conjugated CD45 antibody at a 1:100 dilution. The cells were then subjected to flow cytometry analysis after washing. The ratio of DiI NPs distributed in different cell populations was then calculated. To analysis the TAFs ratio-changes after treatments, tumor tissues were collected after single dose and multiple doses treatment of cisplatin NPs, siWnt NPs, or combination of the two. siCont NPs were injected into the cisplatin NPs treated group as a control of siWnt NPs. Tumor tissues were dissociated and the ratio of GFP labeled fibroblasts in the dissociated cells was analyzed by flow cytometry on a BD FACSAria instrument (Beckon Dickinson). DiI-labeled cationic liposomes (DOTAP/Chol: 1:1) were used as a tool to monitor the effect of TME remodeling on NPs perfusion. DiI labeled liposomes were prepared by mixing 2% DiI into the lipid membrane and followed by sequential extrusion. To quantify the accumulation ratio of DiI labeled cationic liposomes in tumors subjected to different treatments (including single or multiple doses), 1 day after liposomes injection, mice were sacrificed and single cells were subjected to flow cytometry for DiI positive cells calculation. All the experiments were conducted in triplicate. The flow data were analyzed using FlowJo 7.6.1 (FLOWJO, Ashland, OR)

3.3.14 *In vivo* Imaging of NPs Distribution and TME Remodeling

For the imaging of NPs distribution, DiI labeled cisplatin NPs were prepared by mixing 2% DiI with DOTAP, cholesterol and cisplatin nanocores to formulate the final NPs. Mice were administrated with DiI labeled NPs at a dose of 0.1 mg/kg DiI and were sacrificed 8h post IV injection. To localize and visualize of NPs penetration, tumor was frozen and sectioned. Frozen tumor sections were fixed with cold methanol for 15 min and 1% triton for 5 min, double stained with CD31 and αSMA primary antibodies at 4ºC overnight followed by incubation with FITC-labeled secondary antibody for 1h at room temperature. The sections were also directly stained with DAPI and covered

with a coverslip. The sections were observed using a Nikon light microscope (Nikon Corp., Tokyo). Five randomly selected microscopic fields were quantitatively analyzed by using Image J software. For imaging the remodeling of TME, tumor tissues were collected after single or multiple doses of treatment, and processed for paraffin sections. Paraffin block sections of desmoplastic UMUC3/3T3 with different treatments were then deparaffinized, antigen recovered, blocked and probed with ECM markers (including αSMA, fibronectin) and Wnt16 for immune-fluorescence staining and immuno-histochemical staining. Collagen content was visualized using Masson trichrome staining. Apoptotic cells were analyzed by TUNEL assay. All staining protocols are detailed in the supplemental methods.

3.3.15 Enzyme-Linked Immunosorbent Assay (ELISA) of Wnt16 in the CM

Activated NIH3T3 were pretreated with siWnt NPs or siCont NPs followed by cisplatin (NPs), washed and recovered overnight. Wnt16 concentration in the CM was measured by ELISA with the mouse Wnt16 ELISA KIT (BioSource) according to the manufacturer's protocol, using recombinant mouse Wnt16 protein as a standard.

3.3.16 Western-Blot Analysis

Please refer to **Section 2.3.15**

3.3.17 Lentiviral Luciferase Reporter Assays

The activation of Wnt pathway in the neighboring naïve fibroblast by damaged fibroblast was evaluated using TCF/LEF reporter assay. To produce stable Wnt-reporter cell lines, NIH3T3 cells were transduced with the Cignal Lenti TCF/LEF Reporter (luc) kit for 48h. Following transduction, the cells were cultured under puromycin selection to generate a homogenous population of transduced cells. Acitivated NIH3T3 and Wnt-reporter cell lines were seeded on to the upper chamber and lower chamber of the non-direct contact co-culture system respectively. The upper chamber received different treatments as previously mentioned. Four hour post co-culture, bottom cells were collected

and luciferase assays were performed using a Luciferase Assay Kit (Promega, Inc.) according to the manufacturer's instruction.

3.3.18 Immunohistochemical Staining of Wnt16

Immunohistochemical staining (IHC) was performed using a standard strepavidin-biotin-peroxidase complex method as previously reported. In brief, one day post the small tumor inhibition study on the desmoplastic UMUC3/3T3 model, tumor tissues were collected and processed for paraffin sections. Paraffin block sections of UMUC3/3T3 tumors with different treatments were then deparaffinized, antigen recovered, blocked and probed with Wnt16 primary antibody (1:100 dilution) at 4 C overnight, and then detected using a rabbit specific HRP/DAB dectection IHC kit as recommended by the manufacturer (Abcam, Cambridge, MA). Cell nuclei were counter-stained with hematoxylin. Percentage of Wnt16 coverage were quantified by Image J of five representative microscopic fields.

3.3.19 TUNEL Assay

Paraffin-embedded tumor sections was deparaffinized and rehydrated. The slides were then stained using a TUNEL assay kit (Pierce) according to the manufacturer’s instruction.

3.3.20 Mason Trichrome Staining

Paraffin-embedded tumor sections was deparaffinized and rehydrated. The slides were then stained using a Masson Trichrome Kit (St. Louis, MO) according to the manufacturer's instruction.

3.3.21 Immunofluorescence Staining

Paraffin embedded tissues were prepared by the UNC Tissue Procurement Core and the slices were deparaffinized, antigen recovered, permeablized and fixed if necessary, and blocked with 1% BSA at room temperature for 1h. Cell markers were detected with antibodies conjugated with fluoreophores as indicated. Images were taken using fluorescence microscopy. For the purpose of double staining, primary antibodies with different species origins were applied and different

secondary antibodies with non-overlap flureophores were adopted. For the immunofluorescence staining of *in vitro* cell samples, cell were fixed with 2% PFA for 15 min, washed, permeablized, and processed to staing with the same protocol as the *in vivo* tumor samples. Confocal images were taken accordingly (Laser Sacning. Zeiss 510 Meta).

3.3.22 Serum Biochemical Value Analysis and Hematology Assay

Mice that were IV injected with PBS, siCont NPs, siWnt NPs, cisplatin NPs and cisplatin NPs plus siWnt NPs every other day for a total 5 doses were subjected to a toxicity assay. One day post treatments, blood was collected from mice of different treatments and centrifuged at 4000 rpm for 5 min to obtain the serum. Creatinine, blood urea nitrogen (BUN) serum aspartate aminotransferase (AST) and alanine aminotransferase (ALT) were assayed as indicators of renal and liver function. As to the hematology assay, whole blood was collected and white blood cells (WBC), red blood cells (RBC), platelets (PLT), hemoglobin (HGB) and hematocrits (HCT) were counted for the detection of myelosuppression. Organs including heart, liver, spleen, lung and kidney were collected and fixed for H&E staining by UNC histology facility to evaluate the organ-specific toxicity.

3.4 Results

3.4.1 Elevated Expression of Wnt16 in the Cisplatin NPs Treated Desmoplastic UMUC3/3T3 Tumor Fostered Drug Resistance

Cisplatin NPs was prepared according to the previously published protocol with minor adjustments [177, 194]. Anisamide targeted cisplatin NPs (cisplatin NPs, if no specific indication) were spherical and had a small particle size (~ 30 nm measured by TEM, ~35 nm measured by ZetaSizer) with homogeneous distribution and a high drug loading (**Figure 3.2A**). As shown in **Figure 3.2B**, cisplatin NPs (1mg/kg) significantly inhibited the growth of the desmoplastic UMUC3/3T3 model compared with free cisplatin. However, relapse and resistance occurred in the cisplatin NPs treated group after repeated injections. To determine the underlying mechanism of acquired-resistance to cisplatin NPs treatment, tissues were collected after multiple PBS or cisplatin

NPs exposures and analyzed for Wnt16 expression. Elevated levels of Wnt16 were found in the cisplatin NPs treated desmoplastic UMUC3/3T3 tumors over tumors treated with either PBS or free cisplatin (**Figure 3.2C**). To examine the role of Wnt16 in basal type bladder cancer resistance, we tested the ability of recombinant Wnt16 protein to induce cisplatin resistance *in vitro* (**Figure 3.2D**). The IC_{50} of cisplatin to basal type UMUC3 cells continually increased from 12.4 to 30 μM as the concentration of Wnt16 was increased from 0 to 12 μg/mL. To evaluate whether the effective concentration of Wnt16 that induced cisplatin resistance *in vitro* was physiologically relevant, we quantified the concentration of Wnt16 upregulated by cisplatin NPs *in vivo*. Wnt16 concentrations in cisplatin NPs treated tumors (up to 6.5 μg/ml) was within the concentrations of Wnt16 sufficient to induce cisplatin resistance (**Figure 3.2** and **Figure 3.3**). Thus, results confirm that elevated Wnt16 (as a major DRP molecule) can attenuate tumor cells' sensitivity to cisplatin treatment. Furthermore, recent studies correlate the basal subtype of bladder cancer with increased stromal content and a poor prognosis due to resistance [225, 226]. Basal-like bladder tumors also demonstrated increased levels of Wnt16 (**Figure 3.2E**), indicating the role of Wnt16 in facilitating drug resistance in clinical samples. Increased Wnt16 expression after treatment has therefore been associated with elevated tumor drug resistance. Evidence points to the validity of using Wnt16 as a molecular target for translational and investigatory purposes to determine the efficacy of systems designed mediate treatment induced drug resistance.

3.4.2 Off-target Distribution of Cisplatin NPs to TAFs Facilitated the TAF-specific Upregulation of Wnt16

We next sought to determine the cellular origin of Wnt16 production within tumors. Wnt16 expression has been detected on uterine stroma and was overexpressed by damaged stromal cells surrounding prostate tumors [70, 227]. To examine whether stromal cells were responsible for Wnt16 upregulation in the desmoplastic UMUC3/3T3 model, major cellular components of the desmoplastic UMUC3/3T3 model (UMUC3 cells and the mouse fibroblast NIH3T3) were treated *in vitro* with cisplatin. In order to mimic *in vivo* TAFs, NIH3T3 was pre-conditioned with TGF-β to obtain a TAF-

like phenotype. Results showed elevated amounts of Wnt16 in both the cell lysate and conditioned medium from TGF-β activated NIH3T3 cells after exposure to either free cisplatin or cisplatin NPs treatment (**Figure 3.4A**). In contrast, Wnt16 expression was not induced in UMUC3 cells or other epithelial cancer cell lines (**Figure 3.4** and **Figure 3.5**). To further confirm the origin of the upregulated Wnt16 level *in vivo,* a UMUC3 tumor model was developed without the addition of NIH3T3. This model contained a lowered amount of TAFS [74]. Cisplatin NPs therefore failed to induce Wnt16 in the UMUC3 model, which further confirms the TAF-origin of Wnt16 and eliminated potential confounding sources such as macrophages and endothelial cells (**Figure 3.4C**). A patient derived xenograft model of human basal type bladder cancer (**Figure 3.4** and **Figure 3.7**) was also investigated for clinical relevance and exhibited upregulation Wnt16 after repeated cisplatin NPs treatment. Wnt16 upregulation is therefore not an artifact of NIH3T3, but also exists in primary fibroblasts. Consistent with previous reports, these studies confirm the TAF-origin of cisplatin induced Wnt16.

Off target distribution of therapeutic agents to TAFs can foster the secretion of DRP molecules, in particular Wnt16, and facilitate the off-target resistance [70]; therefore the cell types responsible for uptake of cisplatin NPs in the desmoplastic UMUC3/3T3 model were further investigated. A single cell suspension was prepared with tumor samples (150~200 mm^3) from tumor bearing mice treated intravenously with DiI-labeled cisplatin NPs. Stable transgene expression of GFP, RFP and fluorophore conjugated antibody against mouse CD45 defined fibroblasts, cancer cells and leukocyte populations. Data indicated that fibroblasts were responsible for ~36% uptake of non-targeted cisplatin NPs, while tumor cells and leukocytes took up ~52% and ~8% respectively (**Figure 3.6A**). When particle surfaces modified with the active targeting ligand for Sigma R, AA, increased the percentage of fibroblast NPs uptake from ~20% to ~30% (**Figure 3.6B**). Western-blot analysis confirmed Sigma R expression on TAFs and explained the positive internalization of targeted cisplatin NPs (data not shown). These observations indicate that fibroblasts are responsible for majority off target internalization of targeted and non-targeted cisplatin NPs. The distribution of

targeted DiI NPs was visualized through immunofluorescence staining of different intratumoral cell types (**Figure 3.6C**). It was found that TAFs located in close proximity to blood vessels were responsible for uptake of NPs (**Figure 3.6C**), indicating that fibroblast distribution of therapeutic NPs is inevitable due to the spatial distribution and the proximity of fibroblasts to blood vessels. To assess the off-target distribution induced damage responses, which could facilitate the subsequent secretion of Wnt16, we examined the cisplatin-induced apoptosis in tissues from tumor bearing mice treated with cisplatin NPs or PBS (data not shown). Apoptosis assay shown that approximately half of apoptotic cells were TAFs, which correlates with the aforementioned off-target internalization ratio of cisplatin NPs by fibroblasts and confirmed the damage responses. Therefore, TAFs are a significant off target deposition site for cisplatin NPs. Deposition of cisplatin NPs in TAFs are followed by DNA damage and the paracrine secretion of Wnt16, which contributes to the development of drug resistance.

3.4.3 Wnt16 Knockdown Inhibits Growth and Invasion of Neighboring Bladder Cancer Cells

Due to the prominent role of Wnt16 in mediating tumor cell resistance, combined delivery of cisplatin NPs with siRNA targeting Wnt16 in fibroblasts was suspected to enhance anti-tumor efficacy. Liposome-hyaluronic acid-protamine nanoparticles (LPH NPs) were previously optimized for systemic delivery of siRNA to tumor sites. LPH NPs was formed by combining siRNA against Wnt16 with hyaluronic acid and condensed with cationic protamine to form negatively charged polyplexes. Polyplexes were then coated with cationic lipids via electrostatic interaction with PEG to prolong systemic circulation. The final LPH-NPs was about 50 nm in diameter with surface charge of 25 mV, as determined by Zetasizer (**Figure 3.8**) [217]. To improve fibroblast internalization and ensure fibroblast specific knockdown of Wnt16, AA was conjugated onto LPH for enhanced internalization. Furthermore, mouse specific siRNA was used to increase selectivity to mouse fibroblasts. With these precautions in place, LPH NPs loaded with mouse anti-Wnt16 siRNA (siWnt NPs) were able to decrease cisplatin induced Wnt16 protein levels in activated NIH3T3, without

affecting UMUC3 tumor cells (**Figure 3.8B**). To determine whether the level of secreted Wnt16 would be affected by siRNA, concentration of Wnt16 in the CM from fibroblasts exposed to different treatments was quantified by an ELISA Assay. Fibroblasts were pretreated with LPH NPs, followed by cisplatin (NPs) for 3h, washed and incubated with full media overnight to obtain the CM. Results indicated that both free cisplatin and cisplatin NPs induced paracrine secretion of Wnt16. NPs induced limited secretion compared to free cisplatin due to the insufficient drug release within the 3 h incubation. Though control siRNA and lipids that composed the NPs didn't affect Wnt16 secretion; siWnt NPs abolished expression of Wnt16 (**Figure 3.8C**). These findings further confirm the efficient knockdown of Wnt16 using LPH. Knockdown of Wnt16 was then revealed by the inhibition of the secreted Wnt16-mediated paracrine effect. The aforementioned CMs were added to cisplatin (10 μM) treated UMUC3 cells to evaluate the paracrine effect. As expected, CM from cisplatin treated fibroblasts showed higher activity in protecting UMUC3 cells from cisplatin induced apoptosis compared with conditioned media from cells without cisplatin treatment. Activity was abolished if fibroblasts were treated with siWnt NPs (**Figure 3.8D**). These experiments also indicated that Wnt16 secreted from cisplatin damaged fibroblasts is both necessary and sufficient to induce resistance in a paracrine manner in neighboring cancer cells.

Next, possible mechanisms of Wnt16 induced tumor cell resistance were investigated. A non-contact co-culture system of NIH3T3 in the upper chamber and UMUC3 in the lower chamber was established using a transwell configuration (**Figure 3.9A**) [218]. Previous studies indicated that Wnt16 mainly activates the canonical Wnt/β-catenin pathway [70, 228]. In an attempt to confirm that the Wnt/β-catenin signaling pathway in UMUC3 cells was activated by the Wnt16 secreted from cisplatin NPs treated fibroblasts, immunofluorescence was used to visualize β-catenin localization in UMUC3 cells in the lower chamber at different time points after co-culture [219]. As shown in **Figure 3.9B**, β-catenin was primarily located in the membrane during the initial 2 h of co-culture. However, cisplatin NPs treated NIH3T3 cells promoted increased β-catenin and nuclear localization in UMUC3 cells, particularly 4h after co-culture, suggesting activation of Wnt pathway. As expected,

siWnt NPs treatment of fibroblasts suppressed nuclear translocation of β-catenin in UMUC3 cells. In addition, downstream targets of β-catenin including c-Myc and Cyclin-D1, were up-regulated in tumor cells co-cultured with cisplatin or treated fibroblasts (**Figure 3.9C**) [229, 230]. Such observations was absent when co-culturing UMUC3 with fibroblasts treated with siWnt NPs alone or in combination with cisplatin. Control siRNA NPs (siCont NPs) and human specific siWnt NPs were controls and no biological functions were found.

The paracrine function of Wnt16 on tumor cells was further investigated. Cell apoptosis was measured by the cleavage of major apoptotic protein (PARP). Results paralleled aforementioned findings, which indicated the role of Wnt16 on attenuating cisplatin-induced apoptosis (**Figure 3.8C**). The Wnt signaling pathway is known to enhance cell motility and invasiveness via epithelial-mesenchymal transition (EMT) [70, 219]. EMT is a known mechanism for cisplatin induced resistance in pancreatic cancer [231]. Loss of E-cadherin and gain of N-cadherin are the main characteristics of EMT [70]. Consistent with this notion, UMUC3 cells in the lower chamber exhibited decreased expression of E-cadherin and increased expression of N-cadherin when co-cultured with cisplatin treated NIH3T3 in the upper chamber (**Figure 3.9C**). This EMT phenotype was abolished when UMUC3 cells exposed to siWnt NPs treated fibroblasts. EMT also indicates tumor cell mobility. A scrape assay was performed to evaluate cell mobility using the non-contact co-culture system. Twenty hours after co-culture, cisplatin treated NIH3T3 enhanced mobility of neighboring UMUC3 cells in the lower chamber. This finding was reversed with Wnt16 downregulation in fibroblasts (**Figure 3.9D**). Experiments identify Wnt16 as a mediator of tumor cell resistance and metastasis; therefore, knockdown of Wnt16 in fibroblasts using siRNA sensitizes neighboring tumor cells to cisplatin treatment and improves patient prognosis.

3.4.4 Wnt16 Knockdown Blocks the Biological Function and Increases Cisplatin Sensitivity of Neighboring Stroma Cells

TAFs that were not directly treated with cisplatin NPs (hereafter referred to as naïve TAFs) were also affected by paracrine Wnt16 secreted from cisplatin treated fibroblasts. To determine if

Wnt signaling was activated in the neighboring naïve TAFs, we generated an activated NIH3T3 cell strain with stable expression of Wnt reporter using a Cignal Lenti T cell factor/lymphoid enhancer-binding factor (TCF/LEF) Reporter Kit and seeded these cells on the lower chamber of the non-contact co-culture system (**Figure 3.10B**). Results indicated that cisplatin treated TAFs in the upper chamber of the system could activate the canonical Wnt signaling in naïve fibroblasts in the lower chamber. Enhanced luciferase intensity was observed 4 h after co-culture, which was temporally consistent with the direct stimulation of fibroblasts in the lower chamber a by Wnt16 recombinant protein. Only siWnt NPs suppressed the expression of Wnt16 and completely blocked the activation of β-catenin signaling. Fibronectin secreted from functional TAFs has been shown to increase extracellular matrix (ECM) rigidity and promote tumor malignancy [55]. Fibronectin levels can serve as an important indicator to evaluate the relationship of Wnt16 knockdown on ECM remodeling as fibronectin expression is closely regulated by the canonical β-catenin mediated Wnt pathway [232]. Results indicated elevated fibronectin levels in cisplatin treated naïve fibroblasts relative to the untreated fibroblasts (**Figure 3.10C**). Such effects were abolished in the presence of siWnt NPs. This observation was further confirmed by immunofluorescence staining of fibronectin in the lower chamber (**Figure 3.10D**). Finally, an MTT assay was carried out to show that a deficiency of Wnt16 did not influence the cell viability of the activated fibroblasts (**Figure 3.10E**). This finding further confirmed Wnt16 protein does not play a pro-proliferative or pro-apoptotic role in regulating fibroblasts growth, but rather protects the cells from cisplatin induced cell death. In keeping with this notion, the combination of activated fibroblasts with siWnt, and cisplatin facilitated cell death, while siCont NPs did not (**Figure 3.10F**). Overall, the data concluded that paracrine secretion of Wnt16 activated the canonical Wnt pathway in neighboring fibroblasts, inducing the secretion of fibronectin, facilitating collagen crosslinking and fostering their resistance to future cisplatin assault.

Endothelial cells are another group of stroma cells that neighbor the cisplatin NPs treated fibroblasts. The paracrine functions of Wnt16 on endothelial cells were further investigated using a non-contact co-culture tube formation assay (**Figure 3.10G**). A recent study indicated that a plasmid

encoding the Wnt16 gene accelerated tube formation in cultured primary mouse cavernous endothelial cells, suggesting a role in cavernous angiogenesis [233-235]. Therefore, it was further hypothesized that knockdown of Wnt16 could also inhibit angiogenesis. Data in this study indicated that Wnt16 secreted from both NIH3T3 fibroblasts (in the upper chamber of the co-culture system) and recombinant Wnt16 protein induced tube formation of endothelial HUVECs (**Figure 3.10H**), confirming the hypothesis and suggesting anti-angiogeneic properties caused by siWnt NPs would likely foster tumor inhibition.

3.4.5 Dynamic Monitoring of the Tumor Microenvironment Remodeling by Cisplatin NPs and siWnt NPs

The consequences of the paracrine effects of Wnt16 on neighboring stroma cells was examined. Based on a previous study of TAFs role in TME and endothelial cells' role in angiogenesis [236, 237], paracrine effects of Wnt16 was hypothesized to regulate TME remodeling and blood vessel angiogenesis in neighboring TAFs. To investigate this dynamic remodeling process, single dose and multiple doses of solo or combo treatments were carried out in the desmoplastic UMUC3/3T3 model. Parameters including TME markers, NPs distributions and cisplatin accumulation were characterized to elucidate the remodeling process. Consistent with a previous study, a single dose of cisplatin NPs was efficient in remodeling the TME [74]. Representative immunostaining images (**Figure 3.11A**) indicated that cisplatin significantly modulated TME modification through reducing the expression of α SMA, a marker of TAF-activation, and fibronectin, which facilitates the deposition and crosslinking of collagen and elastin in cancerous tissues.[55, 238] Consistently, both collagen content and collagen crosslinking were reduced in cisplatin NPs treated groups (**Figure 3.11A** and **B**). The changes in expression levels of major ECM proteins were further confirmed by western blot analysis **(Figure 3.11C**).

A desmoplastic UMUC3/3T3 consisting of GFP expressing NIH3T3 cells and UMUC3 cells was generated to determine the basis for TME remodeling after a single dose of cisplatin NPs. Survival of GFP^+ fibroblasts decreased significantly in the cisplatin NPs treated group compared to

other treatment groups (**Figure 3.11D**), suggesting that the depletion of TAFs was a driving force for the disruption of ECM. Meanwhile, DRP molecules such as Wnt16 did not reach sufficient concentrations to induce drug resistance. It was hypothesized that decreasing collagen content would improve the intratumoral distribution of NPs based on previous studies of the tumor interstitial matrix [52, 105]. To test the hypothesis, intratumoral accumulation of DiI-labeled liposomes (70 nm in diameter) was quantified via flow cytometry. Consistent with the hypothesis, improved NPs accumulation was observed in tumors treated with cisplatin NPs compared to the control (siCont NPs) **(Figure 3.11E**). Improved NPs penetration indicated a better therapeutic effect.

While a single dose of cisplatin NPs induced antitumor efficacy, efficacy was temporary as the resistant phenotype gradually reappeared in both tumor cells and neighboring TAFs. To examine acquired resistance in TAFs, desmoplastic UMUC3/3T3 models were dosed with multiple rounds of cisplatin NPs or siWnt NPs. After 4 doses, the Wnt16 expression level was significantly elevated in the cisplatin NPs group (**Figure 3.11F**), driving the balance between efficacy and resistance towards the end of TAFs resistance. Results were consistent with upregulation of ECM markers, including αSMA, FAPα, fibronectin and collagen (**Figure 3.11F-H**). The resistance of TAFs to cisplatin NPs after multiple doses was assessed by quantitative analysis of the GFP^+ fibroblast percentage in residual tumors. In contrast to decreasing GFP^+ cell ratios found in the single dose cisplatin NPs group (**Figure 3.11D**), the survival ratio of GFP^+ fibroblasts increased by ~2-fold after repeated cisplatin NPs doses (**Figure 3.11I**).

In order to overcome resistance induced by dynamic cisplatin NPs treatment, a combinatory nano-therapy or solo nanoformulations designed to kill more than 80% TAFs were utilized to improve TAF-depletion efficiency [72, 74]. With these platforms, prolonged tumor inhibition was observed, but resistance relapsed in residual fibroblasts. Furthermore, fibrotic internalization of high dose chemotherapy risks inducing systemic toxicity. As most DRP molecules are upregulated in treatment-induced cells, specific knockdown of DRP molecules to baseline would be beneficial to improve chemotherapy outcomes. In addition, since DPR molecules, such as Wnt16, lack pro-

apoptotic properties, the combination of DPR inhibitors over chemotherapy would be a safer and less toxic route. In the current study, siWnt NPs in combination with cisplatin NPs fosters the efficacy of solo cisplatin NPs treatment after a single dose and reversed the cisplatin NPs induced resistance after multiple doses (**Figure 3.11A-C, F-H**). Efficacy was measured in terms of depletion of TAFs and ECM markers. Furthermore, siWnt NPs alone could decrease the expression of TME markers, rather than deplete fibroblasts. This confirms the previous hypothesis that solo siWnt NPs induced tumor inhibition through TME remodeling but did not induce killing effects.

Wnt 16 is also thought to regulate blood vessel remodeling. Results indicated that, multiple cisplatin NPs treatments increased the density of CD31 (an indicator of blood vessels), which correlates with the observation in the previous tube formation study (**Figure 3.12A**). Downregulation of Wnt16 through siWnt NPs induced decreased angiogenesis and vascular remodeling in the desmoplastic UMUC3/3T3 model (**Figure 3.12A**). Since angiogenesis accelerates tumor progression, it is highly likely that the anti-angiogeneic properties caused by siWnt NPs foster tumor inhibition [219]. However, inhibition of angiogenesis weakens the enhanced permeability and retention (EPR) effect and is likely to compromise NPs-mediated drug delivery efficiency [8]. Yet, results indicated that multiple doses of cisplatin NPs/siWnt NPs, promote the penetration of both DiI labeled liposomes (**Figure 3.11E and J**) and cisplatin NPs (**Figure 3.12B**) compared to cisplatin NPs alone. The discrepancy between weakened EPR and enhanced NPs penetration was most likely due to the argument that siWnt NPs treatment may prune immature vessels and remodel the vasculature to more closely resemble the structure of normal vessels. Consistent with previous research, this so-called "tumor vessel normalization" benefits the delivery of small molecule chemo drugs to tumors, and also the accumulation of soft NPs such as liposomes (less than 100 nm) and small, solid NPs such as cisplatin NPs [8]. In addition, the decreased collagen crosslinking and remodeled TME could also decrease the overall interstitial fluid pressure and contribute to the enhanced NPs distribution and penetration.

3.4.6 Intravenous Administration of siWnt NPs with Cisplatin NPs Effectively Inhibited Desmoplastic UMUC3/3T3 Tumor Growth at Early or Late Stage

Based on the aforementioned effects of Wnt16 knockdown on neighboring tumors and the overall TME, the therapeutic efficacy of systemically delivered siWnt NPs with cisplatin NPs in the desmoplastic UMUC3/3T3 model was conducted as a proof of concept study. Real-time expression of Wnt16 under cisplatin NPs treatment were carefully monitored by western blot (**Figure 3.13B**). Results indicated a gradual upregulation of Wnt16 in response to cisplatin treatment. Therefore, simultaneous administration of siWnt NPs with cisplatin NPs was selected as the treatment course rather than sequential dosing or two-staged dosing methods to achieve continuous inhibition of Wnt16 expression (**Figure 3.13B**). Dose levels and dosing schedules of siWnt16 were adjusted via tiered optimizing procedures (Error! Reference source not found.). When tumor sizes reached 150-200 mm^3, treatment was administered every other day (**Figure 3.13A**). The combination of cisplatin NPs (1mg/kg) and siWnt NPs (0.6 mg/kg) exhibited the greatest antitumor efficacy, resulting in progression-free survival for up to 7 days after the last treatment. By comparison, tumors in mice treated with cisplatin NPs without siWnt NPs aggressively relapsed up to approximately 10x their original size 7 days after the last dosing (Error! Reference source not found. and **Figure 3.13A**). siCont had no influence on tumor growth, ruling out potential from the delivery vehicle. Western blot analysis confirmed stable knockdown of Wnt16 expression in siWnt NPs and combo treated groups over the course of treatment (**Figure 3.13B**). Immunohistochemistry (IHC) images revealed a 4 to 5-fold silencing of Wnt16 expression in the combo group over cisplatin NPs treated groups one day after the last dosing (**Figure 3.13C**), which was consistent with the western results (**Figure 3.13D**). In addition, siWnt NPs could also sensitize an desmoplastic UMUC3/3T3 model towards cisplatin NPs treatment and lead to extensive apoptosis accounting for better therapeutic outcomes in the combo treatment (**Figure 3.13E**).

Late stage solid tumors are notorious for well-structured tumor stroma, composed of intricate blood vessels in the basement membrane secreted by local TAFs. Recent studies indicated off-target

distribution of NPs in fibroblasts of the late stage tumor is greatly intensified compared to small tumors (data not shown). Therefore, the combinatory therapeutic outcome of siWnt NPs with cisplatin NPs in late stage tumors was further investigated. 700 mm^3 tumors received daily injections to ensure a better therapeutic outcome. As shown in Error! Reference source not found., cisplatin NPs and siWnt NPs showed a mild tumor inhibition effects when administered separately. However, combinatory therapy presented potent efficacy, even in large tumors. Results indicated the combination could effectively knockdown Wnt16, shrink the tumor and delay tumor growth (**Figure 3.14**). Only negligible decreases in body weight and no abnormal blood parameters were observed in all groups (**Table 3.1, Figure 3.15** and **Figure 3.16**). Altogether, these results verified our hypothesis that the cisplatin NPs combined with siWnt NPs indeed exhibited superior antitumor efficacy in both small and large aggressive desmoplastic UMUC3/3T3 tumors, and considered as a promising therapeutic regimen for future clinical evaluations.

3.5 Discussion and Conclusion

Our study discussed the off-target distribution of NPs into non-tumor stroma cells and underlined the controversial consequence of TAF dispositions of therapeutic NPs. Internalization of cisplatin into TAFs resulted in their immediate killing, blocking the secretion of stroma factors, and violating the communication between fibroblasts and tumor cells, subsequently inhibited tumor growth. However, chronic exposure of TAFs to cisplatin activated the DRP and promoted the secretion of DRP molecules, leading to tumor cell resistance and metastasis, stroma reconstruction and angiogenesis (Figure 3.17). To address the problem, we proposed the combination of DRP inhibitors as a proof of concept to enhance the anti-tumor outcome of chemotherapy in the stroma-rich cancer models. From coherent studies, we determined Wnt16 as one of the major DRP molecules that regulated the treatment-induced cisplatin resistance, and developed LPH NPs as a carrier that efficient deliver siRNA against Wnt16 to TAFs to foster the cisplatin NPs efficacy. Most importantly, we found a dramatically enhanced antitumor effect for the combination therapy even in the late stage

stroma-rich bladder cancer with prolonged survival and few side effects. Moreover, detailed mechanistic studies revealed multiple benefits of downregulating Wnt16, mainly through regulating paracrine interaction with different neighboring cell populations, including sensitizing neighboring tumor cells towards cisplatin, remodeling neighboring fibroblasts and TME, and inhibiting neighboring vessel angiogenesis. Therefore, our study suggest that exploring the major secreted DRP molecules in tumor-stroma crosstalk and co-delivering two regiments that could kill the fibroblasts as well as inhibit the secretion of these major factors would be of significant clinical potential. The results of this study will serve as a gateway for future development of NPs to explore the complicated tumor microenvironment.

Table 3.1 Effect of different treatments on serum ALT, AST, BUN and creatinine levels

Treatment	BUN mg/dL	Creatinine mg/dL	AST U/L	ALT U/L
PBS	22 ± 2	0.1	149 ± 33	41 ± 12
siCont NPs	22 ± 2	0.2	176 ± 25	30 ± 4
Cisplatin NPs	22 ± 5	0.2	168 ± 28	33 ± 5
siWnt NPs	20 ± 3	0.1	193 ± 35	56 ± 5
siWnt NP/cisplatin NPs	21 ± 1	0.2	245 ± 22	54 ± 4
Normal Range	12 - 33	0.2 - 0.9	54 – 298	17 - 132

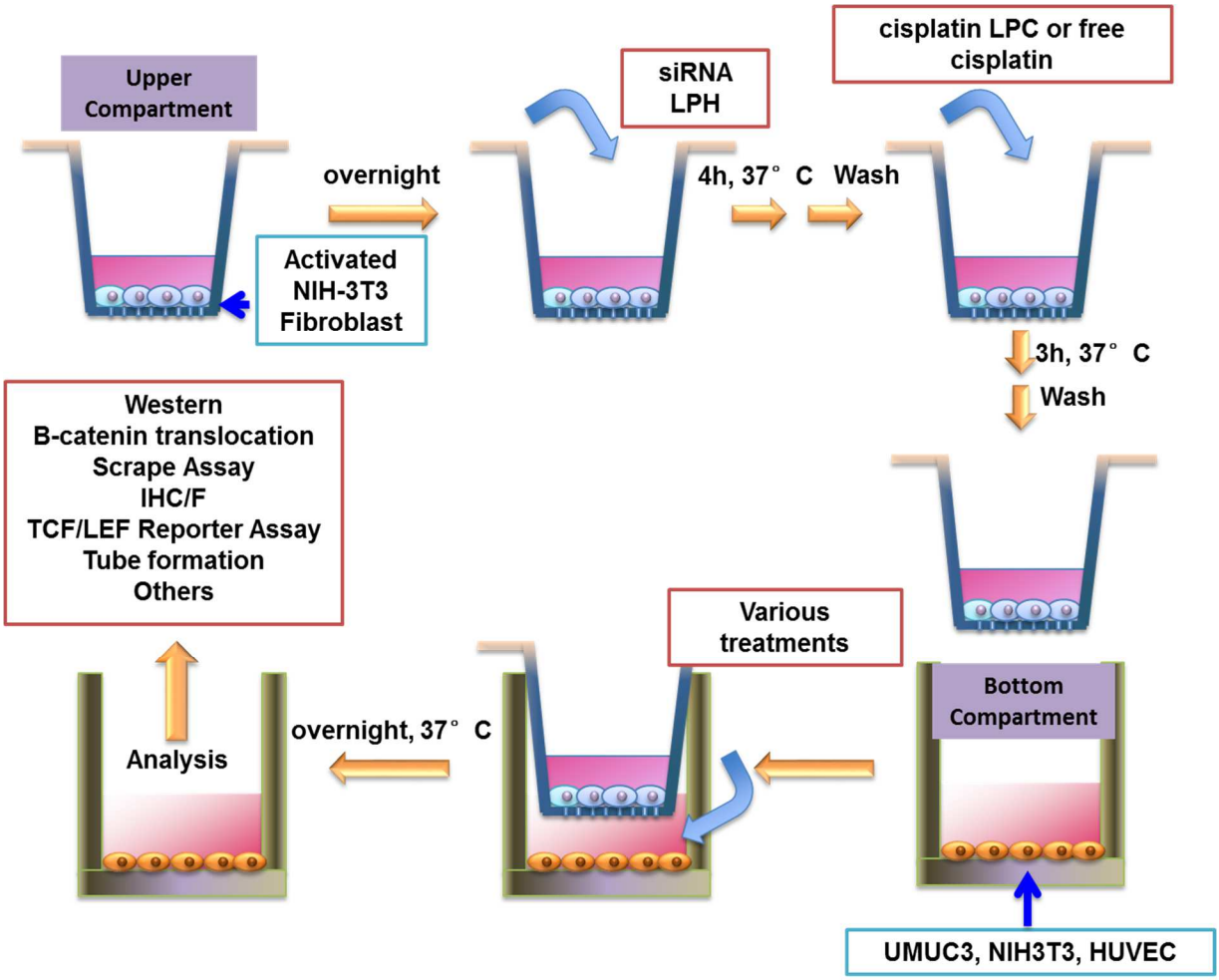

Figure 3.1 Illustration of the Non-contact Co-culture Model for mechanistic study

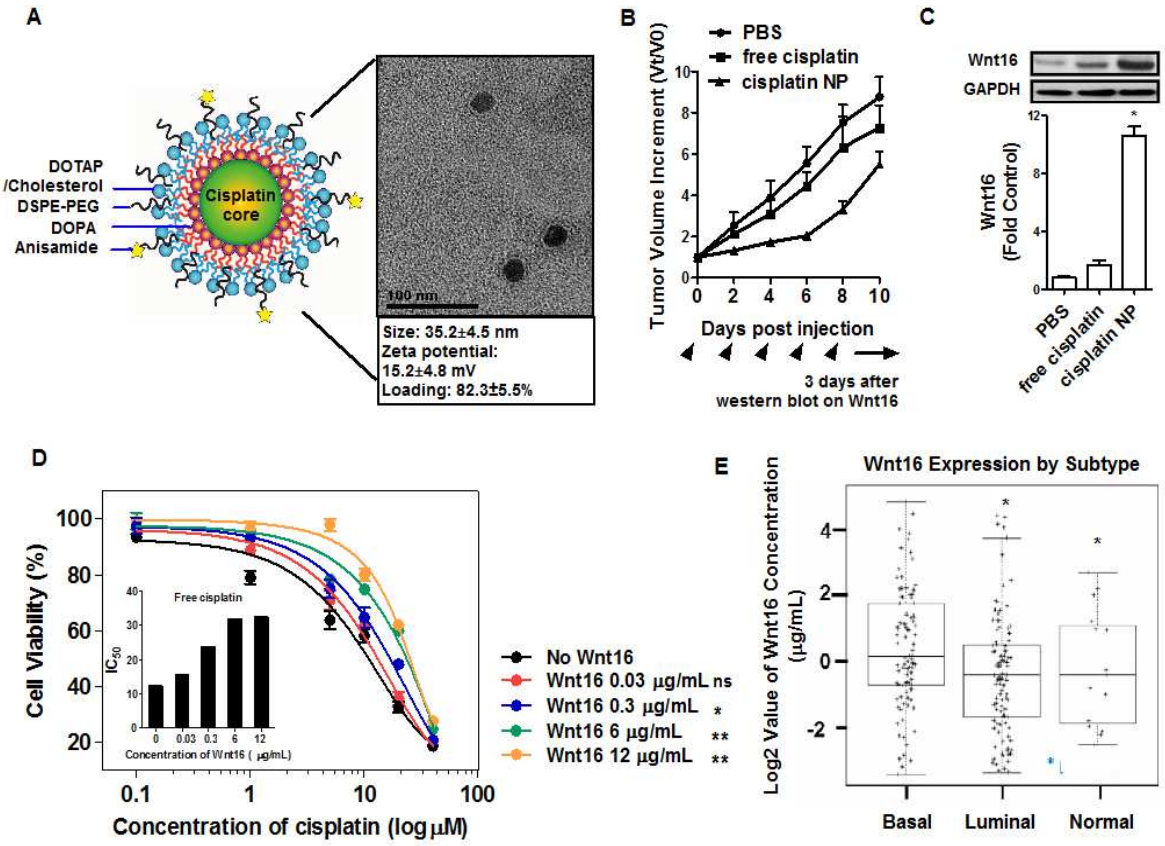

Figure 3.2 Cisplatin NPs induced UMUC3/3T3 tumor resistance through elevated expression of Wnt16.

A. Graphical presentation and TEM images of the cisplatin NPs. Particle size, zeta potential and drug loading were characterized and presented. B. Tumor growth inhibition of cisplatin NPs or free cisplatin (of 1.0 mg/kg cisplatin) in the demosplatic UMUC3/3T3 tumor model. The arrowhead indicates dosing time. C. Western blot analysis of Wnt16 protein level in the resistant tumors. Intensity of the protein bands was quantified using Image J (n = 3, * $P < 0.05$). Wnt16/GAPDH value in PBS group was set as 1. D. Dose response curves of UMUC3 cells treated with different levels of recombinant Wnt16 protein (n = 4, * $P < 0.05$, ** $P < 0.01$, compared with the untreated group). E. Expression level of Wnt16 in different subtypes of bladder cancers in patients. Data were collected and analyzed from The Cancer Genome Atlas (TCGA) database (* $P < 0.05$, compared to the basal type).

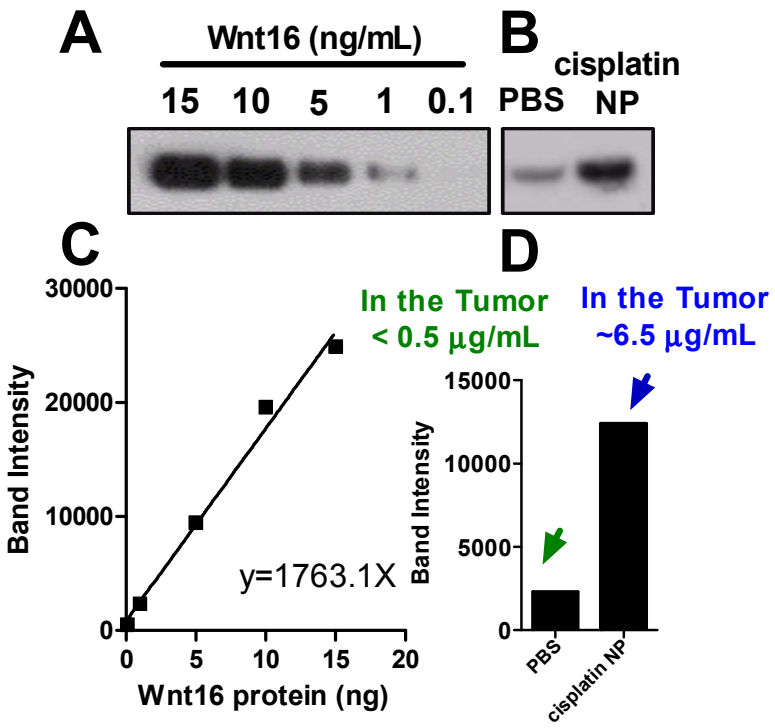

Figure 3.3 Quantification of *in vivo* Wnt16 protein level.

A. Standard curve was established by western blot using recombinant Wnt16 protein from 0.1 ng to 15 ng. Quantification of protein band was calculated by image J and shown in C. Certain amount of tissue samples were collected from PBS treated tumor and cisplatin NPs treated tumor, tumor lysate was collected and the protein content in the tumor was measured by western and calculated based on the standard curve. The concentration of Wnt16 in the tumor was calculated based on the sample volume and Wnt16 content and shown in Figure D. In the PBS treated tumor, Wnt16 concentration was ~0.5 µg/mL, indicating a baseline level of Wnt16 existed in the untreated tumor. In the cisplatin NPs treated tumor, protein level was increased up to ~6.5 µg/mL, which was consistent with the concentration of Wnt16 *in vitro* that induced bladder cancer resistance.

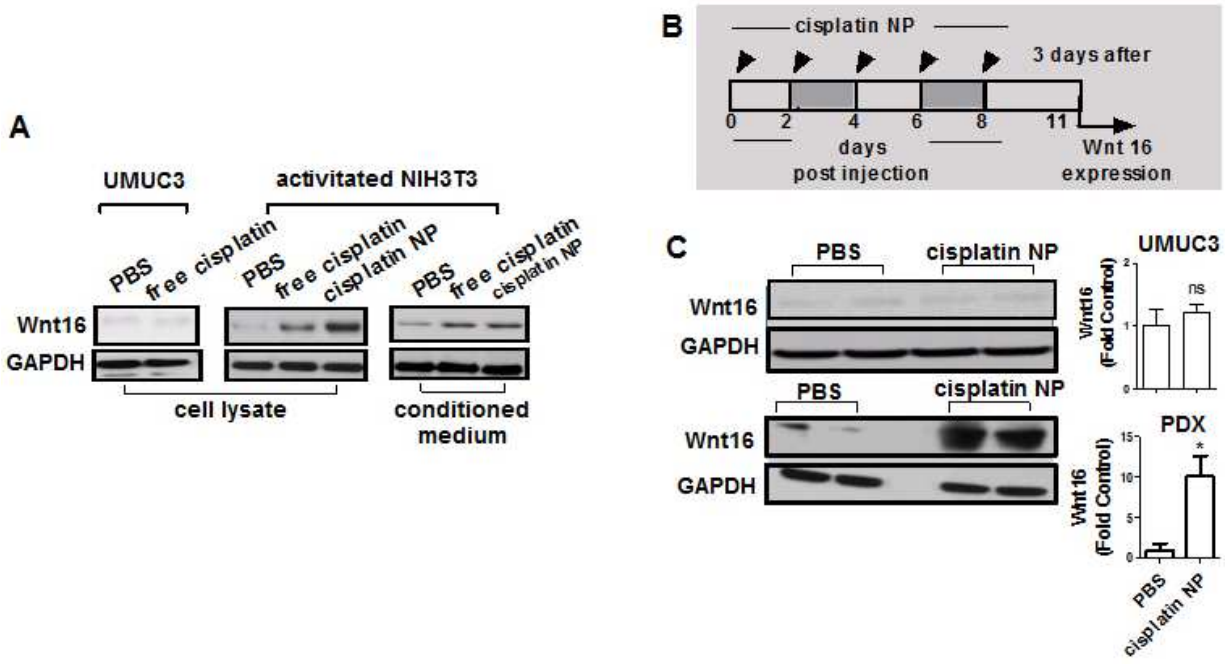

Figure 3.4 TAF-origin of cisplatin induced Wnt16.

A. *In vitro* western blot analysis of Wnt16 level in cisplatin treated UMUC3, activated fibroblast NIH3T3 cells and its conditioned medium. B. Scheme of cisplatin NPs (1 mg/kg) treatment regimen on the UMUC3 xenograft and PDX tumors, which is same with the UMUC3/3T3 tumors. C. Western blot analysis of Wnt16 protein level in the UMUC3 xenograft and PDX tumors. Two representative samples of each group were presented. Intensity of the protein bands was quantified using Image J (n = 3, * $P < 0.05$), compared to GAPDH as a loading control. Wnt16/GAPDH value in PBS group was set as 1.

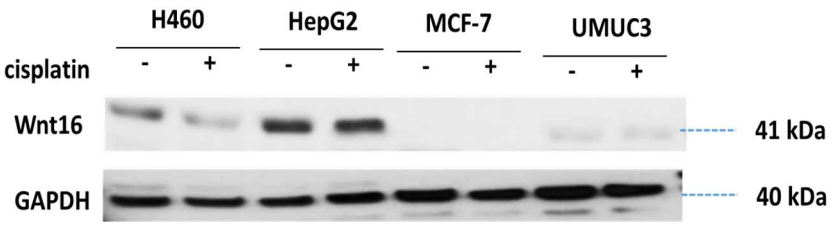

Figure 3.5 Wnt16 level in different tumor cell lines treated with cisplatin

Results shown that Wnt16 were not elevated in response to cisplatin treatment on all the listed cancer cell lines.

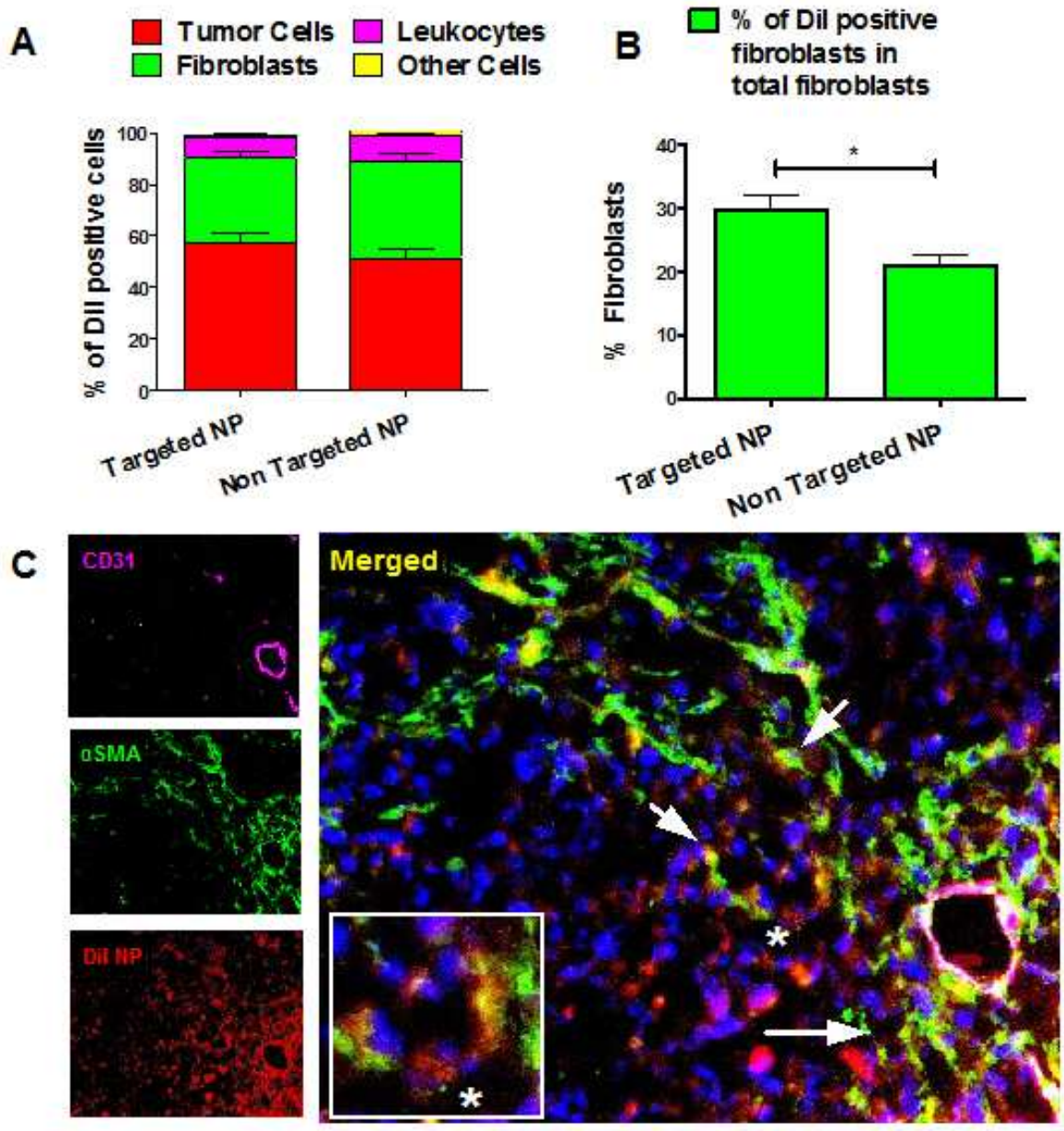

Figure 3.6 Cisplatin NPs were delivered off-target to TAFs in the UMUC3/GFP-3T3 tumors after intravenous injection.

A and B. Flow cytometry analysis of the cell populations that took up cisplatin NP in the UMUC3/GFP-3T3 tumors. Compositions of the DiI positive cells were shown in (A). Ratios of fibroblasts (of total fibroblasts) that took up NP were shown in (B) (n = 3, * $P < 0.05$). C. Fluorescence imaging of intratumoral cisplatin NP distribution. TAF (αSMA: green), blood vessels (CD31: magenta), DiI-labeled NP (red) and nucleus (DAPI: blue) were shown. Arrowhead and the asterisk insert indicate the off-target distribution of NPs in TAFs.

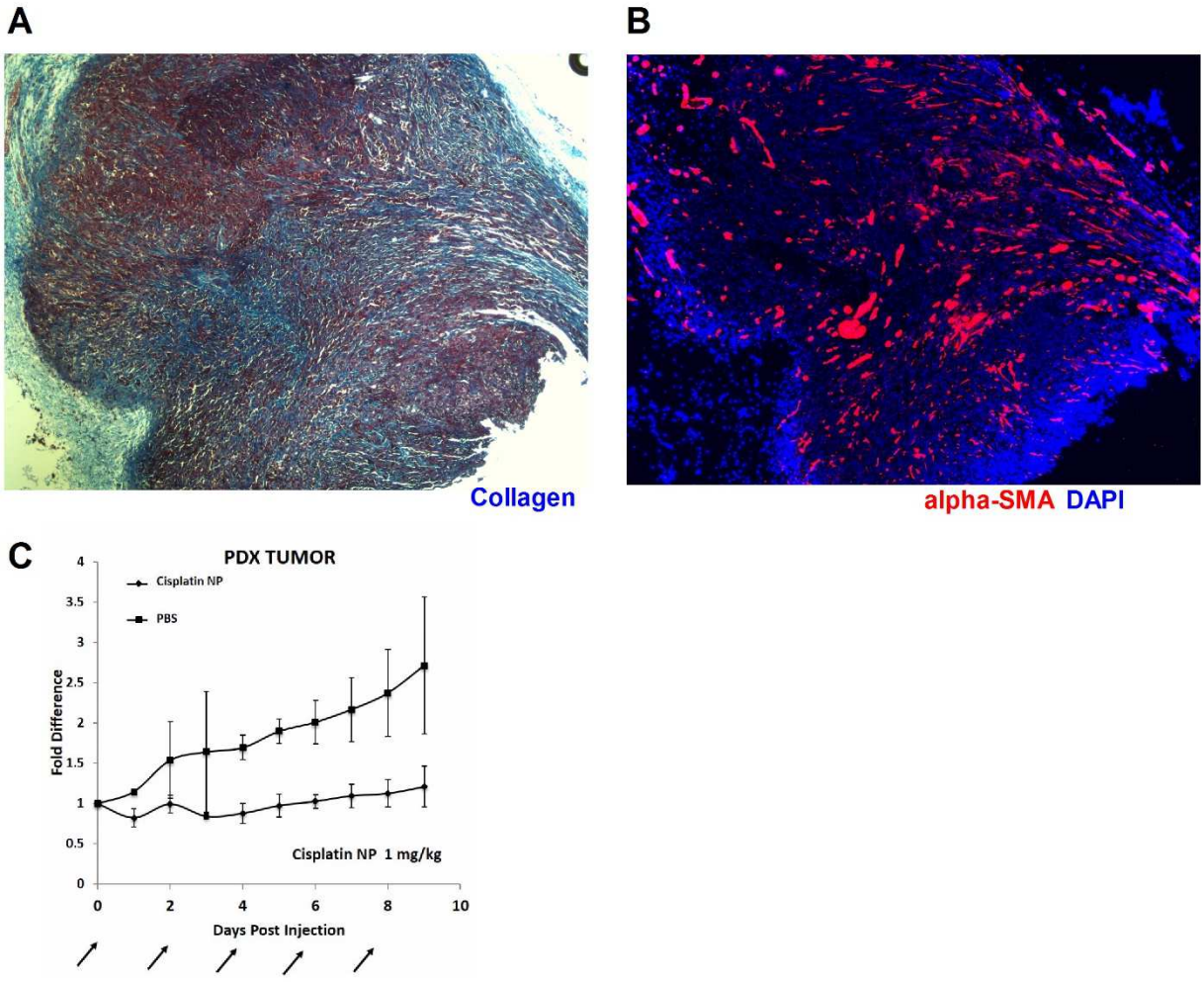

Figure 3.7 Pathology and treatment of PDX model

A. Masson trichrome staining of the collagen. B. Fluorescence staining of αSMA revealed the stroma-rich pathology of the PDX model. C. PDX tumor growth inhibition curve.

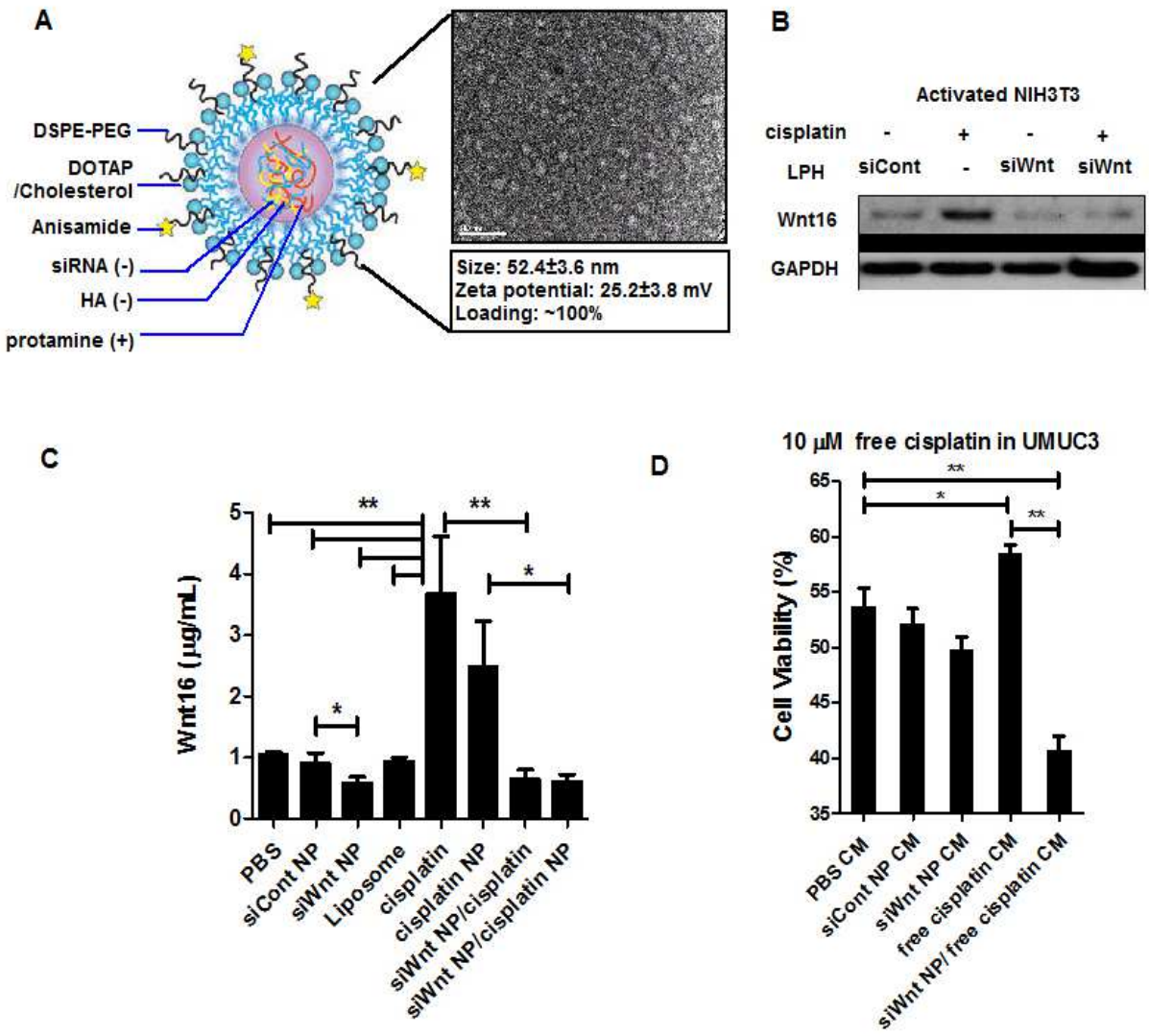

Figure 3.8 ***In vitro*** **gene transfection of siWnt NPs.**

A. Graphical and TEM images of the LPH NPs. Particle size, zeta potential were characterized and presented. B. Western blot analysis of the Wnt16 expression in NIH3T3 cells as an indicator of *in vitro* transfection of the siRNA encapsulated LPH NPs. C. Knockdown of Wnt16 excretion was assayed by ELISA in the conditioned media from different treatments. DOTAP/Chol liposomes were set as a material control for cisplatin NP (n = 3). D. MTT assay of UMUC3 treated with the aforementioned CM along with cisplatin (n = 4). (For all listed analysis, * $P < 0.05$, ** $P < 0.01$). Note that, since both the free and NP form of cisplatin shown comparable effect in (C), either was applied to all the studies, only representative results were shown.

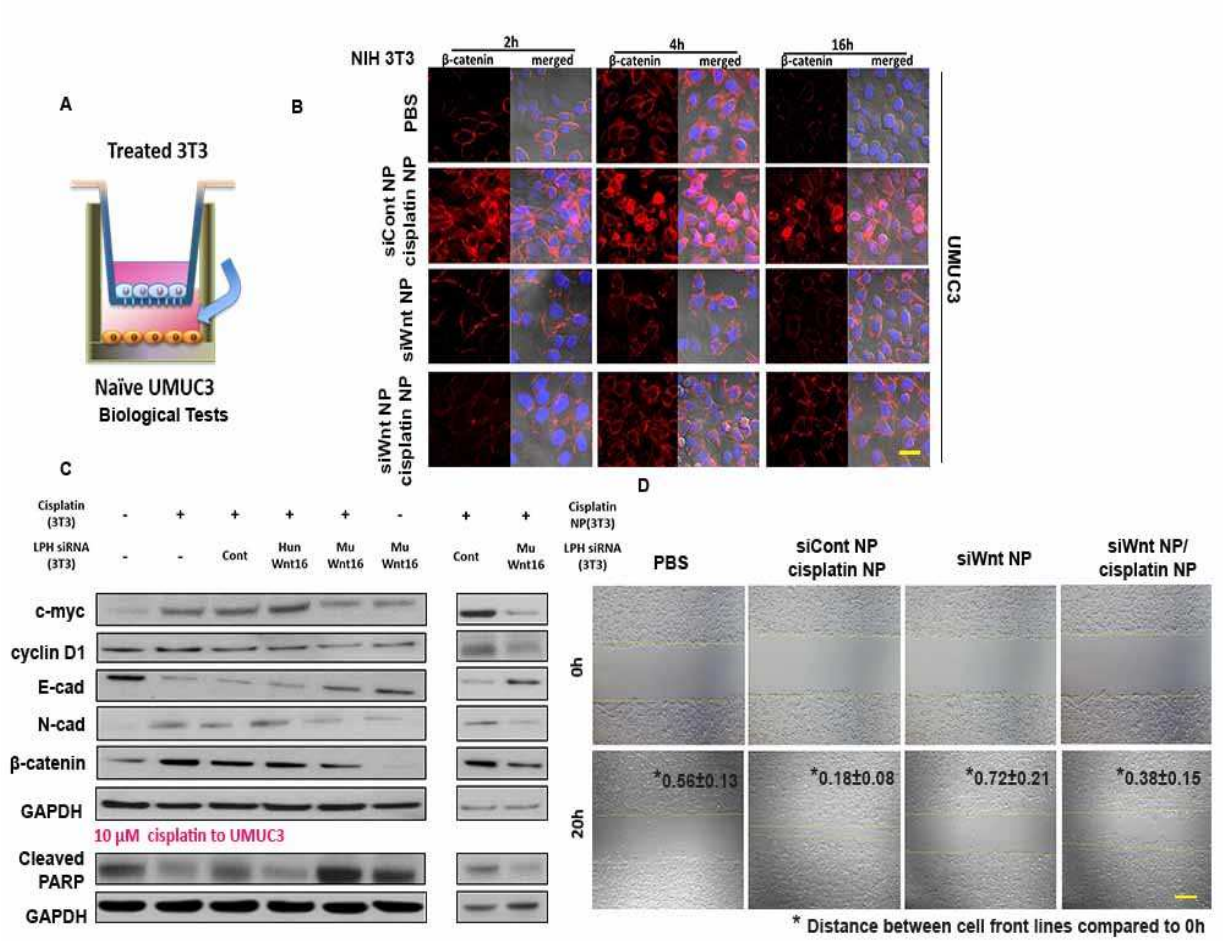

Figure 3.9 Mechanistic study of Wnt16 on neighboring tumor cells.

A. Scheme of a non-contact co-culture system (upper: NIH3T3, lower: UMUC3). This system was used in the scratch assay, β–catenin translocation assay and western blot. B. Confocal images of β-catenin nucleus translocation in the lower UMUC3 (Scale bars 20 μm). C. Western blot analysis of Wnt pathway down-stream proteins (c-myc and cyclin D1), EMT markers (E-cadherin (E-cad) and N-cadherin (N-cad)) and apoptotic marker (cleaved PARP) in the lower UMUC3 chamber after co-culture. D. Scratch assay in the lower UMUC3 20 h after co-culture. * Moving distance compared to 0h, n = 3. Scale bar is 100 μm.

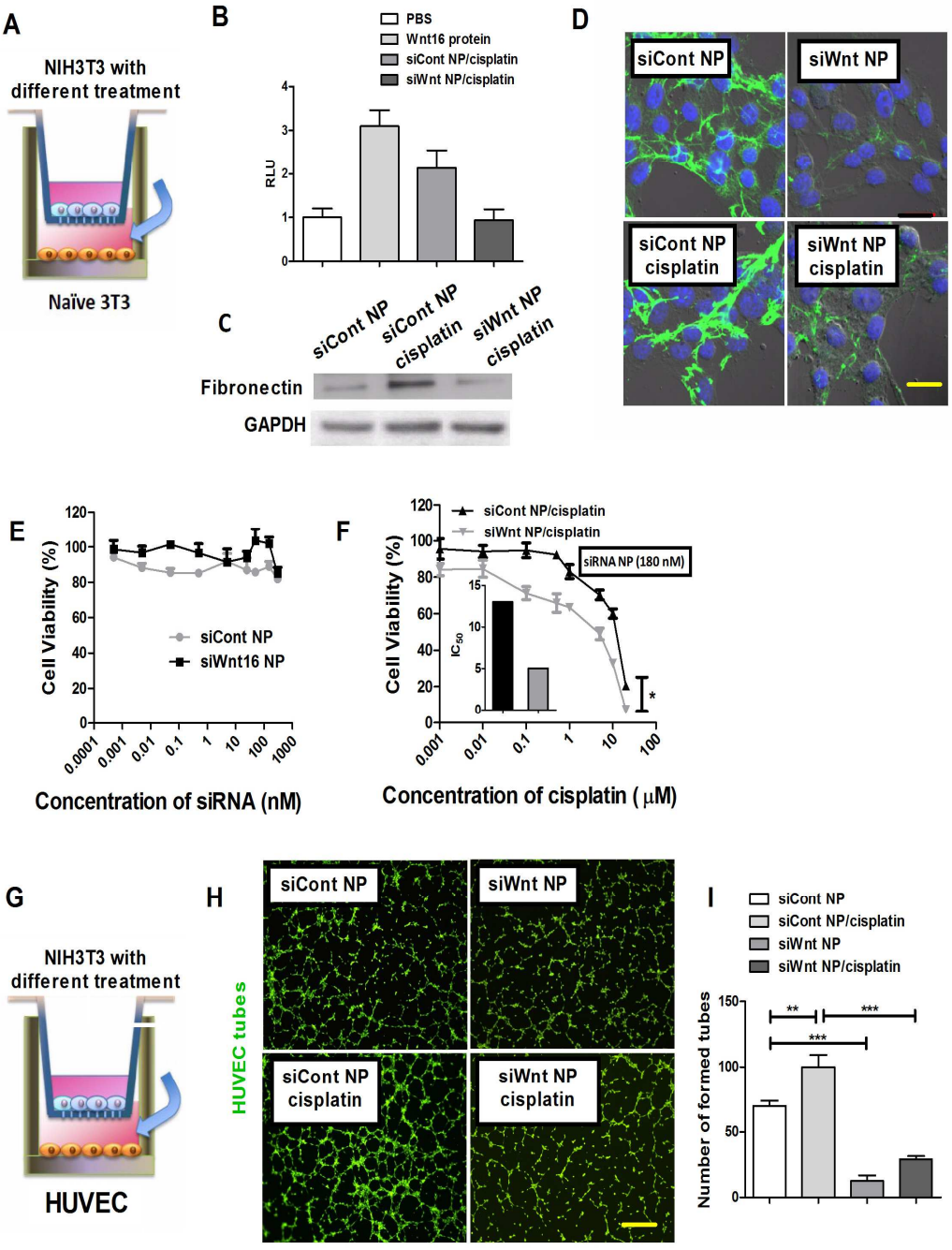

Figure 3.10 ***In vitro*** **mechanistic study of Wnt16 on neighboring stromal cells.**

A. Scheme of a non-contact co-culture system (upper and lower: NIH3T3). B. Assay of canonical Wnt pathway signaling through activation of luciferase labeled fibroblasts was performed in the lower chamber after co-culture. Relative luciferase units (RLU) were quantified (n = 4), Wnt16 protein, 1 μg/mL. C. Western blot analysis of fibronectin in the lower chamber when upper chamber was pretreated with cisplatin. D. Confocal images of immunofluorescence (IF) staining of fibronectin in the lower chambers (fibronectin: green, cell nucleus: blue), scale bar represents 20 μm. E. Cell proliferation of activated NIH3T3 transfected with siWnt NPs or siCont NPs at different

concentrations (n = 4). F. Viability of activated NIH3T3 across a range of cisplatin concentrations with transfection of anti-Wnt16 or control siRNA (concentration of siRNA was 180 nM) (n = 4, * $P <$ 0.05) (G) Scheme of a non-contact co-culture system (upper: NIH3T3 and lower: HUVEC). H. Tube formation was monitored in HUVEC cells as indicators for angiogenesis 4h after co-culture. HUVEC cells were stained by calcium AM (green). I. The number of formed tubes was calculated. Five randomly selected microscopic fields were quantitatively analyzed by Image J. Scale bar represents 100 μm. (n = 5, * $P < 0.05$, ** $P < 0.01$, *** $P < 0.001$).

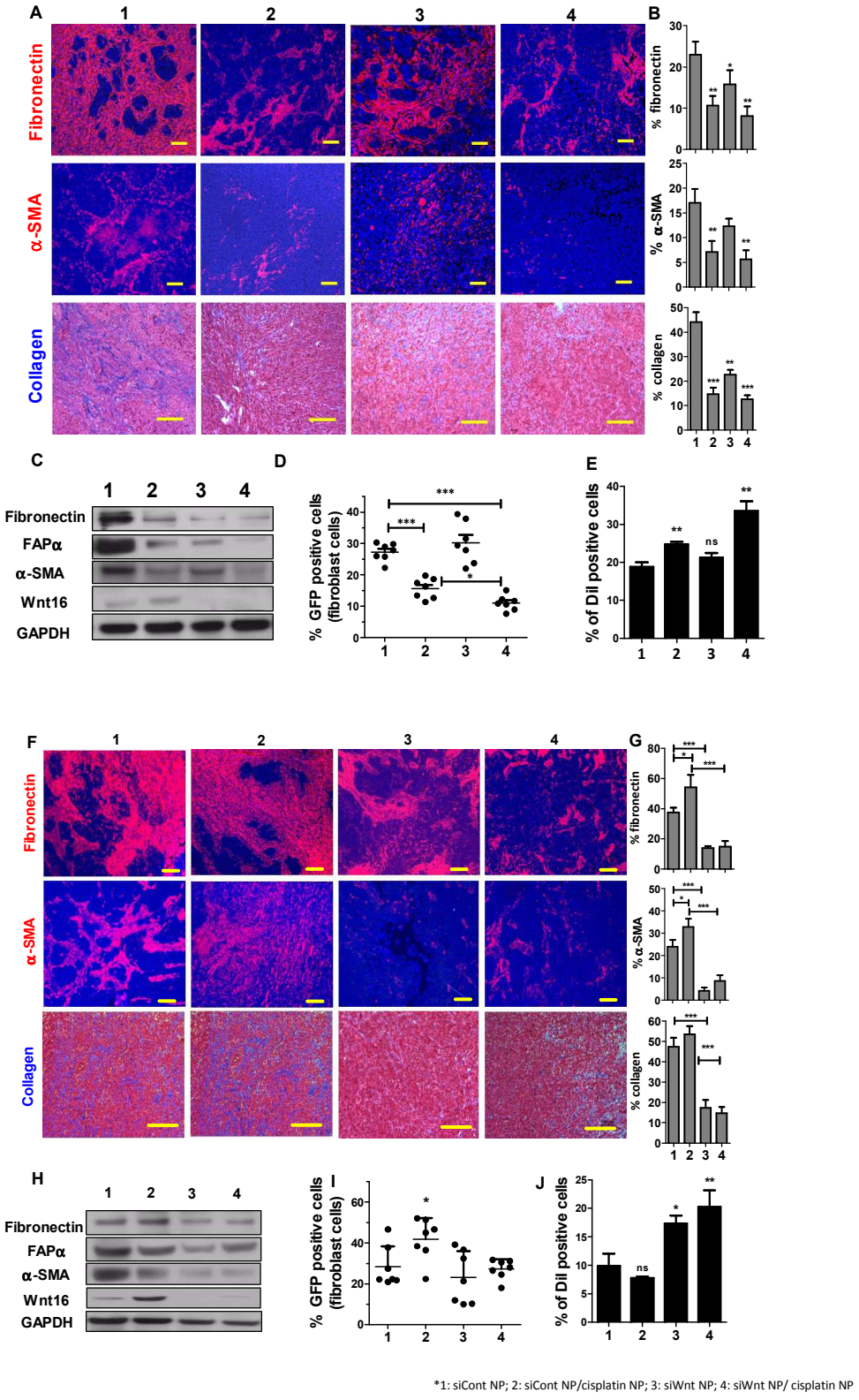

Figure 3.11 Dynamic tumor microenvironment remodeling by cisplatin NPs and siWnt NPs.

Single (A-E) and 4-dose treatment (F-J) of siCont NPs (1), siCont NPs/cisplatin NPs (2), siWnt NPs (3) and siWnt NPs/cisplatin NPs (4) were intravenously administered to mice separately with cisplatin 1.0 mg/kg and siRNA 0.6 mg/kg. Tissue samples were collected 2 days after injection. (A) and (F). IF staining of fibronectin, αSMA. The nuclei were stained with DAPI (blue), fibronectin and αSMA were stained red. Collagen was stained using Masson trichrome. The blue color represents collagen content, while the cytoplasm was stained red. Scale bar is 100 μm. (B) and (G) Quantitative analysis of fibronectin, αSMA and collagen content using Image J from 5 randomly selected microscopic fields. (C) and (H) Western blot analysis of TAF markers: FAP α, αSMA, fibronectin and Wnt16 protein levels in the tumors after treatment. (D) and (I) GFP-3T3 was used to form the UMUC3/3T3 model. The ratio of GFP positive TAFs was quantified by flow cytometry after treatment (n = 8). (E) and (J) DiI-labeled liposomes (~70 nm) were IV injected one day before sacrificing the mice. Fluorescent liposome accumulations and penetrations in the UMUC3/3T3 tumors were quantified by flow cytometry (n = 3). For all statistical analysis, * $P < 0.05$; ** $P < 0.01$; *** $P < 0.001$, the statistical analysis was calculated by comparison with the untreated group if not specifically mentioned.

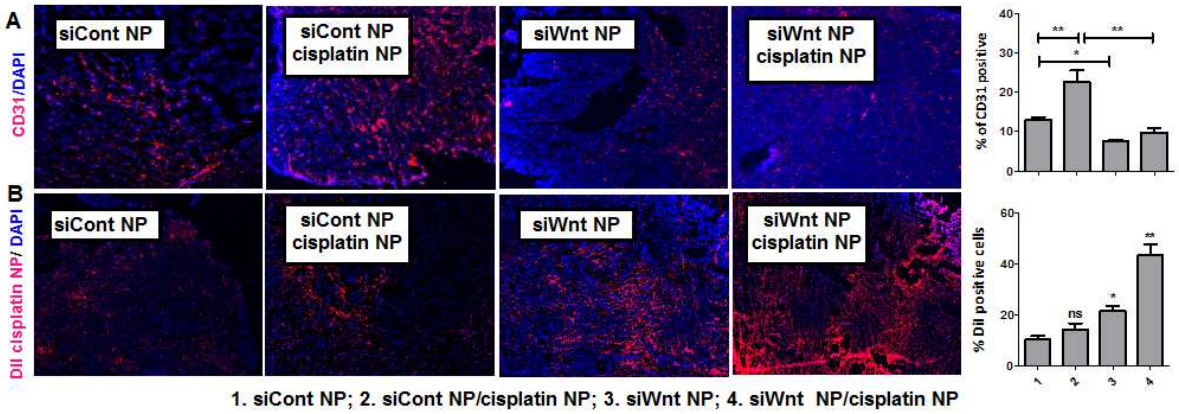

Figure 3.12 Blood vessel remodeling by cisplatin NPs and siWnt NPs after multiple doses.

A. Influence of Wnt16 on blood vessel was evaluated *in vivo* by IF staining endothelial cells with CD31 (red) after multiple treatments. B. Distribution of DiI labeled cisplatin NPs 8h after IV injection in different treatments of the UMUC3/3T3 model. Five images of each group from the two experiments were quantified and the result is shown on right. For all the statistical analysis, the difference was calculated by comparison with the untreated group if not specifically mentioned. In all quantifications, * $P < 0.05$, ** $P < 0.01$, *** $P < 0.001$.

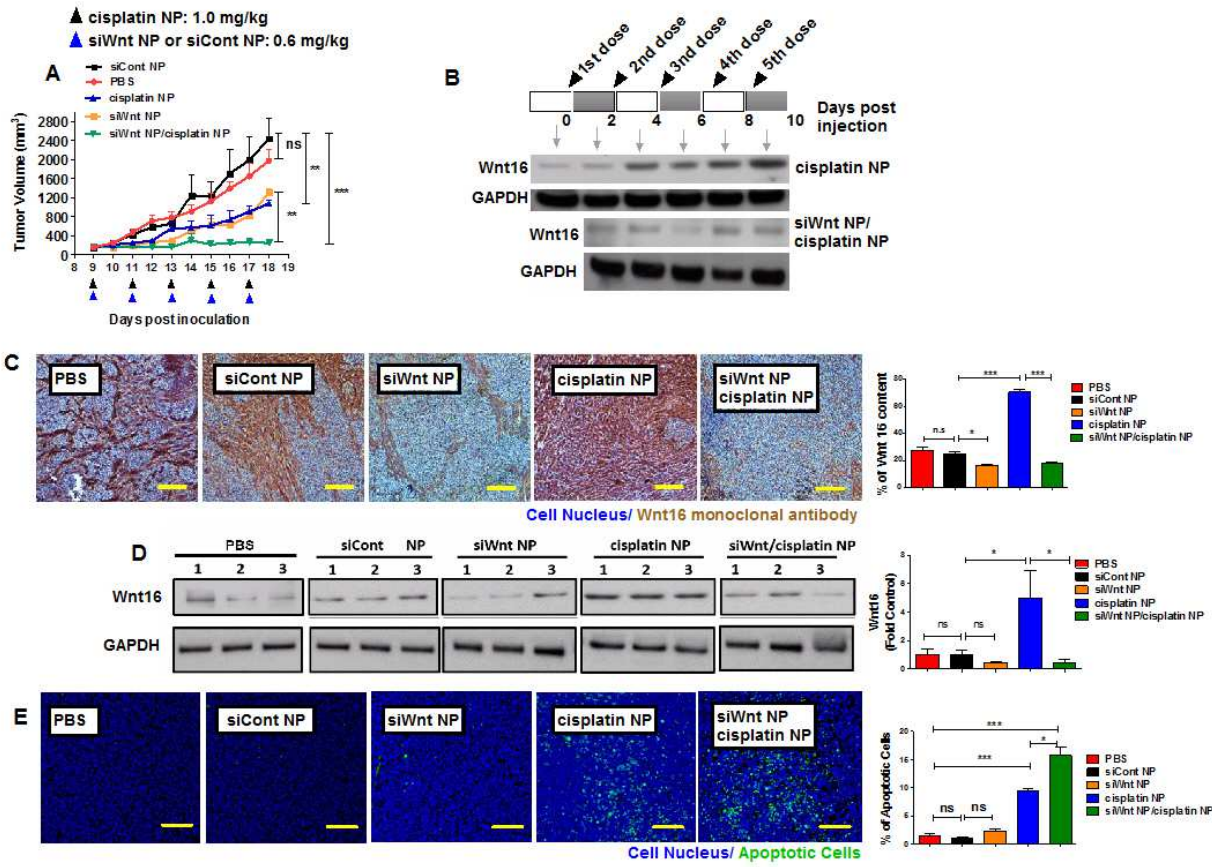

Figure 3.13 IV injection of siWnt NPs with cisplatin NPs inhibited UMUC3/3T3 tumor growth.

A. Intravenous injection of siWnt NPs with cisplatin NPs inhibited the growth of the desmoplastic bladder xenografts (UMUC3/3T3) when the tumor was small (volume ~150 mm3, n = 5-7). B. Expression of Wnt16 in the cisplatin NPs and the combo group over the course of treatment by western blot analysis. Tumor tissues were collected 1 day after each dosing intervals. C. IHC staining of Wnt16 on tumor tissues at the end point of tumor inhibition study. Wnt16 was stained brown and the cell nuclei were stained blue. The scale bar represents 100 μm. The Wnt16 content of 5 randomly selected microscopic fields was quantified using Image J. The quantification bar chart is shown on the right. D. Western blot analysis of Wnt16 levels in tumors 1 day after treatment. Three samples were taken randomly from three mice in each treatment group. The intensity of the Wnt16 western band was analyzed by Image J and calculated based on content of GAPDH. Wnt16/GAPDH value in PBS group was set as 1. Quantification is shown on right. E. Effect of NPs on the UMUC3/3T3 model apoptosis using TUNEL assay. The scale bar represents 100 μm. Five images were quantified and the data is shown on right. In all quantifications, * $P < 0.05$; ** $P < 0.01$; *** $P < 0.001$.

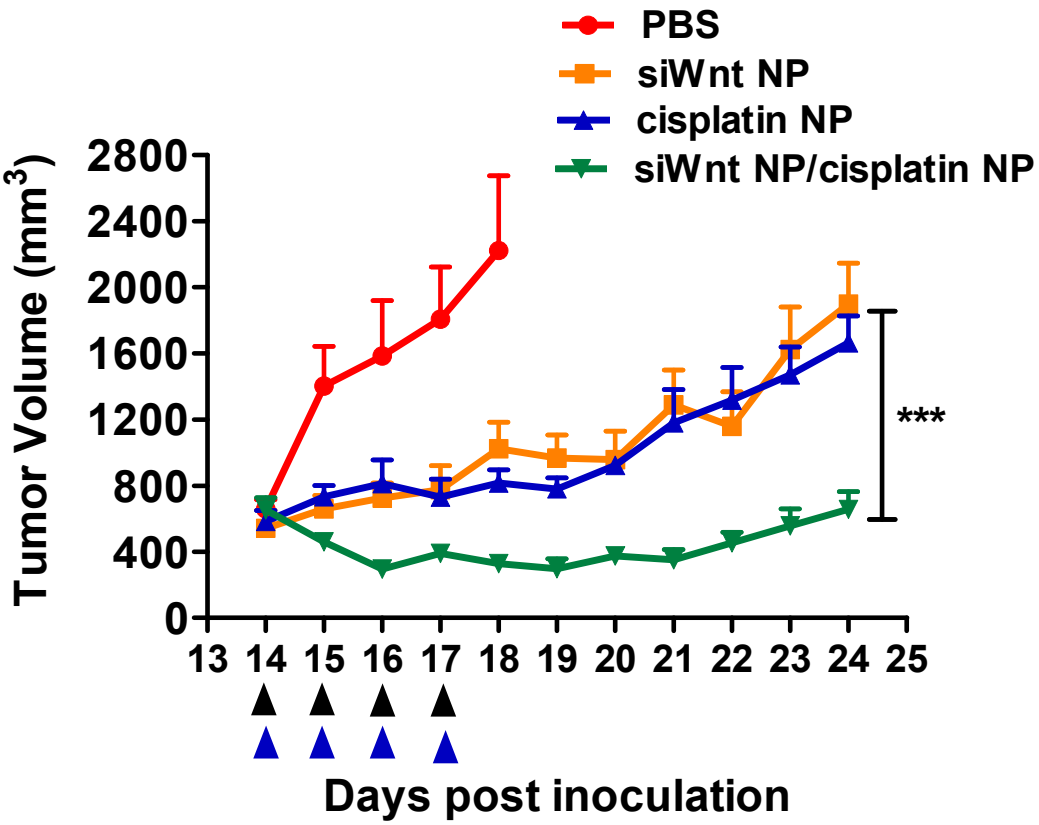

Figure 3.14 IV injection of siWnt NPs (0.6 mg/kg) with cisplatin NPs (1 mg/kg) led to tumor regression when the tumor is big (volume ~700 mm^3).

Arrow heads indicate the dosing schedule of siWnt NPs (blue) and cisplatin NPs (black) (n = 4, *** $P < 0.001$).

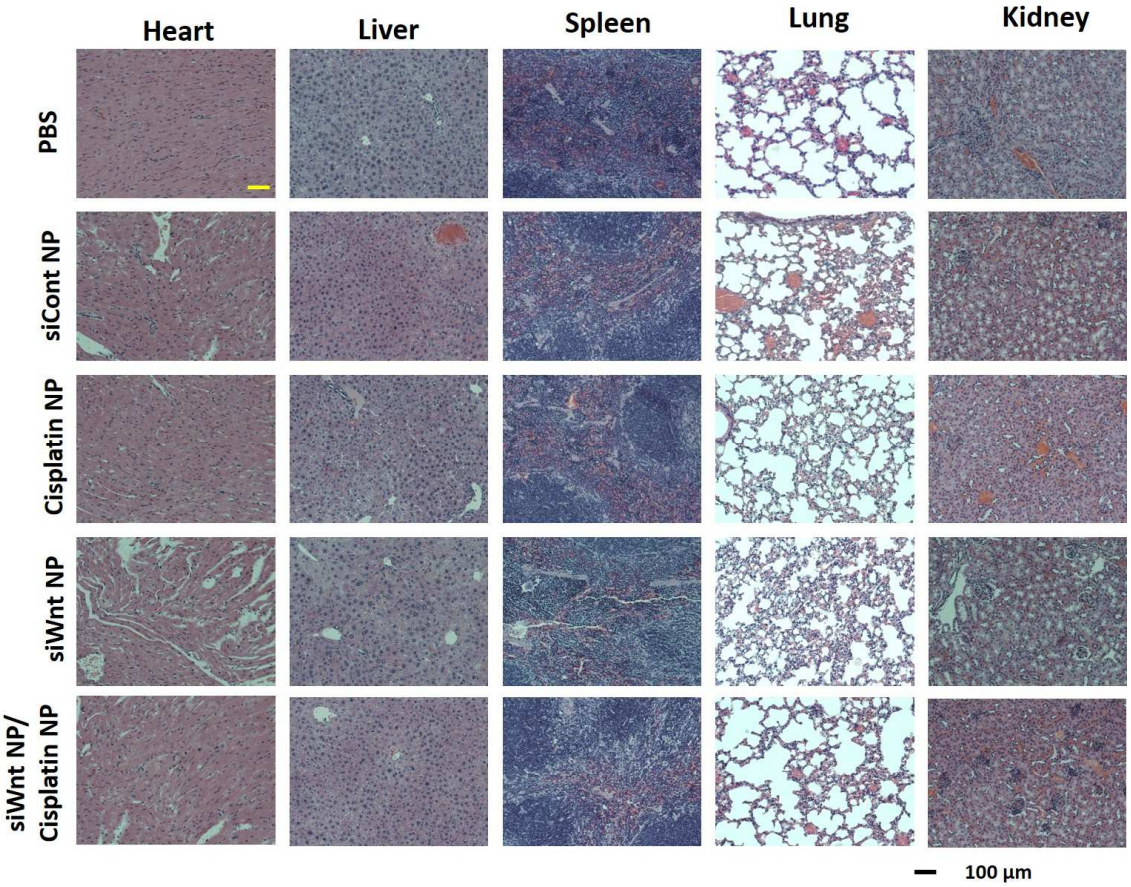

Figure 3.15 HE staining of major organs from 5 injections of PBS, siCont NPs, cisplatin NPs, siWnt NPs and siWnt NPs/cisplatin NPs.

No toxicity was found to the major organs after different therapy.

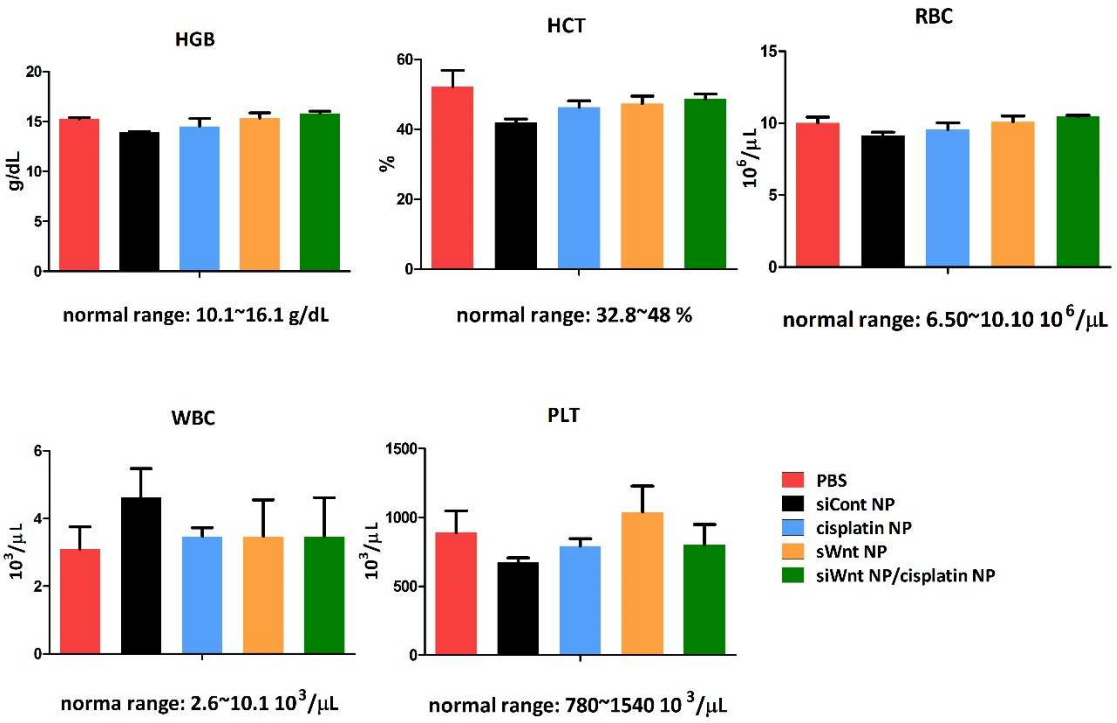

Figure 3.16 Hematological test of whole blood collected from healthy nude mice treated with 5 doses of different treatments as indicated.

No significant difference between PBS group and the treatment group. WBC, white blood cell; HCT, hematocrit; PLT, platelet; HGB, hemoglobin; RBC, red blood cell (n = 4).

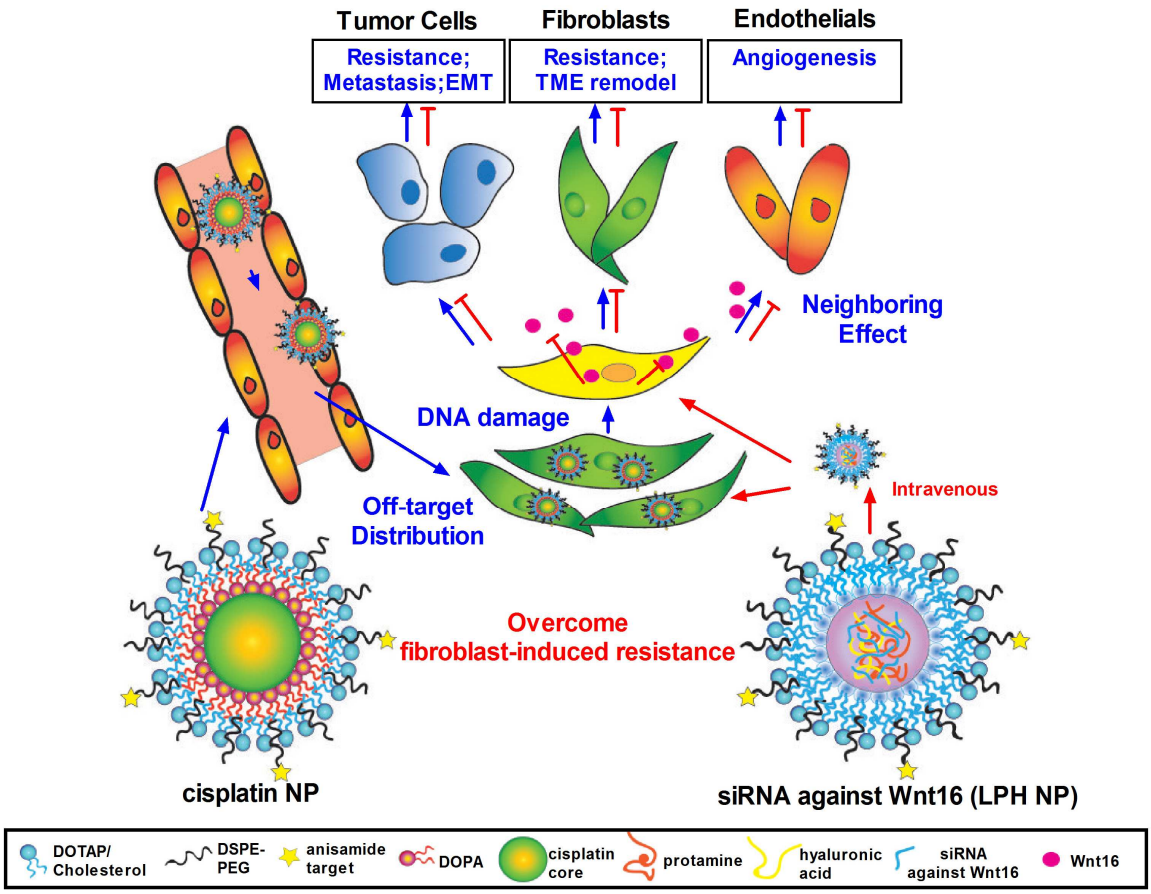

Figure 3.17 Diagram of the proposed mechanism

CHAPTER 4: IN SITU GENERATION OF TUMOR-SUPPRESSIVE FIBROBLASTS BY HARNESSING OFF-TARGET DISPOSITIONS OF NANOPARTICLES IN TUMOR ASSOCIATED FIBROBLASTS[5]

4.1 Summary

The off-target distribution of nanoparticles (NPs) to fibroblasts illustrates a delivery barrier; compromising treatment of desmoplastic tumors. However, fibroblasts' uptake of NPs can be utilized to modify fibroblasts into synthesizing secretable cytotoxic proteins. To achieve this, plasmids encoding secretable TNF-related apoptosis-inducing-ligand (sTRAIL) were loaded in lipid-coated protamine DNA complexes (LPD) and delivered to fibroblasts in desmoplastic bladder xenografts. After 3 doses, ~70% of sTRAIL producing cells were fibroblasts. The secreted TRAIL induced apoptosis within neighboring tumor nests. Additionally, residual fibroblasts reverted to a quiescent state due to insufficient activation, further compromising tumor growth and remodeling the microenvironment to favor second-wave nano-therapy. This strategy was also applied to treat an orthotopic pancreatic cancer xenograft, where the desmoplastic reaction remains overhanging issue limiting delivery of therapeutic NPs. Promisingly, sTRAIL LPD efficiently delayed pancreatic tumor growth. Collectively, the targeting and *in situ* modification of fibroblasts provides a new paradigm for treating desmoplastic malignancies.

---

[5]This chapter previously appeared as a manuscript soon to be submitted

4.2 Introduction

The enhanced permeation and retention (EPR) effect describes the increased intra-tumoral accumulation and cellular uptake of therapeutic nanoparticles (NPs) in oncology, which demonstrates promising *in vitro* and preclinical responses [239]. Unfortunately, the early promises of several therapeutic NPs have failed to translate clinically [240]. One of the major mechanisms proposed for this failure regards heterogeneous drug uptake and off-target response in stromal cells within the tumor [241]. Specifically, tumor associated macrophages (TAMs) are a major off-target depletion site for NPs [240, 242]. Additionally, in desmoplastic condition, the tumor associated fibroblasts (TAFs), as the major stroma cells wrapping around blood vessels, constitute another barrier for NPs extravasation [169, 239]. The case is most prominent in pancreatic ductal adenocarcinoma (PDAC), where activated alpha smooth muscle (αSMA) positive pancreatic stellate cells compose 15 to 40% of total tumor mass [115, 243, 244].

Off-target distribution of therapeutic NPs can result in adverse effects. In a previous study, we found a nano-formulation of cisplatin delivered to TAFs led to the secretion of survival factors, such as Wnt16 to support the proliferation of neighboring tumor cells [169]. In another study, disposition of DC101, a VEGFR2-blocking antibody, in pericytes or myofibroblast-like cells was found to be a major resistance mechanism in VEGF inhibitor therapy [245].

To circumvent stroma-induced resistance, depleting stroma cells has been proposed to improve tumor cells' capture of therapeutic agents [110, 246]. However, stromal depletion strategies run the risk of eliminating stromal components needed for tissue homeostasis, paradoxically facilitating tumor metastasis [117]. Stromal components can produce small proteins (e.g. cytokines) secreted *in situ*, which can bypass stromal cells barriers and bind avidly to targeted cells causing overexpression of their receptors. For example, proinflammatory cytokines (e.g. TNF-α, IL-6) secreted from infiltrated macrophages inhibit the growth of tumor cells [247]. Owing to the ability for

cytokines to modulate tumor growth, the idea of engineering an *in-situ* stromal depot capable of secreting cytotoxic proteins emerged in the current study.

The best way to generate this theoretical stromal depot is gene therapy, as gene therapy allows proteins to be produced locally at higher rates and quantities than through systemic delivery of recombinant proteins [248]. While the off-target delivery of therapeutic NPs to stromal components traditionally compromise the efficacy of tumor specific treatments, this phenomena can be exploited to specifically deliver genes to stroma cells, to provide the basis for *in-situ* synthesis and secretion. Since macrophages and fibroblasts are the major off-target sites of NPs in *stroma-vessel type* (this term is used to define the common structure of desmoplastic tumors that blood vessels are embedded in stroma area) desmoplastic tumors, they are excellent candidates for the *in-situ* programming. However, expression of plasmids in macrophages is limited by the macrophages natural enzymes for degradation [249]. In addition, the regeneration of macrophage or other circulating monocytes limits the persistency of gene expression [239]. Therefore, TAFs may be a more suitable protein producing reservoir as a locally recruited cell population.

The TNF-related apoptosis-inducing ligand (TRAIL) efficiently induces apoptosis in a wide range of tumor cells while sparing normal cells, making it an ideal candidate for cancer therapy [250]. Full-length TRAIL is a transmembrane protein lacking a leader sequence for extracellular secretion. It can then only be proteolytically cleaved to bind to the death domain-containing receptors on the cell surface, leading to caspase-dependent apoptosis [248]. Therefore, effects of TRAIL are limited to cells near the plasmid transfected cells, compromising the therapeutic efficacy [251]. Thereby, a secretable form of TRAIL (sTRAIL) was engineered. sTRAIL consists of an extracellular domain of TRAIL fused with an the extracellular domain of Flt3L at the NH_2 terminal. Flt3L is a ligand for flt3 tyrosine kinase receptor, whose extracellular domain aids in the secretion of various proteins from cells [252]. It was then necessary to utilize the off-target distribution of NPs to target sTRAIL containing NPs toward fibroblasts, seeking to make them tumor inhibitive. The overarching goal was to use *in-situ* gene expression of sTRAIL in fibroblasts to reprogram fibroblasts to secrete cytotoxic

cytokines and induce the apoptosis of neighboring tumor cells in desmoplastic tumors. The utilization of TRAIL-resistant low proliferating fibroblasts as a gene producing reservoir has two important advantages: (a) allow a comparatively long gene expression compared to sensitive tumor cells and (b) maintain the stroma cell components for tissue homeostasis.

To confirm the proof of concept, a stroma-vessel desmoplasia model was established by co-inoculating UMUC3 bladder cancer cells with NIH3T3 fibroblasts. The fibroblast content was adjusted to ~25% corresponding to the average level in desmoplastic tumors. Lipid coated protamine DNA complexes (LPD) was developed and utilized for encapsulating sTRAIL plasmids. The fibroblasts' expression of sTRAIL and the apoptosis of neighboring tumor cells were assessed. The concept was further evaluated on a clinical relevant orthotopic desmoplastic PDAC model BXPC3. As expected, the expression of sTRAIL was primarily in fibroblasts. The *in situ* expression of sTRAIL by fibroblasts induced potent tumor inhibition. However, residual TAFs unexpectedly reverted to quiescence, presumably due to death of neighboring tumor cells. This led to the remodeling of tumor microenvironment (TME) and provides a new paradigm for second-wave nanoparticle therapy.

4.3 Materials and Methods

4.3.1 Materials

1,2-dioleoyl-3-trimethylammonium-propane chloride salt (DOTAP) was purchased from Avanti Polar Lipids, Inc. (Alabaster, AL). 1,2-distearoryl-sn-glycero-3-phosphoethanolamine-N-[methoxy (polyethyleneglycol-2000) ammonium salt (DSPE-PEG2000) was obtained from NOF America Corporation. The hydrophobic dye, 1,1'-Dioctadecyl-3,3,3',3'-tetramethylindocarbocyanine perchlorate (DiI) was purchased from Thermo Fisher Scientific, Inc. (Carlsbad, CA). Cholesterol and protamine were purchased from Sigma-Aldrich (St Louis, MO) Cisplatin was purchased from Acros Organics (Fair Lawn, NJ). DSPE-PEG-AA was synthesized based on the previous established protocols [173]. An expression vector containing the human TRAIL open reading frame was

purchased from InvivoGen (San Diego, CA). Primers for PCR, qPCR were purchased from Integrated DNA Technologies (Coralville, IA), Invitrogen (Grand Island, NY), and Bio-rad (Hercules, CA). All the other chemicals were purchased from Sigma-Aldrich unless otherwise mentioned.

4.3.2 Cell lines, Animals and Antibodies

The mouse embryonic fibroblast cell lines NIH3T3 and the human lung fibroblasts MRC-5 were purchased from UNC Tissue Culture Facility. The human bladder transitional cell line UMUC3 was provided by Dr. William Kim (University of North Carolina at Chapel Hill, NC). The human pancreatic cancer BXPC3-Luc2 was purchased from PerkinElmer (Waltham, MA). UMUC3 and NIH3T3 were maintained in Dulbecco's Modified Eagle's Media (Invitrogen, CA), supplemented with 10% feta bovine serum (FBS) (Sigma, MO) or 10% bovine calf serum (Sigma, MO), 1% penicillin and streptomycin (100 μg/mL) (Invitrogen, CA). BXPC3-Luc2 were cultured in RPMI-1640 medium (Invitrogen, CA), supplemented with 20% FBS, while MRC-5 were cultured in αMEM (Invitrogen, CA) supplemented with 10% FBS. Female nude mice of 6-8 weeks-old were obtained from and raised by the University of North Carolina animal facility. All animal handling procedures were approved by the University of North Carolina at Chapel Hill's Institutional Animal Care and Use Committee. Primary and secondary antibodies used for western blot (WB), flow cytometry (flow cyt), immunofluorescence staining (IF) and immunohistochemistry (IHC) staining are listed in **APPENDIX I** .

4.3.3 Preparation and Characterization of LPD

LPD were prepared through a stepwise self-assembly process based on a well-established protocol [217]. Briefly, DOTAP and cholesterol (1:1, mol/mol) were dissolved in chloroform and solvent was removed by rotary evaporator. The lipid film was then hydrated with distilled water to make the final concentration of 10 mmol/L cholesterol and DOTAP. Then, the liposome was sequentially extruded through 200 nm, and 100 nm polycarbonate membranes (Millipore, MA) to form 70–100 nm unilamellar liposomes. The LPD polyplexes core were formulated by mixing 140 μL

of 36 μg protamine in 5% glucose with equal volume of 50 μg plasmid in 5% glucose. The mixture was incubated at room temperature for 10 minutes and then 60 μl cholesterol/ DOTAP liposomes (10 mmol/L each) were added. Post insertion of 15% DSPE-PEG and DSPE-PEG-AA were further performed at 60 °C for 15 minutes. The size and surface charge of the NPs were determined by Malvern ZetaSizer Nano series (Westborough, MA). TEM images were acquired where NPs were negatively stained using a JEOL 100 CX II TEM (JEOL, Japan).

4.3.4 sTRAIL and TRAIL Construction

The p-sTRAIL containing genes encoding a Flt3L leader sequence, isoleucine zipper, the extracellular domain of TRAIL, followed by an internal ribosome entry site and GFP under a CMV promoter were previously constructed and provided by Dr. Shawn Hingtgen (University of North Carolina at Chapel Hill, NC). To establish the p-TRAIL construct, the sTRAIL sequence was cleaved from the p-sTRAIL vector via digesting with XhoI/BamHI (New England Biolabs, CA). Then the full length TRAIL cDNA was amplified by PCR using a sense primer containing the XhoI site (5'-CAGCCTCGAGCGACCATGGCTATGATGGAGGTC-3') and an antisense primer containing the BamHI site (5'-CAGCGGATCCTTAGCCAACTAAAAAGGCCCCG-3'). The amplified DNA was digested with XhoI/BamHI, and inserted into the XhoI/BamHI site of the pre-removed p-sTRAIL construct. The insertion of the full length TRAIL was confirmed by double digestion and PCR. The p-sTRAIL sequence was verified using Applied Biosystems 3730xl Genetic Analyzers.

4.3.5 *In vitro* Transfection of LPD-encapsulating sTRAIL and TRAIL

Activated NIH3T3 cells (incubating with 10 ng/mL TGF-β overnight) were grown until 80% confluent in 6-well plates. Then LPD loaded with sTRAIL and TRAIL (1μg of the plasmids) were added to each well in the presence of Opti-MEM. The medium was refreshed 4h post-transfection and incubated overnight. The expression of TRAIL and sTRAIL was measured at mRNA level by qPCR analysis with GAPDH as a loading control. Lipofectamine®-2000 (Invitrogen, CA) was used as a positive control for the transfection study following the manufacturer's protocol.

4.3.6 GFP and RFP Lentivirus Transduction in NIH3T3 Fibroblasts.

Protocols are similar to that discussed in the previous chapter (**Section 2.3.6**).

4.3.7 Non-contact Co-culture Model for Mechanistic Study

A non-contact co-culture system was established according to a previous protocol with little adjustment [218]. In brief, activated NIH3T3 cells were seeded into a transwell filter (polycarbonate membrane insert, 0.45-μm pore, Corning Inc.). Before co-culture, transwell insert were transfected with sTRAIL, TRAIL, GFP and PBS using Lipofectamine®-2000 for 4 h. Immediately after the insert cells were washed thoroughly with PBS, the co-culture started by putting the insert into the lower chambers pre-seeded with UMUC cells. After a determined time of co-culture, the bottom cells were used in the following experiments. **Cell number counts.** Twenty-four hours after co-culture, UMUC3 cells were stained with calcein AM (Invitrogen, CA) and visualized using a fluorescence microscope. The number of cells was quantified using Image J from 5 randomly selected microscopic fields. **Annexin V/Propidium Iodide apoptosis assay.** Twenty-four hours after co-culture, tumor cells were collected and stained with Annexin V and propidium following the manufacturer's protocol (BD Pharmingen™, CA). Early apoptosis and late apoptosis were quantified using flow cytometry on a BD FACSAria instrument (Beckon Dickinson, CA).

4.3.8 *In vitro* Analysis of Cell Proliferation

UMUC3 and activated NIH3T3 cells were cultured with sTRAIL LPD, TRAIL LPD, and GFP LPD, respectively, at different concentrations for 4h, and then washed and cultured overnight. Cell viability was assayed by 3-(4,5-dimethylthiazol-2-yl)-2,5-diphenyltetrazolium bromide (MTT) to address cytotoxicity of TRAIL in fibroblasts and tumor cells.

4.3.9 Collection of Conditioned Medium

Conditioned medium (CM) was collected as described elsewhere [207, 218]. Activated NIH3T3 cells were treated with GFP LPD, sTRAIL LPD and TRAIL LPD respectively with Opti-

MEM medium for 4 h. After treatments, the cells were rinsed thrice with PBS and left overnight in DMEM medium with 5% BCS. The culture medium was then collected and centrifuged at 900 rpm for 5 min, and then supernatant was filtered through a 0.45-μm filter and collected as CM for further study. **Cytotoxicity in tumor cells.** The CM from different treatments groups were used to culture UMUC3 cells pre-seeded in 96-well plates. Twenty-four and 36 h after incubation, cell viabilities of UMUC3 were quantified using an MTT assay respectively. **Enzyme-linked Immunosorbent Assay (ELISA) of sTRAIL in the CM.** To measure the concentration of TRAIL, CM collected from 3T3 cells and MRC-5 cells pretreated with different amounts of sTRAIL or TRAIL LPD were subjected to an ELISA for human TRAIL (R&D Systems, MN) following the manufacturer's instructions. Recombinant human TRAIL protein was used as a standard.

4.3.10 Tumor Growth Inhibition

The stroma-vessel UMUC3/NIH3T3 model was established as previously reported with little modification [74, 195]. In brief, UMUC3 cells (5×106 and NIH3T3 cells (2.5×106) were subcutaneously co-inoculated into the right flank of mice with Matrigel (BD biosciences, CA) at a ratio of 1:1 (V/V). Treatments were initiated on the 11th day when tumor sizes reached ~500 mm3. Mice were then randomized into 4 groups (n~7 per group) as follows: Untreated group (PBS), GFP LPD, TRAIL LPD and sTRAIL LPD. IV injections were performed Q.O.D for a total of 4 doses of 50 μg plasmid/mice. Tumor volume (1/2*length*length*width) was measured every day with a digital caliper (Thermo Fisher Scientific, PA) and body weight was also recorded. The desmoplastic BXPC3-Luc2 model was established by orthotopic injection of 1X106 cells into the tail of pancreas. Injections of sTRAIL, TRAIL, GFP LPD were started 15 days after inoculation and dosed every 2 days, in total of 4 times. Tumor growth was monitored using IVIS® kinetics Optical System (Perkin Elmer, CA) twice a week. The increases of tumor volumes were calculated as the radiance of the intensities.

4.3.11 Flow Cytometry Analysis

To study the cell population that took up NPs within tumors, mice were administrated with DiI-labeled LPD at a dose of 0.1 mg/kg DiI and were sacrificed 10, 24, 48 and 72h post IV injection. Fresh tumor tissues were dissociated with 1 mg/mL collagenase Type IV (Invitrogen), 1 mg/mL hyaluronidase (Sigma, MO) and 200 μg/mL DNAase I (Invitrogen, CA) in DMEM/ 2% FBS for 40 min to generate a single cell suspension (1×106 cells/mL). The fibroblasts were pre-transfected with green fluorescence protein (GFP). Leukocytes portion were stained with APC conjugated CD45 antibody at a 1:100 dilution. The cells were then subjected to flow cytometry analysis after washing. The ratios of DiI-labeled NPs distributed in different cell populations were then calculated. To analysis the expression of IRES GFP in fibroblasts and other cells within the bulk tumor, tumor tissues were collected after single dose or multiple doses treatments. To study the distribution in UMUC3/3T3, fibroblasts were pre-transfected with RFP; in BXPC3 tumors, TAFs were labeled with αSMA primary antibody, followed by Alex Fluor® 647 conjugated secondary antibody. Tumor tissues were dissociated and the ratio of GFP expressed fibroblasts in the dissociated cells was analyzed by flow cytometry on a BD FACSAria instrument (Beckon Dickinson, CA). To quantify the expression of TRAIL and TAFs markers in RFP-fibroblasts of the UMUC3/3T3 model, the dissociated cells were sorted using MoFlo XDP (Beckman Coulter, CA), and the collected fibroblasts and other cells counterpart were processed through RNA extract, DNA reversion and qPCR analysis.

4.3.12 Quantitative Real-time PCR (qPCR) Assay

Total RNA was extracted from the cell lysates, tumor tissues, or cells sorted from MoFlo XDP (Beckman Coulter, CA) using RNeasy Kit (Qiagen, CA). The cDNA was reverse-transcribed with the First-Strand Synthesis System for qPCR (Invitrogen, NY). Then ~100ng cDNA was amplified using the Taqman Universal Probes Supermix system (Bio-rad, CA) or iQTM SYBR® Green Supermix system (Bio-rad, CA). All the human or mouse specific primers for qPCR reactions

are listed in **APPENDIX II**. GAPDH was used as the endogenous control. Reactions were conducted with the 7500 Real-Time PCR System and the data were analyzed using the 7500 software.

4.3.13 Western-blot Analysis

Please refer to **Section 2.3.15**.

4.3.14 Fluorescence Images of GFP in the RFP-positive Fibroblasts

At determined time points after treatment, tumors were excised and fixed in 4% paraformaldehyde for 2 h, and then submersed and frozen in O.C.T. After cryosectioning, the 5μm frozen cryosections were washed with PBS twice, and mounted with Prolong® Gold antifade reagent with DAPI (Invitrogen, CA). GFP and RFP were visualized in the cryosections using Eclipse Ti-U inverted microscope (Nikon Corp., Japan) at 10X magnification and analyzed on Image J.

4.3.15 Immunofluorescence Staining

Paraffin-embedded tissues were prepared by the UNC Animal Histopathology Core. The slices were deparaffinized, and the antigen was recovered, permeablized, and fixed, if necessary, and blocked with 1% BSA at room temperature for 1h. Cell markers were detected with primary antibodies followed by secondary antibodies conjugated with fluorophores as indicated. Images were taken using Eclipse Ti-U inverted microscope (Nikon Corp, Japan) or confocal microscopy (Laser Sacning. Zeiss 510 Meta, Japan).

4.3.16 Immunohistochemical Staining of pSMAD2 and Blood Vessels

Immunohistochemical stainings of pSMAD2, αSMA and CD31 from adjacent sections of paraffin-embedded tumor samples were prepared by UNC Translational Pathology Laboratory. Images were taken by an Aperio ScanScope CS Digital Slide Scanner.

4.3.17 Masson's trichrome Staining

Paraffin-embedded tumor sections were deparaffinized and rehydrated. The slides were then stained using a Masson's Trichrome Kit (Sigma, MO) following the manufacturer's instructions.

4.3.18 TUNEL and αSMA Immunofluorescence Co-staining

Paraffin-embedded tumor sections were deparaffinized and rehydrated. GFP fluorescence from GFP-plasmid or GFP transfected cells was quenched during the embedding and fixing process. αSMA staining was performed following the immunofluorescence staining protocol. The slides were then stained using a TUNEL assay kit (Promega, MI) according to the manufacturer's instructions. Five to ten representative images from each treatment were processed using Eclipse Ti-U inverted microscope (Nikon Corp., Japan) and analyzed on Image J.

4.3.19 Serum Biochemical Value Analysis and Hematology Assay

Mice that were IV-injected with PBS, TRAIL LPD, sTRAIL LPD, and GFP LPD Q.O.D for a total of 4 doses were subjected to a toxicity assay. For 1-day post treatments, blood samples were collected from mice of different treatment groups and centrifuged at 4000 rpm for 5 min to obtain the serum. Serum aspartate aminotransferase (AST), alanine aminotransferase (ALT), creatinine and blood urea nitrogen (BUN) were assayed as indicators of liver and renal functions. As to the hematology assay, whole blood was collected, and then platelets (PLT), hemoglobin (HGB), hematocrits (HCT), white blood cells (WBC) and red blood cells (RBC) were counted as to detect myelosuppression. Organs including heart, liver, spleen, lung, and kidney were collected and fixed for H&E staining by the UNC Animal Histopathology Core to evaluate the organ-specific toxicity.

4.3.20 Statistical analysis

Statistical analysis was undertaken using Prism 5.0c Software. A two-tailed t-test or a one-way analysis of variance (ANOVA) was performed when comparing two groups or more than two groups, respectively. In one-way ANOVA analysis, only statistical analysis between important comparison

groups was presented. Statistical significance was defined by a value of $p < 0.05$. Data were shown as mean ± SD.

4.4 Results

4.4.1 Identification of Fibroblasts as the Major Off-target Cell Population for LPD Uptake within a *Stroma-vessel* Tumor Model

The LPD preferentially deliver macromolecules, including siRNA, mRNA and plasmid DNA to the malignant cells for anticancer therapy *in vivo*. To prepare LPD, anionic plasmid was condensed with cationic protamine to form a slightly anionic complex core. The core was coated with the preformed cationic liposomes (DOTAP, cholesterol and DSPE-PEG). Anisamide (AA) was further conjugated onto the surface of NPs as a ligand for cells overexpressing the sigma receptor (Sigma R) (including tumor cells and TAFs). The final NPs were ~ 70 nm in diameter, with a surface charge of ~25 mV, as measured by a Zetasizer (**Table 4.1**). TEM images confirm the size of LPD and indicate its spherical shape and homogenous distribution (**Figure 4.1**). 0.5 % DiI was incorporated into the lipid membrane of LPD (DiI-labeled LPD) as an *in vivo* tracker for evaluatng the time-lapse bio-distribution of the NPs.

A stroma-vessel type desmoplastic tumor model was generated from simultaneous subcutaneous inoculation UMUC3 bladder cancer cells along with NIH3T3 fibroblasts (UMUC3/3T3) (**Figure 4.2A**). DiI-labeled LPD reached UMUC3/3T3 tumors within 10 h of intravenous injection, and plateaued over 48 h (Supplementary Fig. S1C). Consistant with other NPs of similar size, the liver and spleen were the major organs of uptake for fluorescent NPs. Flow cytometry was performed to determine LPD accumulation in various cell populations within the bulk tumor mass. NIH3T3 was pre-transfected with GFP and inoculated together with UMUC3 (UMUC3/GFP-3T3). Stably expressed GFP and fluorophore conjugated antibody against mouse CD45 defined fibroblasts and leukocytes populations, respectively. Results show that ~27% of the cells within the bulk tumor are fibroblasts (GFP positive) while ~16% are $CD45^+$ leukocytes. The majority of remaining cells, as

shown in a previous study, are tumor cells (**Figure 4.2B**) [169]. The time-lapse association of DiI-labeled LPD within different cell populations *in-situ* was then determined by flow cytometry. More than ~60% of fibroblasts took up LPD at 10 h post intravenous injection, accounting for ~65% of the total NP-associated cells (**Figure 4.2 and Figure 4.3**). Despite gradual clearance or degradation of the fluorescent NPs, ~20% of fibroblasts still remain DiI positive 72 h after NPs injection. On the contrary, only ~20% $CD45^+$ leucocytes took up DiI LPD initially. Furthermore, while tumor cells comprise 40% of cells within the total tumor mass, less than 10% of tumor cells took up NPs over the time of the observation. These analyses ultimately indicate that fibroblasts are the major off-target cell populations responsible for LPD uptake in the stroma-vessel type tumor models.

4.4.2 *In vitro* Transfection of Fibroblasts with sTRAIL in LPD Induces Apoptosis of Neighboring Tumor Cells

A bioactive secretable form of TRAIL was constructed by Hingtgen et al, through fusing coding sequences for the extracellular domain of Flt3L (a.a1-81) and an isoleucine zipper (ITZ) to promote trimerization, with the aa.114-281 of TRAIL [253, 254]. p-TRAIL encoding the human full-length TRAIL cDNA, and p-GFP encoding GFP, were constructed as controls, respectively (**Figure 4.4**). To simultaneously monitor the cellular origin of the gene expression, intracellular protein GFP was co-expressed with sTRAIL or TRAIL by fusing the internal ribosomal entry site (IRES) sequence and genes encoding GFP with the aforementioned sequences. The prepared plasmid constructs were then encapsulated into LPD through the aforementioned self-assembly process. Particles size and zeta potential remained constant in regardless of types of plasmids encapsulated (**Table 4.1**). The gene expression efficiency of LPD encapsulating TRAIL or sTRAIL plasmid was assessed *in-vitro* with NIH3T3. NIH3T3 was pre-conditioned with TGF-β to obtain a TAF-like phenotypes. Twenty-four hours after transfection, mRNA levels of the extracellular domain of TRAIL (exTRAIL, same for both TRAIL and sTRAIL) were determined using the Real-Time Quantitative Reverse Transcriptase-Polymerase Chain Reaction (qPCR). Data suggests the expression efficiency of sTRAIL LPD and TRAIL LPD are similar in activated fibroblasts. Moreover, the LPD delivered plasmids showed

slightly lower, but comparable transfection efficiency compared with those delivered with the commercial transfection agent lipofectamine®-2000 (**Figure 4.5**).

TRAIL activates the Caspase 3/8 dependent apoptosis pathway and thereby amplifies the apoptotic response in epithelial-derived cells [35]. Indeed, we found that the viability of UMUC3 transfected with TRAIL or sTRAIL, but not GFP, was drastically decreased (**Figure 4.4B**). No significant difference was observed between cells treated with TRAIL or sTRAIL, most likely due to the sufficient transfection of cells with the plasmids. Therefore, secretion was not a limiting step *in-vitro* for cytotoxicity [36]. Consistently, normal fibroblasts (e.g. murine NIH3T3, or human MRC-5) were resistant to the TRAIL, likely from the overexpression of decoy receptors or an alternate downstream pathway [251]. Secretion is a major requirement for overcoming the stroma barriers and benefiting antitumor therapy in desmoplastic tumors. To this end, the secretion of sTRAIL was evaluated. Equal amounts of sTRAIL, TRAIL, GFP were transfected into the activated NIH3T3 using LPD. Supernatant was collected 48 h post transfection and assayed using ELISA for the secreted TRAIL protein. Consistent with previous studies, abundant sTRAIL was detected in media while the concentration of full-length TRAIL was ~50 times lower in media of NIH3T3; suggesting that the leader sequence is essential for sTRAIL released (**Figure 4.4C**) [28]. Next, sTRAIL released into the culture media was assayed for biologically activity (data not shown). The growth media for UMUC3 was replaced with culture supernatants from NIH3T3 cells transfected with sTRAIL, TRAIL or GFP as a control. UMUC3 with modified culture supernatant was then incubated for another 24 h or 36 h. The culture supernatant containing sTRAIL, but not TRAIL, exerted a significant cytotoxic effects on UMUC3. The neighboring effect between fibroblasts and tumor cells were further confirmed by non-direct contact co-culture (**Figure 4.4D**). In brief, UMUC3 (bottom layer) was co-cultured with activated fibroblasts (upper layer) preloaded with different plasmids. The total cell number was significantly lower in the sTRAIL co-culture group. Further, ~13.2% early apoptosis and ~6.7% late apoptosis was observed in the sTRAIL co-culture group as compared to other treatment groups (**Figure 4.4D**). All together, these data verify the prerequisites for *in-situ* gene modification of

fibroblasts: (a) fibroblasts are resistant to both sTRAIL and TRAIL, while tumor cell are sensitive to them; (b) sTRAIL can be efficiently released within the supernatant allowing (c) the neighboring effect to occur instantly.

4.4.3 Secreted TRAIL Induces Superior Antitumor Efficacy in the Stroma-vessel Desmoplastic Bladder Cancer Model

The efficacy of systemically delivering sTRAIL was then evaluated on the UMUC3/3T3 tumor model. Treatment began when tumor sizes reached 500 mm^3, allowing the stroma-vessel structure to be well-formed. Equal amounts of plasmids in LPD NPs were intravenously injected into mice Q.O.D for a total of four injections. As shown in **Figure 4.6A**, the mean tumor growth in mice treated with sTRAIL LPD was significantly inhibited compared to the GFP-LPD treated group. It is reasonable to assume that GFP-LPD exhibited a slight antitumor effect, likely from the non-specific induction of inflammatory cytokines from the cargos and DNA backbones [255]. To demonstrate the neighboring effect induced from sTRAIL, the full-length TRAIL LPD, representing a form of TRAIL which could not be highly secreted, was administrated as a control. As expected, full length TRAIL showed minimal antitumor efficacy compared to sTRAIL. qPCR analysis of the mRNA expression using primers positioned simultaneously at the extracellular domain (exTRAIL) for both TRAIL and sTRAIL suggest comparable expression of sTRAIL and TRAIL in tumors treated with four doses LPD treatment (**Figure 4.6C**). This, in conjunction with the *in vitro* transfection data (**Figure 4.5**), indicates a similar transfection efficiency between these two plasmids and dismisses the possibility that a difference in expression levels between sTRAIL and TRAIL affect the antitumor effect. Notably, both TRAIL and sTRAIL LPD induced >7 times greater expression of exTRAIL compared to the PBS treated group with a baseline level of endogenous TRAIL. Additionally, the expression of mRNA persisted at least four days after the endpoint dose, suggesting relatively long gene expression profiles. qPCR assay using primers specific for sTRAIL confirms the expression of sTRAIL plasmid. With a lower baseline level compared to exTRAIL mRNA, the relative sTRAIL production was ~200 times higher relative to the control. Results indicate the potency of gene transfection and suggest a

promising therapeutic outcome (**Figure 4.6D**). There was no significant decrease in body weight observed in any of the four treatment groups (**Figure 4.6B**), indicating that none of the plasmids caused toxicity. The results verified the hypothesis that sTRAIL secreted *in situ* indeed exhibited superior antitumor efficacy in a stroma-vessel desmoplastic tumor model.

4.4.4 The sTRAIL LPD were Delivered to and Expressed in Fibroblasts *in situ*

To elucidate whether the superior efficacy of sTRAIL resulted from *in situ* engineering of fibroblasts, the loco-regional expression of sTRAIL was assessed in the cell populations within the tumor mass. Since the intracellular protein GFP was fused with sTRAIL through an IRES sequence, the cells that expressed GFP represented cells that secrete sTRAIL. Moreover, to visualize the fibroblasts, RFP-3T3 was inoculated with UMUC3 using a similar method described above. Notably, the xenograft developed from UMUC3 cell lines alone had minimal to no endogenous fibroblasts. Therefore, the RFP-fibroblasts constitute the majority of fibroblast populations in the UMUC3/3T3 model. As shown in **Figure 4.7A-D**, clear indications of fibroblast components (RFP) were present, sparing the GFP auto-fluorescence in the untreated group. Mice that were treated with a single dose of sTRAIL LPD exhibited a moderate GFP expression, exclusively localized within the RFP-fibroblasts. The expression of GFP was enhanced following the second injection of NPs, but still overlapped with RFP-fibroblasts. The strongest GFP expression was elicited after four doses of NPs. The expression of GFP was quantitatively confirmed using flow cytometric analysis (**Figure 4.7E**). Consistent with the fluorescent images, overall expression of GFP increased in a dose dependant manner, but the majority of expression was limited to RFP-fibroblasts. This data confirmed that fibroblasts are the major reservoir for *in-situ* generation of LPD delivered proteins. This was most likely due to off-target distribution of NPs and relatively high and stable expression of genes in fibroblasts compared to other off-target cell populations, mainly leucocytes (macrophages). Notably, the expression of GFP in other cells were observed two days after endpoint dose (**Figure 4.7D and E**), suggesting that a portion of NPs have overcome the fibroblast elicited barriers and entered into the tumor nest.

However, the expression of GFP in this group of cells decreased dramatically four days after the endpoint injection while the expression in fibroblasts remained constant. There are two hypothesized mechanisms related with the observations: (a) the tumor cells (within the other cell populations) may internalize the NPs but undergo apoptosis immediately or (b) the infiltrating leukocytes take up the NPs, but cells circulate afterwards. Either cell population demonstrated transient expression of the genes compared with local TRAIL resistant fibroblasts, confirming fibroblasts as the most suitable candidate for an engineered reservoir. The expression level of sTRAIL mRNA was further assayed in the RFP-fibroblasts sorted from tumors with three doses sTRAIL or GFP LPD treatments (**Figure 4.7F**). As expected, only the fibroblasts treated with sTRAIL LPD elicited the synthesis of sTRAIL mRNA, ~60 times higher than other cells in the same tumor or in GFP LPD treated cells within other tumors. Again, this confirms fibroblasts as the major and most suitable *in-situ* engineering reservoir for sTRAIL protein.

4.4.5 Neighboring Effect Unveiled the Apoptotic Effect of TRAIL in the *Stroma-vessel* Desmoplastic Bladder Cancers

In support of our hypothesis that the *in-situ* engineering of fibroblasts with sTRAIL bypassed the stroma barriers and induced the efficient death of neighboring tumor cells. The distribution of apoptotic cells was then examined using terminal deoxynecluotidyl transferase dUTP nick end labeling (TUNEL) assay. TAFs were simultaneously visualized by staining with α-SMA. **Figure 4.8A** show that the apoptotic area grows in area around α-SMA positive TAFs as the doses increases. Tumor sections from several areas in different tumors after each dose (in total 3 doses) were then analyzed to quantify the average distances between apoptotic cells and the nearest α-SMA positive TAFs. Only 3 doses were recorded since most of the sTRAIL were synthesized by fibroblasts within the 3 doses. After single injection, nearly all apoptotic cells were within just 50 μm of the nearest α-SMA positive TAF. The distribution radius of apoptotic cells increases with dose and over time (**Figure 4.8B**). The data therefore substantiates the claim that a neighboring effect of fibroblasts is

indeed present in fibroblasts *in situ*, facilitated by diffusion, and amplified with escalated dosing schedules. The apoptotic assay was also performed in other treatment groups two days after the endpoint treatments (**Figure 4.8C**). As expected, minimal apoptosis was observed in the PBS and GFP LPD group, whereas a small amount of TUNEL-positive nuclei were observed in groups treated with TRAIL LPD. We hypothesized that the proteolytically cleaved extracellular domain of the full-length TRAIL induced apoptosis of neighboring tumor cells, or a paucity of NPs diffused through TAFs layer, inducing the synthesis of TRAIL and apoptosis in neighboring tumor cells, thus explaining the limited apoptotic cells observed in the TRAIL LPD NPs in vicinity of TAFs. In comparison, an extensive amount of apoptotic cells was observed in the sTRAIL LPD group. In addition, the residual fibroblasts (especially TAFs) were clustered, sparing the tumor nest structure. Potent, well-dispersed apoptosis along with this disordered and clustered fibroblast structure suggested a tumor microenvironment less structurally and functionally capable of growth and progression. Therefore, the superior antitumor activity of sTRAIL LPD compared to other treatment groups was verified.

4.4.6 Apoptosis of Neighboring Tumor Cells Induced by sTRAIL LPD Causes Reprogramming of Residual Fibroblasts, Facilitating the Delivery of Second-wave Therapeutic NPs

The function of residual fibroblasts was then examined. The level of collagen, a major extracellular matrix (ECM) protein, was assessed after multiple sTRAIL treatments in mice bearing UMUC3/RFP-3T3 [69]. Unexpectedly, the collagen content decreased ~3-fold compared to other treatment groups (**Figure 4.9**). Reductions were also observed on other proteins unique to fibroblast activation which are of functional significance in the TME, including fibronectin and hepatocyte growth factor (HGF) (**Figure 4.10A**) [117, 169, 201]. In addition, the activation marker of fibroblasts within the bulk tumor mass, including αSMA and fibroblasts activation protein alpha (FAPα) decreased by ~ 90% and ~84% (compared to total RFP-fibroblasts), respectively (**Figure 4.10B**) [117, 169, 256]. These data suggest that residual TAFs are shifting from an activated toward a quiescent

state. However, the proteins described above are not exclusively secreted by fibroblasts. For example, expressions of FAPα and fibronectin have been found in tumor cells [257, 258]. To further confirm the state shift of fibroblasts within the TME, we sorted the RFP fibroblasts from the dissociated cells collected from the tumor mass after 3 doses of sTRAIL LPD. Indeed, we found the mRNA level of collagen and ACTA2 (α SMA) in sTRAIL treated fibroblasts decreased 2 to 5 fold compared to untreated fibroblasts (**Figure 4.10C**). Meanwhile tumors treated with full length TRAIL or GFP-LPD failed to affect desmoplasia, which eliminates any possibility of TRAIL directly inducing fibroblast reprogramming (**Figure 4.9** and **Figure 4.10**). Since it is commonly accepted that the majority of TAFs are transdifferentiated from resident fibroblasts in response to TGF-β [259], the downstream portions of TGF-β signaling, including pSMAD2 and plasminogen activator inhibitor type 1 (PAI-1) was examined [256, 259, 260]. Indeed, data revealed a decreased level of pSmad2 nuclei staining and an inhibition of the transcriptional activation of PAI-1 in fibroblasts of sTRAIL treated tumors (**Figure 4.10C** and **Figure 4.11**). Again this supports the reprograming of TAFs.

It is conceivable that reprogrammed TAFs re-establish a physiological and metabolic environment adverse to tumor growth. The restoration of normal stroma also released the interstitial fluid pressure (IFP) and opened up the compressed intratumoral vasculature (**Figure 4.12**). Therefore, it was questioned whether the remodeled TME would be more sensitive to second-wave nanocarriers: which describes an additional course of chemotherapy following microenvironment modulation. A lipid coated cisplatin nanoparticle (LPC NPs, ~30 nm) was previously developed in our lab and used for the tumor accumulation study herein. Detailed characterizations of the NPs were described by Guo et al [177]. A single dose of cisplatin NP (1.9 mg/kg of cisplatin) was intravenously injected into mice bearing UMUC3/3T3 xenografts. Twenty-four hours post injection, tumor tissues were collected and the level of platinum was quantified using inductively coupled plasma mass spectrometry (ICP-MS). As shown in **Figure 4.13B**, pre-treatment of the tumors with sTRAIL LPD leads to a ~2 -fold increase of cisplatin retention. To demonstrate the possible therapeutic benefits of the two-wave therapBy, mice were first pretreated with 3 doses of sTRAIL LPD as shown in **Figure 4.13**. Results

herein suggest that the two-wave therapy significantly inhibits and delays the tumor growth more than single modality therapy. In conclusion, the data suggest residual fibroblasts and TME after sTRAIL treatment are remodeled, benefiting not only the sTRAIL-mediated antitumor efficacy, but also the delivery of a second-wave chemotherapy.

4.4.7 *In situ* Engineering of Pancreatic Stellate Cells with sTRAIL LPD Shows Promising Antitumor Efficacy in an Orthotopic Desmoplastic Pancreatic Cancer BXPC3

To evaluate if the above-mentioned findings could be recapitulated in more clinically relevant desmoplastic tumors, the anti-tumor efficacy of sTRAIL LPD was assessed on mice bearing human pancreatic adenocarcinoma BXPC3. This study, along with others, has shown that BXPC3 are stroma-vessel type desmoplastic tumors characterized with nests of tumor cells surrounded by vessel-embedded fibrotic tissues (**Figure 4.14**) [52, 68, 92]. The cultured BXPC3 had greater sensitivity to TRAIL compared to other pancreatic cancer cell lines [261]. To visualize tumor growth *in vivo*, BXPC-3 cells were stably transfected with luciferase vector (BXPC3-Luc2). BXPC3-Luc2 was orthotopically injected into the tail of the pancreas. Dosing schedule of sTRAIL LPD is presented in **Figure 4.15A**. Consistent with the aforementioned UMUC3/3T3 study, PBS, GFP LPD and TRAIL LPD were set as controls. Bioluminescence images were obtained twice a week. Tumor volume correlated from the number of photons emitted from the tumor were assessed (**Figure 4.15B**) and quantified (**Figure 4.15C**). Results demonstrate that sTRAIL LPD, but not other treatment groups effectively inhibit tumor growth. To verify that the hypothesis regarding in-situ engineering of fibroblasts occurred in BXPC3 model, the expression of GFP (the IRES-GFP from sTRAIL and TRAIL LPD or GFP from GFP LPD) in fibroblasts and other cells was examined. Indeed, more than ~25% of fibroblasts expressed GFP, accounting for 40% of the total GFP expressing cells within tumor mass (**Figure 4.15D**). In addition, only 8% within the $CD45^+$ leucocytes population expressed GFP (**Figure 4.16**). This, again, supports the claim that fibroblasts are the primary engineered *in-situ* population for sTRAIL secretion. To verify fibroblasts induced neighboring effect and the remodeling of TME, the post-treatment apoptosis and collagen level was shown in Error! Reference source not

found.**A** and **B**. Consistently, an increased amount of TUNEL positive cells was localized in vicinity of fibroblasts and the overall level of collagen decreased. Once again, the results above clearly demonstrate that *in-situ* engineering of fibroblasts benefits anti-cancer therapy in stroma-vessel desmoplastic tumors.

4.4.8 Toxicity Evaluation for the Different Treatments and Blood Chemistry Analysis

The results of the toxicological evaluation demonstrates little to no noticeable morphological changes in major distribution organs of LPD, e.g. liver and spleen for all of the treatment groups (**Figure 4.18A**). The serum biochemical value analysis demonstrated that the sTRAIL treatment group had no liver (aspartate aminotransferase and alanine aminotransferase) or kidney (creatinine and blood urea nitrogen) toxicity caused by tumor progression (**Table 4.2**). Hematology performed on the blood samples shows no significant reduction of cell in sTRAIL treated mice compared to the control groups, suggesting the treatment did not cause anemia (**Figure 4.18B**).

4.5 Discussion and Conclusion

Despite recent advances in nano-therapeutics, efficacy against desmoplastic tumors including pancreatic cancer and advanced urothelial carcinoma, has not changed in decades [117]. In part, the dense stromal barrier captures NPs, preventing them from reaching the tumor [74, 239]. Given the large amount of NPs delivered to fibroblasts, it makes sense to utilize this natural feat and target cancer treatment through fibroblasts. Inspired by fibroblast's ability to secrete tumor supportive cytokines to neighboring tumor cells [262, 263], modification of fibroblasts to secrete tumor suppressive cytokines through gene delivery with NPs was proposed in the current manuscript. The *in situ* engineering of fibroblasts harnesses the location of fibroblasts between blood vessels and tumor cells, bypassing major cellular barriers for NPs delivery; subsequently converting fibroblasts from a tumor supporting role to a tumor depletion center.

The choice of a secretable tumor suppressive factor should not be understated. TRAIL is a highly selective, tumor apoptosis-inducing cytokine. The resistance of mesenchymal stroma cells, especially fibroblasts to TRAIL was a conceivable mechanism for the clinical failure of TRAIL [251]. However, this feature demonstrates fibroblasts as a durable synthesis reservoir for TRAIL, with prolonged expression compared to other TRAIL-sensitive cells. In reality, TRAIL-secreting human mesenchymal stem cells have demonstrated prolonged delivery of TRAIL in glioma therapy [264]. In order to achieve the original hypothesis, TRAIL was fused with a leader sequence into a bioactive secretable form (sTRAIL). Despite the comparable cytotoxicity observed *in vitro* with both sTRAIL and TRAIL plasmid, only sTRAIL encapsulated in LPD induced superior antitumor efficacy in desmoplastic tumors. Consistent with *the in situ fibroblast engineering* hypothesis, we found the majority of sTRAIL was expressed within fibroblasts within 3 doses of sTRAIL LPD. The penetration of sTRAIL protein is another concern for the *in situ* engineering of fibroblasts. Compared to most monoclonal antibodies, the trimerized sTRAIL with a smaller molecular weight offered rapid diffusion. The current work illustrated that apoptotic tumor cells induced by sTRAIL LPD can be observed 500 μm away from the nearest fibroblast **(Figure 4.8B**). Compared to the average diameter (400 μm) of tumor nests in the UMUC3/3T3 model, the depth of penetration was undoubtedly sufficient to induce potent efficacy.

The apoptosis of tumor cells destroyed the nest structure within tumors; keeping fibroblasts as the major population of remaining cells. A quiescent characteristic marked by a reduction in ECM protein synthesis and decreased TAFs marker expression in the residual fibroblasts was found only after sTRAIL treatment. Down regulation of pSMAD2 in fibroblasts suggested this process may be mediated by TGF-β [259, 265]. Though further mechanistic studies should be conducted, the original hypothesis stated the apoptosis of neighboring tumor cells reciprocally contribute to reprogramming of TAFs due to insufficient TGF-β signaling activation. Support for this can be found in that pSMAD was also downregulated in apoptotic tumor cells, which was mediated through autocrine signaling of TGF-β. Additionally, the phenotype of fibroblasts in TRAIL treatment group remained constant,

demonstrating TRAIL had minimal direct effect on fibroblasts. Reverting of TAFs has a dual benefit. Firstly, the cellular and structural changes of the stroma resulted from "normalized" fibroblasts are reported to exert tumor-suppressive forces and signals, potentially inhibiting tumor growth [117, 266]. The second benefit is the reduction of the fibrotic content, which decompresses the intratumoral vasculature, creating a window for a second-wave nanotherapy [6, 117]. Such expectations were presented both in theory and in the current study. Treatment with sTRAIL LPD significantly enhanced the delivery, retention and efficacy of additional cisplatin NPs.

Moreover, the potency of sTRAIL LPD monotherapy, observed on a hypovascular orthotopic pancreatic carcinoma (BXPC3) further, verified the feasibility of this *in situ* engineering approach. The result is promising as only a small population of therapeutic NPs have shown efficacy against desmoplastic pancreatic cancer.

Collectively, a novel regimen for the treatment of desmoplastic tumors was developed by taking advantage of the NPs' natural intratumoral off-target distribution (**Figure 4.19**). Three advantages highlight the sophistication of this approach: (1) the traditionally problematic binding site barrier was used to induce potent apoptosis within the tumor nest with only a single conventional gene therapy agent. (2) The fibroblasts *in situ* were not only engineered to secrete a cytotoxic protein, but mechanistically reprogrammed to be tumor suppressive in a feedback fashion. (3) Lastly, reprogramming of fibroblasts paved the way for coupling signal-dependent stromal reprogramming with tumor-directed cytotoxic NPs and perhaps immunologic drugs, offering a new paradigm in the treatment of desmoplastic tumors. Furthermore, fibroblasts could be engineered to produce various cytokines, orchestrating the overall suppressive tumor microenvironment to achieve a more sustained antitumor response.

Table 4.1 Characterization of LPD NPs

Sample	Size (nm)	PDI	Zeta Potential (mV)
Luciferase LPD	74.6±3.1	0.23±0.02	25.1±3.2
GFP LPD	78.6±2.5	0.25±0.04	24.9±4.8
TRAIL LPD	76.8±1.2	0.22±0.01	25.7±5.6
sTRAIL LPD	76.9±2.3	0.28±0.03	27.3±3.8

Table 4.2 Blood chemistry after treatments

Samples	AST U/L	ALT U/L	BUN mg/dL	Creatinine
PBS	239±45	43.5±7.5	16.7±2.5	0.1
GFP LPD	239±32	40.5±4.5	22.0±4.2	0.1
TRAIL LPD	206±25	50.0±8.4	16.8±3.2	0.1
sTRAIL LPD	214±32	51.3±10.4	16.2±4.6	0.1
Range	54~298	17-132	12-33	0.1~0.9

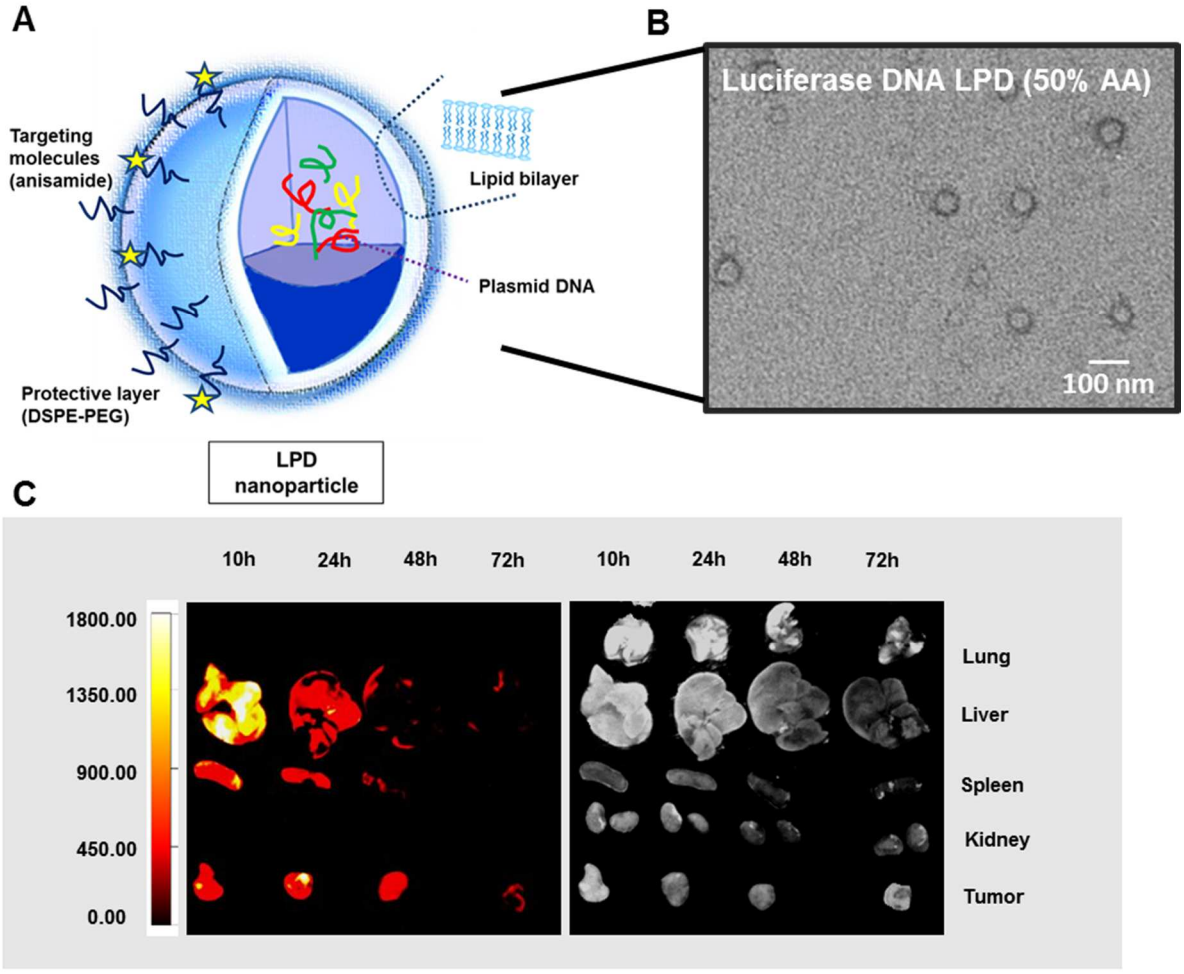

Figure 4.1 Characterization of LPD.

A. Scheme of the structure of LPD. B. Representative TEM image of LPD. C. Fluorescent imaging of the biodistribution of DiI-labeled LPD at determined time points.

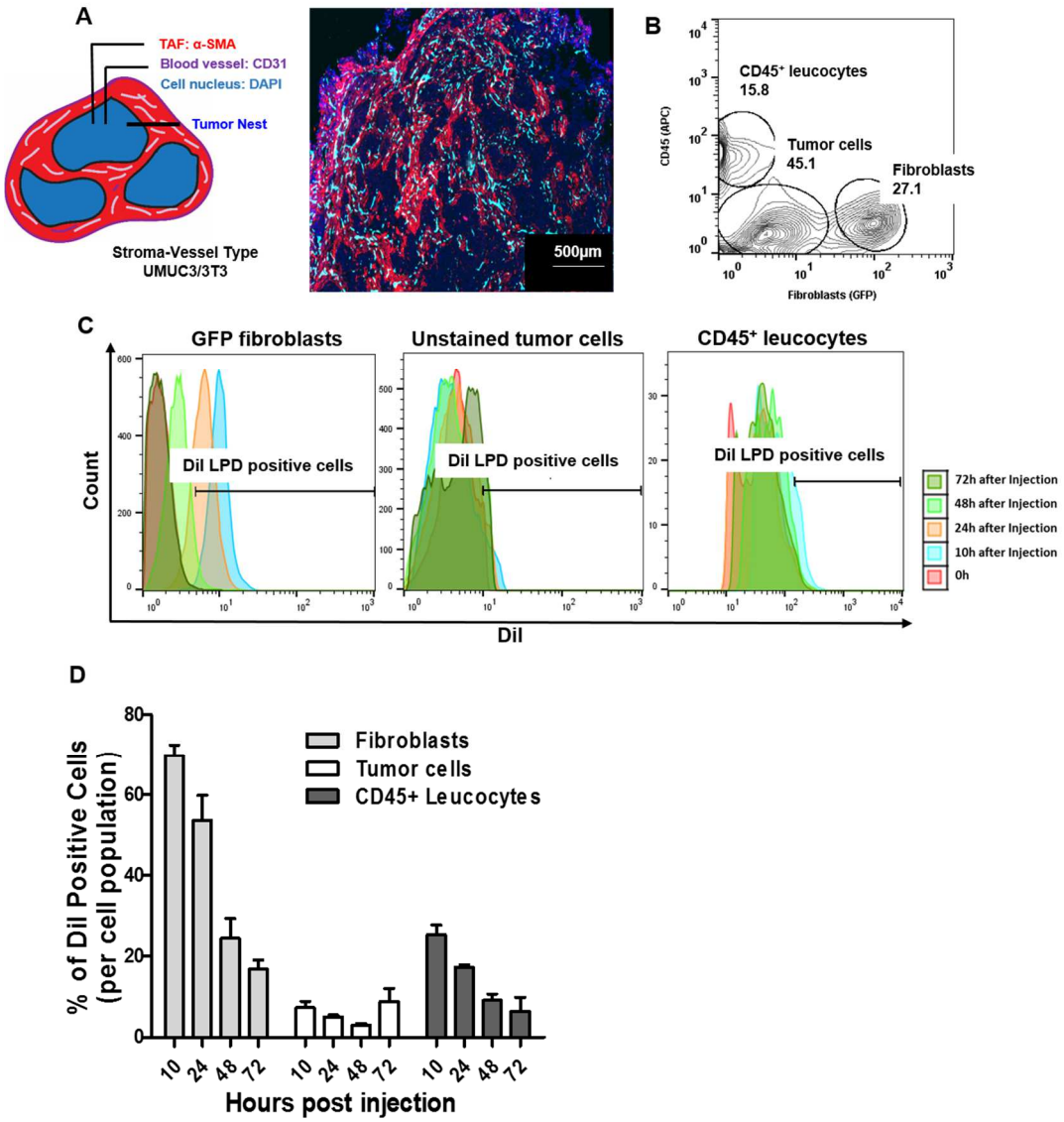

Figure 4.2 Cell populations that take up LPD in the stroma-vessel type tumors.

A. The schematic architecture of stroma-vessel tumors. The immunofluorescence (IF) staining (on the right) shows the histology of a *stroma-vessel* tumor model: UMUC3/3T3. Examination reveals nests of tumor cells, with areas rich in fibrotic components (filled by αSMA positive TAFs, shown in red) between them. CD31 positive blood vessels (shown in cyan) are embedded in the interstitium near the fibroblasts, almost no vessels are observed inside the nests of tumor cells. B. Flow cytometry gating of the cell populations in the UMUC3/GFP-3T3 tumors. ~16% of dissociated cells are $CD45^+$ leucocytes, while ~27% are GFP fibroblasts (NIH3T3 was pre-transfected with the GFP gene). Other cells are mainly tumor cells. C. Flow cytometry histograms of the percentage of cells that took up DiI-labeled LPD in each cell population in the UMUC3/GFP-3T3 tumor models. Mice bearing UMUC3/GFP-3T3 tumors were intravenously injected with DiI-labeled LPD. At determined time points, tumors were dissociated and analyzed by flow cytometry. D. Quantitation of the percentage of DiI positive cells in each population (based on the flow data), n = 4.

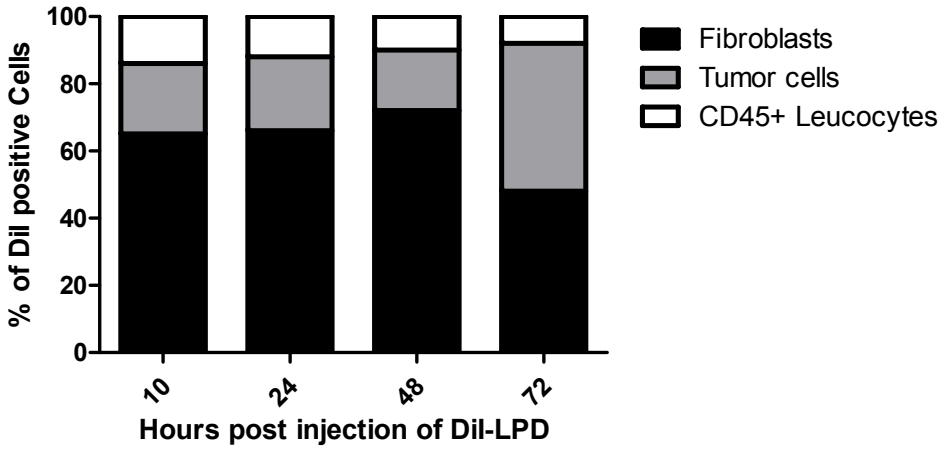

Figure 4.3 Calculation of DiI positive cells in each cell population by flow cytometry (n = 4). Only mean values are presented at each time points.

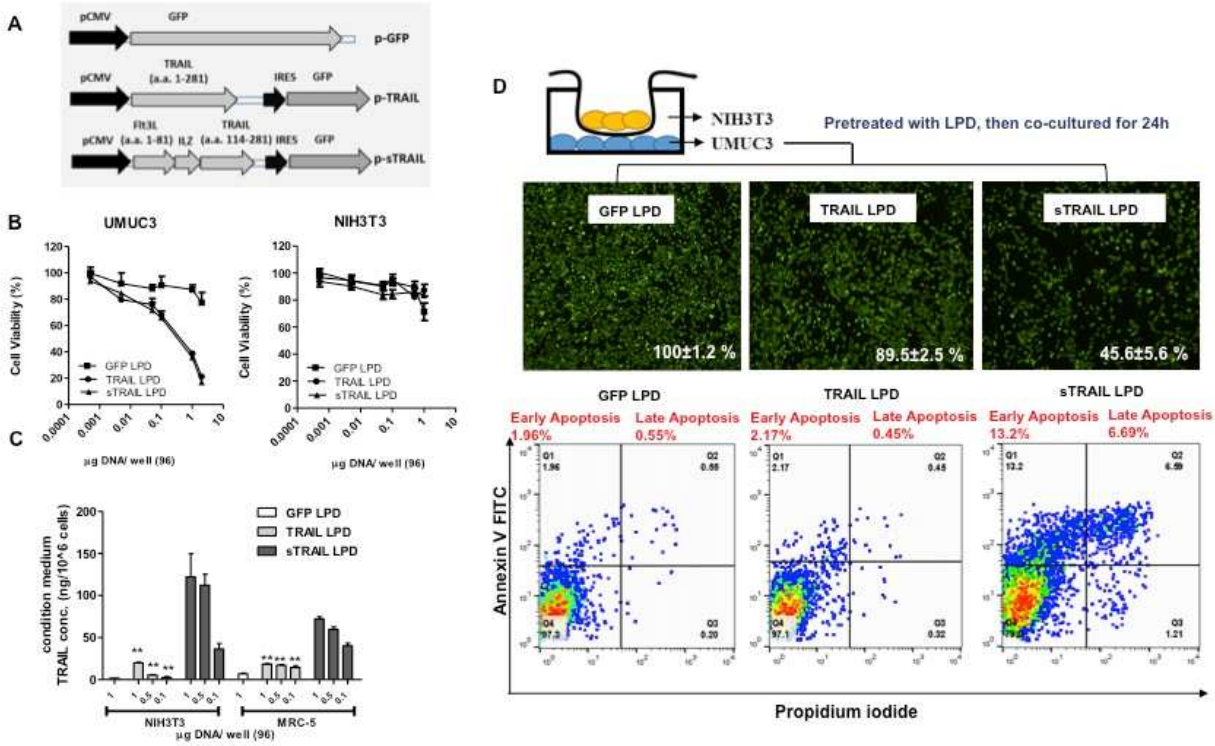

Figure 4.4 Secretable TRAIL produced by fibroblasts induces apoptosis of neighboring UMUC3 tumor cells.

A. schematic representation of plasmid encoding green fluorescence protein (GFP) fused with sTRAIL or TRAIL (as a less secretable control). B. Cell proliferation of cancer cells, UMUC3 and fibroblasts, NIH3T3 transfected with TRAIL, sTRAIL, GFP at different concentrations (MTT assay, n = 4). UMUC3 cells are sensitive to both TRAIL and sTRAIL treatment, while NIH3T3 are resistant. C. The releasing of sTRAIL protein into the supernatant were determined using ELISA (against TRAIL). Both NIH3T3 and MRC-5 (lung fibroblasts) transfected with sTRAIL secreted TRAIL protein. However, minimal soluble TRAIL was detected in both cell line when transfecting with TRAIL (n = 3, ** $P < 0.01$, compared to sTRAIL LPD treatment). D. The neighboring effect of the sTRAIL protein was determined by a non-contact co-culture study. After co-cultured for 24 h, the total number of UMUC3 cells in the bottom were counted. Cells were visualized by Calcein AM staining (shown in green). Apoptosis of bottom UMUC3 cells were assessed using annexin V/PI staining and flow cytometry (n = 3).

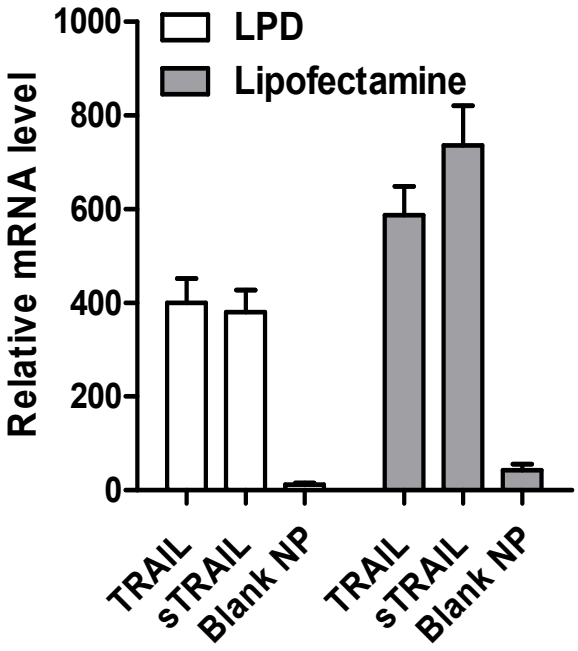

Figure 4.5 *In vitro* transfection efficiency of LPD.

sTRAIL or TRAIL plasmid was encapsulated into LPDs respectively. Transfection efficiency was determined by qPCR analysis of the mRNA level of TRAIL 24 h after transfection. Lipofectamine®-2000 was used as a positive control, and GFP NP was set as a negative control. LPD induced comparable expression of protein compared to lipofectamine®-2000. The expression efficiency for TRAIL is similar to that of sTRAIL (n=3).

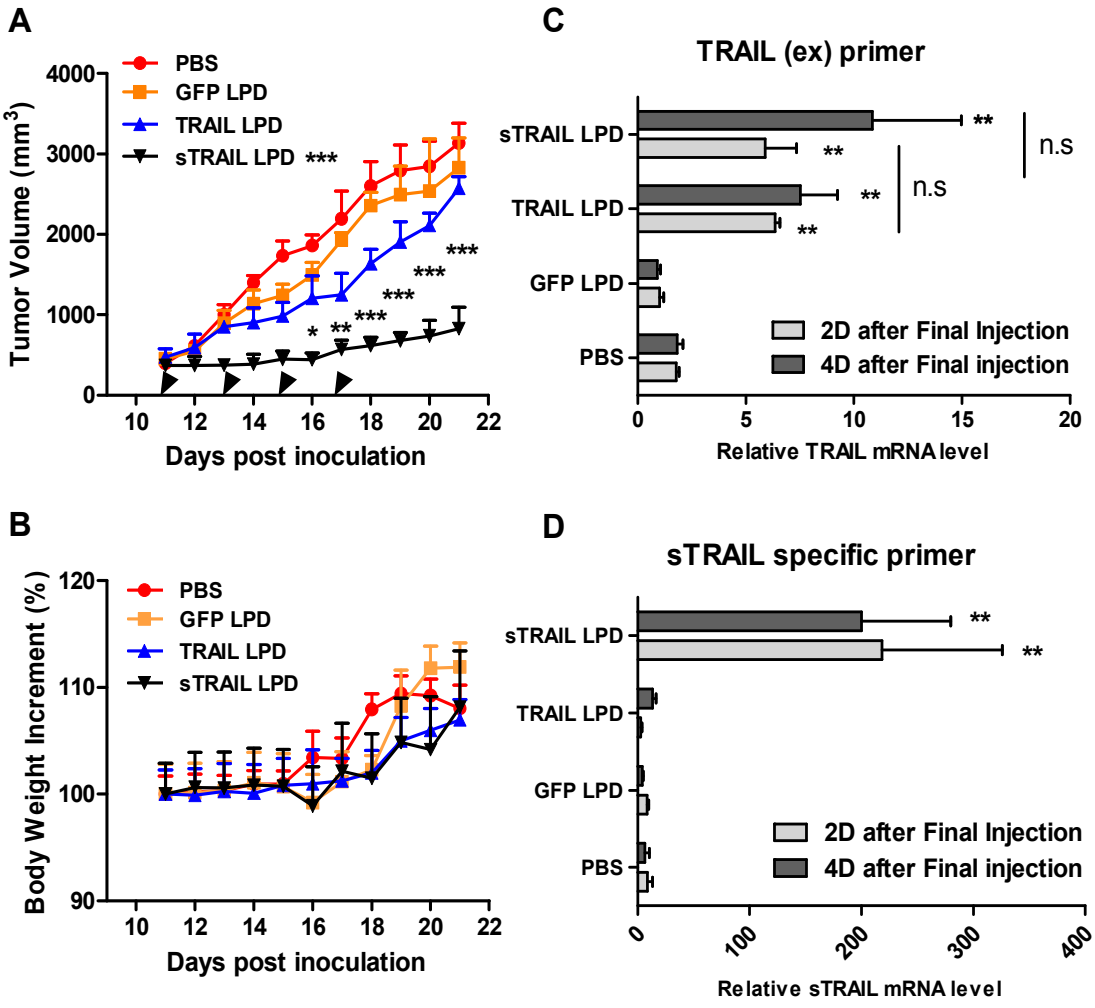

Figure 4.6 Intravenous administration of sTRAIL LPD inhibited *stroma-vessel* UMUC3/3T3 tumor growth.

A, B tumor inhibition curve and body weight changes, respectively, of mice bearing stroma rich bladder cancer (UMUC3/3T3). Mice were treated with PBS, GFP LPD, TRAIL LPD or sTRAIL LPD at a plasmid concentration of 50 μg/mice, for 4 times (n = 6~8, * $P < 0.05$, ** $P < 0.01$, *** $P < 0.001$, in the legend, compared to PBS group; in the data, compared to each time point of the TRAIL LPD group). C, D. qPCR quantitation of relative mRNA levels of TRAIL or sTRAIL in the treated tumors. The primers for the extracellular domain of TRAIL (C) or primers specifically for sTRAIL were used for the detection (n = 6, ** $P < 0.01$, n.s, no significant difference, compared to PBS group).

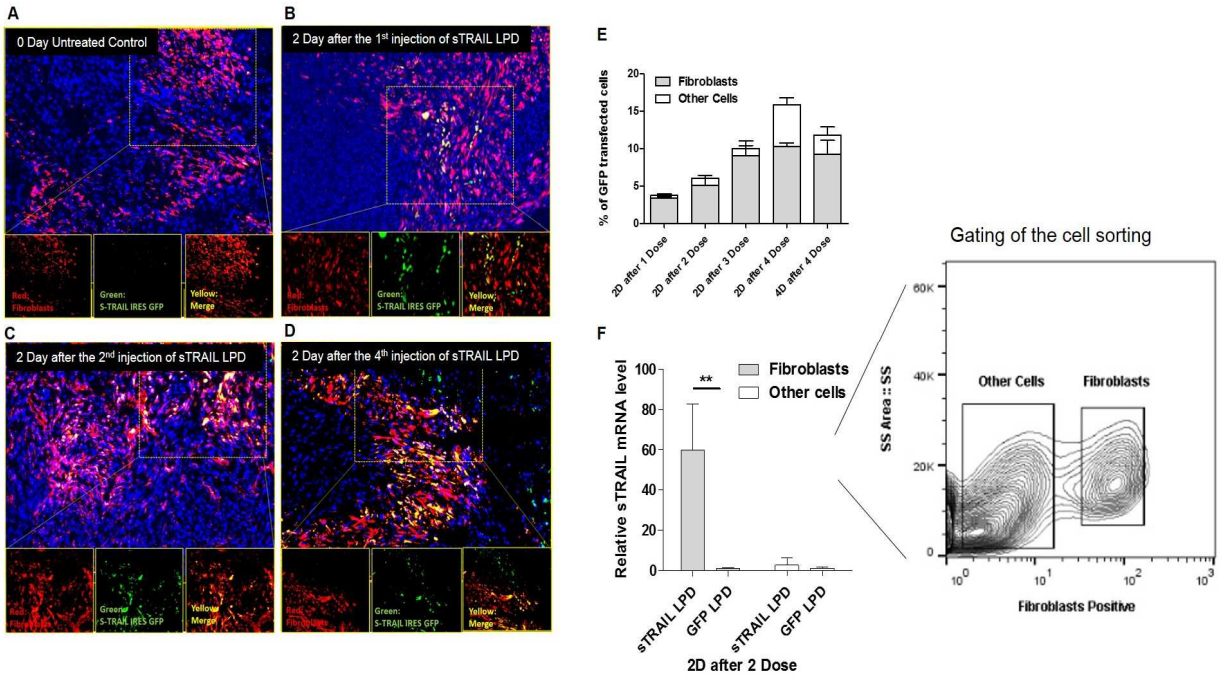

Figure 4.7 Expression of TRAIL (or fusion GFP) in the fibroblasts *in situ*.

A-D, IF staining of green fluorescence protein (GFP) (shown green), RFP-fibroblasts (shown red) and cell nuclei (DAPI, shown blue) at indicated time points after treatment on cryo-tumor tissues collected. Results showed that the majority of expression of GFP fusion protein co-localized with the RFP-labeled fibroblasts. E. Flow cytometry analysis of GFP's association with RFP-fibroblasts at indicated time points in the dissociated cells from the collected tumor tissues (n = 4). The association of GFP in fibroblasts increased dose-dependently. F. One day after 3 doses of sTRAIL LPD, the RFP-labeled fibroblasts were sorted by flow cytometry. sTRAIL mRNA level in the RPF-labeled fibroblasts and other unlabeled cells were analyzed and compared with the untreated group (n = 4, ** $P < 0.01$). The inserted chart indicates gating of the RFP fibroblasts.

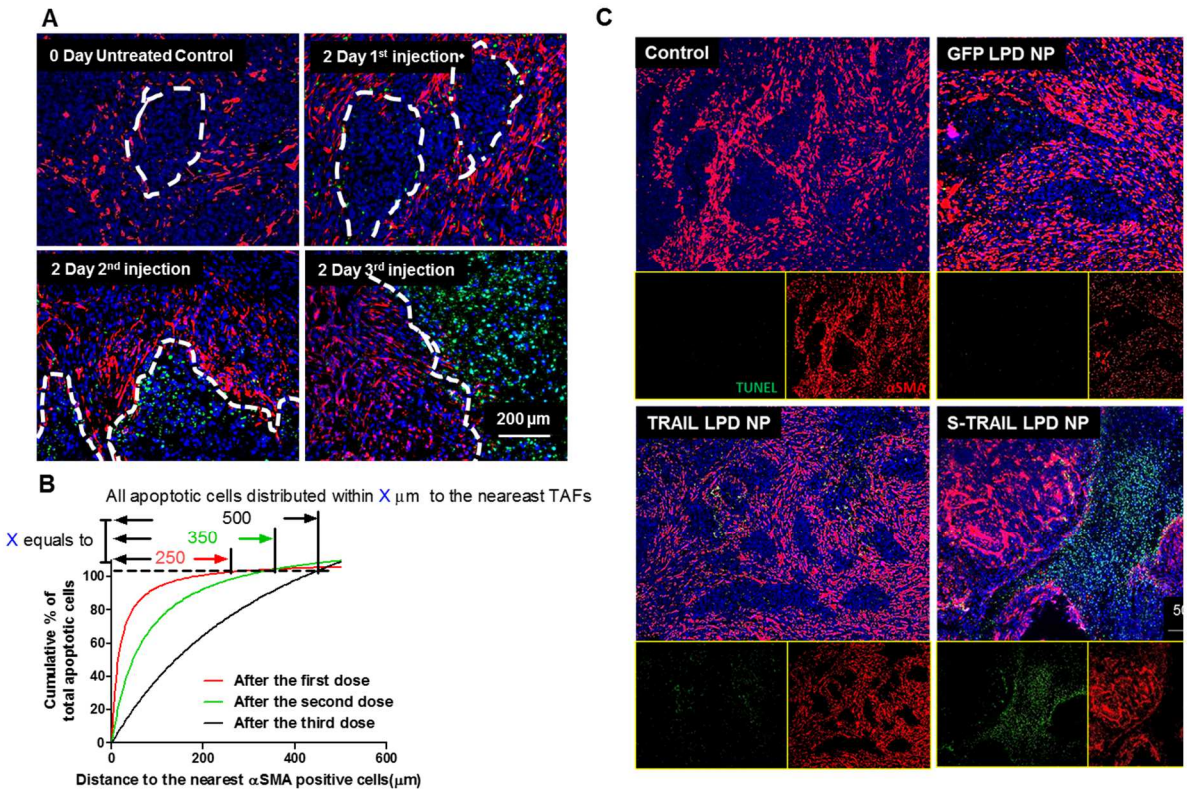

Figure 4.8 Fibroblasts (*in situ*) that secreted TRAIL induced the apoptosis of neighboring tumor cells.

A. IF staining of αSMA and TUNEL from tumor tissues (paraffin-embedded sections) after dose escalation of sTRAIL LPD NPs. Dashed lines indicate edge of the tumor nests. B. Quantification of relative apoptotic cells' distance from the nearest αSMA positive fibroblasts after different doses of sTRAIL LPD NPs. Numbers on top indicate the furthest distance of apoptotic cells to αSMA after different treatments. C. Paraffin-embedded tissues sections from UMUC3/3T3 tumors 2 days after final treatments were stained for αSMA (red, myofibroblasts) and TUNEL (green, apoptosis).

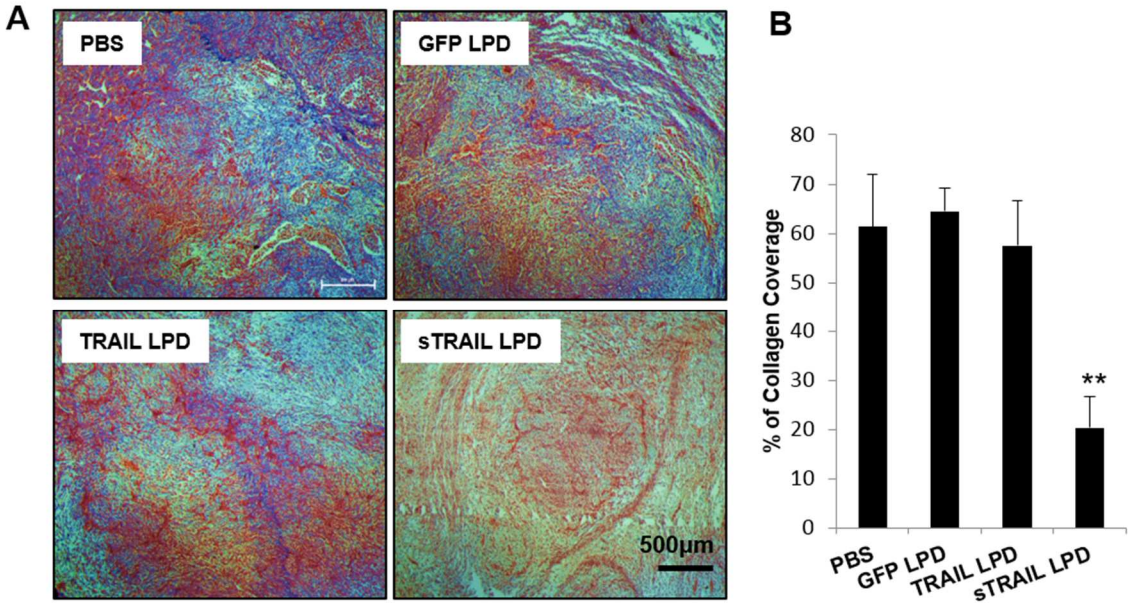

Figure 4.9 sTRAIL LPD decreases the collagen content

A. Masson's trichrome staining of the collagen after endpoint treatments. B. Quantification of the trichrome staining (n = 5, ** $P < 0.01$, compared to PBS group).

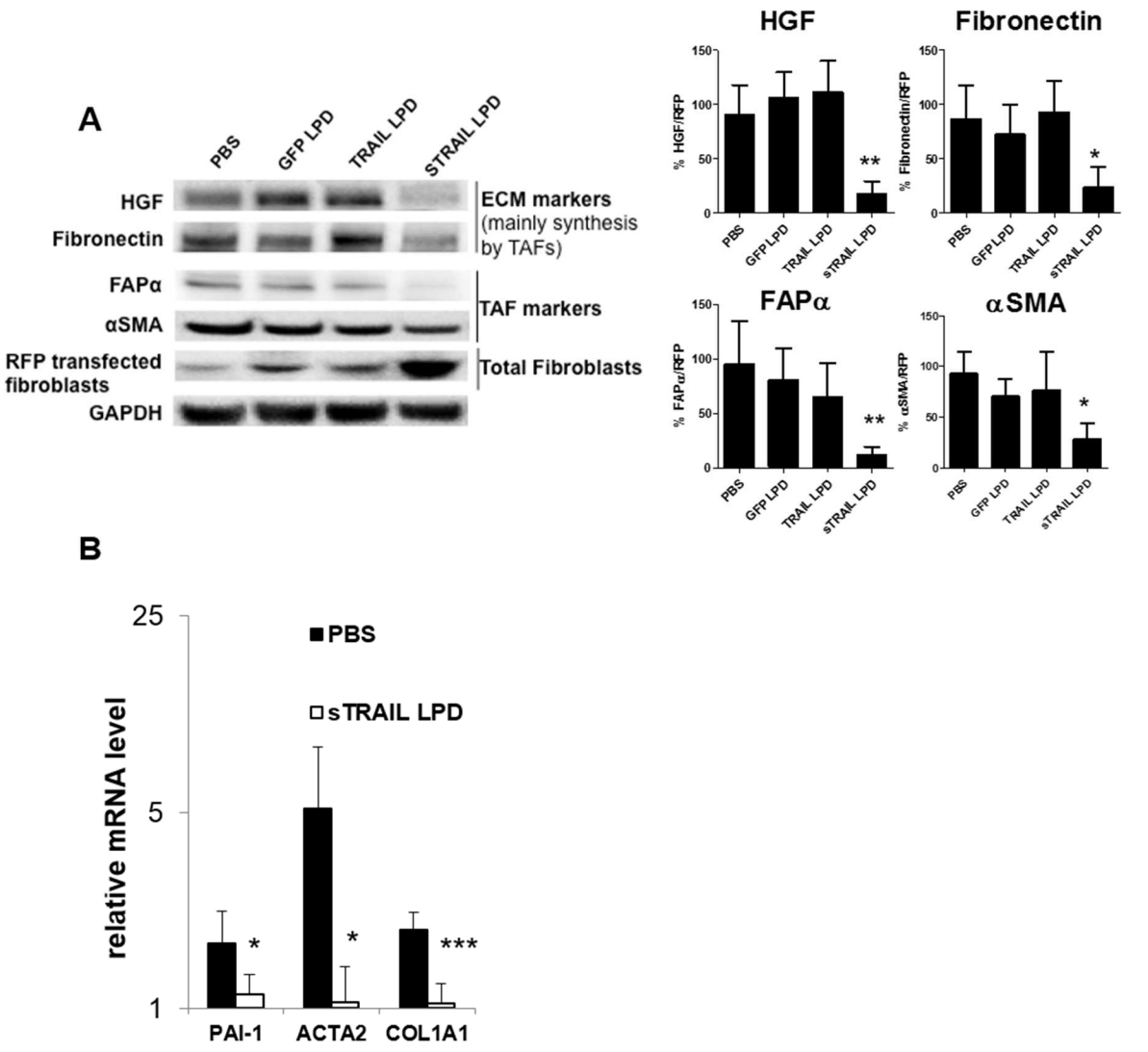

Figure 4.10 sTRAIL LPD induces the reprogramming of residual fibroblasts and remodeling of TME.

A. Western blot analysis of the TME markers mainly secreted by TAFs, and TAF markers. Intensities of each ECM protein were calculated by comparing to the RFP-transfected fibroblasts and shown on right. Protein/RFP ratios in the PBS group were set as 1 (n = 3, * $P < 0.05$, ** $P < 0.01$, compared to the PBS group). B. mRNA levels of TAF markers in the sorted RFP-fibroblasts after sTRAIL treatment (n = 5, * $P < 0.05$, *** $P < 0.01$, compared to the PBS group).

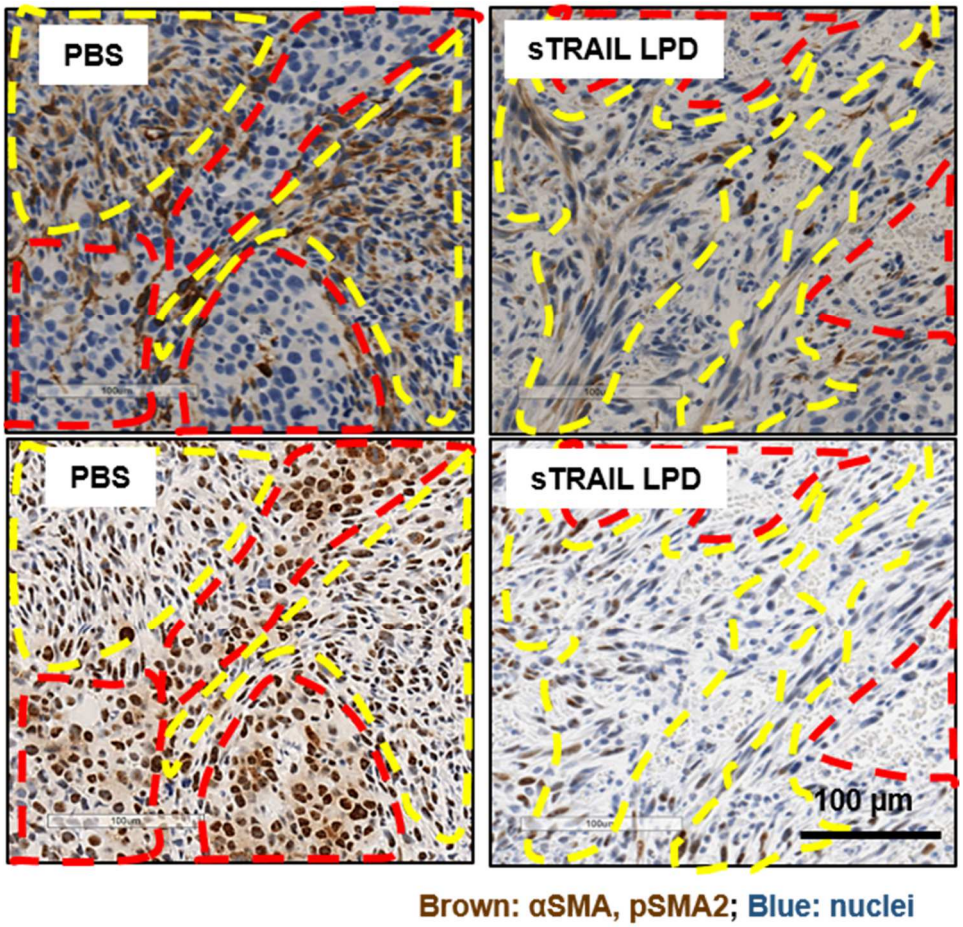

Figure 4.11 TGF-β pathway was downregulated after sTRAIL LPD treatment

Immunohistochemistry (IHC) staining of αSMA and pSMAD2 in the adjacent sections of PBS and sTRAIL LPD groups. Red dotted circles indicate tumor nests; yellow dotted circles indicate fibroblasts.

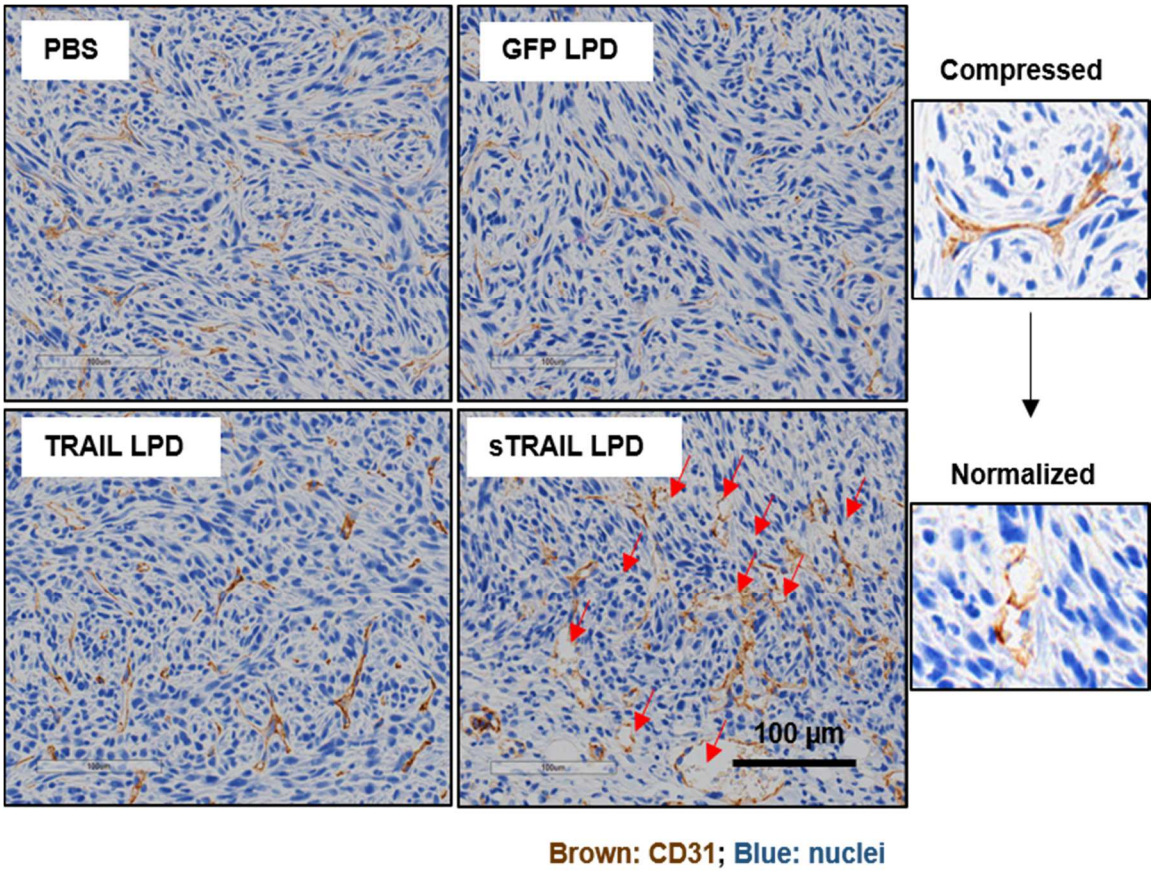

Figure 4.12 sTRAIL LPD induces normalization of blood vessel

IHC staining of blood vessel (CD31, shown as brown) after different treatments. sTRAIL LPD induces decompression of blood vessels. Red arrows indicate the decompressed vessels.

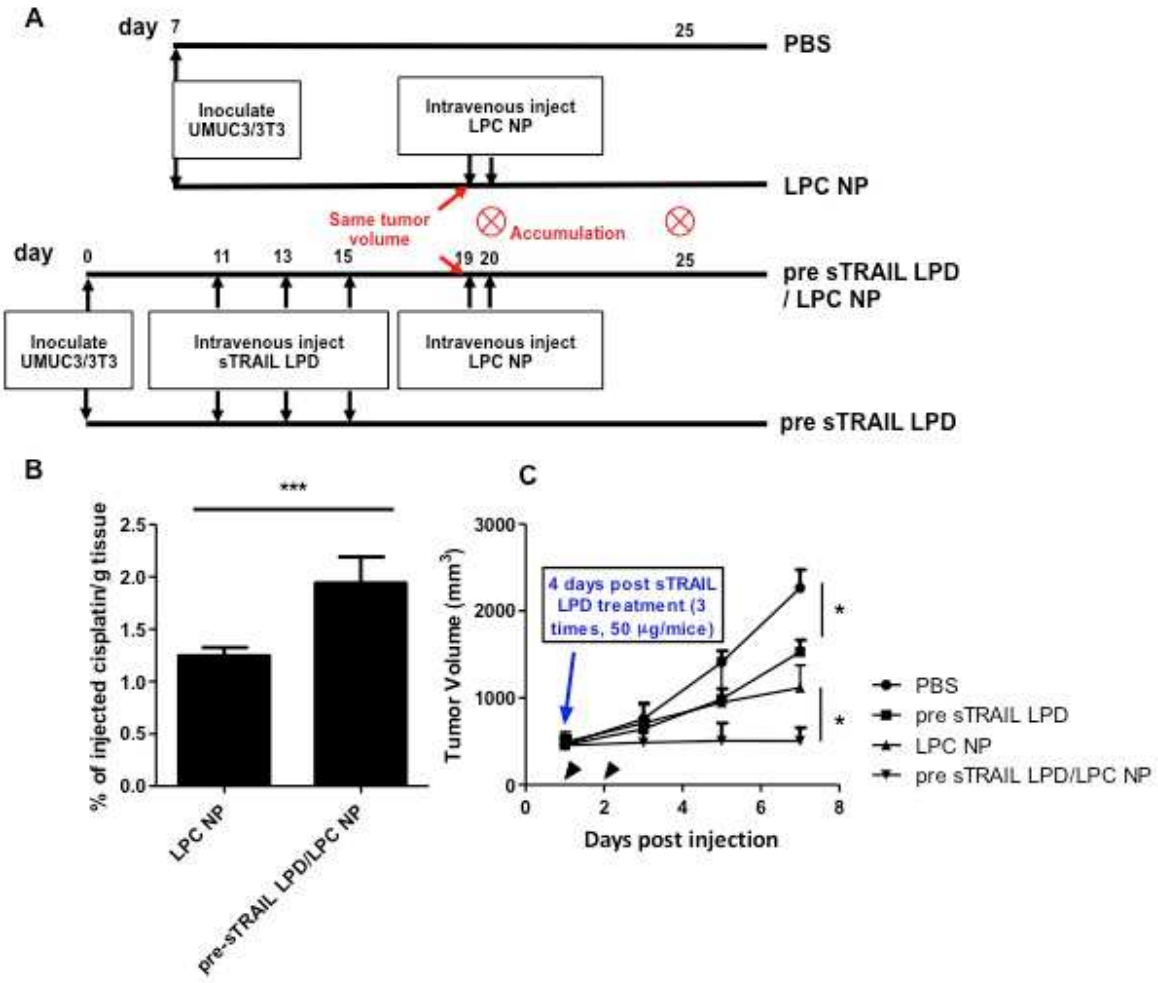

Figure 4.13 Remodeling of TME facilitates the delivery and antitumor effect of a second-wave nanoformulated cisplatin.

A. Dosing schedule of the second-wave chemotherapy. B. ICP-MS analysis of cisplatin accumulation 1 day after a single dose of cisplatin NP (LPC NP) in mice pre-treated with sTRAIL LPD or without pre-treatment (n = 5, *** $P < 0.001$). C. Tumor inhibition curve of LPC NP after treating the tumors with sTRAIL LPD. Cisplatin (1.9 mg/kg) was dosed (n = 5, * $P < 0.05$).

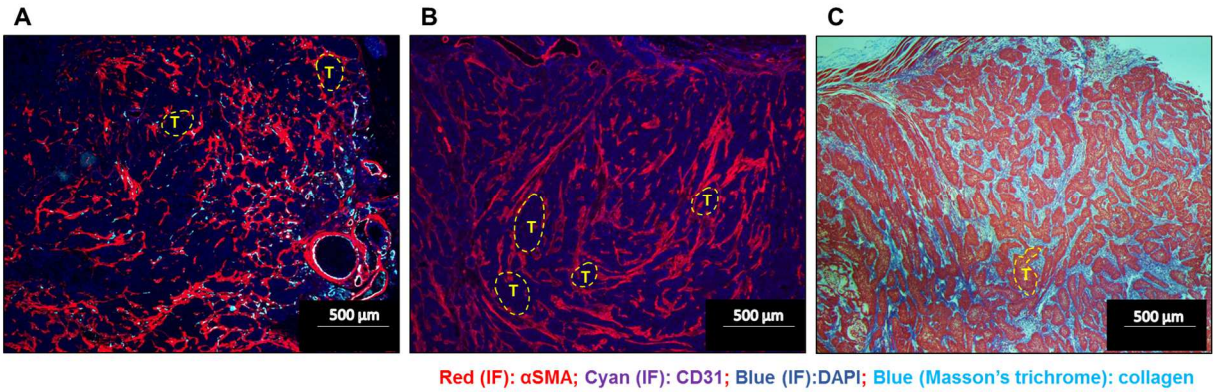

Figure 4.14 Histology of orthotopic BXPC3-Luc2 xenograft.

(A) and (B) immunofluorescence staining of fibroblasts and blood vessels. Examination revealed a stroma-vessel architecture, where nests of tumor cells (representative tumor nests are highlighted with yellow dotted circles) are surrounded by αSMA-positive fibroblasts (shown in red). Most of the CD31-positive blood vessels (only in A, shown in cyan) were embedded between αSMA-positive fibroblasts. (C) Masson's trichrome staining was used to visualize the collagen structure (shown in blue) in the BXPC3-Luc2 tumors. Tumor nests were also observed.

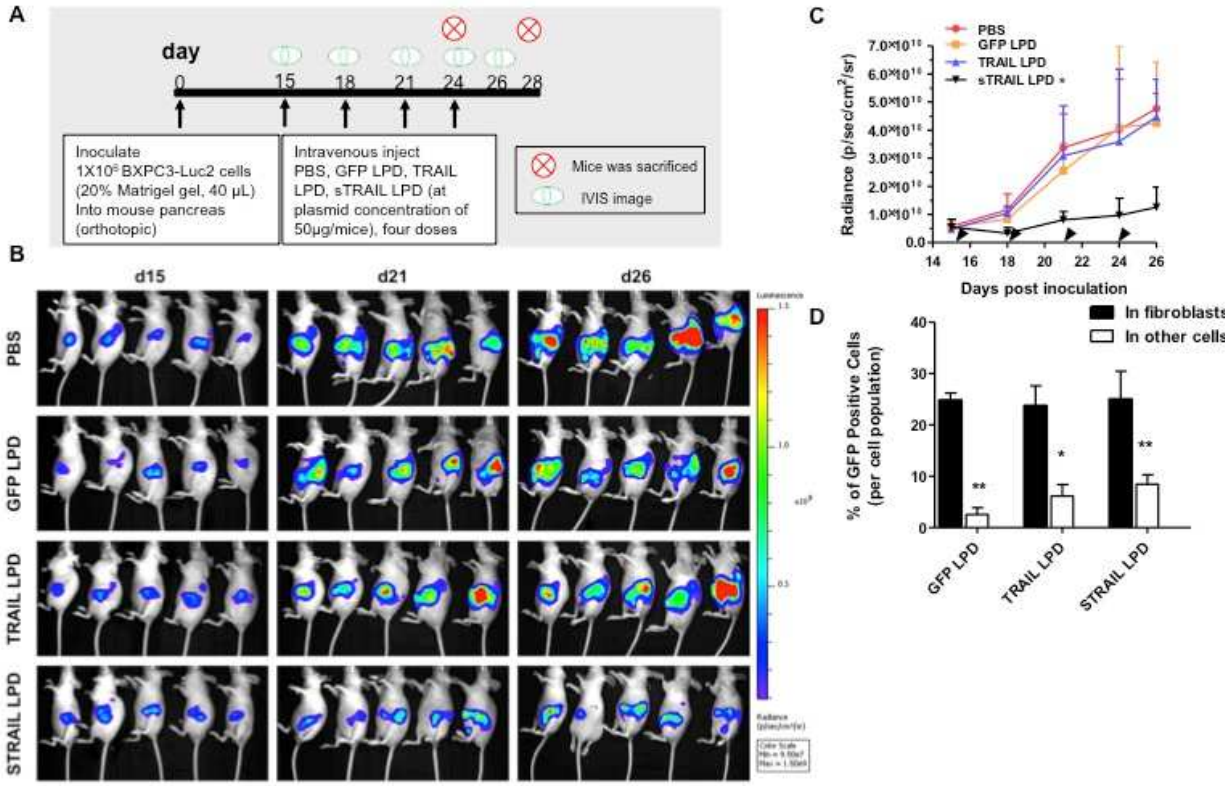

Figure 4.15 Intravenous administration of sTRAIL LPD inhibited the orthotopic desmoplastic BXPC3 tumor growth.

A. dosing schedule of sTRAIL treatment on BXPC3. B. IVIS images of BXPC3 tumor after different treatments (n = 5). C. Tumor inhibition curve o BXPC3 (n = 6-10, *P < 0.05 compared to PBS group). D. Flow cytometry analysis of GFP's association with αSMA positive fibroblasts 2 days after the third injection of the LPD (n = 4, * $P < 0.05$, ** $P < 0.01$).

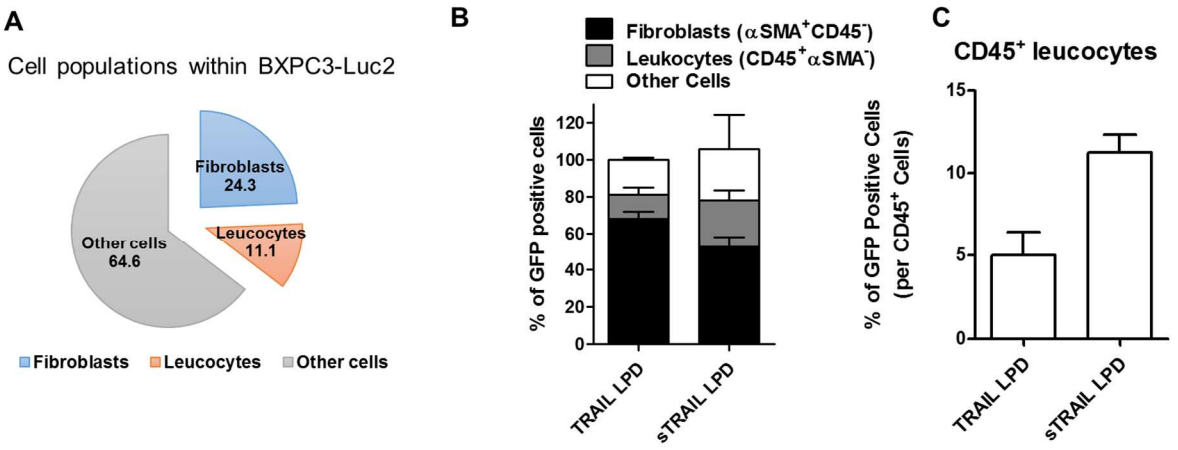

Figure 4.16 Expression of GFP within different cell populations of BXPC3-Luc2 tumors after 3

doses of NPs.

(A) Single-cell suspensions of the bulk tumor mass were stained with αSMA and CD45 and gated into various cell populations, quantified here as fractions of the total number of cells analyzed. (B) Flow cytometry analysis of the cell population that expresses GFP (the protein co-synthesized with TRAIL or sTRAIL) in the tumors. The total GFP-positive cells were considered as 100%. The % of each cell population that expressed GFP are shown. (C) The fraction of GFP-positive CD45 positve cells in the entire CD45 positive cell population was calculated.

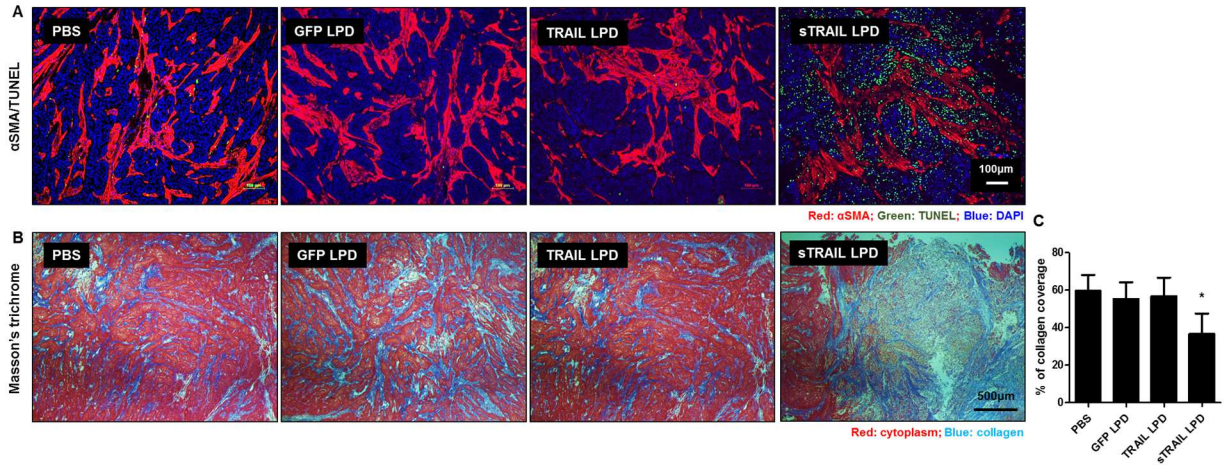

Figure 4.17 Tumor environment changes after treatments in BXPC3 model.

A. Immunofluorescent staining of αSMA and TUNEL from BXPC3-Luc2 tumor tissues after different treatments. B. Masson's trichrome staining for collagen from BXPC3-Luc2 tumors after different treatments. C. The quantification of collagen levels (n = 4~5, * $P < 0.05$).

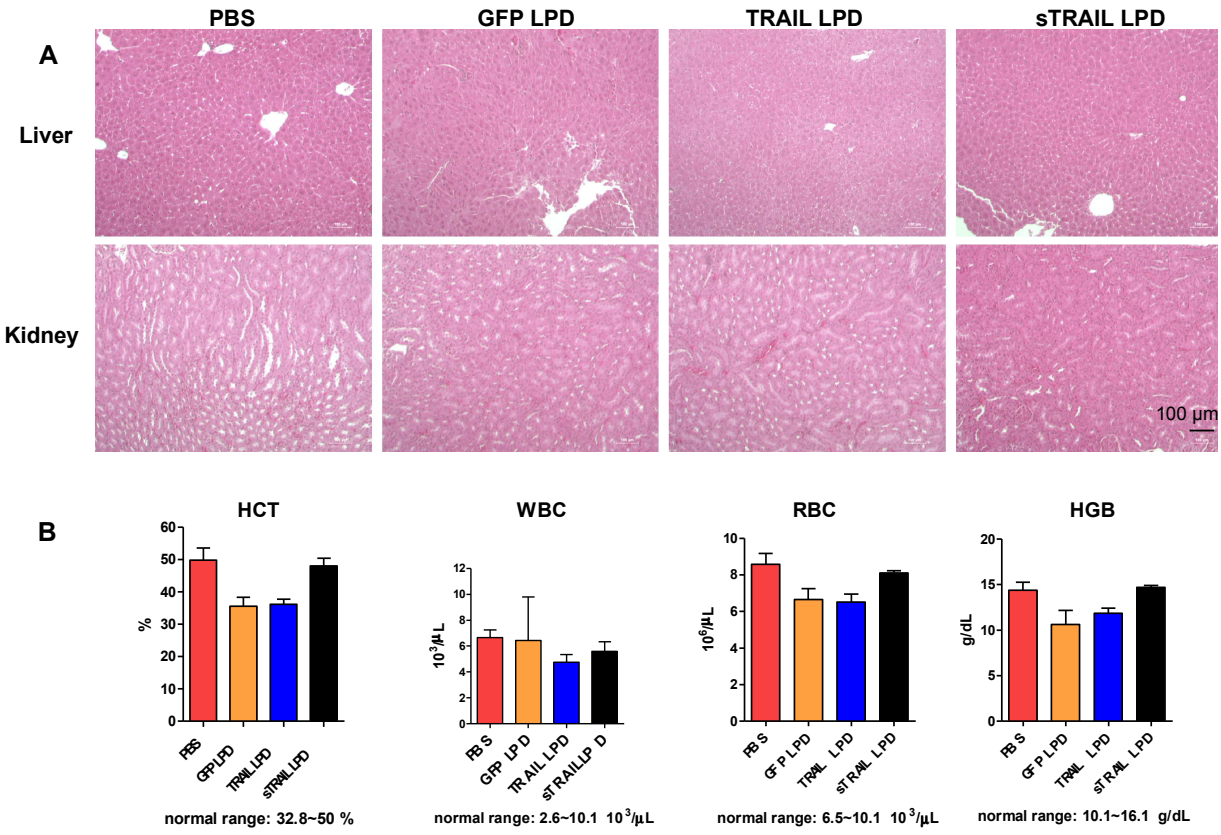

Figure 4.18 Cytotoxicity of LPD.

A. H&E staining of the major organs indicates minimal toxicity after sTRAIL LPD and TRAIL LPD treatment. B. Whole blood count assay indicates no obvious cell counts changed after therapy.

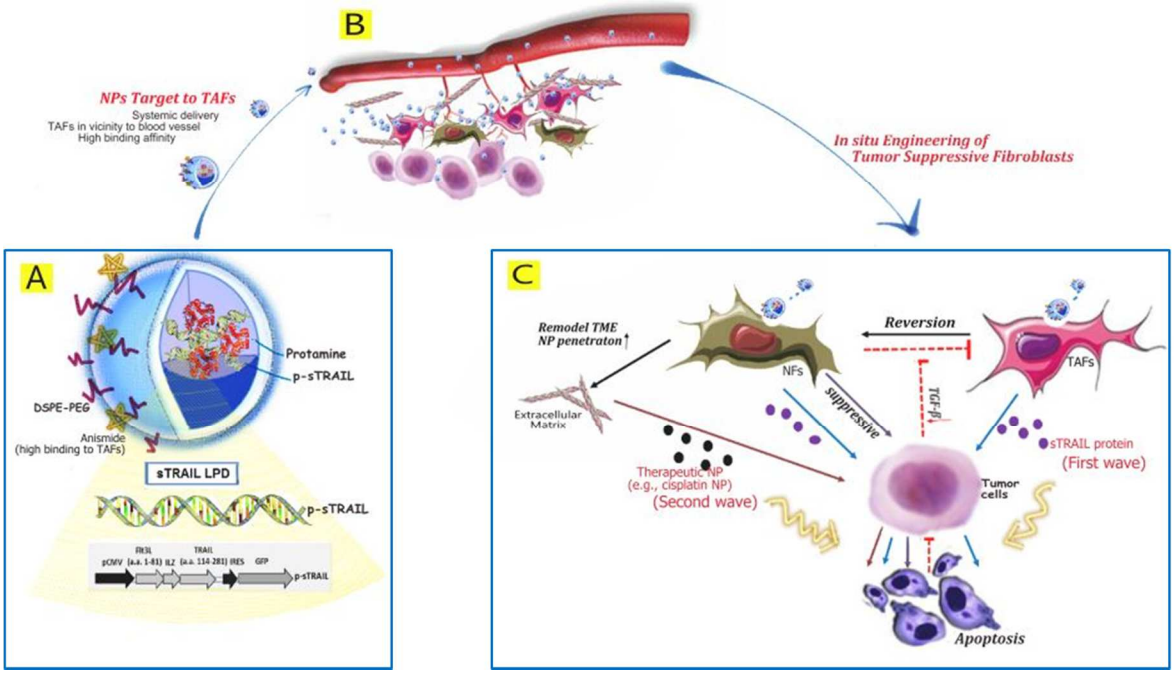

Figure 4.19 Diagram of proposed mechanism

A. Plasmid encoding secretable TRAIL protein is condensed with protamine, and further encapsulated into PEGylated liposomes coating with AA targeting motif (LPD). Diagram of the p-sTRAIL LPD is shown. B. LPD is systemically delivered to tumor region, and then extravasated from blood vessel due to the EPR effect. In most desmoplastic tumors, a thick layer of fibroblasts wraps around the blood vessel. Tumor associated fibroblasts (TAFs) are the major cells taken up the targeted LPD. C. sTRAIL protein issynthesized by TAFs and diffuses to the neighboring tumor cells. Apoptotic tumor cells, reciprocally failed to activate local fibroblasts, reverting the TAFs to normal fibroblasts (NFs). NFs can suppress tumor growth on one end, remodel the TME and increase the penetration of a second wave chemotherapeutic NPs on the other. Collectively, this multi-wave therapy can induce potent growth inhibition of the desmoplastic tumors.

CHAPTER 5: SYNERGISTIC DEPLETION OF TUMOR ASSOCIATED FIBROBLASTS VIA COMBINED GEMCITABINE AND CISPLATIN NANOPARTICLES IMPROVES DESMOPLASTIC BLADDER CANCER TREATMENT[6]

5.1 Summary

Previous chapters discussed the potential of either priming the damaged TAFs or reverting TAFs to quiescent state for improved NP penetration and anti-cancer efficacy. Another direct and efficient strategy to improve therapeutic outcome of NPs is to deplete TAFs. Our previous study have shown that single dose of cisplatin NPs could partially remove TAFs, but resistant occurred, conversely increasing desmoplasia after multiple times of treatment. This is partly due to the insufficient removal of TAFs. To prolong the stroma depleting effect, a more potent depletion agent should be used. Combination therapy can result in synergistic effect that superior than the monotherapy of each regimen. Therefore, we proposed the use of a nano-formulation of gemcitabine in combination with the previously used cisplatin NPs. As expected, this combination not only induced potent killing of tumor cells, but was detrimental to TAFs compared to cisplatin NPs monotherapy. Using the desmoplastic bladder cancer xenograft (UMUC3/3T3), we show that 85% of TAFs were depleted and 87% of the remaining TAFs were apoptotic 4 day after a single injection of combo NPs. The effect continued after 4 doses of combo NPs, where the recruitment of αSMA-positive fibroblast was decreased by more than 87%. Combo NPs nearly halted tumor growth with little evidence of general toxicity.

[6]This chapter previously appeared as a research article in Journal of Controlled Release. The original citation is as follows: Jing Zhang, Lei Miao, Shutao Guo, Yuan Zhang, Lu Zhang, Andrew Satterlee, William Y. Kim and Leaf Huang, synergistic anti-tumor effects of combined gemcitabine and cisplatin nanoparticles in a stroma-rich bladder carcinoma model, Journal of Controlled Release, 2014, 182 (28):90-96. Lei Miao was listed as a co-first author.

And the combo NP treated tumors became 2.75-fold more permeable than those treated with monotherapy. We concluded that the stroma depletion through combination therapy would be a promising strategy for the treatment of desmoplastic tumors.

5.2 Introduction

Bladder cancer, the fourth most common cancer diagnosed in men and the eighth in women, remains a concern due to its prevalence and tendency to progress and recur [1-3]. Advances in drug delivery are needed and nanomedicine in particular holds promise as a means to improve bioavailability and systemic circulation [4,5]. These therapies exploit the enhanced permeability and retention (EPR) effect in tumors, thereby increasing the chemotherapeutic dose to tumor tissue, at the same time sparing normal tissue from exposure [6].

Cancer has long been believed to be cell-autonomous and to date most research has focused directly on the malignant cells themselves. Several recent studies, however, suggests that carcinogenesis is also determined by a favorable tumor microenvironment (TME) [7]. Fibroblasts are the principal cellular component of the TME. Fibroblasts that have been recruited, activated and accumulated in vicinity to tumor cells are referred to as tumor-associated fibroblasts (TAFs) or myofibroblasts. TAFs can even be the most abundant type of cell within the desmoplastic tumors, notably pancreatic and breast carcinoma [8,9]. They contribute to tumor growth and invasiveness by remodeling the extracellular matrix (ECM), secreting various soluble factors (growth factors and cytokines), and suppressing immune responses. Though direct depleting of stroma cells have brought up a lot of paradoxical concerns, such as promoting resistance and diminishing immune surveillance; this strategy is still considered as a potential approach to improve NPs' perfusion and enhance the anti-cancer effect if potent and suitable depleting agents are chosen [10].

Myofibroblasts tend to be present in invasive bladder tumors [13]. To identify and verify the potency of the TAF-targeted stroma depleting agent for treatment of bladder cancer, we used the desmoplatic bladder cancer model (UMUC3/3T3) previously developed in our study. In this specific

model, fibroblasts were subcutaneously co-injected along with cancerous cells and Matrigel, a permissive extracellular matrix preparation. This desmoplastic tumor model recapitulates the stroma structure of the original invasive urothelial carcinoma found in patients.

Data in previous chapter suggest that chemo-drug cisplatin is a stroma-depleting candidate. The AA-targeted cisplatin NPs developed in our lab can target to fibroblasts that wrap around tumor vessels, with an upregulated expression of receptor for AA, namely the Sigma R. However, insufficient apoptosis of fibroblasts paradoxically induce the resistance of neighboring cells through damage-induced secretion of Wnt16, subsequently promoting tumor expansion. Thereby, we hypothesize that combination strategy that potentiates the stroma-depleting function of cisplatin NPs would enhance the overall anti-tumor performance. Gemcitabine has been utilized in combination cisplatin in the treatment of bladder cancer. A novel NPs developed in our lab that encapsulate gemcitabine monophosphate (GMP, the bioactive form of gemcitabine) have shown promising anticancer effect for the treatment of non-small-cell lung cancer [16]. In both cases of GMP NPs and cisplatin NPs, high drug entrapment efficiency was achieved with NPs diameters of approximately 45 nm and 40 nm for GMP NPs and Cisplatin NPs, respectively. So, we proposed that combination of GMP NPs and cisplatin NPs should be a potent stroma depleting agent.

Our current work aimed to use the desmoplastic bladder cancer xenograft (UMUC3/3T3) developed in our lab to evaluate GMP NPs and Cisplatin NPs combination therapy (Combo NPs) in terms of TAF-targeting and depletion capability. Similar to combination strategies towards cancer cells, combination of cisplatin NP and GMP NP induced superior apoptosis of TAFs compared to monotherapy of each. We also investigated the time-lapse changing of collagen deposition and tumor permeability after combination therapy. Since cisplatin NP and GMP NP combination also exhibited strong synergy towards tumor cells, the anti-tumor activities plus stroma depleting efficacy were also evaluated.

5.3 Material and Methods

5.3.1 Materials

Gemcitabine monophosphate disodium salt (GMP, purity≥97%) was provided by Qualiber, Inc. (Chapel Hill, NC). Cisplatin (cis-diamminedichloroplatinum (II)) was purchased from Sigma-Aldrich (Dorset, UK). GMP NPs (including ^{3}H-labeled GMP NPs) and Cisplatin NPs were prepared as described previously [16,17]. Size distribution and zeta potential were measured on a Malvern ZetaSizer Nano series (Westborough, MA).

The human bladder transitional cell line UMUC3 was from the American Type Culture Collection (ATCC), and the mouse embryonic fibroblast cell line NIH3T3 (UNC Tissue Culture Facility) were cultured in Dulbecco's modified Eagle's Media (DMEM) (Invitrogen, Carlsbad, CA) supplemented with penicillin (100 U/mL) and streptomycin (100 μg/mL) (Invitrogen), and 10% fetal bovine serum (Sigma, St. Louis, MO)/10% Bovine calf serum (Hyclone, Logan, Utah), respectively. Cells were cultivated in a humidified incubator at 37 ºC and 5% CO_2 and harvested with 0.05% trypsin-EDTA before subculture.

Female nude mice 6-8 weeks of age were used in all studies. All work performed on animals was approved by the Institutional Animal Care and Use Committee at University of North Carolina at Chapel Hill.

5.3.2 Preparation of GMP NP and Cisplatin NP

The GMP cores were formulated using 180 μL of 60 mM GMP mixed with 12.5 mM Na_2HPO_4 (pH=9.0) (final concentration) to reach a total volume of 600 μL. This solution was then added into 20 mL of oil phase containing cyclohexane/Igepal CO-520 solution (71/29). Then 400 μL of 20 mM dioleoylphosphatydic acid (DOPA) in chloroform was added and stired for 10 min. Six-hundred μL 2.5 M $CaCl_2$ was added to a separate 20 mL oil phase The two separate micro-emulsions were then mixed. After stirring for 5 min, another 400μL of 20mM DOPA was added into the emulsion. The emulsion was allowed to continually stir for another 20 min before 40mL of absolute

ethanol was added. The ethanol emulsion mixture was centrifuged at 10,000 g for 15 min to pellet the cores and the supernatant was then discarded. The GMP core was washed twice with absolute ethanol and dried under N_2. The GMP core pellets were suspended in chloroform. 330μL GMP core in chloroform was mixed with 38.7 μL of 25 mg/ml cholesterol, 28 μL of 25 mg/ml 1,2-Dioleoyl-3-trimethylammonium-propane chloride salt (DOTAP), 76.8 μL of 25 mg/ml 1,2-distearoryl-sn-glycero-3-phosphoethanolamine-N-[methoxy(polyethyleneglycol-2000) ammonium salt (DSPE-PEG2000) and 19.2 μL of 25 mg/ml DSPE-PEG-AA (DSPE-PEG-AA). The lipid mixture was evaporated to remove chloroform. The film on the vial wall was dissolved in 30 μL tetrahydrofuran followed by 50 μL absolute ethanol, and then suspended in 160 μL distilled water. After brief sonication, the solution was dialyzed in distilled water to obtain GMP NP. The Cisplatin cores were prepared avoiding of light. Briefly, 200 mM cis-$[Pt(NH_3)_2(H_2O)_2]$ $(NO_3)_2$ and 800 mM KCl in water were separately dispersed in a solution composed of cyclohexane/Igepal CO-520 (71:29, v/v) and cyclohexane/Triton-X100/hexanol (75:15:10, v/v/v) (3:1) to form a well-dispersed, water-in-oil reverse microemulsion. One hundred microliters of DOPA (20 mM) was added to the Cisplatin precursor phase and the mixture was stirred. Then, the two emulsions were mixed for another 30 min while the reaction proceeded. After that, ethanol was added to the microemulsion and the particles were collected by centrifugation at 12,000 g. After being extensively washed with ethanol 2-3 times, the pellets were redispersed in chloroform. Finally, 1.0 mL of Cisplatin core, 50 μL of 20 mM DOTAP, 50 μL of 20 mM cholesterol and 50 μL of 10 mM DSPE-PEG2000 or DSPE-PEG-AA were combined. After evaporating the chloroform, the residual lipids were dispersed in 1.0 mL of distilled H_2O. After brief sonication, the solution was dialyzed in distilled water to obtain Cisplatin NP.

5.3.3 Characterization of NPs

Nano-sized GMP and Cisplatin cores were viewed under a JEOL 100CX II TEM (Tokyo, Japan). Particle size distribution and zeta potentials of the nanoparticles were determined by dynamic light scattering and electrophoretic light scattering, respectively, both using a Malvern ZetaSizer

Nano series (Westborough, MA). GMP entrapment efficiency was measured by a UV spectrophotometer (Beckman Coulter Inc., DU 800 spectrophotometer) and the EE % of Cisplatin was determined by ICP-MS (NexIONTM 300, Perkin Elmer Inc), respectively.

For drug loading study, ^{3}H-labeled GMP NPs were prepared as described previously and 1% (molar ratio) of N-4-nitrobenzo-2-oxa-1,3-diazole phosphatidylethanolamine (NBD-PE) was incorporated to the outer leaflet. The final GMP NPs and Cisplatin NPs were centrifuged at 13,200 rpm for 3 times, and each time was 15 minutes. Then, the supernatant was removed and the final pallet was resuspended and lyophilized for 48 hours. Dried NPs were weighted and the ^{3}H radioactivity and Cisplatin measurement were determined using the liquid scintillation analyzer (the instrument has been described in the materials section) to calculate the amount of GMP and ICP-MS (NexIONTM 300, Perkin Elmer Inc) to calculate the amount of Cisplatin. The drug loading for GMP NP and Cisplatin NP were determined by the weight of GMP (Cisplatin)/ the weight of purified NPs, respectively.

5.3.4 Desmoplastic Subcutaneous Xenograft Bladder Tumor Model

To establish the xenograft model, UMUC3 (5×10^{6}) and NIH3T3 cells (2×10^{6}) in 100 μL of PBS were subcutaneously co-injected with Matrigel (BD Biosciences, CA) at a ratio of 1:1 (v/v) into the right flank of mice. For the standard subcutaneous bladder tumor model, only UMUC3 cells (5×10^{6}) were injected. Tumor volume was measured every three days starting on day seven after inoculation. The formula: $V=(L\times W^{2})/2$ was applied to calculate tumor volume, where V is the tumor volume, L the larger perpendicular diameter and W the smaller perpendicular diameter. Tumor growth normalized to the original volume calculated on the first day of measurement. Tumor sections collected on day eight for the two animal models and also those of clinical patients (kindly supplied from Dr. William Kim, Lineberger Comprehensive Cancer Center, UNC) were stained with hematoxylin and eosin (H&E), immunofluorescent staining for αSMA (FITC labeled) and CD31 (Alexa Fluor 647 labeled). For immunofluorescence, slides were deparaffinized with xylene and a

graded alcohol series. After antigen retrieval, sections were blocked with 10% goat serum and then incubated with polycolonal rabbit anti-αSMA antibody (Abcam, Cambridge, MA, USA) and anti-CD31 (BD Biosciences, CA, USA) at 1:100 dilution overnight at 4 ºC. Immunocomplexes were visualized with the corresponding FITC-labeled and Alexa Fluor 647 secondary antibody at a 1:1000 and 1: 100 dilution respectively for 1 h at room temperature in the dark. Slides were rinsed with PBS and cover slipped with Vectashield containing DAPI (Vector laboratories, Burlingame, CA). Digital images were acquired by an Eclipse Ti-U inverted microscope (Nikon Corp., Tokyo, Japan) ×20 magnification and quantitatively analyzed on Image J (National Institutes of Health).

5.3.5 *In vitro* Cell Viability of Free GMP and Cisplatin on UMUC3 Cells and Analysis of Synergistic Effects of Free Drug Combinations.

MTT (3-[4,5-dimethylthiazol-2-yl]-2,5-diphenyltetrazolium bromide) assay was conducted to evaluate *in vitro* viability of free GMP, Cisplatin and their combinations. Briefly, cells were seeded in 96-well plates at a density of 3,000 cells per well 24 h prior to drug treatment. Subsequently, cells were treated with free drugs and drug combination with various molar ratio at series of dilutions in full medium. Following 48 h treatment, 20 μL MTT (5 mg/mL) reagent was added for an additional 4 h incubation at 37 °C. The medium was discarded, the formed formazan salt was dissolved in 150 μL of DMSO and absorbance was read at 570 nm using a multidetection microplate readers (Plate CHAMELEON™ V-Hidex). Cell survival rates were calculated as normalized to control untreated wells. Each concentration was tested in four wells and data presented in means±standard error means (SD). The mean drug concentration required for 50% growth inhibition (IC_{50}) was determined using CompuSyn software (Version 1.0, Combo-Syn Inc., U.S.) using the median effect equation: $Fa=[1+(IC_{50}/D)m]-1$, where Fa is the fraction of affected cells, D is drug concentration and m is the Hill slope.

Combination Index (CI) Analysis of free drug combination based on the Chou and Talalay method [18] was performed using CompuSyn software. Briefly, for each level of Fa the CI values for GMP and Cisplatin combinations were calculated according to the following equation:

CI=(D)1/(Dx)1+(D)2/(Dx)2, where (D)1 and (D)2 are the concentrations of each drug in the combination resulting in Fa×100% growth inhibition, and (Dx)1 and (Dx)2 are the concentrations of the drugs alone resulting in Fa×100% growth inhibition. CI values for drug combinations were plotted as a function of Fa. CI values less than 1 or more than 1 demonstrate synergism or antagonism of drug combinations, respectively.

5.3.6 Pharmacokinetic Study

Pharmacokinetic studies were performed on xenograft tumor-bearing nude mice innoculated subcutaneously with a mixture of UMUC3 and NIH3T3 cells. Animals were randomly divided into two groups (n=4) and intravenously injected with free GMP containing a tiny fraction of ^{3}H-Labeled free cytidine monophosphate, and Cisplatin (Combo Free) and Combo NP at a dose of 16 mg/kg and 1.6 mg/kg respectively. At 5 min, 20 min, 40 min, 1h, 2h, 4h, 8h and 24h post injection, approximately 45 mg whole blood was collected from the tail vein (For free Cisplatin and Cisplatin NP groups, only data of first 8 hours were recorded since data collected from the last two time points were under detection<0.2 ng/mL).. Pharmacokinetic data was expressed as a percentage of injected dose for each drug. For measurement of GMP, 10 to 20 mg of blood was immediately mixed with 10× NCS® II Tissue Solubilizer (Amersham Biosciences, Inc) and digested at 60°C overnight. Three hundred μL of hydrogen peroxide (30% in water, Fisher) was added to the samples and vortexed to bleach the blood color, and then the sample was mixed with 4 mL scintillation cocktail (Fisher Inc). The ^{3}H radioactivity in the blood samples was counted using a liquid scintillation analyzer (TRI-CARB 2900 TR, Packard Bioscience Co.). For the measurement of cisplatin, approximately 30 mg of blood was digested with 400 μL 60% nitric acid (Acros Organic) at 70°C overnight and measured by Inductively Coupled Plasma-Mass Spectroscopy (ICP-MS, NexIONTM 300, Perkin Elmer Inc).

5.3.7 Platinum Adduct Staining

Tumor-bearing mice were randomized into four groups (n=5) as follows: Control group, Cisplatin NP (Cisplatin: 1.6 mg/kg), Combo NP #1 (Cisplatin: 1.6 mg/kg, GMP: 12 mg/kg) and

Combo NP #2 (Cisplatin: 1.6 mg/kg, GMP: 16 mg/kg). Single i.v. injection was performed for each treatment. Twenty-four hours later, tumor was fixed in 10% formalin and paraffin-embedded sectioned for platinum adduct staining. The sections were incubated with anti-platinum modified DNA antibody [CP9/19] (1:250 dilution) from Abcam Inc. overnight at 4 ºC. FITC-labeled goat anti-rat IgG antibody (1:200, Santa Cruz biotechnology, Inc.) was used for 1 h at room temperature in dark place. The sections were also stained by DAPI and observed by an Eclipse Ti-U inverted microscope (Nikon Corp., Tokyo, Japan) at ×20 magnification and analyzed on Image J (National Institutes of Health).

5.3.8 Tumor Accumulation of GMP and Cisplatin in Established Animal Model

To measure tumor accumulation of Combo Free and Combo NPs, animals were randomly divided into two groups (n = 6) and intravenously injected with free GMP containing a tiny fraction of ^{3}H-Labeled free cytidine monophosphate, which is believed to have the similar pharmacokinetic profile as GMP [16] and Cisplatin (Combo Free) and Combo NPs at a dose of 16 mg/kg and 1.6 mg/kg respectively. Three mice of each group were sacrificed at each predestinate time point, and approximately 45 mg of blood was withdrawn using the tail bleeding method. Tumor uptake of GMP and Cisplatin were expressed as the percentage of the injected dose per gram tumor. For measurement of GMP, 10 to 20 mg of blood was immediately mixed with 10× NCS® II Tissue Solubilizer (Amersham Biosciences, Inc) and digested at 60°C overnight. Three hundred μL of hydrogen peroxide (30% in water, Fisher) was added to the samples and vortexed to bleach the blood color, and then the sample was mixed with 4 mL scintillation cocktail (Fisher Inc). The ^{3}H radioactivity in the blood samples was counted using a liquid scintillation analyzer (TRI-CARB 2900 TR, Packard Bioscience Co.). For the measurement of Cisplatin, approximately 30 mg of blood was digested with 400 μL 60% nitric acid (Acros Organic) at 70°C overnight and measured by Inductively Coupled Plasma-Mass Spectroscopy (ICP-MS, NexIONTM 300, Perkin Elmer Inc).

5.3.9 Anti-tumor Efficacy in desmoplastic Xenograft Bladder Tumor Model

On day seven after implantation, mice were randomized into seven groups (n=5) as follows: Saline (Control group), free GMP (GMP Free), free Cisplatin (Cisplatin Free), combination of free GMP and Cisplatin (Combo Free), GMP NPs, Cisplatin NPs and combination of GMP NPs and Cisplatin NPs (Combo NPs). IV injections were performed every three days for a total of 3 injections with the GMP dose at 16 mg/kg and Cisplatin at 1.6 mg/kg. Tumor volume was measured every three days using the aforementioned method. Body weight was also recorded. Mice were sacrificed two days after the last injection by CO_2 asphyxiation and tumors were excised. A portion of the tumor was fixed in 10% formalin and paraffin-embedded sectioned for H&E staining, TUNEL assay, and αSMA immunofluorescence by an operator blinded to the treatment groups.

5.3.10 *In vivo* Toxicity Analysis

After three daily injections, blood was collected from the venous plexus of the eye and centrifuged at 4,000 rpm for 5 min. Serum alanine aminotransferase (ALT), aspartate aminotransferase (AST), blood urea nitrogen (BUN) and creatinine levels were assayed as indicators of hepatic and renal function. Organs (heart, liver, spleen, lung, kidney) were fixed and sectioned for H&E staining.

5.3.11 Tissue Analysis

Tumor sections were stained for TUNEL assays as recommended by the manufacturer (Promega, Madison, WI). DAPI mounting medium was dropped on the sections for nuclear staining. Apoptosis was also determined by H&E staining. Tumors were also prepared for αSMA immunofluorescence (FITC label). Images were acquired by an Eclipse Ti-U inverted microscope (Nikon Corp., Tokyo, Japan) at ×20 magnification and analyzed on Image J (National Institutes of Health).

5.3.12 TAF-Targeting Efficacy in the Desmoplastic Bladder Tumor Model

Mice with 200 mm^3 tumors were treated with a single dose of Combo NPs (GMP 16 mg/kg, Cisplatin 1.6 mg/kg) (n=24). Every 24 hours, mice were sacrificed. Tumors were excised and sectioned for αSMA (Alaxa Fluor 647)/TUNEL immunofluorescence double staining and Masson's trichrome (Sigma, USA).

5.3.13 Analysis of Tumor Permeability

Drug permeability in the tumor was evaluated by Evans Blue assay [19]. Tumor-bearing mice were randomized into three groups (n=3) as follows: Control group, Combo Free and Combo NPs. Single i.v. injection was performed for each treatment with the GMP dose at 16 mg/kg and Cisplatin at 1.6 mg/kg. Twenty-four hours later, 100 mg/kg of Evans Blue (10 mg/ml in 0.9% NaCl) was intravenously injected. After 30 min, mice were sacrificed and blood and tumor tissue were homogenized in a 0.1% sodium sulfate/acetone mixture (7:3 v/v) at a ratio of 1:9. Samples were maintained at ambient temperature in the dark overnight and then centrifuged at 1,000 g for 5 min. Supernatants were used to determine absorbance at 620 nm. The amount of Evans Blue in tumor tissue was expressed as μg/g tissue.

5.3.14 Statistical Analysis

Results were expressed as a mean ± standard deviation. Student's t-test and one-way analysis of variance (ANOVA) test were used to evaluate statistical significance. A P value of $P < 0.05$ was considered to indicate statistical significance.

5.4 Results and Discussion

5.4.1 Characterization of GMP NPs and Cisplatin NPs

The dioleoylphosphatydic acid (DOPA) was employed as a pre-coating reagent for the nano-sized CaP cores. The lipid coating prevents the core from aggregation during the centrifugal separation step and makes it soluble in chloroform. The DOPA layer coating CaP core served as the

inner leaflet lipid and a variety of lipids for the outer leaflet could simply be added into the CaP core solution in chloroform. The choice of the asymmetric outer lipids plays an important role in the pharmacokinetics and tissue distribution of the final nanoparticles [20]. Asymmetric lipid bilayer-modified nanoparticles for GMP and Cisplatin were prepared as previously reported [16,17]. Particles with a core-shell shape were 44.5±0.2 nm and 40.6±0.2 nm for GMP NPs and Cisplatin NPs, respectively. Particles exhibited high entrapment efficiency at around 49.5% and 44%, and zeta potential of 11.5±0.6 mV and 5.6 ±0.3 mV for GMP NPs and Cisplatin NPs, respectively. The drug loading was 23±2 wt % and 82±5 wt % for GMP NPs and Cisplatin NPs, respectively (data not shown).

5.4.2 Histopathology for the Desmoplastic Bladder Cancer Model (UMUC3/3T3)

Xenografts with UMUC3 and/or NIH3T3 cells and patient tumor sections were stained with H&E and αSMA (FITC labeled). Results suggest that the UMUC3/3T3 was enriched with stroma structure (H&E) and αSMA positive cells (17.5±3.2%), compared to the subcutaneous bladder model with injection of UMUC3 cells alone (1.8±0.6%, UMUC3). This UMUC3/3T3 model recapitulates the human bladder tumor structure (14.8±2.1%, Patient) (**Figure 5.1A**). Alpha-SMA-positive fibroblasts located near CD31-positive blood vessel endothelial cells, suggesting a stroma-vessel architecture of this model, which was consistent with previous studies (**Figure 5.1B**). Moreover, the desmoplastic UMUC3/3T3 xenografts grew more aggressively compared to UMUC3 only xenograft (**Figure 5.1C**). Whereas, no tumor growth was observed when NIH3T3 cells alone were inoculated (data not shown). Therefore, such desmoplastic tumor closely mimics the structure of human bladder cancer isolates, enabling us to better understand the synergistic effect of Combo NP on tumor inhibition and TAF-targeting effect.

5.4.3 Combo NPs depletes TAFs in the tumor, modifies collagen deposition

Taking advantage of the desmoplastic UMUC3/3T3 model, the interaction of TAFs with the combined drugs was then investigated. The ratio of αSMA positive cells were firstly evaluated after

multiple injections. As shown in **Figure 5.2**, Combo Free, GMP NPs and Cisplatin NPs exhibited partial efficacy in reducing fibroblasts, but the Combo NPs showed the fewest αSMA positive cells compared to all the treatment groups ($P < 0.05$). To examine the mechanism of the potent TAF depleting effect of Combo NPs, we conducted a single injection of Combo NPs and detected the apoptotic fibroblasts every 24 h after injection. **Figure 5.3A-C** presents the double staining for TUNEL and αSMA and the quantitative results. Firstly, 4.9% cells were induced to undergo apoptosis one day after Combo NPs injection, among which 56.6% apoptotic cells were αSMA-positive. It suggests that the fibroblasts are more likely to be killed compared to tumor cells. From day one to day two, the apoptotic fibroblasts in total apoptotic cells increased dramatically and more than 60% fibroblasts were apoptotic. The apoptotic cells in fibroblasts even reached 87.2% on day four, which was 45% higher than that in tumor cells. The results indicate that the apoptosis of fibroblasts not only began before that of carcinoma cells but also substantially resulted in fibroblasts depletion. By the last two days, the apoptotic fibroblast (%) in total fibroblast was significantly decreased to nearly 1%. Secondly, the collagen on Day four became 14.9% of the original collagen on day 0, which is also different from that of Day three. It shows that the killing effect of Combo NPs on TAFs in the first three days resulted in the decreased deposition of collagen on Day four, which also started to increased since day five (**Figure 5.3D**). Two hypothesizing reasons explained the efficient depleting of fibroblasts. One is that the *stroma-vessel* structure of desmoplastic bladder cancer determines the distribution pattern of systemic delivered NPs. TAFs that distributed along the vessels would be the first target for combo NPs. The other is that myofibroblasts were likely to be more sensitive to Combo NPs than that of bladder carcinoma cells.

5.4.4 Synergistic effect induced by tumor accumulation of GMP NPs and Cisplatin NPs

To examine the aforementioned hypothesis*, in vitro* toxicity analysis of combined GMP and Cisplatin free drugs and nanoparticles was performed after 48 h treatment of UMUC3 cells (**Figure 5.4A** and **B**) or NIH3T3 cells (data not shown). The combination index (CI) was calculated using a

series of molar ratios and amounts of GMP and Cisplatin. CI values were analyzed according to Chou and Talalay [18] using CompuSyn software (ComboSyn, Inc., Paramus, NJ, USA). From the CI vs Fa plot (**Figure 5.4C**), Synergy, as indicated by a CI < 1, occurred over a broad range of drug ratios. The CI fell between 0.1 and 0.3 occurred when GMP and Cisplatin were present at molar ratios ranging from 10: 1 to 1: 1. When the cytotoxicity study of GMP NPs and Cisplatin NPs was investigated, the combination of GMP NPs and Cisplain NPs at ratio of (10:1) was indicated to exhibit better performance over single nanoparticles alone over a range of concentration with the lowest IC_{50}. Synergy was also observed in **Figure 5.4D** when molar ratio of GMP NPs to Cisplatin NPs at 10:1 with CI < 1. Further evaluation on NIH3T3 using the same ratio NPs combination suggest that NIH3T3 has similar and comparable sensitives (data not shown). Gemcitabine has been reported to affect the expression of key proteins involved in nucleotide excision repair (NER) and mismatch repair (MMR), thereby inhibiting repair of DNA damage caused by Cisplatin (**Figure 5.7**) [21]. Synergy between gemcitabine and Cisplatin might be related to the reduced DNA repair of intra-strand and possibly inter-strand cross-links of Cisplatin [22]. The comparably potent synergistic effect in fibroblasts is one important mechanism for the observed potent stromal depletion effect.

Next, we investigated the synergistic effect of Combo NPs and Combo Free *in vivo*. The resulting pharmacokinetics (**Figure 5.5**) suggests that Combo NPs provides advantages over Combo Free. About 40% to 45% of the GMP NPs were retained in the blood circulation after 2 h after bolus administration, while the free GMP was rapidly cleared within 20 min. AUC and half life of Cisplatin NPs 1.4 to 1.7 times higher than that of Cisplatin free drug, which had more than 80% been cleared at the first 20 min. Incorporation of GMP and Cisplatin in lipid bilayer coated nanoparticles modified with hydrophilic polyethylene glycol increased the drug retention in the circulation, reduced the drug clearance, consistent well with our previous pharmacokinetic studies [16]. However, there are significant discrepancy in the PK profile of GMP NPs and Cisplatin NPs. One explanation for the difference is that GMP NPs with highly positive charges (11.5 mV) are more likely to bind with serum proteins, leading to longer circulation in the system but lower tissue distribution; however,

Cisplatin NPs with relatively neutral charges (5.6 mV) worked in the opposite way. Moreover, Cisplatin NPs produced a slightly higher accumulation than GMP NPs in tumor after a single injection (**Figure 5.4E**). Both nanoparticles showed significantly higher tumor accumulation (more than 10% of injected dose per gram remained in the tumor 10 h post injection) than the free drugs (less than 2% of injected dose per gram left 10 h post injection). The possible reason is the phenomenon known as enhanced permeability and retention (EPR). The vasculature of tumors is comprised of poorly aligned and defective endothelial cells lacking innervation [23,24]. Nanoparticle formulations can increase tumor accumulation through the EPR effect and with a specific targeting ligand can enhance tumor cell uptake through a receptor mediated pathway.

The ratio of GMP to Cisplatin (mol: mol) in tumor after Combo NPs injection, which is in the synergistic range of nanoparticles (**Figure 5.4B**) was 8.35:1, and 6.75:1 at 5 h and 10 h after injection (**Figure 5.4E**); therefore, a synergistic effect took place. The GMP to Cisplatin molar ratio for the Combo Free injection was much higher than for Combo NPs, and out of the synergistic range (**Figure 5.4C**). Since synergistic effect of Combo NP was observed both on tumor cells and fibroblasts (*in vitro*), we further hypothesize that this Combo NP can result in potent anti-tumor effects by simultaneously inhibiting the growth of both the tumor cells and fibroblasts [25,26].

5.4.5 Anti-tumor effect of combined therapy

As expected, we report the potent anti-tumor efficacy of the Combo NPs in our stroma-rich bladder tumor model at a dose of 16 mg/kg for GMP and 1.6 mg/kg for Cisplatin. We first determined whether Combo NPs can exhibit synergistic anti-tumor effects without significant adverse effects (**Figure 5.6**).

When treatment began on day seven after inoculation, free Cisplatin (1.6 mg/kg) monotherapy showed little anti-tumor effect, with Cisplatin NPs being more effective than free drug ($P < 0.05$). Tumor growth was delayed significantly in mice treated with free GMP and GMP NPs compared to the control group after multiple doses. In comparison, Combo NPs treated tumors had

significantly smaller volume than the other six groups at the end of the experiment, showing growth of only 0.3-fold more than the day one tumor volume. No weight loss was observed in any treatment group, indicating that the treatment was well tolerated (data not shown). The enhanced tumor growth inhibition exhibited by nanoparticles should be attributed to the endocytosis mediated by the Sigma R and EPR effect [27], which is also indicated by the tumor accumulation study aforementioned. Nanoparticle formulation with specific targeting ligand can increase tumor accumulation through EPR effect and enhanced tumor cell uptake through receptor-mediated pathway. Furthermore, *in vivo* maintenance of drug ratios shown to be synergistic *in vitro* was proved to provide increased efficacy in preclinical tumor model [28]. Therefore, the synergistic effect proved by the tumor accumulation study, enable the Combo NPs to show the most outstanding effect on tumor growth inhibition in comparison with GMP NPs and Cisplatin NPs alone.

Stroma-rich tumor-bearing mice were sacrificed two days after the final injection and the tumors were sectioned for TUNEL assay. In the TUNEL assay(refer to [74]), the Combo NPs exhibited the most effective killing effects and induced a 16.1-fold higher amount of apoptotic cells compared with control group . This was more potent than the Combo Free treatment group, which showed 55.5% less apoptosis than that of the Combo NPs. There was no significant difference among Combo Free, GMP NPs and Cisplatin NPs groups ($P > 0.05$). Free Cisplatin treatment had limited ability to induce apoptosis in tumor cells. The results indicate the combination of GMP NPs and Cisplatin NPs augment the intrinsic cytotoxicity. This finding is consistent with data in Figure 3 that the Combo NPs exerts synergistic anti-tumor effects.

5.4.6 Tumor vessel permeability

Passive targeting of liposomal formulations is mediated mainly by the enhanced vascular permeability of tumor vessels. To evaluate vascular permeability after Combo Free and Combo NPs treatment, tumor bearing mice were intravenously injected with Evans Blue, which binds to serum albumin and then tend to accumulate in tissues with leaky vasculature [19]. Vascular permeability

was found to be nearly 21.3 and 2.7 times higher in the Combo NPs group than in the Control and Combo Free groups, respectively (**Figure 5.8**). Besides the increasing transport through vasculature, the enhanced intratumoral uptake of Evans Blue might also be contributed to tumor priming effect by substantial apoptosis caused by pretreatment with single injection of Combo NPs (**Figure 5.8**), which could reduce tumor cell density, expend the interstitial space and then promote the penetration into three-dimensional tumor histocultures [31,32]. Further investigation is desired for the mechanism of greater tumor uptake of Evans Blue.

The more pronounced accumulation from Combo NPs could be attributed to the synergistic effect of GMP NPs and Cisplatin NPs on the tumor blood vessels: (1) Combo NPs could significantly reduce the expression of vascular endothelial growth factor (VEGF) (**Figure 5.9**), which is an important mediator of tumor angiogenesis, and enhance the extent of tumor vasculature abnormalities, which impairs the tumor growth [33-35]. This finding is consistent with previous result that Combo NPs exerts higher tumor inhibition (Fig. 3); (2) Because of their sensitivity or proximity to tumor blood vessels, the TAFs will be first killed by nanoparticles distributed in the stoma and the collagen in stroma will be depleted. This depleting effect could possibly be helpful for better distribution of antitumor compounds in the tumor area which would hardly have access to the tumor cells otherwise [36], and enhance the total drug tumor accumulation and transport to carcinoma cells.

5.5 Conclusions

In this study, anti-tumor effects of Combo NPs were investigated in a stroma-rich xenograft bladder cancer model. GMP and Cisplatin accumulated in treated tumor tissue at a molar ratio and concentration expected to have synergistic anti-tumor effects. Combo NPs' ability to inhibit tumor growth was enhanced relative to Combo Free with no obvious toxicity. The effectiveness of Combo NPs could be attributed to its effect on both carcinoma cells and TAFs. The anti-tumor activity of Combo NPs may result from the combined effects of TAFs depletion with alterations in collagen deposition, increased uptake of chemotherapeutic drugs by the tumor and apoptosis of carcinoma

cells. Since the standard first line chemotherapy for muscle invasive bladder cancer is now gemcitabine plus Cisplatin [37,38], the result of our study suggest that Combo NPs could be tested clinically to replace free drug combination.

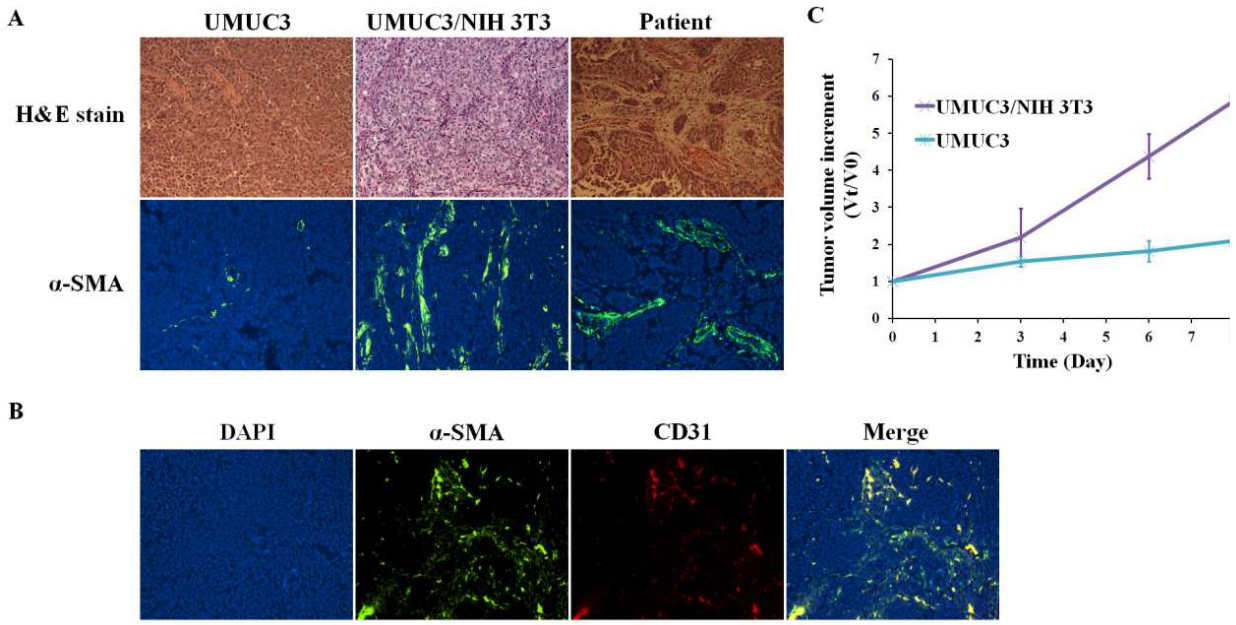

Figure 5.1 Histopathology of bladder cancer

Representative H&E and αSMA staining of tumors formed by injection of UMUC3 cells (20×) without or with NIH3T3 cells and from patient sections. B. Stroma-vessel architecture of UMUC3/3T3 was visualized by immunofluorescence co-staining of αSMA positive TAFs (shown as green) and CD31 positive blood vessels (shown as red) C. Tumor growth curve of UMUC3 xenografts and UMUC3/3T3 xenografts. Measurements were initiated when the tumor volume reached ~200 mm^3. Tumor growth increment was presented by normalizing to the original volume on the 1st day of measurement (Vt/V0) (n = 5).

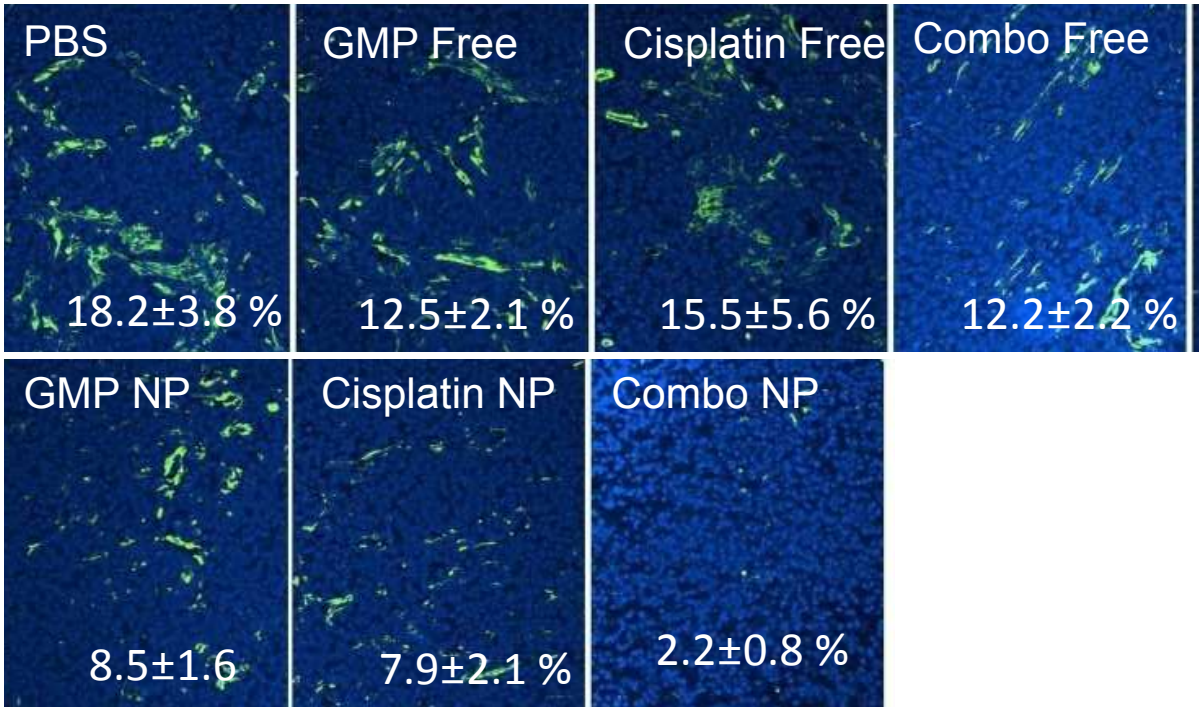

Figure 5.2 Effects of different treatments on the inhibition of fibroblast growth

Fibroblasts were shown as αSMA positive cells (green). Quantitative results were analyzed by Image J and shown as white insert.

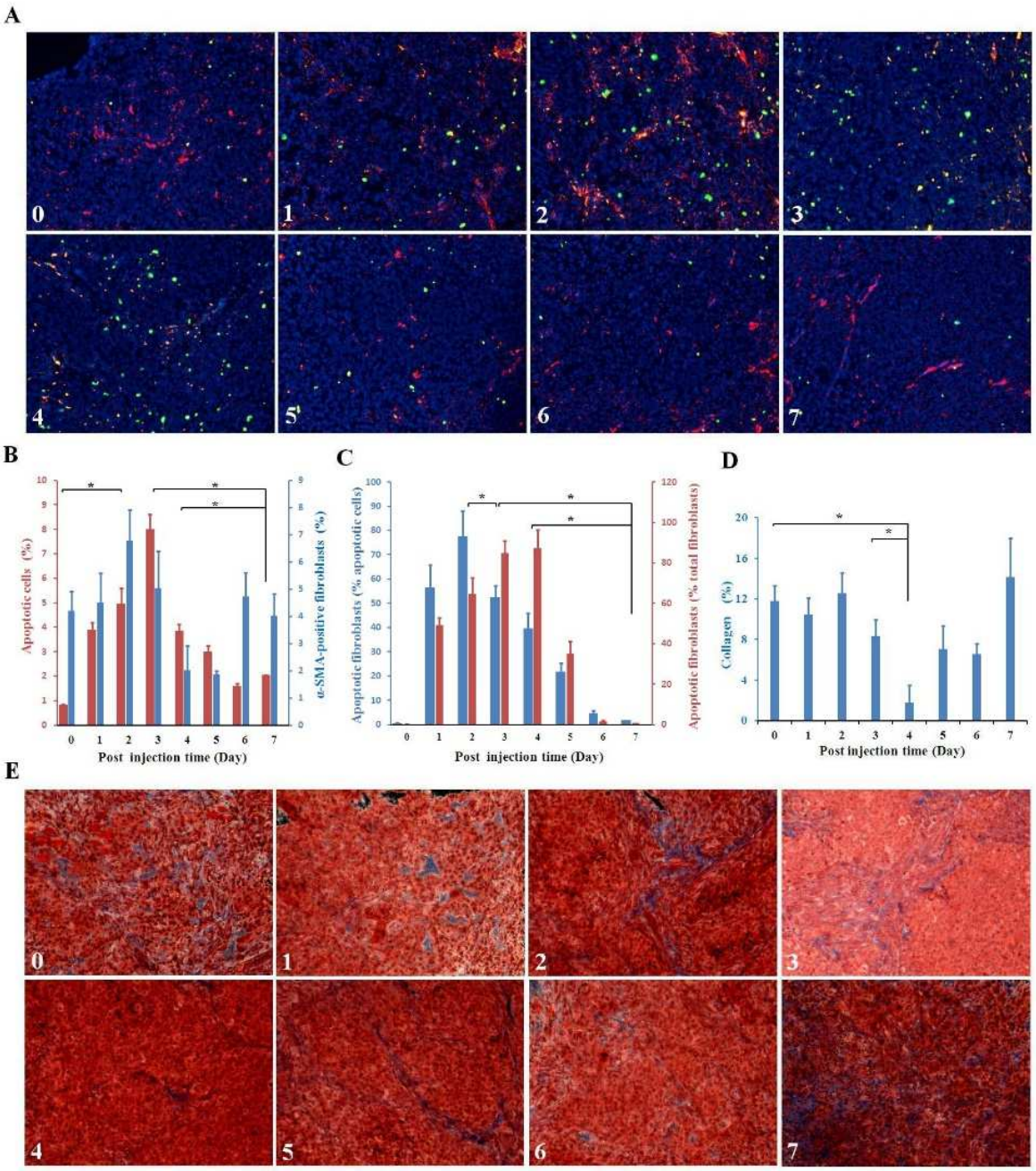

Figure 5.3 Stroma depletion after single dose of combo NPs.

A. Immunofluorescence double staining for αSMA-positive fibroblasts (red), TUNEL (green) and apoptotic fibroblasts (yellow). B. Quantitative results for TUNEL-positive cells and αSMA-positive fibroblasts. C. Quantitative results for apoptotic fibroblasts expressed as the percentage of total apoptotic cells and fibroblasts. D. Quantitative results for collagen expressed by the area (%). E. Masson's trichrome stain for collagen (blue) in tumor-bearing mice treated with a single injection of the Combo NP. Tumors were excised on Day 0 and every 24 h for 7 days for analysis and expressed as 0 (Day 0) to 7 (Day 7) in the image. * P <0.05.

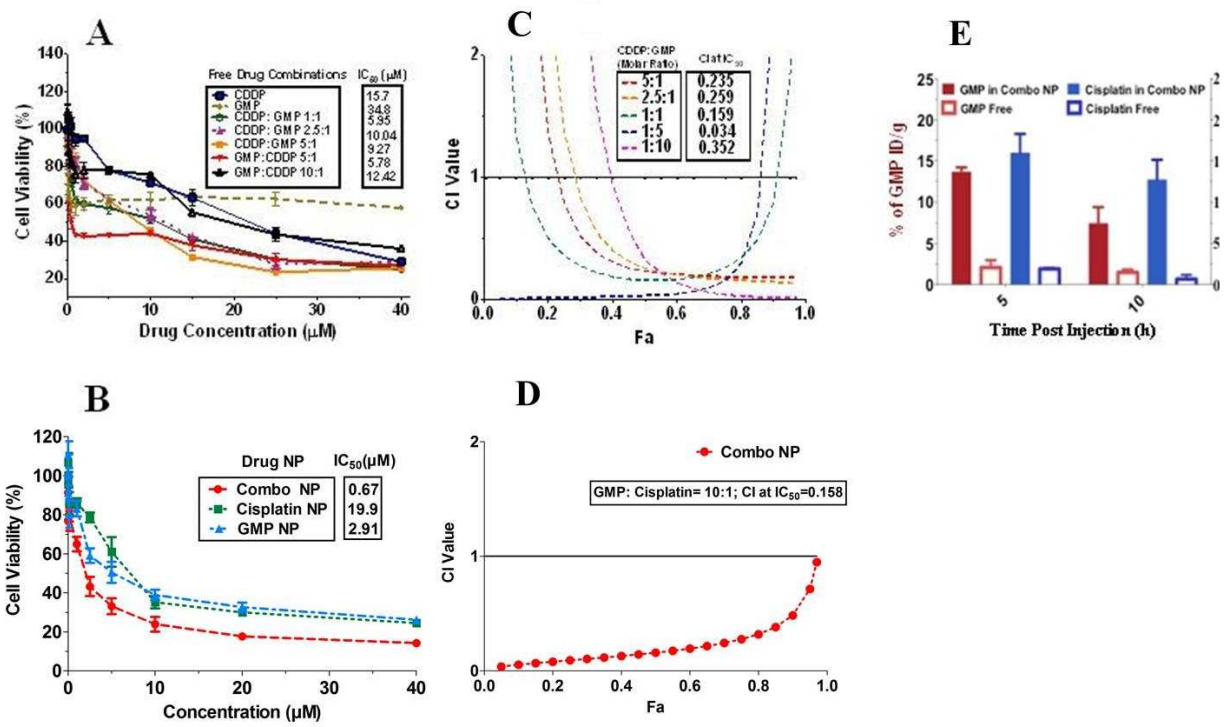

Figure 5.4 *In vitro* sensitivities of UMUC3 and NIH3T3 to GMP and cisplatin

Cytotoxicity study of free drug combination (A) and drug nanoparticles combination (B) at variable molar ratios; the corresponding CI vs Fa plot for free drug combination (C); the corresponding CI vs Fa plot for drug nanoparticles combination (D), and tumor accumulation of GMP NP and GMP Free (Red bars) and Cisplatin NP and Cisplatin Free (Blue bars) at 5 h and 10 h after administration (n = 3) (E).

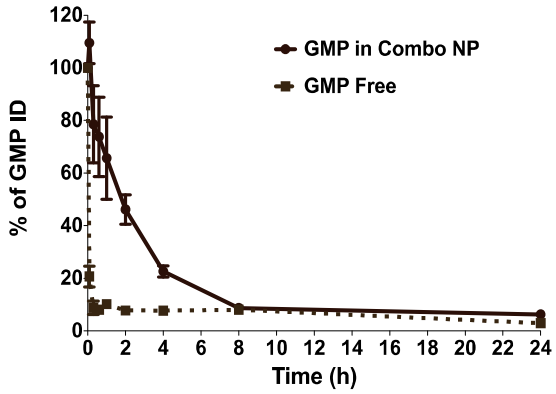

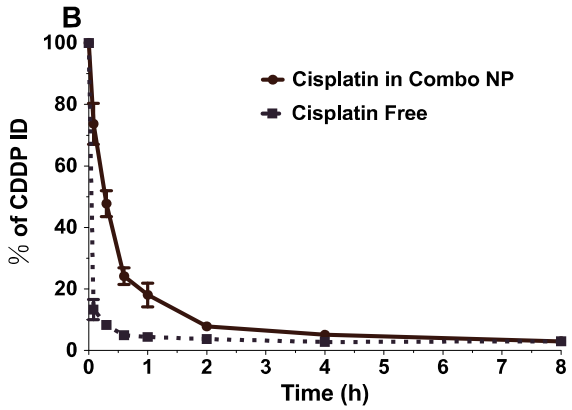

Parameter	GMP NP	GMP Free
AUC (0-t) (mg/L*h)	866.6±43.4	144.7±0.9
$T_{1/2}$ (h)	3.4±1.8	-

Parameter	GMP NP	GMP Free
AUC (0-t) (mg/L*h)	16.7±2.5	11.9±7.2
$T_{1/2}$ (h)	2.41±0.9	-

Figure 5.5 Pharmacokinetics profiles of GMP (free or NPs) and cisplatin (free or NPs).

Pharmacokinetic parameters were calculated and listed in the tables. (n = 4)

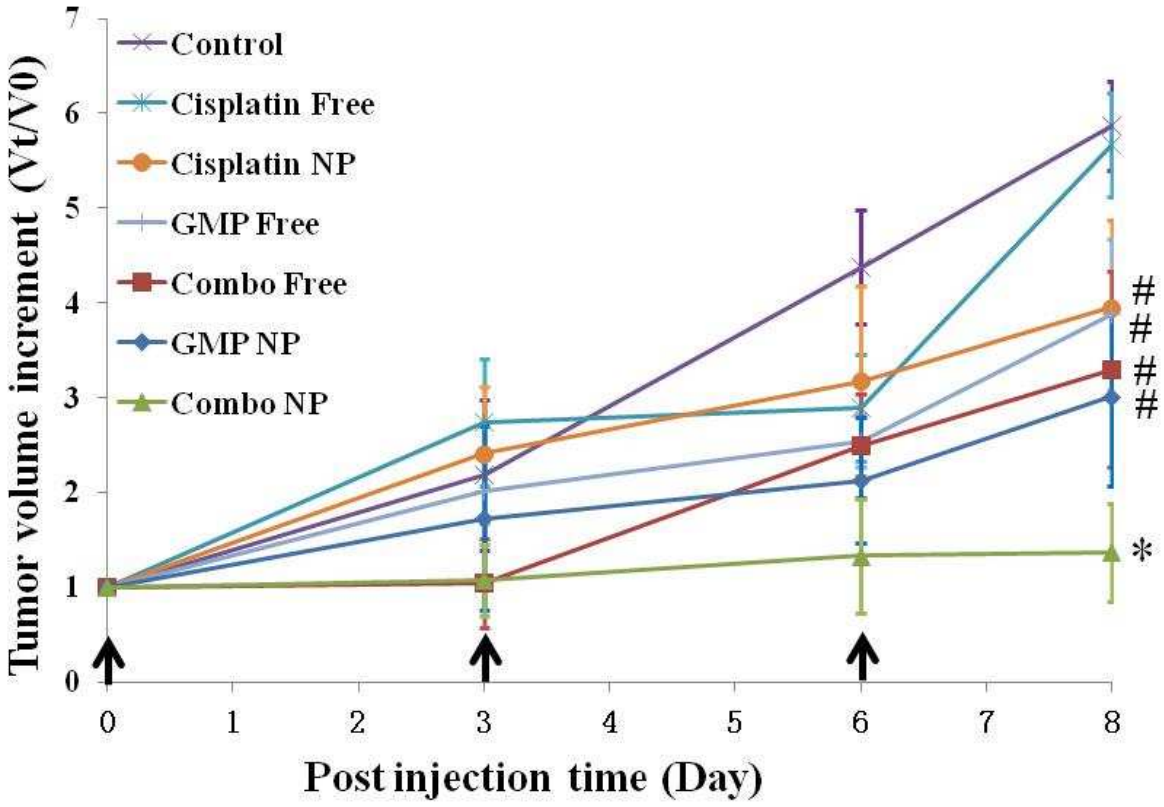

Figure 5.6 Tumor growth inhibition effects of different formulations on desmoplastic bladder cancer model (UMUC3/3T3)

GMP Free, Cisplatin Free, Combo Free, GMP NPs, Cisplatin NPs and Combo NPs were administered intravenously every third day for total three injections. Data are mean ± S.D. Statistics are as follows: * $P < 0.05$ vs. Control; #$P < 0.05$ vs. Combo NP; there is no significant difference among groups marked with "#", n = 5.

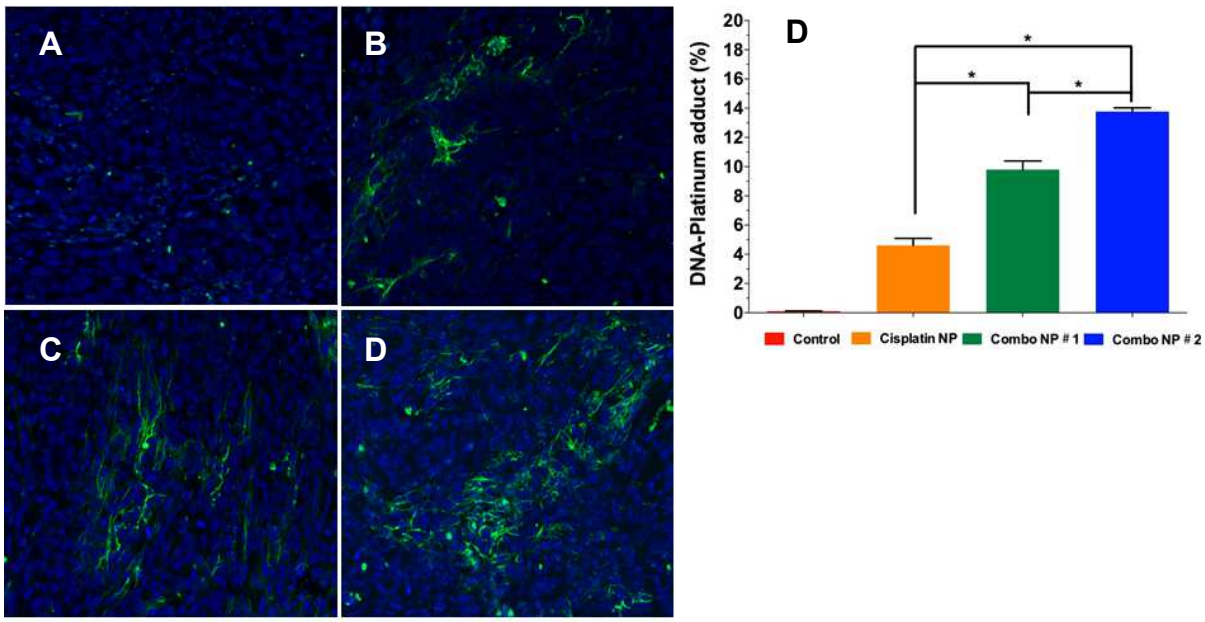

Figure 5.7 DNA-Platinum adduct formation after combo NPs treatment

The detection of DNA-Platinum adduct (green) (20×) of Control group (A),Cisplatin NP (Cisplatin: 1.6 mg/kg) (B), Combo NP #1 (Cisplatin: 1.6 mg/kg, GMP: 12 mg/kg) (C) and Combo NP #2 (Cisplatin: 1.6 mg/kg, GMP: 16 mg/kg) (D); E. Quantitative results expressed as the percentage of DNA-Platinum adduct of each group. *: $P < 0.05$.

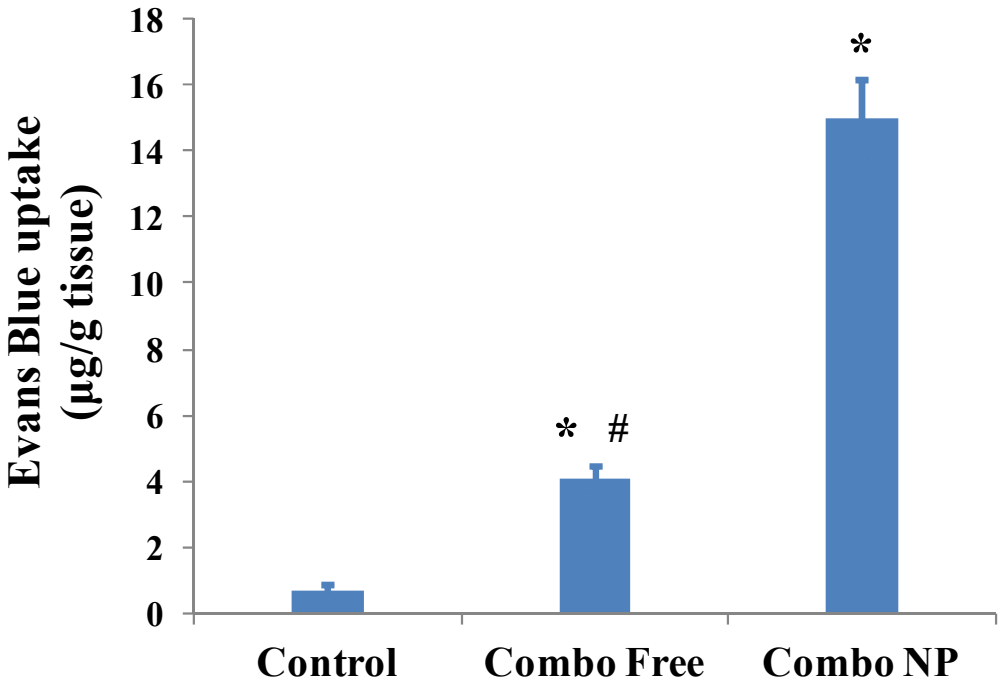

Figure 5.8 Evaluation of the tumor vessel leakiness

Evans Blue staining of mice to determine tumor vessel leakiness. Mice were injected with 100 mg/kg of Evans blue. After 30 min, the mice were sacrificed, and samples from the tumors were removed. The concentration of Evans Blue was then determined spectrophotometrically. Results are shown as the mean weight of Evans Blue per gram tissue. * $P < 0.05$ vs. Control; # $P < 0.05$ vs. Combo NP (n = 3).

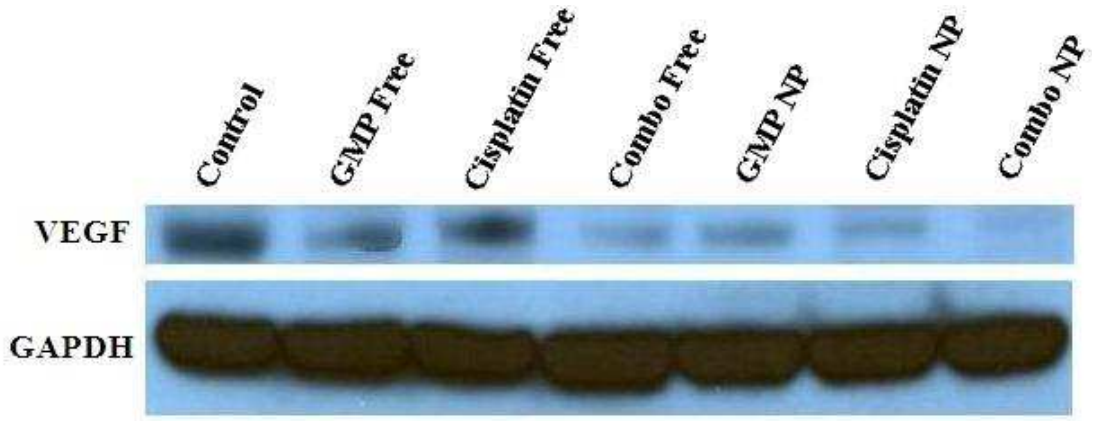

Figure 5.9 Effects of the combination of GMP NPs and Cisplatin NPs on VEGF expression in UMUC3/3T3 bearing mice

CHAPTER 6: NANOPARTICLES WITH PRECISE RATIOMETRIC CO-LOADING AND CO-DELIVERY OF GEMCITABINE AND CISPLATIN FOR TREATMENT OF DESMOPLASTIC BLADDER CANCER[7]

6.1 Summary

Previous chapter shows that combination of gemcitabine monophosphate (GMP) NPs and cisplatin NPs is an efficient stroma depletion strategy and also a potent management of malignancy. Synergistic therapeutic outcome is only achieved when cells are exposed to the two regimens at an optimal ratio. However, due to diverse physicochemical properties of gemcitabine and cisplatin, no free drug cocktails or nanomaterials are capable of co-loading and co-delivering these two drugs at an optimal ratio. Herein, we develop a novel nano-platform with precise ratiometric co-loading and co-delivery of gemcitabine and cisplatin for synergistic anti-tumor effects. Based on previous work, we utilize a solvent displacement method to ratiometrically load dioleoyl phosphatidic acid (DOPA)-gemcitabine monophosphate (GMP) and DOPA coated cisplatin-precipitate nanocores into the same PLGA NPs. These cores are designed to have similar hydrophobic surface properties. GMP and cisplatin are engineered into PLGA NPs at an optimal synergistic ratio (5:1, mol:mol) with over 70% encapsulation efficiency and were ratiometrically taken up by tumor cells in vitro and in vivo.

[7]This chapter previously appeared as a research article in *Advanced Functional Materials*. The original citation is as follows: Lei Miao, Shutao Guo, Jing Zhang, William Y. Kim and Leaf Huang, Nanoparticles with precise ratiometric co-loading and co-delivery of gemcitabine monophosphate and cisplatin for treatment of bladder cancer, Advanced Functional Materials, 2014, 24 (42):6601-6611. Shutao Guo was listed as a co-first author

These PLGA NPs exhibit synergistic anti-cancer effects in the desmoplastic bladder cancer model (UMUC3/3T3). A single injection of dual drugs in PLGA NPs can significantly inhibit tumor growth. This nanomaterial-system solves problems related to ratiometric co-loading and co-delivery of different hydrophilic moieties and provides possibilities for co-loading hydrophilic drugs with hydrophobic drugs for combination therapy.

6.2 Introduction

Combination therapy is particularly effective in the treatment of HIV/AIDs and cancer. It provides a general means to maximize therapeutic efficacy, overcome treatment resistance, and diminish adverse effects [267, 268]. Optimized doses and molar ratios of combined drugs are critical to promote synergistic rather than antagonistic effects [269-271]. However, differential pharmacokinetics and distribution of individual drugs within the conventionally administered "cocktail" lead to deviation from the optimized ratio during systemic delivery. This fact makes predicting improved *in vivo* therapeutic outcomes from *in vitro* synergistic effects a real clinical challenge [272]. Nanomaterial-based delivery is one approach to unifying dual-drug pharmacokinetics [271]. However, it is rather difficult to load drugs with drastically different physical chemistry into the designed nano-carriers, which is why only a few nanoparticulate formulations [273-276] were able to reach the goal. Although attempts have been made, precise loading and ratiometric delivery of drugs with diverse solubility, steric configuration and other physicochemical properties still remains a challenge.[277, 278] Moreover, combining individual therapeutic blocks together without interference their own functionalities adds to the complexity of compact nanostructures for combination drug delivery [279, 280].

Cisplatin is considered the gold standard in several first-line combination therapies.[281] A nano-particulate approach used to enhance the ratio-dependent synergistic cisplatin-related combination therapy is rarely reported due to the difficulties in loading cisplatin along with other types of drugs into a single NPs and the possible chemical interference with other groups of drugs

such as nucleic acids [196, 282]. Limited solubility of inorganic cisplatin in both water and oil significantly hinders the development of NPs with high drug loading and encapsulation efficacy [177]. Gemcitabine monophosphate (GMP), an organic hydrophilic drug, was chosen for combination therapy with cisplatin. It is well known that Gemcitabine is widely used as a first line therapy in combination with cisplatin for the treatment of bladder cancer. However, Gemcitabine relies on nucleoside transporters [283] to enter into cells where it is subsequently phosphorylated by deoxycytidine kinase to form active intermediates for DNA synthesis interference. GMP is one of the active intermediates of Gemcitabine [284]. Since the addition of the first phosphate group in GMP formation is the rate-limiting step, we anticipate GMP to be an efficient therapeutic drug candidate with great commercial value that can exhibit a synergistic effect in combination with cisplatin [285, 286]. Due to the significant difference in physicochemical properties, co-encapsulation of cisplatin and GMP is difficult. Therefore, NPs that can ratiometrically co-encapsulate and co-deliver native cisplatin and GMP while not compromising the drug activity, are highly desired.

In the previous chapter, we have prepared dioleoyl phosphatidic acid (DOPA) coated calcium phosphate cores with the capability of loading GMP (GMP core) [287]; as well as DOPA coated cisplatin cores (CP core), where cisplatin serves as both nanocarrier and anti-cancer drug [177, 288]. The surface and size similarities between these two categories of cores provide us a methodology to unify these two drugs with drastically disparate solubility and polarity into a standardized hydrophobic physicochemical property. Unifying physicochemical characteristics of dual drugs is the prerequisite for ratio-controlled loading and delivery.

Based on this rationale, we report a novel strategy to achieve both precise ratiometric loading and delivery of cisplatin with GMP. Cisplatin and GMP were originally formulated into DOPA coated CP cores and DOPA coated GMP cores. As shown in **Figure 6.1A**, PLGA NPs are used to incorporate these two separate hydrophobic cores through the solvent displacement method. Ratiometric loading of GMP and cisplatin were first examined. With the confirmation of ratiometric loading property of PLGA NPs, we further proposed that this dual-drug containing NPs could be

ratiometrically delivered to the site of malignancy at the optimal ratio (**Figure 6.1B**). This hypothesis was tested *in vitro via* release kinetics study and cellular uptake study, and *in vivo* via tumor accumulation analysis. We then hypothesized that co-delivery of both drugs at an optimized ratio would result in synergistic anticancer efficacy. A stroma-rich human bladder cancer xenograft model was used to evaluate the anti-tumor efficacy of dual-drug containing NPs at optimized ratio [289]. Synergistic anti-cancer effect was further determined *via* protein based mechanistic analysis. To our knowledge, this is the first time that cisplatin has been reported to be co-encapsulated with another hydrophilic drug in the same NPs with precise ratiometric control.

6.3 Materials and Methods

6.3.1 Chemicals and Materials

Cisplatin was purchased from Sigma-Aldrich (Dorset, UK). Gemcitabine monophosphate disodium salt (GMP, purity ≥97%) was kindly provided by Qualiber, Inc. (Chapel Hill, NC). Dioleoyl phosphatidic acid (DOPA) was purchased from Avanti Polar Lipids, Inc. (Alabaster, AL). tBOC-PEG_{3500}-NH_2.TFA and $mPEG_{3000}$-NH_2.HCl were ordered from JenKem Technology USA Inc. (Allen, TX). Acid terminated PLGA was purchased from DURECT Corporation (Cupertino, CA). p-Anisic acid, EDC, NHS, DIPEA, dichloromethane, Igepal® CO-520, triton™ X-100, cyclohexane and silver nitrate were obtained from Sigma-Aldrich (St Louis, MO) without further purification.

6.3.2 Cell Culture and Animals

The human bladder transitional cell line UMUC3, kindly provided by Dr. William Kim (University of North Carolina at Chapel Hill, NC), and the mouse embryonic fibroblast cell line NIH3T3 (UNC Tissue Culture Facility) were cultured in Dulbecco's modified Eagle's Media (DMEM) (Invitrogen, Carlsbad, CA) supplemented with penicillin (100 U/mL), streptomycin (100 μg/mL) (Invitrogen), and 10% fetal bovine serum (Sigma, St. Louis, MO)/10% Bovine calf serum (Hyclone, Logan, Utah), respectively. Cells were cultivated in a humidified incubator at 37 ºC with 5% CO_2 and harvested with 0.05% trypsin-EDTA before subculture.

Female athymic nude mice, 6-8 weeks of age and weighting 18-22 g were supplied by the University of North Carolina animal facility and used in all studies. Animals were maintained in the Center for Experimental Animals (an AAALAC accredited experimental animal facility) at the University of North Carolina. All procedures involving experimental animals were performed in accordance with the protocols approved by the University of North Carolina Institutional Animal Care and Use Committee and conformed to the Guide for the Care and Use of Laboratory Animals (NIH publication No. 86-23, revised 1985).

6.3.3 Synthesis of PLGA-PEG-MBA and PLGA-mPEG

Briefly, for the synthesis of PLGA-PEG-MBA, tBoc-PEG_{3000}-NH_2.HCl (1 eq), Anisic acid (8 eq) and DIPEA (4 eq) were dissolved in DCM and added with DIC (8 eq) to react for 26 h to obtain MBA-PEG-Boc. After purification and structure confirmation by NMR, Boc was removed using a TFA/DCM (1:2, v/v) mixture to achieve MBA-PEG-NH_2.TFA. Afterwards, MBA-PEG-NH_2.TFA was conjugated to PLGA (15 kDa, 0.1 mmol) in the presence of DIPEA and DIC for 26 h and purified. PLGA-PEG-MBA structure was confirmed by NMR. In the synthesis of PLGA-mPEG, mPEG-NH_2.TFA (3000, 0.126 mmol), PLGA (15 kDa, 0.1 mmol) and DIPEA (0.5 mmol) were dissolved in 6 ml DCM and reacted with DIC (1.0 mmol) for 24 h.

6.3.4 Preparation of CP cores and GMP cores.

Preparations of CP cores and GMP cores were described in the previous chapter.

6.3.5 Preparation of PLGA/PLGA-PEG/PLGA-PEG-MBA (4:4:2) NPs (PLGA NPs) Loaded with cores

Drug encapsulated cores were loaded into PLGA NPs using a single step solvent dispersion method. Briefly, the cores and 2 mg of polymers were dissolved in 200 μl of THF and added dropwise into 2 ml of water under constant stirring at room temperature. The resulting NPs suspension was allowed to stir uncovered for 6 h at room temperature to remove the THF. The NPs were further purified by ultrafiltration (15 min, 3000 × g, Amicon Ultra, Ultracel membrane with

50,000 NMWL, Millipore, Billerica, MA). Then, the PLGA NPs were re-suspended, washed with water, and centrifuged at 14,000 rpm for 20 min to remove free lipids and micelles, re-suspended and centrifuged again at 800 rpm to remove nanocore aggregations.

6.3.6 Characterization of PLGA NPs

DL and EE of cisplatin were measured using Inductively Coupled Plasma-Mass Spectroscopy (ICP-MS, NexIONTM 300, Perkin Elmer Inc); LE and EE of GMP were measured both by Ultraviolet–Visible Spectrometer (UV, DU®800, Beckman Coulter) and ^{3}H labeled cytidine 5' monophosphate (CMP) [5-^{3}H] disodium salt (Moravek Bio Inc, 1 mCi/mL) incorporation using a Liquid Scintillation Analyzer (TRI-CARB 2900 TR, Packard Bioscience Co). The size distribution of particles was determined using a Malvern ZetaSizer Nano series (Westborough, MA). TEM images of NPs were acquired using a JEOL 100CX II TEM (JEOL, Japan). The NPs were negatively stained with 2% uranyl acetate. The composition of PLGA combo NPs was studied using Electron Dispersive Spectroscopy (EDS) (Oxford instruments, INCA PentaFET -x3) and X-ray photoelectron spectroscopy (XPS) (Kratos Axis Ultra DLD X-ray Photoelectron Spectrometer).

6.3.7 Cellular Uptake Study in UMUC3 Cell Lines

UMUC3 cells were seeded into a 12-well plate (1.5×10^{5} cells/well) containing 1 ml of media. Twenty-four hours later, 1 ml of the free drug combination, targeted PLGA Combo NPs, targeted PLGA Sepa NPs, 20%-targeted PLGA Combo NPs and non-targeted PLGA Combo at a concentration of 20 μM GMP and 3.8 μM cisplatin were incubated with cells in a serum-free medium. Four hours later, cells were treated with RIPA buffer (Sigma-Aldrich). The concentration of cisplatin was measured using ICP-MS and GMP was measured as ^{3}H-CMP using a scintillation counter as previously mentioned.

6.3.8 *In Vitro* Release and Intracellular Release of cisplatin and GMP from PLGA NPs

The dialysis technique was employed to study the *in vitro* release of GMP and cisplatin from PLGA in phosphate buffered saline (PBS) (pH 7.4) at 37 °C. Five hundred μL PLGA NPs loaded with 100 μg/mL GMP and cisplatin separately or co-loaded with 100 μg/mL GMP and cisplatin at a ratio of 5.33:1 were added into the dialysis tube with a molecular weight cut off of 3000 Da and dialyzed against 15 mL PBS (pH 7.4) in a thermo-controlled shaker with a stirring speed of 200 rpm at 37 °C for 96 h. In the preparation of GMP cores, a trace amount of radioactive ^{3}H-CMP was mixed with GMP to serve as a marker for the entrapped GMP. At each predetermined time point, 400 μL samples were withdrawn and replaced with fresh media. Platinum and GMP concentrations were then determined by ICP-MS and scintillation analyzer respectively at specified times. All experiments were performed in triplicate and the data were reported as the mean ± SD of the three individual experiments. Intracellular release of free drugs from the cargos was carried out according to a previous protocol. A twelve-well plate of UMUC3 cells was prepared as is mentioned in the uptake study and incubated with 20 μM GMP and 3.8 μM cisplatin encapsulated into PLGA Combo NPs. After 1, 4, and 16 hours, the cells were treated with 50 μL RIPA buffer (Sigma-Aldrich) at 4°C for 10 min and the cell lysate was centrifuged at 14,000 rpm for 20 min at 4°C to separate nanoparticle and cell lysate from free drugs. Free Drugs and Nanoparticles were measured using ICP-MS and ^{3}H-labeled scintillation. All experiments were performed in four replicates and the data reported as the mean ± SD of three.

6.3.9 *In vitro* Cell Viability on UMUC3 Cells and Analysis of Synergistic Effects of Drug Combinations

MTT (3-[4,5-dimethylthiazol-2-yl]-2,5-diphenyltetrazolium bromide) assay was conducted to evaluate *in vitro* viability of free GMP, cisplatin and their combinations as well as PLGA GMP NPs, PLGA cisplatin NPs and PLGA Combo NPs. In Brief, cells were seeded in 96-well plates at a density of 3,000 cells per well 24 h prior to drug treatment. Subsequently, cells were treated with free drugs and the drug combination with various molar ratios at a series of dilutions in full medium. Following

48 h of treatment, 20 μL MTT (5 mg/mL) reagent was added for an additional 4 h incubation period at 37 °C. The medium was discarded, the formed formazan salt was dissolved in 150 μL of DMSO and absorbance was read at 570 nm using a multidetection microplate reader (Plate CHAMELEON™ V-Hidex). Cell survival rates were calculated as normalized to untreated control wells. Each concentration was tested in five wells and data presented as mean ± SD. The mean drug concentration required for 50% growth inhibition (IC50) was determined with CompuSyn software (Version 1.0, Combo-Syn Inc., U.S.) using the median effect equation: $Fa=[1+(IC_{50}/D)^{m}]^{-1}$, where Fa is the fraction of affected cells, D is drug concentration and m is the Hill slope.

Combination Index (CI) Analysis of free drug combination based on the Chou and Talalay method[290] was conducted using CompuSyn software. Briefly, for each level of Fa, the CI values for GMP and Cisplatin combinations were calculated according to the following equation: $CI=(D)_1/(D_x)_1+(D)_2/(D_x)_2$, where $(D)_1$ and $(D)_2$ are the concentrations of each drug in the combination resulting in Fa×100% growth inhibition, and $(D_x)_1$ and $(D_x)_2$ are the concentrations of the drugs alone resulting in Fa×100% growth inhibition. CI values for drug combinations were plotted as a function of Fa. CI values less than 1 or more than 1 demonstrate synergism or antagonism of drug combinations, respectively. Notably, CI values between Fa 0.2 to 0.8 are considered validate.[291]

6.3.10 Tumor Accumulation of GMP and Cisplatin in Stroma-rich Xenograft Bladder Tumor Model

A stroma-rich subcutaneous xenograft bladder tumor model was established previously in our lab (ref). Briefly, UMUC3 (5×10^6) and NIH3T3 cells (2×10^6) in 100 μL of PBS were subcutaneously co-injected into the right flank of mice with Matrigel (BD Biosciences, CA) at a ratio of 3:1 (v/v). When the tumor reached 100-150 mm^2 in size, animals were randomly divided into three groups (n=8) and intravenously injected with free GMP containing a trace fraction of ^{3}H-CMP and cisplatin (Combo Free), PLGA Combo NPs and PLGA Sepa NPs at a dose of GMP 12 mg/kg and cisplatin 1.9 mg/kg respectively. Four mice from each group were sacrificed at each predestined time point, and approximately 45 mg of blood was withdrawn using the tail bleeding method. Tumor uptake of GMP

and cisplatin was expressed as the percentage of the injected dose per gram tumor. For measurement of GMP, 10 to 20 mg of blood was immediately mixed with 10× NCS® II Tissue Solubilizer (Amersham Biosciences, Inc) and digested at 60°C overnight. Three hundred μL of hydrogen peroxide (30% in water, Fisher) was added to the samples and vortexed to bleach the blood color, and the sample was then mixed with 4 mL scintillation cocktail (Fisher Inc). The ^{3}H radioactivity in the blood samples was counted using a liquid scintillation analyzer (TRI-CARB 2900 TR, Packard Bioscience Co.). For the measurement of cisplatin, 25 to 35 mg of blood was digested with 400 μL 60% nitric acid (Acros Organic) at 70°C overnight and measured by ICP-MS.

6.3.11 Biodistribution of Dual Drug in Major Organs

Mice were administered a single dose of Combo Free, PLGA Sepa NPs and PLGA Combo NPs respectively at the dose of 1.9 mg/kg cisplatin and 12 mg/kg GMP. Each group contained four mice, which were sacrificed 10 h following injection. Tissue samples were digested as previously mentioned in the tumor accumulation study and proceeded to quantify cisplatin *via* ICP-MS and GMP *via* scintillation counter.

6.3.12 Anti-tumor Efficacy in Desmoplastic Bladder Cancer Xenografts

On day seven after tumor implantation (tumor size 100-150 mm^2), mice were randomized into eight groups (n=5) as follows: Untreated Control (PBS), free GMP (GMP free), free cisplatin (Cisplatin Free), combination of free GMP and cisplatin (Combo free), PLGA GMP NPs, PLGA cisplatin NPs, GMP and cisplatin PLGA NPs mixtures (PLGA Sepa NPs) as well as PLGA Combo NPs. IV injections were performed every three days for a total of three injections with a GMP dose of 12 mg/kg and a cisplatin dose of 1.9 mg/kg. Tumor volume was measured every day. Body weight was also recorded. Mice were sacrificed two days after the last injection by CO_2 asphyxiation and tumors were excised.

6.3.13 TUNEL Assay

TUNEL Assay was described in the previous chapter.

6.3.14 PCNA Assay

Proliferation of tumor cells after the aforementioned treatments and dosing schedule was detected by immunohistochemistry, using an antibody against proliferating cell nuclear antigen (PCNA) (1:200 dilution, Santa Cruz). The immuno-histochemistry was performed using a mouse-specific HRP/DAB detection IHC kit as recommended by the manufacturer (Abcam, Cambridge, MA). The percentage of proliferative cells was obtained by dividing the number of PCNA positive cells (shown as brown dots) from the number of total cells (blue nuclei stained by hematoxylin) in each microscopic field. Ten representative microscopic fields were randomly selected in each treatment group for counting.

6.3.15 Platinum Adduct staining

The platinum-DNA adducts were detected using anti-cisplatin modified DNA antibodies [CP9/19] (Abcam, Cambridge, MA). The sections were incubated with a 1:250 dilution of anti-cisplatin modified DNA antibody [CP9/19] at 4°C overnight followed by incubation with FITC-labeled goat anti-rat Ig antibody (1:200,Santa Cruz, CA) for 1 h at room temperature. The sections were also stained by DAPI and coverslipped. The sections were observed using a Nikon light microscope (Nikon Corp., Tokyo, Japan).

6.3.16 Western-blot Analysis

Twenty-four hours after three daily IV injections, UMUC3 bearing mice were sacrificed and tumor lysates were prepared. Mouse monoclonal poly(ADP-ribose) polymerase-1 (PARP-1) antibodies, mouse monoclonal ERCC1, mouse monoclonal XPA (12F5) and rabbit polyclonal SMA antibodies (1:500 dilution; Santa Cruz biotechnology, Inc.) were used as primary antibodies. β-actin antibody (1:4000 dilution; Santa Cruz biotechnology, Inc.) was probed as the loading control.

6.3.17 Serum biochemical value analysis and hematology assay

After three injections, blood was collected directly from heart and centrifuged at 4000 rpm for 5 min. Serum alanine aminotransferase (ALT), aspartate aminotransferase (AST), blood urea nitrogen (BUN) and creatinine levels were assayed as indicators of hepatic and renal function. Whole blood was collected from healthy nude mice after three repeated treatments. Red blood cells (RBC), white blood cells (WBC), platelets (PLT), hemoglobin (HGB) and hematocrits (HCT) were counted for the detection of myelosuppression. Organs (heart, liver, spleen, lung, kidney) were fixed and sectioned for H&E staining.

6.3.18 Statistical Analysis

Quantitative data were expressed as mean ± SD. The analysis of variance was completed using a one-way ANOVA. $P < 0.05$ was considered statistically significant.

6.4 Results

6.4.1 Preparation and Characterization of Single Drug Loaded PLGA NPs

GMP cores and CP cores were prepared as previously mentioned[177, 287] and characterized as 8-12 nm in diameter as determined by transmission electron microscopy (TEM) (**Figure 6.2**). Encapsulation efficiency (EE) of GMP in the GMP core was 60.6 ± 4.3% as measured by absorbance of GMP at 273 nm. CP cores were also prepared with an EE of 40.4 ± 1.4% as measured by inductively coupled plasma mass spectrometry (ICP-MS). Both GMP cores and CP cores could be well dispersed into organic solvent, such as tetrahydrofuran (THF). The above results indicated that hydrophilic GMP and cisplatin have been successfully loaded into hydrophobic cores respectively and these cores were ready to be further incorporated into PLGA NPs.

High and comparable encapsulation efficiency of each component is a prerequisite for controlled loading of several modalities in the same nanoparticle. Therefore, single drug loaded PLGA NPs were initially investigated and characterized. PLGA NPs were originally conjugated with polyethylene glycol (PEG) to prolong systemic circulation time and then self-assembled with PLGA

and DOPA coated cores into PLGA NPs *via* single step solvent displacement (**Figure 6.1**). Briefly, polymer and drug containing cores were dissolved in THF, a water-miscible solvent, and poured drop wise into water. NPs was formed instantaneously during this rapid solvent diffusion process. AA, an agonist of the Sigma R, was also introduced into PLGA NPs as a ligand to enhance internalization in epithelium-derived cancer cells, which overexpress the Sigma R [292, 293]. Results in **Figure 6.3** indicate that both GMP and cisplatin in DOPA coated core structures can be encapsulated into PLGA NPs separately with high EE (70.6 ± 2.5% and 74.0 ± 10.1%, respectively) at drug loading (DL) of up to approximately 5 wt%. This is the first time that GMP and cisplatin have been engineered into PLGA NPs using solvent displacement method. This method proved much more efficient than loading free gemcitabine and cisplatin into PLGA NPs *via* the double emulsion method, whose maximum loading is only around 1 wt% [294, 295]. Notably, free cisplatin and GMP are quite polar and cannot be loaded into PLGA NPs using the solvent displacement method; and thus, DOPA coated cores not only provide an approach to load different types of drugs, especially hydrophilic drugs, into PLGA NPs using solvent displacement, but also facilitate hydrophilic drugs to be loaded into PLGA NPs with higher DL and EE. More importantly, the EE for single free drugs in PLGA NPs using this novel preparation method is quite comparable to each other, suggesting the possibility of loading different drug moieties simultaneously into the same NPs at similar EE but different dual-drug ratios，which is one indispensable parameter for ratiometric loading.

6.4.2 Precise Ratiometric Control over Dual-Drug Loading in Combo NPs

The success of loading GMP cores and CP cores into PLGA NPs provides us with the possibility to encapsulate two different drug-containing cores into a single NPs in a ratiometric manner. To confirm that CP cores and GMP cores can be ratiometrically co-loaded into PLGA NPs (Combo NPs), several further studies were investigated. Firstly, total feed loading of GMP and cisplatin in Combo NPs was fixed at 6 wt% while the feed molar ratio between GMP and cisplatin was altered from 0.5:1 to 5:1 (**Figure 6.4A**). Results indicated that the measured molar ratio between

the two drugs in Combo NPs was almost the same as the feed molar ratio (0.52 vs 0.5; 0.97 vs 1; 3.3 vs 3, 5.3 vs 5) and the EE of both drugs, which all remained above 70% with subtle fluctuation, was almost identical as well. Next, the feed molar ratio of GMP to cisplatin was set at 5 (**Figure 6.4B**). It was found that the measured molar ratio of GMP to cisplatin in Combo NPs was approximately 5 when the total loading of the two drugs was below 6 wt%. Additionally, greater than 80% EE was achieved. In both experiments, particle size measured by dynamic light scattering (DLS) was under 120 nm and polydispersity of the dual drug particles was around 0.2 (**Figure 6.5)**. Thus, these results demonstrated that ratiometric loading of distinct types of drugs in DOPA coated cores could be achieved over a wide dual drug ratio range and loading efficiency.

6.4.3 Characterization of Dual-Drug Loaded Combo NPs using TEM and XPS

To demonstrate that GMP cores and CP cores are homogenously distributed in each Combo NPs, we further characterized the Combo NPs with total drug feeding ratio of 6 wt% and feed GMP/cisplatin ratio of 5, whose determined loading was 5.5 ± 0.8 wt% and molar ratio between GMP and cisplatin was 5.3. TEM revealed Combo NPs as spherical and mono-dispersed with a diameter of approximately 90-120 nm (**Figure 6.4C**), which is consistent with the value measured by DLS (average 120 nm) (**Figure 6.6**). In addition, large quantities of well-dispersed cores were clearly clustered in each NPs, further confirming the hypothesis of a nanocapsule-like structure with high and efficient drug loading. Notably, each NPs contained a similar amount of cores. However, TEM result alone cannot show the homogeneous distribution of cores in NPs. Therefore, we further characterized the Combo NPs using high resolution TEM with energy dispersive spectroscopy (EDS) analysis and x-ray photoelectron spectroscopy (XPS). Chemical element analysis using EDS indicated that both fluorine (characteristic element of GMP) and platinum (characteristic element of cisplatin) were present in single NPs (**Figure 6.4D**). Over 20 particles were analyzed to determine the average molar ratio of GMP and cisplatin inside each NPs. The ratio of fluorine to platinum, representing the ratio of GMP to cisplatin, was approximately 4.9 ± 1.9, which is comparable to the feed ratio of 5 and the

determined ratio in bulk solution of 5.3. This result demonstrated that the two distinct cores were present in single NPs and their ratio was precisely controlled. To avoid disturbance of neighboring oxygen on fluorine quantification, XPS was carried out to further confirm the ratiometric distribution of the two drugs. Combo NPs was dissolved in THF, and a 5 nm layer of particle lysates were analyzed by XPS. The spectrum in **Figure 6.4E** indicates that fluorine could be separated well from oxygen, and the calculated molar ratio of GMP to cisplatin was approximately 5.6, similar to the results determined using other techniques. Therefore, quantifications from the single particle nano-layer of particle lysate as well as the bulk solution strongly suggest the fact that the dual-drug combination has been successfully, homogenously loaded into single Combo NPs with relatively precise ratiometric control.

6.4.4 *In Vitro* Ratiometric Control over Dual-drug Cellular Uptake

In vitro synergy studies of free cisplatin and GMP (Combo free) using Chou-Talalay method [290] indicated that Combo free exhibited the strongest synergy at a GMP/cisplatin ratio of 5 in human urinary bladder carcinoma UMUC3 cell line [289]. We incorporated ^{3}H-labeled CMP (cytidine monophosphate) into single GMP cores in PLGA NPs (GMP NPs) as a marker to detect the concentration of GMP. *In vitro* cellular uptake (**Figure 6.6**) of free GMP and free cisplatin indicated that UMUC3 cells exhibited an equivalent uptake of GMP and cisplatin, suggesting that the feed ratio and the actual intracellular ratio of the drug combination was almost identical in the *in vitro* assay (**Figure 6.7A**). However, the uptake of drugs in the tumor cells *in vivo* will be much different due to differing PK profiles and the complicated tumor microenvironment. In order to maintain the ratio of drugs *in vivo* and utilize the strongest synergy of Combo free at a GMP/cisplatin ratio of 5, PLGA NPs with a total drug loading of 5.5 ± 0.8 wt% and molar ratio between GMP and cisplatin of 5.3 were further investigated in the following studies. Single drug PLGA NPs with a feed ratio of 6 wt% was used for comparison (**Table 6.1**). Notably, the size of CP cores in single PLGA NPs (cisplatin NPs) was smaller (approximately 60 nm) than that of GMP NPs and Combo NPs. This is not

surprising considering that CP cores are denser than GMP cores which are mainly composed of calcium phosphate.

Ratiometric cellular uptake of both GMP and cisplatin by UMUC3 cells is a prerequisite to evaluating synergistic effects. Cellular uptake of GMP and cisplatin in separate NPs was compared with that of the dual-drug combination in Combo NPs (**Figure 6.7A**). Results indicated that Combo NPs ratiometrically transported drugs into cells, which is consistent with the results from Combo free, while a mixture of separate NPs (Sepa NPs) cannot maintain the predetermined ratio of drugs because smaller cisplatin NPs deliver their cargo into cells more efficiently than the larger GMP NPs. This ratiometric uptake of Combo NPs was also observed over a longer incubation of NPs with cells (**Figure 6.7B**).

6.4.5 *In Vitro* Ratiometric Control over Dual-drug Release from PLGA NPs

After verifying that Combo NPs can ratiometrically transport the drugs into cells, we then studied the extracellular and intracellular release of Combo NPs. The *in vitro* release kinetics of cisplatin and GMP from Combo NPs, cisplatin NPs and GMP NPs were first investigated *via* dialysis in PBS (pH=7.4) at 37 °C for 96 h. The amount of platinum released from NPs was measured by ICP-MS, while ^{3}H-labeled CMP served as a marker for the measurement of GMP. It is notable that only negligible burst release was observed when the drugs inside DOPA-coated cores were encapsulated in PLGA NPs (**Figure 6.7C**), although burst release phenomenon is well known and commonly observed for hydrophilic drugs in PLGA nanoparticulate formulation [294-296]. For example, cisplatin incorporated $PLGA_{15K}$-PEG_{5000} NPs have shown a burst release in the initial 4 h with a release fraction of approximately 50% and gemcitabine encapsulated PLGA NPs have shown 60% liberated drug in the initial 6 h [294, 297]. This suggests that the DOPA layer prevents burst release of GMP and cisplatin from PLGA NPs. Release kinetics of these two drugs in combination was further analyzed by grouped *t*-tests, which showed that there was no significant difference between these two drugs (P = 0.78). This observation suggests that dual drugs in Combo NPs followed a

ratiometric release profile. The subtle difference in release rate may be due to the different composition of CP cores and GMP cores, yet the difference can be neglected when compared to the release rate of drugs from PLGA NPs, which is a key rate-limiting step of the procedure. This indicates that release of cisplatin and GMP can be controlled at a similar rate and in a ratiometric manner when co-encapsulated into single PLGA NPs.

Intracellular release of drugs from Combo NPs was then studied. UMUC3 Cells were first incubated with Combo NPs for 1, 4, or 16 h and subsequently washed. At each time points, cells were lysed with RIPA buffer, followed by separation of NPs and free drugs *via* centrifugation at 16,000 g for 20 min. We found this method can extract more than 98% of NPs and free drugs from cells with little destruction of NPs. Results in **Figure 6.7D** indicated that a controlled and ratiometric release of cisplatin and GMP were also observed in the UMUC3 at the cellular level.

6.4.6 *In Vitro* Synergistic Effect of Combo NPs

The *in vitro* cytotoxicity of free drugs and drug-loaded PLGA NPs were evaluated by using the 3-(4,5-dimethylthiazol-2-yl)-2,5-diphenyltetrazolium bromide (MTT) assay. Results showed that although subtle differences between the half-maximal inhibitory concentration (IC_{50}) of free cisplatin and cisplatin NPs existed, GMP NPs resulted in a much lower IC_{50} of 17.8 μM compared with GMP free drug (IC_{50} of 34.8 μM), indicating that targeted NPs delivery can maintain or enhance the cytotoxicity *in vitro* (**Figure 6.7E**). In addition, data revealed blank PLGA NPs containing CaP core with negligible toxicity (data not shown). To validate the *in vitro* synergistic effect of Combo NPs with dual-drug molar ratio of 5.3:1 (GMP:cisplatin), the combination index (CI) was further determined using the isobologram equation of Chou–Talalay [290]. As shown in **Figure 6.7F**, Combo NPs displayed an overall CI value < 1 when Fa value was in the validated range of 0.2 to 0.8, indicating the pronounced and clear synergy of PLGA combo therapy *in vitro*.

6.4.7 *In Vivo* Anti-cancer Efficacy of Combo NPs on Stroma-riched Bladder Xenograft Tumor Model

As previously mentioned, one of the most fundamental principles behind this formulation is to controllably deliver dual drugs into the tumor with an optimized ratio so as to achieve an enhanced anti-tumor efficacy *in vivo*. Therefore, different treatments were evaluated in an aggressive stroma-rich bladder cancer model, which was established by subcutaneously co-inoculating UMUC3 cells along with fibroblast NIH3T3 cells in matrigel. Tumors were allowed to develop until their volume reached 100~150 mm^3. Tumor bearing mice were then treated with a total of 3 injections at a dose of 12 mg/kg GMP and 1.9 mg/kg cisplatin in Combo NPs. Cisplatin and GMP prepared in separate PLGA NPs (Sepa NPs) were administrated simultaneously in a mixture for comparison. Previous study in our lab has shown that blank PLGA NPs have no tumor inhibition effect [298]. As shown in **Figure 6.8A**, free drugs showed little inhibitory effect at the same dose and dose schedule, possibly due to low tumor accumulation; while single drugs in PLGA NPs demonstrated an enhanced therapeutic efficacy compared with free drugs. This is due to the EPR effect and receptor mediated endocytosis mentioned earlier. Dual drugs in Combo NPs inhibited the growth of UMUC3 tumors most significantly **(Figure 6.8**) without reducing the body weight (data not shown), indicating the enhanced anti-cancer effect and the safety of cisplatin and GMP in combination compared to single drugs. However, when the dual drugs were dosed together in a mixture (i.e., Sepa NPs), tumor inhibition seemed to be compromised and the tumor weight on the last day of measurement was significantly higher than that of the Combo NPs (**Figure 6.8A**). To further confirm the potent anti-cancer efficacy of Combo NPs in the aggressive UMUC3 tumor model, a single injection of high dose Combo NPs was administered and compared with low dose at regular dosing intervals. Results indicated that GMP and cisplatin in single high dose Combo NPs showed potent efficacy, which is comparable to the effect of low dose at regular dosing intervals. Thus, only single injection could inhibit tumor growth in the aggressive stroma-rich tumor model (**Figure 6.8C**).

6.4.8 *In Vivo* Ratiometric Control over Dual-drug Tumor Accumulation in Xenograft Tumor Model

We postulated that Combo NPs were more efficient in inhibiting growth of the tumor than Sepa NPs due to the fact that Combo NPs may deliver cisplatin and GMP into the tumor at the predetermined optimized synergistic ratio and dose. Tumor accumulation data indicated ratiometric accumulation of GMP and cisplatin from Combo NPs over 10 h post injection (**Figure 6.8B**). However, higher uptake of cisplatin NPs and lower uptake of GMP NPs was observed after dosing with Sepa NPs. On one hand, smaller particle size (around 60 nm) can account for higher tumor accumulation of cisplatin in single PLGA NPs, while on the other hand, compared with 5.5 wt% loading of dual drugs in single PLGA NPs, the same dose of 4.4 wt% cisplatin and 4.2 wt% GMP in separate PLGA NPs doubles the amount of injected AA modified PLGA NPs, which can result in saturation of Sigma Rs and subsequently reduce the accumulation of GMP in tumors. This observation suggests advantages in controlling the ratio of drugs in DOPA coated cores in single PLGA NPs over a mixture of separate NPs, which have variant physicochemical properties and distinct pharmacokinetics. Variations in the loaded ratio and actual amount of drug taken up by tumor tissues can directly affect the anti-tumor efficacy induced by synergy. In addition, nanoparticles also increased the tumor accumulation of free drugs from 2% ID/g to more than 10% ID/g due to the EPR effect and enhanced internalization into tumor cells through a receptor mediated pathway.

6.4.9 Combo NPs Triggered Significant Tumor Cell Apoptosis and Inhibited Tumor Cell Proliferation Effectively *In Vivo* in Stroma-rich UMUC3 Xenografts.

Enhanced antitumor efficacy of Combo NPs was confirmed *via* analysis of apoptosis and proliferation. Tumor tissues after treatment were further sectioned for TUNEL (terminal deoxynucleotidyl transferase dUTP nick end labeling) assay and PCNA (proliferating cell nuclear antigen) immunohistochemistry (**Figure 6.9A** and **B**). Results indicated that Combo NPs induced apoptosis in 28.8% of cells in UMUC3 xenograft tumors. Dual drugs in Sepa NPs caused more cell apoptosis compared with cisplatin NPs and GMP NPs treatment, but were still significantly less

efficient in inducing apoptosis than Combo NPs. Free drugs induced few apoptotic cells *in vivo*, probably because the majority of the free drugs were metabolized and cleared before they accumulated in the tumor. In addition, the inhibition of tumor cell proliferation was investigated using PCNA assay. PCNA is expressed in the cell nuclei during DNA synthesis and can be used as a marker for cell proliferation. PCNA results were consistent with those of TUNEL assay. Combo NPs showed minimal amounts of PCNA positive cells. These data further illustrated that combined drugs in a single NPs inhibited the growth of the tumor through enhanced induction of apoptosis and reduced cell proliferation.

6.4.10 Mechanism of Synergistic Effect of the Dual-Drug Combo NPs

In order to validate the observed enhanced antitumor effect of Combo NPs is a synergistic effect imposed by GMP and cisplatin in the NPs, subsequent studies were designed accordingly from a mechanistic basis. It is reported that gemcitabine potentiates the accumulation of cisplatin damage by suppressing the expression of key proteins involved in nucleotide excision repair (NER) and mismatch repair (MMR), leading to a decreased repair of Pt-DNA adducts, and thereby suppressed repair of cisplatin-induced DNA lesions [286, 299, 300]. Therefore, intensified inhibition of DNA repair and Pt-DNA adduct removal are two signs of synergistic interaction. The effect of combination therapy on ERCC1 and XPA [286], two major proteins with key roles in NER was first examined by western blotting and showed that down-regulation of ERCC1 and XPA was induced by GMP free drug and enhanced by GMP NPs treatment (**Figure 6.9C**). Combo NPs almost completely depleted the expression of ERCC1 and XPA and was more efficient than Sepa NPs. To study the effect of down-regulation of ERCC1 and XPA on Pt-DNA repair, Pt-DNA adducts were stained with FITC-labeled anti Pt-DNA adduct antibody. As shown in **Figure 6.9D**, a significant increase in the amount of Pt-DNA adducts was observed when tumors were treated with Combo NPs, compared with that of Sepa NPs.

The level of cleaved PARP and Caspase-3 were observed in order to further investigate the relationship of the suppressed DNA repair proteins and apoptosis. During the execution phase of apoptosis, intact PARP is mainly cleaved by caspase-3 or caspase-7 to a larger fragment and a smaller fragment. Therefore, PARP cleavage serves as a reliable marker of apoptosis [287, 301]. **Figure 6.10** indicated that cleaved PARP was significantly elevated after treatment with Combo NPs, which is consistent with the results of the DNA repair proteins and Pt-DNA adduct formation. Caspase-3 was also elevated after Combo NPs treatment. Conclusively, Combo NPs exhibited greater efficacy in inhibiting DNA repair and suppressing the removal of Pt-DNA adducts, leading to intensified apoptosis compared to dual drugs in separate NPs *in vivo*. These results further verify that Combo NPs acted in a synergistic fashion rather than only additive fashion to induce the enhanced anti-cancer effect in the stroma-rich bladder cancer xenograft model.

6.4.11 Evaluation of Systemic Toxicity of Combo NPs

Another important issue involved with combination therapy is the dual-drug distribution and ratio in major organs, as well as, the association of synergistic effects with toxicity in these organs. Quantitative bio-distribution analyses of GMP and cisplatin in Combo NPs indicated that the ratio of dual drugs remained constant in almost all organs (**Figure 6.11**). Similar to other nano-platforms, the major particle uptake organs were the liver (approximately 20% ID/g tissue) and the spleen (approximately 40% ID/g tissue) 10 h post injection. However, free drugs were eliminated rapidly from the body leaving the kidney as the major accumulation organ, which also explains the common nephrotoxicity of free cisplatin. Due to different particle size, cisplatin and GMP in separate nanoparticles presented very different distribution behaviors *in vivo*. Notably, cisplatin NPs showed significantly higher accumulation in spleen, which might be a potential factor for inducing spleen toxicity.

Since the major side effect of GMP is myelosuppression and cisplatin can also induce an accumulated decrease in hematopoietic cell counts, a blood routine test was performed on healthy

nude mice with three dosages of the 8 treatment groups. Both free GMP and cisplatin significantly reduced the levels of red blood cells (RBC), platelets (PLT) and white blood cells (WBC) compared to untreated control **(Figure 6.13).** Combination of these free drugs slightly potentiates the toxicity. Although there was an inevitable amount of accumulation of NPs in the liver and kidney, blood biochemistry tests showed that NPs coating can slightly alleviate the chemo-drug induced myelosuppression. There is no noticeable aggravation of blood toxicity in Combo NPs. WBC, RBC, hematocrit (HCT), hemoglobin (HGB) of Combo NPs were all close to the value of the untreated control **(Figure 6.13).**

Other hematological parameters showed that no detectable damage was caused; aspartate aminotransferase (AST), alanine aminotransferase (ALT) and blood urea nitrogen (BUN) analyses were all within the normal range (**Table 6.2**). No noticeable histological changes were seen in H&E-stained tissue sections of the liver, kidney and spleen (**Figure 6.12**). These studies demonstrated that Combo NPs, with the most significant synergistic therapeutic efficacy, have elevated tumor uptake and low spleen accumulation, and as well exhibited no significant toxicity to major organs and tissues. Therefore, ratiometric synergistic combination therapy with non-overlapping toxicity is a promising strategy in overcoming drug resistance while enhancing anti-cancer effect.

6.5 Discussion and Conclusion

Developing NPs to simultaneously encapsulate drugs with different physicochemical properties with precise ratiometric loading and delivery is extremely important in the combination chemotherapy of malignant diseases. In the present study, we have successfully developed single nanocapsule-like PLGA particles with payloads of GMP cores and cisplatin cores. These dual-drug loaded NPs exhibited precise ratiometric control over drug loading, cellular uptake, *in vitro* release and *in vivo* tumor accumulation. Furthermore, this single NPs with well-controlled optimal dual-drug ratio exhibited a more significant antitumor efficacy compared with dual drugs in a mixture of separate NPs. Overall, our studies provide a solution to the problems of formulating cisplatin and

other groups of hydrophilic drugs for ratiometric combination therapy and have therefore distinguished this single nanoparticulate delivery platform as an efficient and relatively safe candidate in the treatment of human bladder cancer.

This nanomaterial-system with spatially separated modalities prevents functional interference between individual molecules. Also, this system provides a possible well controlled platform for co-delivery chemotherapy with other hydrophobic ligand coated inorganic NPs (e.g. ion oxide NPs, gold NPs, quantum dots and upconversion NPs) for photothermal and theranostic purposes.

Table 6.1 Characteristic features of the optimized single drug PLGA NP and dual Drug PLGA Combo NP

Optimal	CDDP PLGA NP	GMP PLGA NP	GMP & CDDP PLGA Combo NP
DL (wt%)	4.4 ± 0.6	4.2 ± 0.3	5.5 ± 0.8
EE (%)	74.0 ± 10.0	69.5 ± 1.6	86.6 ± 1.9 & 92.4 ± 1.6

Table 6.2 Effect of different treatments on serum ALT, AST, BUN and creatinine levels

Treatment	BUN mg/dL	Creatinine mg/dL	AST U/L	ALT U/L
PBS	19 ± 1	0.2	228 ± 13	60 ± 14
Cisplatin free	25 ± 1	0.2	216 ± 15	59 ± 1
GMP free	24 ± 2	0.2	122 ± 20	47 ± 3
Combo free	22 ± 5	0.2	116 ± 18	60 ± 4
Cisplatin NPs	28 ± 3	0.2	245 ± 22	58 ± 11
GMP NPs	21 ± 1	0.2	86 ± 6	42 ± 2
Sepa NPs	29 ± 2	0.3	238 ± 10	55 ± 8
Combo NPs	18 ± 3	0.2	122 ± 12	52 ± 12
Normal Range	12 - 33	0.2 - 0.9	54 - 298	17 - 132

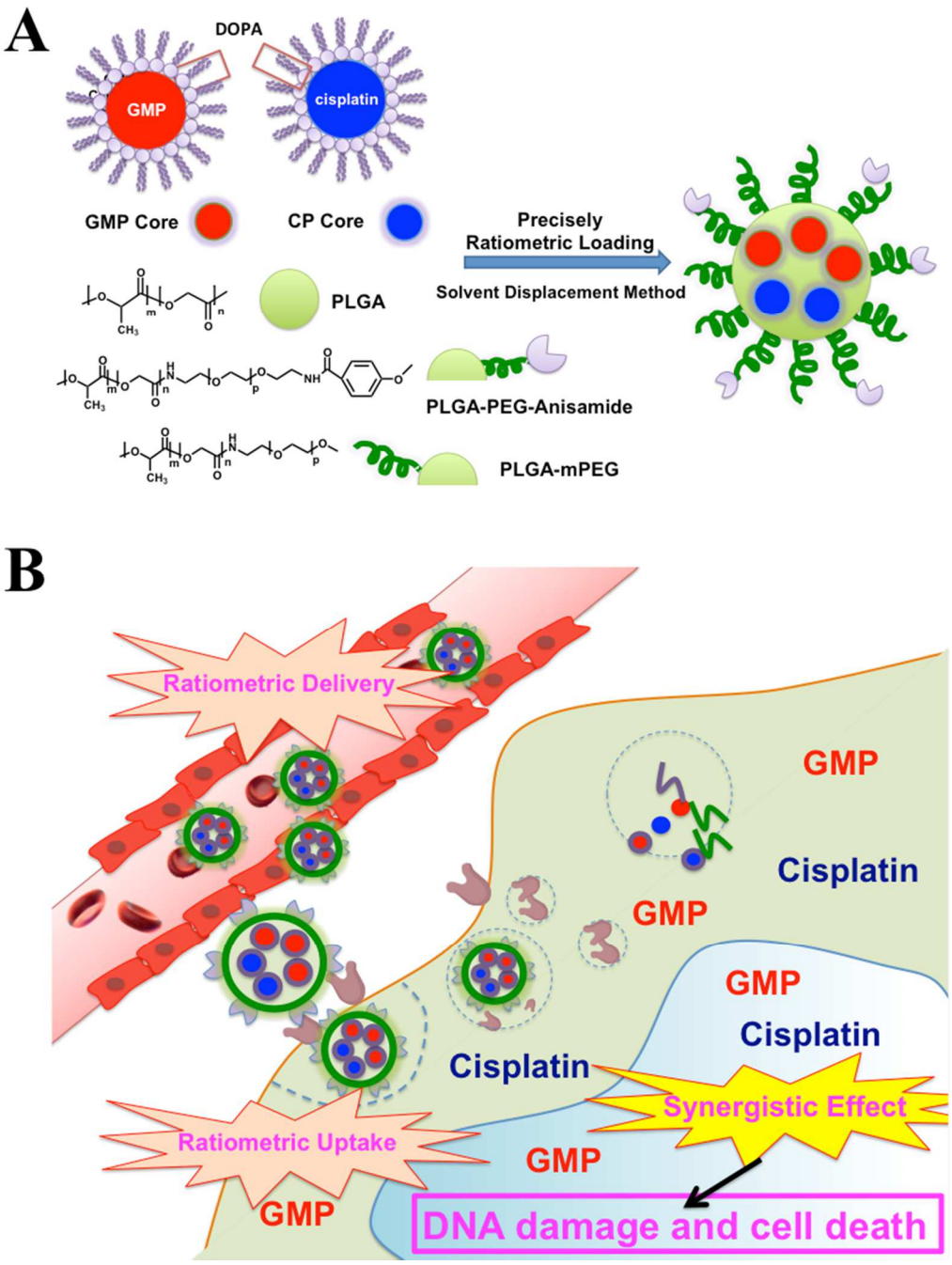

Figure 6.1 Diagram of PLGA NPs and mechanism of combination therapy.

A. Fabrication of PLGA-PEG-AA NP (PLGA NPs) containing CP cores and GMP cores via a single step solvent displacement method. B. Cisplatin and GMP, which are ratiometrically encapsulated in PLGA NPs, are ratiometrically delivered into the tumor and exhibit strong synergistic anti-tumor efficacy

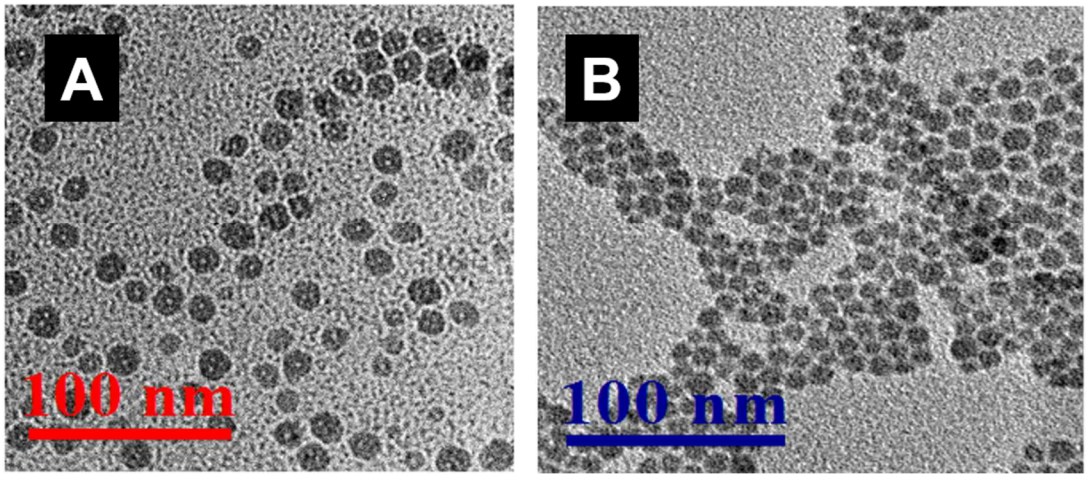

Figure 6.2 TEM image of GMP cores (A) and CP cores (B).

GMP and CP cores have similar size and morphology.

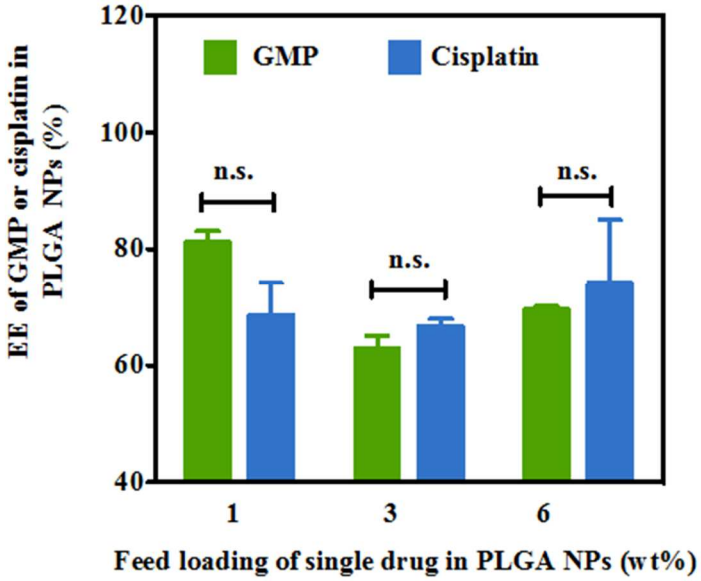

Figure 6.3 EE of GMP in GMP NPs and cisplatin in cisplatin NPs while changing the feed loading of single drug cores in PLGA NPs.

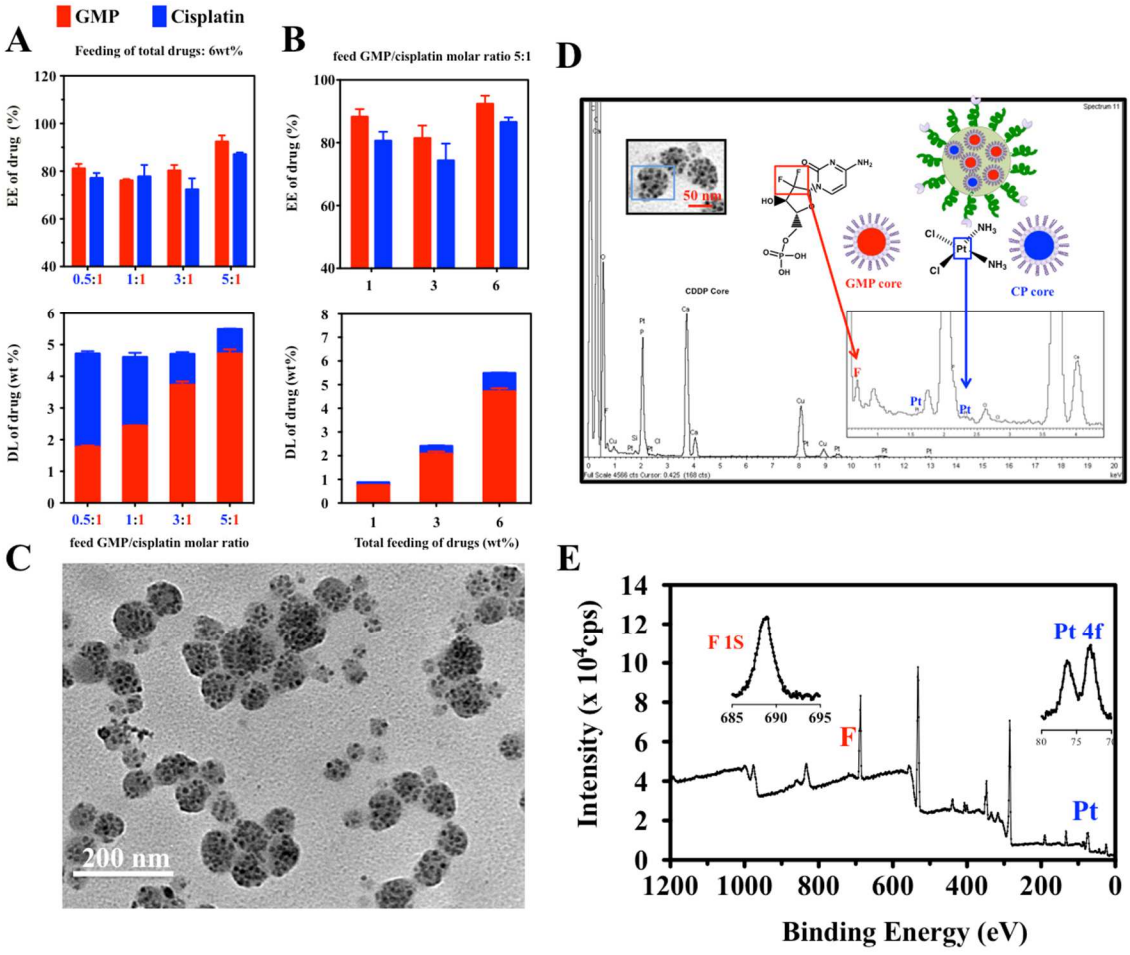

Figure 6.4 Dual-drug ratiometric loading in Combo NPs.

A. EE and DL of GMP and cisplatin in Combo NP while the total loading of drugs was fixed at 6 wt%. **B**. EE and DL of GMP and cisplatin in Combo NPs while the feed molar ratio of GMP to cisplatin was fixed at 5:1. **C**. TEM image of 5.5 wt% total drug loading of Combo NP with molar ratio of GMP and cisplatin of 5.3:1. **D**. EDS spectra of Combo NP. Both platinum from CP cores and fluorine from GMP cores were observed in a single NP indicating actual loading of dual drugs in single NP. **E**. XPS spectrum of Combo NP. Molar ratio of GMP and cisplatin was also quantified using atomic ratio of fluorine and platinum. Spectrum of Pt 4F and spectrum of F 1S, from which, area of peaks are integrated for atom quantification.

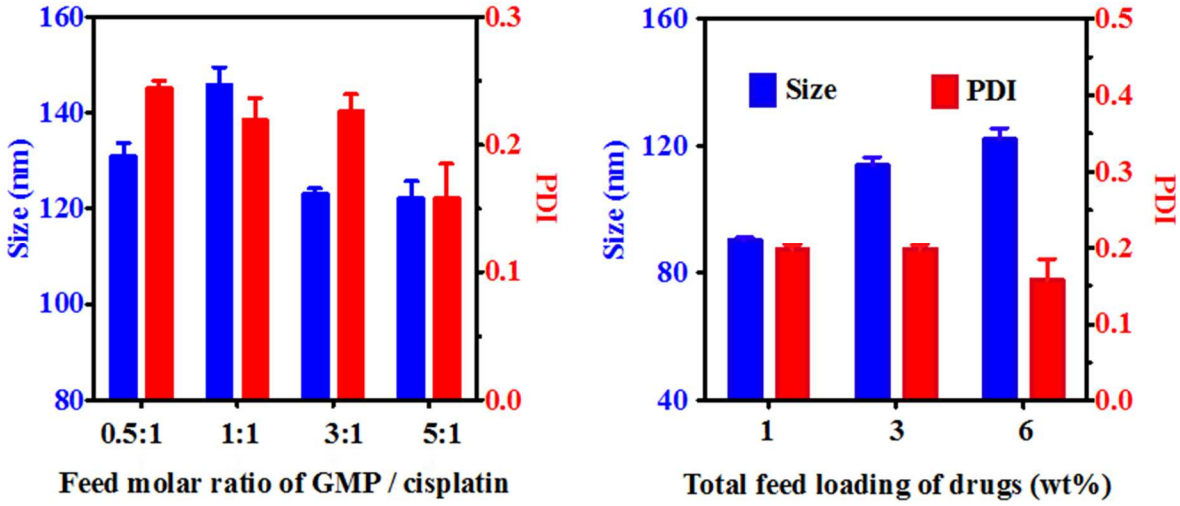

Figure 6.5 EE and LD of NPs

Size and PDI of Combo NPs with total feed loading fixed at 6 wt% (left) or feed molar ratio of GMP/cisplatin fixed at 5:1 (right).

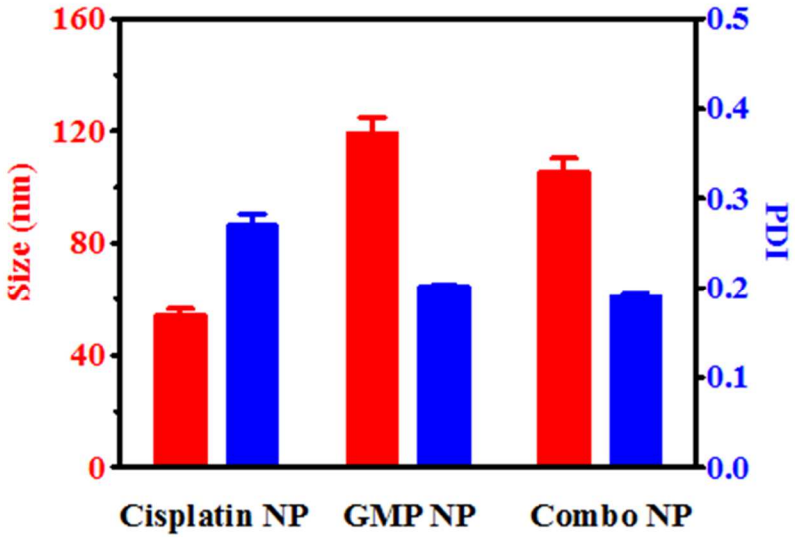

Figure 6.6 Size of PDI of NPs

Size and PDI of 4.4 wt% cisplatin NPs, 4.2 wt% GMP NPs and 5.5 wt % Combo NPs with molar ratio of GMP and cisplatin 5.3:1 were measured by DLS.

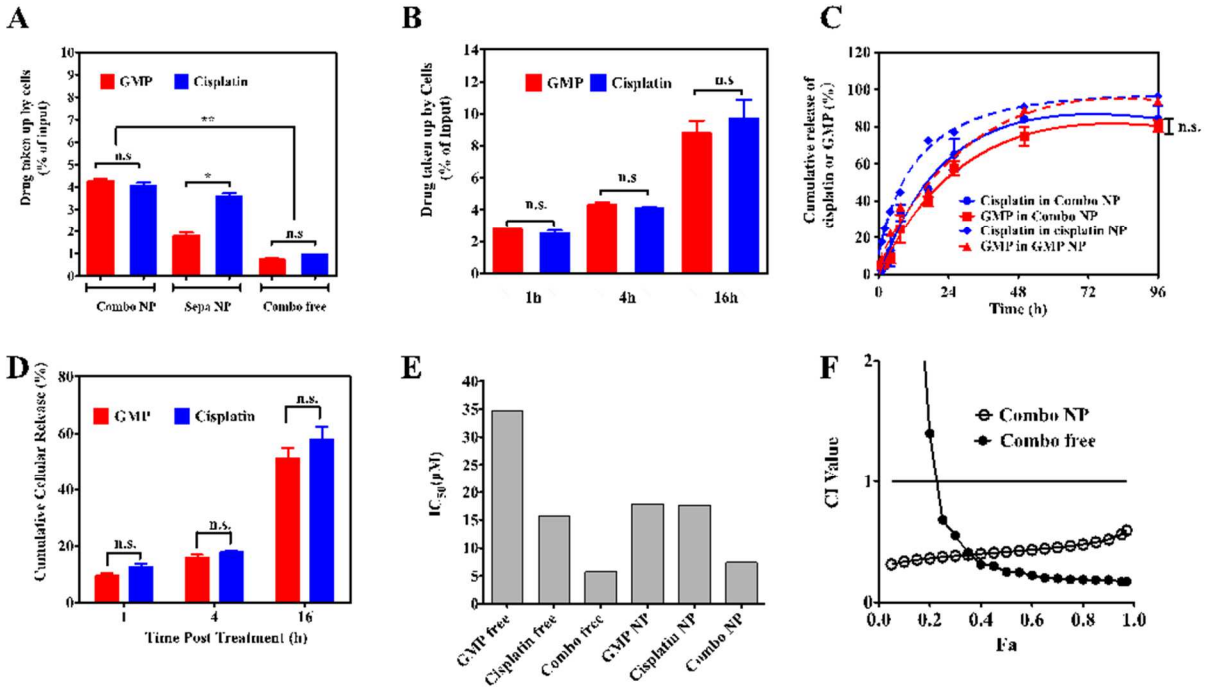

Figure 6.7 Ratiometric cellular uptake and release of dual drugs from Combo NP.

A. Uptake of cisplatin and GMP in Combo NPs, Sepa NPs, and free drugs at 37 °C for 4 h in UMUC3 cells. **B.** Accumulative uptake of Combo NPs loaded with cisplatin and GMP in UMUC3 Cells. **C.** *In vitro* release kinetics of cisplatin and GMP from Combo NPs and single NPs in PBS at 37 °C. **D.** Intracellular release of cisplatin and GMP from Combo NPs. **E.** IC50 of free GMP, cisplatin, and Combo free at molar ratio 5.3:1, as well as single drug NPs and Combo NPs at molar ratio 5.3:1. X-axis indicated the total concentration of dual drugs or single drug formulations. The corresponding CI vs Fa plots of Combo NPs and Combo free were shown (**F**). DL of cisplatin and GMP in Combo NPs is 0.8 wt% and 4.6 wt% respectively, while DL of cisplatin and GMP in single NP is 4.4 wt% and 4.2 wt% respectively. n.s.: no significant difference; * $P < 0.05$; ** $P < 0.01$.

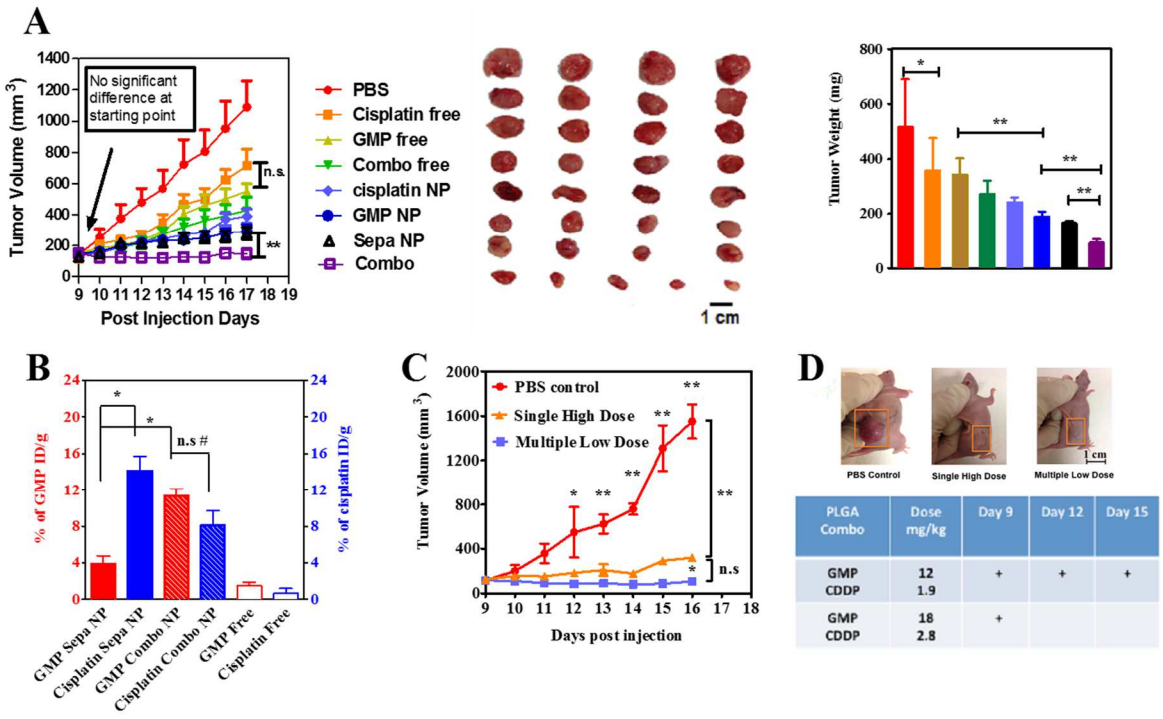

Figure 6.8 Tumor inhibition effects of free drugs, Combo free, cisplatin NPs, GMP NPs, Sepa NPs and Combo NPs on a desmoplastic bladder cancer xenograft (UMUC3/3T3)

A. Red arrows in panel A indicate time of injection. The tumors were treated with 3 intravenous injections at a dose of 1.9 mg/kg cisplatin and 12 mg/kg GMP in all the treatment groups. **B.** Tumor accumulation of cisplatin and GMP was calculated 10 h post injection of Combo NPs, Sepa NPs and Combo free at the injection dose of 1.9 mg/kg cisplatin and 12 mg/kg GMP into nude mice bearing desmoplastic bladder cancer xenograft tumors. **C.** Anti-tumor effects of multiple low dosing schedule and single high dosing schedule were compared. n = 5; * $P < 0.05$; ## $P > 0.5$; n.s: non-significant difference. ID/g: injected dose per gram tissue (tumor) **D.** Representative photo images of mice bearing tumors after indicated treatments.

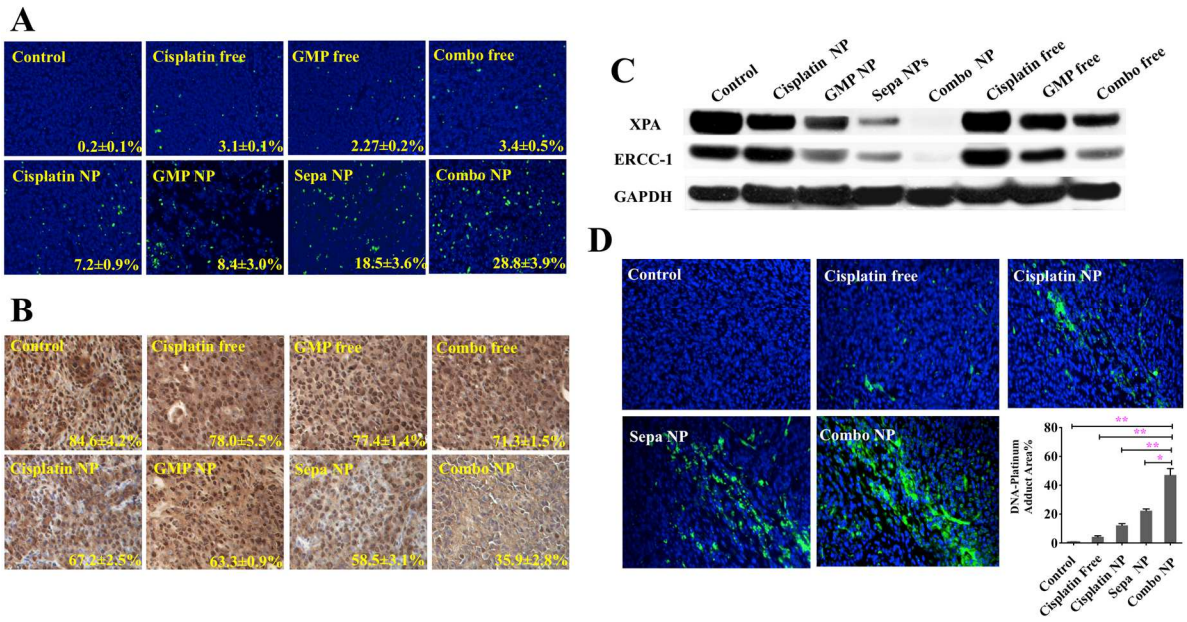

Figure 6.9 Mechanistic studies of the combination therapy.

Apoptosis (A) and proliferation (B) of tumor cells in vivo after administration of different treatments. C. Expression of XPA and ERCC-1, common in nucleotide excision repair (NER) systems, after three dosage systemic treatments. D. The formation of Pt-DNA adduct (green) in tumor cells detected by anti-Pt-DNA adduct antibody after systemic treatment. Bar chart in D is a quantitative analysis of % of Pt-DNA adduct in tissue sections. Five randomly selected microscopic fields were quantitatively analyzed on Image J. * $P < 0.05$; ** $P < 0.01$.

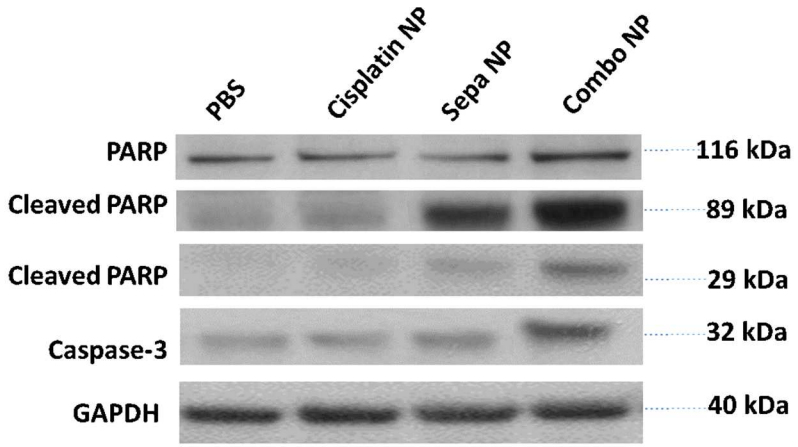

Figure 6.10 Western blot of PARP, cleaved PARP, caspase-3 and GAPDH in the tumor lysates after 3-dose treatment.

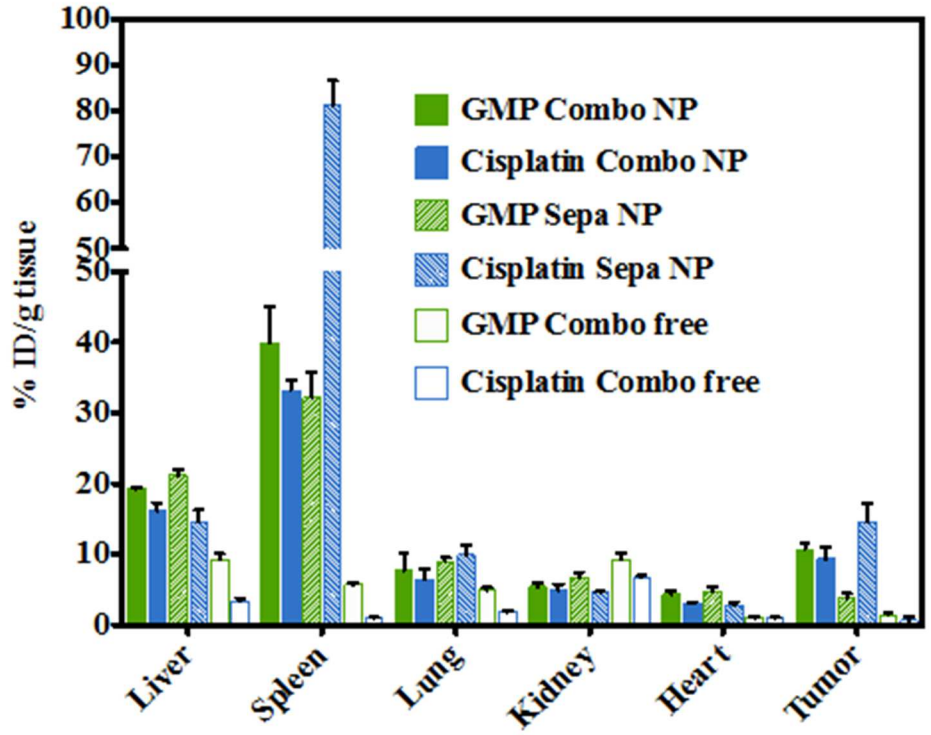

Figure 6.11 Biodistribution of Combo NPs, Sepa NPs, and Combo free in major organs 10 h post intravenous injection into desmoplastic 22MUC3/3T3 bearing nude mice.

(% ID/g tissue: percentage of injected dose per gram tissue)

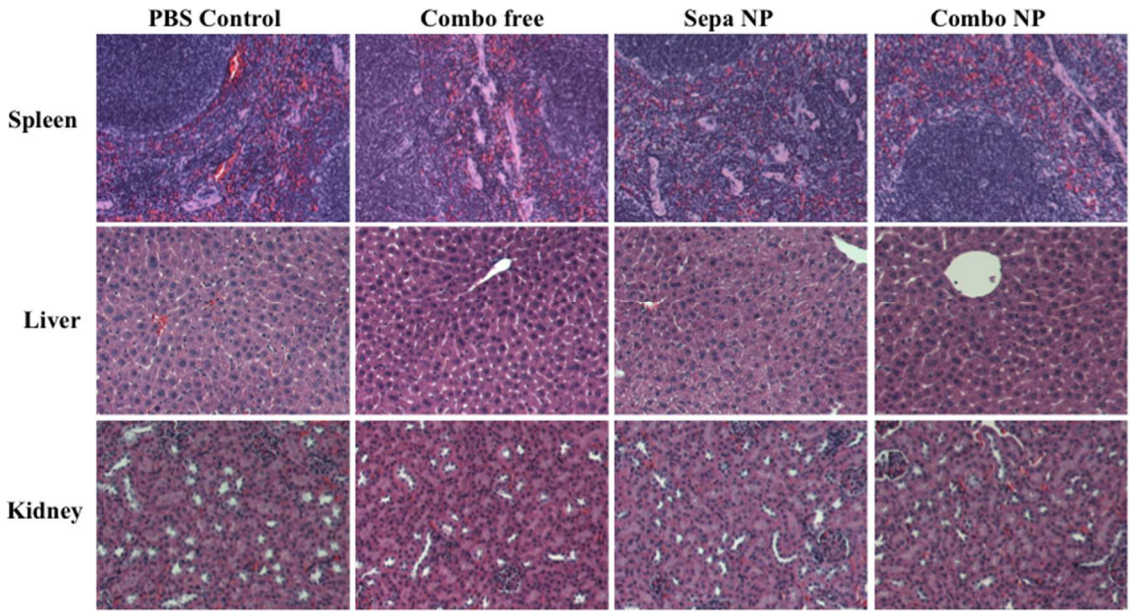

Figure 6.12 HE staining of major drug accumulating organs after three injections of treatments.

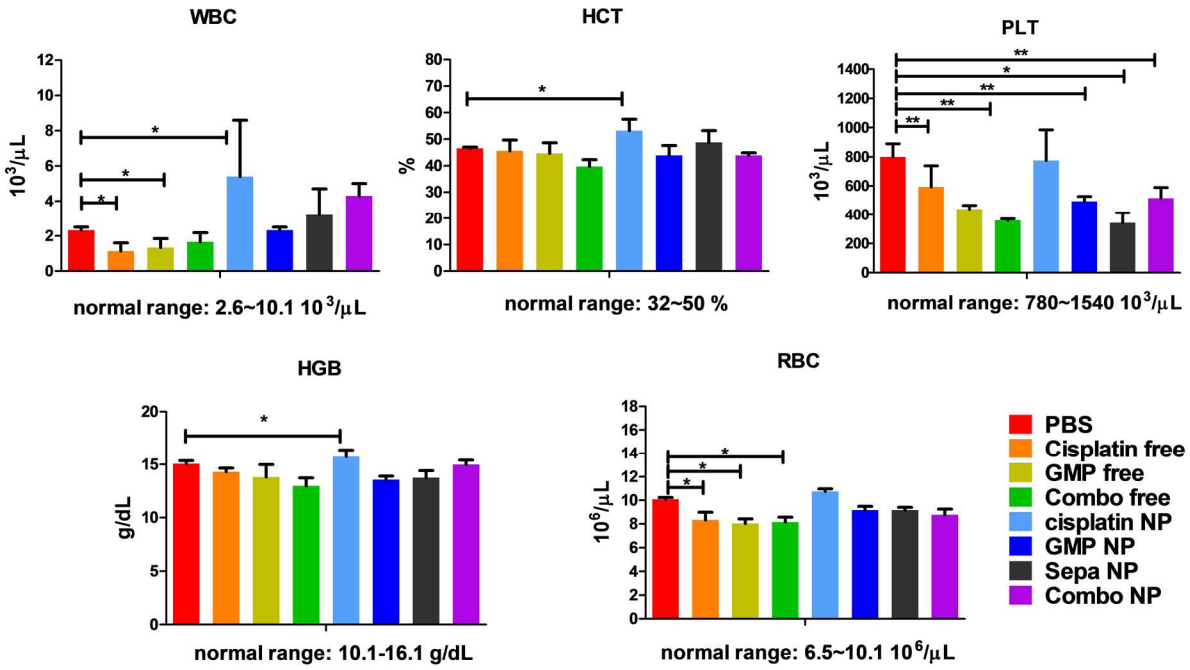

Figure 6.13 Hematological test of whole blood collected from healthy nude mice treated with 3 doses of free drugs and NPs as indicated

WBC, white blood cell; HCT, hematocrit; PLT, platelet; HGB, hemoglobin; RBC, red blood cell. If not indicated, no significant difference between PBS group and the treatment group. * $P < 0.05$; ** $P < 0.01$, n = 4)

CHAPTER 7: SUMMARY AND FUTURE STUDIES

7.1 Summary of Current Work

In this dissertation, the stroma barriers in desmoplastic tumors and the current strategies to overcome the barriers were discussed extensively. In summary, the stroma barriers for nanoparticle (NP) delivery and therapy can be classified into two categories, a physical barrier due to dense ECM and high interstitial fluidic pressure (IFP); and the stroma cells. Current strategies focus on depleting both the ECM and stromal cells to improve the NP perfusion and efficacy. This is particularly for the treatment of desmoplastic tumors, where stroma constitute the majority of the tumor mass. Different from other types of tumors, tumor associated fibroblasts (TAFs) play an important role in desmoplasia. TAFs, on one end, synthesize and secrete major ECM proteins, constituting the physical barriers against therapeutic agents' insult; on the other end, orchestrate an immunosuppressive crosstalk among immune cells and tumor cells, escaping immune surveillance. And also, TAFs directly facilitate tumor growth, resistance and metastasis through paracrine secretion of growth factors and cytokines. Herein, focusing on a stroma-rich desmoplastic bladder cancer xenograft as a model of tumor desmoplasia, we investigated the rule of TAFs in modulating the delivery and therapeutic outcomes of chemotherapeutic NPs. The data demonstrated that the majority of desmoplastic tumors have a stroma-vessel architecture, where TAFs localize in between tumor nests and immature tumor vasculatures. This geometrical feature of TAFs causes them as a major binding site barrier (BSB) for therapeutic NPs. More than 60% of NPs, in regardless of size and the presence of the targeting ligand, are trapped in TAFs after rapid systemic circulation.

These off-target distribution of NPs are detrimental to those NPs designed specifically for targeting tumor cells. For example, VEGF receptor antibodies designed for blocking the receptors in tumor cells failed to respond to the therapy due to internalizations by the less sensitive TAFs. Moreover, TAFs would be very likely to generate unexpected off-target effects. Indeed, in a follow-up study, we found that chronic exposure of fibroblasts to cisplatin NPs activated the synthesis of a major survival factor, Wnt16, paradoxically supporting tumor growth and metastasis. Cisplatin has been used as a first line therapy for the treatment of bladder cancer. Lipid coated cisplatin NPs (LPC) developed previously in our lab have shown promising anticancer effect in various types of tumor xenografts, including bladder cancers. However, consistent with cases in clinical trials, resistance occurs after chronic exposure and ultimately leads to tumor relapse and treatment failure. Thus, in the current dissertation, focusing on the aforementioned observation of TAFs as both a BSB and a resistant niche, cisplatin NPs was utilized as a model therapeutic agent to evaluate the combinatory strategies relating **desmoplasia modulation**.

Since the damage-induced secretion of Wnt16 in TAFs facilitate tumor growth, the first strategy we proposed was to knock down the *in situ* generation of Wnt16. The BSB feature of TAFs can be conversely utilized to deliver NPs specifically for TAFs. Therefore, we proposed systemic NP delivery of siRNA against Wnt16 for Wnt16 knockdown in TAFs. Indeed, we found the downregulation of Wnt16 *in vivo* in a dose dependent manner. As a result, the neighboring effects exposed by Wnt16 to adjacent naïve fibroblasts, blood vessels and tumor cells were abolished. Combination of siRNA with cisplatin NPs prolonged the anti-cancer effect and also remodeled the tumor supportive TME.

A more potent strategy of reverting TAFs from tumor supportive to tumor suppressive was also proposed utilizing the *in situ* engineering strategy. In brief, we delivered a gene encoding secretable TRAIL to TAFs. The TRAIL-resistant TAFs then became a sTRAIL producing depot, inducing the apoptosis of neighboring TRAIL-sensitive tumor cells. The sTRAIL plasmid monotherapy already showed promising therapeutic outcome in both desmoplastic bladder cancer and an orthotopic

pancreatic cancer. We also unexpectedly found that the TRAIL-producing TAFs were reverted to a quiescent state, likely due to the insufficient activation from neighboring apoptotic tumor cells. The fibroblasts with a quiescent phenotype further suppressed tumor growth and remodeled the TME. As a proof of concept, we observed that the remodeled TAFs and TME facilitated the accumulation and anti-cancer efficacy of a second-wave cisplatin NPs, providing a new paradigm for the treatment of desmoplasia.

Another alternative strategy of desmoplasia modulation is stroma depletion. Potent deletion agents for both fibroblasts and tumor cells would overcome the damage-induced resistance. We found that combination of gemcitabine and cisplatin was more effective in killing both tumor cells and fibroblasts compared to monotherapy of each. The combined cisplatin NPs and gemcitabine NPs (in separate formulation) induced a prolonged and efficient stroma depletion within 7 days after single injection, resulting in prolonged survival. The ratio of combined regimens is crucial to induce synergistic rather than antagonist effect. So, in order to improve the combination effect, we designed a capsule-like nano-formulation available to ratiometrically co-load and co-deliver cisplatin and gemcitabine. As expected, this formulation has shown potent anti-tumor effect compared to those being encapsulated separately. Note that, this is the first formulation capable of simultaneously and ratiometrically load a hydrophilic drug with a hydrophobic drug.

7.2 Significance and Novelty of Current Studies

Overall, the proposed **desmoplasia modulating** strategies have following advantages:

(1) The off-target capture of NPs in stroma cells have been originally thought of as a barrier for NP delivery, but was utilized herein to its advantage to induce efficient killing of neighboring tumors cells or benefit the penetration of a second wave chemotherapy.

(2) Cytokines play vital rules in regulating the crosstalk between tumor cells and the stromal cells, and thus having been used as potent anticancer agents for decades [302]. However, the clinical applications of cytokine drugs are usually suffered from severe systemic toxicity. The strategy we

proposed here to engineer TAFs into a depot of protein production, allows locally and transient expression of cytokines, circumventing the systemic toxicities, inducing potent local modulating of the tumor microenvironment.

(3) The capsule-like PLGA NPs provide a platform of encapsulating hydrophilic drugs with hydrophobic moieties with precise ratiometric control. This combination therapy with strong synergy would also be a potent stroma depleting agent that improve the therapeutic outcome of desmoplastic cancers.

7.3 Future Expectations

The idea of *in situ* engineering of fibroblasts have many other applications. For example, engineering the fibroblasts to generate a fusion protein consisting of ligands especially for receptors overexpressing on malignant cells, i.e. EGFR, together with toxins, to specifically improve the necrosis or apoptosis of neighboring tumor cells. At the same time, the apoptotic cells are capable to generate antigen *in situ*. This, in combined with an antigen presenting cell (APC) stimulation agent, would be very likely to facilitate a tumor-specific immune response with a potent memory. Such robust host immune responses are considered as a strategy to prolong the tumor inhibition effect, with potential of reverting cancers from lethal to chronic disease [303].

However, the success of cancer vaccination is strongly hampered by the suppressive tumor microenvironment. *In situ* engineering of fibroblasts also allows the fibroblasts to secrete cytokines or antibodies, orchestrating cytokine-mediated crosstalk between infiltrating lymphocytes and the resident malignant cells, facilitating potent immune response. For example, future work can also investigate the engineering of TAFs to produce Th-1 cytokines, such as IL-12, GM-CSF to boost APC stimulation, or to produce antibodies against chemokines or Th-2 cytokines (i.e. IL-6, IL-10) to prevent the infiltration of suppressive leucocytes, such as regulatory T cells (Treg) and myeloid-derived suppressor cells (MDSC). In all the above mentioned strategies, intratumoral penetration of NPs would not be a limitation for the therapeutic outcome, which is very beneficial for the treatment

of desmoplastic cancers. Besides focusing on TAFs, NPs with tunable size, smart materials and effective targeting ligands can be designed to target different cell populations within the tumor mass. Multiple NPs with different targets and therapeutic purposes would become another promising combination approach for the treatment of desmoplastic cancer in the near future.

APPENDIX I TABLE OF ANTIBODIES USED IN THE STUDY

Antibodies	Company	Catalog	Application
Anti-αSMA	Abcam	Ab5694	WB, IF, IHC, flow cyt
Anti-CD31	Abcam	Ab28364	IF, IHC
Anti-Fibronectin	Abcam	Ab2413	WB
Anti-HGF	Abcam	Ab83760	WB
Anti-FAPα	Abcam	Ab53066	WB
Phosphor-SMAD2 (Ser 465/467)	Cell Signaling	3101	IHC
APC Rat Anti-mouse CD45	BD PharmingenTM	561018	flow cyt
APC Rat IgG2b, κ Isotype Control	BD PharmingenTM	553991	flow cyt
Anti-Rabbit IgG (Alex Fluor® 647 Conjugate)	Cell Signaling	4414	IF, flow cyt
Goat anti-rabbit IgG-HRP	Santa Cruz	Sc-2030	WB
Anti-RFP	Invitrogen	R10367	WB
Anti-E cadherin	Abcam		

Anti-N cadherin	Abcam
mouse monoclonal poly(ADP-ribose) antibody (PARP,	Santa Cruz
rabbit polyclonal anti-Wnt16 antibodies	Santa cruz/abcam

APPENDIX II PRIMERS USED IN THE STUDY

Primer	Species	Sequence or Applied Biosystems/Ref	Amplicon Length	Assay Location	Company	Note
sTRAIL	Human	Forward: GAGGAAATCCTGTCCAAG Reverse: GGTTTCCTCAGAGGTG	98	580 of sTRAIL	Bio-rad, Custom Primer	Assay located in cover of ILZ and extracellular domain of TRAIL, exclusively for sTRAIL
TRAIL	Human	Hs00234355_m1	93	433 of full length TRAIL	Invitrogen, Taqman®primer	Assay located to the part encoding extracellular TRAIL domain, detecting both TRAIL and sTRAIL
αSMA (ACTA2)	mouse	Mm00725412_S1	95	1403	Invitrogen, Taqman®primer	Markers of TAFs, used on the sorted fibroblasts to evaluate the state of fibroblasts
Col1a1	mouse	Mm00801666_g1	89	4071	Invitrogen, Taqman®primer	Markers of TAFs
PaI-1	mouse	Mn00435858_m1	87	1044	Invitrogen, Taqman®primer	Markers of TAFs,

(Serpine1)					
GAPDH	Human	Hs02758991_g1	93	728	Invitrogen, Taqman®primer
GAPDH	mouse	Mm99999915_g1	109	117	Invitrogen, Taqman®primer
GAPDH	Human	qHsaCID0015464	-	-	Bio-rad, PrimePCR™ SYBR® Green Assay

REFERENCE

[1] V.P. Chauhan, T. Stylianopoulos, Y. Boucher, R.K. Jain, Delivery of molecular and nanoscale medicine to tumors: transport barriers and strategies, Annual review of chemical and biomolecular engineering, 2 (2011) 281-298.

[2] R.K. Jain, T. Stylianopoulos, Delivering nanomedicine to solid tumors, Nature reviews. Clinical oncology, 7 (2010) 653-664.

[3] C. Wong, T. Stylianopoulos, J. Cui, J. Martin, V.P. Chauhan, W. Jiang, Z. Popovic, R.K. Jain, M.G. Bawendi, D. Fukumura, Multistage nanoparticle delivery system for deep penetration into tumor tissue, Proceedings of the National Academy of Sciences of the United States of America, 108 (2011) 2426-2431.

[4] Y. Li, J. Wang, M.G. Wientjes, J.L. Au, Delivery of nanomedicines to extracellular and intracellular compartments of a solid tumor, Advanced drug delivery reviews, 64 (2012) 29-39.

[5] A. Pluen, P.A. Netti, R.K. Jain, D.A. Berk, Diffusion of macromolecules in agarose gels: comparison of linear and globular configurations, Biophysical journal, 77 (1999) 542-552.

[6] R.K. Jain, Normalization of tumor vasculature: an emerging concept in antiangiogenic therapy, Science, 307 (2005) 58-62.

[7] T. Stylianopoulos, B. Diop-Frimpong, L.L. Munn, R.K. Jain, Diffusion anisotropy in collagen gels and tumors: the effect of fiber network orientation, Biophysical journal, 99 (2010) 3119-3128.

[8] V.P. Chauhan, T. Stylianopoulos, J.D. Martin, Z. Popovic, O. Chen, W.S. Kamoun, M.G. Bawendi, D. Fukumura, R.K. Jain, Normalization of tumour blood vessels improves the delivery of nanomedicines in a size-dependent manner, Nature nanotechnology, 7 (2012) 383-388.

[9] W.S. Kamoun, S.S. Chae, D.A. Lacorre, J.A. Tyrrell, M. Mitre, M.A. Gillissen, D. Fukumura, R.K. Jain, L.L. Munn, Simultaneous measurement of RBC velocity, flux, hematocrit and shear rate in vascular networks, Nature methods, 7 (2010) 655-660.

[10] M. Leunig, F. Yuan, M.D. Menger, Y. Boucher, A.E. Goetz, K. Messmer, R.K. Jain, Angiogenesis, microvascular architecture, microhemodynamics, and interstitial fluid pressure during early growth of human adenocarcinoma LS174T in SCID mice, Cancer research, 52 (1992) 6553-6560.

[11] E.B. Brown, R.B. Campbell, Y. Tsuzuki, L. Xu, P. Carmeliet, D. Fukumura, R.K. Jain, In vivo measurement of gene expression, angiogenesis and physiological function in tumors using multiphoton laser scanning microscopy, Nature medicine, 7 (2001) 864-868.

[12] B.J. Vakoc, R.M. Lanning, J.A. Tyrrell, T.P. Padera, L.A. Bartlett, T. Stylianopoulos, L.L. Munn, G.J. Tearney, D. Fukumura, R.K. Jain, B.E. Bouma, Three-dimensional microscopy of the tumor microenvironment in vivo using optical frequency domain imaging, Nature medicine, 15 (2009) 1219-1223.

[13] V.P. Chauhan, Z. Popovic, O. Chen, J. Cui, D. Fukumura, M.G. Bawendi, R.K. Jain, Fluorescent nanorods and nanospheres for real-time in vivo probing of nanoparticle shape-dependent tumor

penetration, Angew Chem Int Ed Engl, 50 (2011) 11417-11420.

[14] S.R. Chary, R.K. Jain, Direct measurement of interstitial convection and diffusion of albumin in normal and neoplastic tissues by fluorescence photobleaching, Proceedings of the National Academy of Sciences of the United States of America, 86 (1989) 5385-5389.

[15] G. Alexandrakis, E.B. Brown, R.T. Tong, T.D. McKee, R.B. Campbell, Y. Boucher, R.K. Jain, Two-photon fluorescence correlation microscopy reveals the two-phase nature of transport in tumors, Nature medicine, 10 (2004) 203-207.

[16] T. Stylianopoulos, E.A. Economides, J.W. Baish, D. Fukumura, R.K. Jain, Towards Optimal Design of Cancer Nanomedicines: Multi-stage Nanoparticles for the Treatment of Solid Tumors, Annals of biomedical engineering, (2015).

[17] W. Mok, T. Stylianopoulos, Y. Boucher, R.K. Jain, Mathematical modeling of herpes simplex virus distribution in solid tumors: implications for cancer gene therapy, Clinical cancer research : an official journal of the American Association for Cancer Research, 15 (2009) 2352-2360.

[18] B. Kim, G. Han, B.J. Toley, C.K. Kim, V.M. Rotello, N.S. Forbes, Tuning payload delivery in tumour cylindroids using gold nanoparticles, Nature nanotechnology, 5 (2010) 465-472.

[19] M.M. Schmidt, K.D. Wittrup, A modeling analysis of the effects of molecular size and binding affinity on tumor targeting, Molecular cancer therapeutics, 8 (2009) 2861-2871.

[20] I.A. Khawar, J.H. Kim, H.J. Kuh, Improving drug delivery to solid tumors: priming the tumor microenvironment, Journal of controlled release : official journal of the Controlled Release Society, 201 (2015) 78-89.

[21] G. Kharaishvili, D. Simkova, K. Bouchalova, M. Gachechiladze, N. Narsia, J. Bouchal, The role of cancer-associated fibroblasts, solid stress and other microenvironmental factors in tumor progression and therapy resistance, Cancer Cell Int, 14 (2014) 41.

[22] E. Miele, G.P. Spinelli, E. Miele, F. Tomao, S. Tomao, Albumin-bound formulation of paclitaxel (Abraxane ABI-007) in the treatment of breast cancer, International journal of nanomedicine, 4 (2009) 99-105.

[23] S. Torosean, B. Flynn, J. Axelsson, J. Gunn, K.S. Samkoe, T. Hasan, M.M. Doyley, B.W. Pogue, Nanoparticle uptake in tumors is mediated by the interplay of vascular and collagen density with interstitial pressure, Nanomedicine : nanotechnology, biology, and medicine, 9 (2013) 151-158.

[24] J.A. Nagy, L. Benjamin, H. Zeng, A.M. Dvorak, H.F. Dvorak, Vascular permeability, vascular hyperpermeability and angiogenesis, Angiogenesis, 11 (2008) 109-119.

[25] B.R. Seo, P. Delnero, C. Fischbach, In vitro models of tumor vessels and matrix: engineering approaches to investigate transport limitations and drug delivery in cancer, Advanced drug delivery reviews, 69-70 (2014) 205-216.

[26] R.K. Jain, Transport of molecules across tumor vasculature, Cancer metastasis reviews, 6 (1987) 559-593.

[27] W.G. Roberts, G.E. Palade, Neovasculature induced by vascular endothelial growth factor is

fenestrated, Cancer research, 57 (1997) 765-772.

[28] H.F. Dvorak, M. Detmar, K.P. Claffey, J.A. Nagy, L. van de Water, D.R. Senger, Vascular permeability factor/vascular endothelial growth factor: an important mediator of angiogenesis in malignancy and inflammation, International archives of allergy and immunology, 107 (1995) 233-235.

[29] M. Egeblad, E.S. Nakasone, Z. Werb, Tumors as organs: complex tissues that interface with the entire organism, Developmental cell, 18 (2010) 884-901.

[30] E.M. Sevick, R.K. Jain, Geometric resistance to blood flow in solid tumors perfused ex vivo: effects of tumor size and perfusion pressure, Cancer research, 49 (1989) 3506-3512.

[31] A.A. Manzoor, L.H. Lindner, C.D. Landon, J.Y. Park, A.J. Simnick, M.R. Dreher, S. Das, G. Hanna, W. Park, A. Chilkoti, G.A. Koning, T.L. ten Hagen, D. Needham, M.W. Dewhirst, Overcoming limitations in nanoparticle drug delivery: triggered, intravascular release to improve drug penetration into tumors, Cancer research, 72 (2012) 5566-5575.

[32] N. Raghunand, R.J. Gillies, pH and drug resistance in tumors, Drug Resist Updat, 3 (2000) 39-47.

[33] M.C. Brahimi-Horn, J. Chiche, J. Pouyssegur, Hypoxia and cancer, J Mol Med (Berl), 85 (2007) 1301-1307.

[34] V.R. Devadasu, R.M. Wadsworth, M.N. Ravi Kumar, Tissue localization of nanoparticles is altered due to hypoxia resulting in poor efficacy of curcumin nanoparticles in pulmonary hypertension, Eur J Pharm Biopharm, 80 (2012) 578-584.

[35] A.R. Kirtane, S.M. Kalscheuer, J. Panyam, Exploiting nanotechnology to overcome tumor drug resistance: Challenges and opportunities, Advanced drug delivery reviews, 65 (2013) 1731-1747.

[36] L.E. Huang, Z. Arany, D.M. Livingston, H.F. Bunn, Activation of hypoxia-inducible transcription factor depends primarily upon redox-sensitive stabilization of its alpha subunit, J Biol Chem, 271 (1996) 32253-32259.

[37] T. Thambi, V.G. Deepagan, H.Y. Yoon, H.S. Han, S.H. Kim, S. Son, D.G. Jo, C.H. Ahn, Y.D. Suh, K. Kim, I.C. Kwon, D.S. Lee, J.H. Park, Hypoxia-responsive polymeric nanoparticles for tumor-targeted drug delivery, Biomaterials, 35 (2014) 1735-1743.

[38] C.H. Heldin, K. Rubin, K. Pietras, A. Ostman, High interstitial fluid pressure - an obstacle in cancer therapy, Nat Rev Cancer, 4 (2004) 806-813.

[39] T.P. Padera, B.R. Stoll, J.B. Tooredman, D. Capen, E. di Tomaso, R.K. Jain, Pathology: cancer cells compress intratumour vessels, Nature, 427 (2004) 695.

[40] H. Nehoff, N.N. Parayath, L. Domanovitch, S. Taurin, K. Greish, Nanomedicine for drug targeting: strategies beyond the enhanced permeability and retention effect, International journal of nanomedicine, 9 (2014) 2539-2555.

[41] S. Guo, C.M. Lin, Z. Xu, L. Miao, Y. Wang, L. Huang, Co-delivery of cisplatin and rapamycin for enhanced anticancer therapy through synergistic effects and microenvironment modulation, ACS

Nano, 8 (2014) 4996-5009.

[42] E.K. Rofstad, K. Galappathi, B.S. Mathiesen, Tumor interstitial fluid pressure-a link between tumor hypoxia, microvascular density, and lymph node metastasis, Neoplasia, 16 (2014) 586-594.

[43] H.F. Dvorak, Tumors: wounds that do not heal. Similarities between tumor stroma generation and wound healing, The New England journal of medicine, 315 (1986) 1650-1659.

[44] V.P. Chauhan, R.M. Lanning, B. Diop-Frimpong, W. Mok, E.B. Brown, T.P. Padera, Y. Boucher, R.K. Jain, Multiscale measurements distinguish cellular and interstitial hindrances to diffusion in vivo, Biophysical journal, 97 (2009) 330-336.

[45] S. Inoue, Ultrastructure of basement membranes, International review of cytology, 117 (1989) 57-98.

[46] P.D. Yurchenco, G.C. Ruben, Basement membrane structure in situ: evidence for lateral associations in the type IV collagen network, The Journal of cell biology, 105 (1987) 2559-2568.

[47] P. Baluk, S. Morikawa, A. Haskell, M. Mancuso, D.M. McDonald, Abnormalities of basement membrane on blood vessels and endothelial sprouts in tumors, The American journal of pathology, 163 (2003) 1801-1815.

[48] K. Yokoi, M. Kojic, M. Milosevic, T. Tanei, M. Ferrari, A. Ziemys, Capillary-wall collagen as a biophysical marker of nanotherapeutic permeability into the tumor microenvironment, Cancer research, 74 (2014) 4239-4246.

[49] B. Bauvois, New facets of matrix metalloproteinases MMP-2 and MMP-9 as cell surface transducers: outside-in signaling and relationship to tumor progression, Biochimica et biophysica acta, 1825 (2012) 29-36.

[50] T. Mammoto, A. Jiang, E. Jiang, D. Panigrahy, M.W. Kieran, A. Mammoto, Role of collagen matrix in tumor angiogenesis and glioblastoma multiforme progression, The American journal of pathology, 183 (2013) 1293-1305.

[51] O. Lieleg, R.M. Baumgartel, A.R. Bausch, Selective filtering of particles by the extracellular matrix: an electrostatic bandpass, Biophysical journal, 97 (2009) 1569-1577.

[52] H. Cabral, Y. Matsumoto, K. Mizuno, Q. Chen, M. Murakami, M. Kimura, Y. Terada, M.R. Kano, K. Miyazono, M. Uesaka, N. Nishiyama, K. Kataoka, Accumulation of sub-100 nm polymeric micelles in poorly permeable tumours depends on size, Nature nanotechnology, 6 (2011) 815-823.

[53] H. Sato, T. Takino, Y. Okada, J. Cao, A. Shinagawa, E. Yamamoto, M. Seiki, A matrix metalloproteinase expressed on the surface of invasive tumour cells, Nature, 370 (1994) 61-65.

[54] M.A. Jacobetz, D.S. Chan, A. Neesse, T.E. Bapiro, N. Cook, K.K. Frese, C. Feig, T. Nakagawa, M.E. Caldwell, H.I. Zecchini, M.P. Lolkema, P. Jiang, A. Kultti, C.B. Thompson, D.C. Maneval, D.I. Jodrell, G.I. Frost, H.M. Shepard, J.N. Skepper, D.A. Tuveson, Hyaluronan impairs vascular function and drug delivery in a mouse model of pancreatic cancer, Gut, 62 (2013) 112-120.

[55] M. Egeblad, M.G. Rasch, V.M. Weaver, Dynamic interplay between the collagen scaffold and tumor evolution, Current opinion in cell biology, 22 (2010) 697-706.

[56] M. Kanapathipillai, A. Mammoto, T. Mammoto, J.H. Kang, E. Jiang, K. Ghosh, N. Korin, A. Gibbs, R. Mannix, D.E. Ingber, Inhibition of mammary tumor growth using lysyl oxidase-targeting nanoparticles to modify extracellular matrix, Nano letters, 12 (2012) 3213-3217.

[57] M. Kanapathipillai, A. Brock, D.E. Ingber, Nanoparticle targeting of anti-cancer drugs that alter intracellular signaling or influence the tumor microenvironment, Advanced drug delivery reviews, (2014).

[58] L. Eikenes, I. Tufto, E.A. Schnell, A. Bjorkoy, C. De Lange Davies, Effect of collagenase and hyaluronidase on free and anomalous diffusion in multicellular spheroids and xenografts, Anticancer research, 30 (2010) 359-368.

[59] C.J. Whatcott, H. Han, R.G. Posner, G. Hostetter, D.D. Von Hoff, Targeting the tumor microenvironment in cancer: why hyaluronidase deserves a second look, Cancer discovery, 1 (2011) 291-296.

[60] L. Eikenes, M. Tari, I. Tufto, O.S. Bruland, C. de Lange Davies, Hyaluronidase induces a transcapillary pressure gradient and improves the distribution and uptake of liposomal doxorubicin (Caelyx) in human osteosarcoma xenografts, British journal of cancer, 93 (2005) 81-88.

[61] R.G. Thorne, A. Lakkaraju, E. Rodriguez-Boulan, C. Nicholson, In vivo diffusion of lactoferrin in brain extracellular space is regulated by interactions with heparan sulfate, Proceedings of the National Academy of Sciences of the United States of America, 105 (2008) 8416-8421.

[62] A. Armulik, G. Genove, C. Betsholtz, Pericytes: developmental, physiological, and pathological perspectives, problems, and promises, Developmental cell, 21 (2011) 193-215.

[63] M.R. Kano, Nanotechnology and tumor microcirculation, Advanced drug delivery reviews, 74 (2014) 2-11.

[64] J.I. Greenberg, D.J. Shields, S.G. Barillas, L.M. Acevedo, E. Murphy, J. Huang, L. Scheppke, C. Stockmann, R.S. Johnson, N. Angle, D.A. Cheresh, A role for VEGF as a negative regulator of pericyte function and vessel maturation, Nature, 456 (2008) 809-813.

[65] P. Lindblom, H. Gerhardt, S. Liebner, A. Abramsson, M. Enge, M. Hellstrom, G. Backstrom, S. Fredriksson, U. Landegren, H.C. Nystrom, G. Bergstrom, E. Dejana, A. Ostman, P. Lindahl, C. Betsholtz, Endothelial PDGF-B retention is required for proper investment of pericytes in the microvessel wall, Genes & development, 17 (2003) 1835-1840.

[66] L. Zhang, H. Nishihara, M.R. Kano, Pericyte-coverage of human tumor vasculature and nanoparticle permeability, Biological & pharmaceutical bulletin, 35 (2012) 761-766.

[67] M.R. Kano, Y. Komuta, C. Iwata, M. Oka, Y.T. Shirai, Y. Morishita, Y. Ouchi, K. Kataoka, K. Miyazono, Comparison of the effects of the kinase inhibitors imatinib, sorafenib, and transforming growth factor-beta receptor inhibitor on extravasation of nanoparticles from neovasculature, Cancer science, 100 (2009) 173-180.

[68] M.R. Kano, Y. Bae, C. Iwata, Y. Morishita, M. Yashiro, M. Oka, T. Fujii, A. Komuro, K. Kiyono, M. Kaminishi, K. Hirakawa, Y. Ouchi, N. Nishiyama, K. Kataoka, K. Miyazono, Improvement of cancer-targeting therapy, using nanocarriers for intractable solid tumors by inhibition of TGF-beta signaling, Proceedings of the National Academy of Sciences of the United States of America, 104

(2007) 3460-3465.

[69] P. Lu, V.M. Weaver, Z. Werb, The extracellular matrix: a dynamic niche in cancer progression, The Journal of cell biology, 196 (2012) 395-406.

[70] Y. Sun, J. Campisi, C. Higano, T.M. Beer, P. Porter, I. Coleman, L. True, P.S. Nelson, Treatment-induced damage to the tumor microenvironment promotes prostate cancer therapy resistance through WNT16B, Nature medicine, 18 (2012) 1359-1368.

[71] N.R. Smith, D. Baker, M. Farren, A. Pommier, R. Swann, X. Wang, S. Mistry, K. McDaid, J. Kendrew, C. Womack, S.R. Wedge, S.T. Barry, Tumor stromal architecture can define the intrinsic tumor response to VEGF-targeted therapy, Clinical cancer research : an official journal of the American Association for Cancer Research, 19 (2013) 6943-6956.

[72] M. Murakami, M.J. Ernsting, E. Undzys, N. Holwell, W.D. Foltz, S.D. Li, Docetaxel conjugate nanoparticles that target alpha-smooth muscle actin-expressing stromal cells suppress breast cancer metastasis, Cancer research, 73 (2013) 4862-4871.

[73] H. Lee, H. Fonge, B. Hoang, R.M. Reilly, C. Allen, The effects of particle size and molecular targeting on the intratumoral and subcellular distribution of polymeric nanoparticles, Molecular pharmaceutics, 7 (2010) 1195-1208.

[74] J. Zhang, L. Miao, S. Guo, Y. Zhang, L. Zhang, A. Satterlee, W.Y. Kim, L. Huang, Synergistic anti-tumor effects of combined gemcitabine and cisplatin nanoparticles in a stroma-rich bladder carcinoma model, Journal of controlled release : official journal of the Controlled Release Society, 182 (2014) 90-96.

[75] J.P. Almeida, A.Y. Lin, R.J. Langsner, P. Eckels, A.E. Foster, R.A. Drezek, In vivo immune cell distribution of gold nanoparticles in naive and tumor bearing mice, Small, 10 (2014) 812-819.

[76] S. Mocellin, E. Wang, F.M. Marincola, Cytokines and immune response in the tumor microenvironment, J Immunother, 24 (2001) 392-407.

[77] A. Casazza, M. Mazzone, Altering the intratumoral localization of macrophages to inhibit cancer progression, Oncoimmunology, 3 (2014) e27872.

[78] A. Mantovani, S. Sozzani, M. Locati, P. Allavena, A. Sica, Macrophage polarization: tumor-associated macrophages as a paradigm for polarized M2 mononuclear phagocytes, Trends in immunology, 23 (2002) 549-555.

[79] L.B. Roode, T Perry, J Luft, C Bear, J Davis, I DeSimone, J, Investigation of sub-tumor accumulation of PRINT nanoparticles reveals dose and route of administration dependence on particle association, Cancer research, (2014) 1.

[80] W.C. Zamboni, S. Strychor, E. Joseph, D.R. Walsh, B.A. Zamboni, R.A. Parise, M.E. Tonda, N.Y. Yu, C. Engbers, J.L. Eiseman, Plasma, tumor, and tissue disposition of STEALTH liposomal CKD-602 (S-CKD602) and nonliposomal CKD-602 in mice bearing A375 human melanoma xenografts, Clinical cancer research : an official journal of the American Association for Cancer Research, 13 (2007) 7217-7223.

[81] G. Song, D.B. Darr, C.M. Santos, M. Ross, A. Valdivia, J.L. Jordan, B.R. Midkiff, S. Cohen, N.

Nikolaishvili-Feinberg, C.R. Miller, T.K. Tarrant, A.B. Rogers, A.C. Dudley, C.M. Perou, W.C. Zamboni, Effects of tumor microenvironment heterogeneity on nanoparticle disposition and efficacy in breast cancer tumor models, Clinical cancer research : an official journal of the American Association for Cancer Research, 20 (2014) 6083-6095.

[82] K. Huang, H. Ma, J. Liu, S. Huo, A. Kumar, T. Wei, X. Zhang, S. Jin, Y. Gan, P.C. Wang, S. He, X. Zhang, X.J. Liang, Size-dependent localization and penetration of ultrasmall gold nanoparticles in cancer cells, multicellular spheroids, and tumors in vivo, ACS Nano, 6 (2012) 4483-4493.

[83] T. Stylianopoulos, M.Z. Poh, N. Insin, M.G. Bawendi, D. Fukumura, L.L. Munn, R.K. Jain, Diffusion of particles in the extracellular matrix: the effect of repulsive electrostatic interactions, Biophysical journal, 99 (2010) 1342-1349.

[84] T. Stylianopoulos, K. Soteriou, D. Fukumura, R.K. Jain, Cationic nanoparticles have superior transvascular flux into solid tumors: insights from a mathematical model, Annals of biomedical engineering, 41 (2013) 68-77.

[85] G. Thurston, J.W. McLean, M. Rizen, P. Baluk, A. Haskell, T.J. Murphy, D. Hanahan, D.M. McDonald, Cationic liposomes target angiogenic endothelial cells in tumors and chronic inflammation in mice, The Journal of clinical investigation, 101 (1998) 1401-1413.

[86] A. Albanese, P.S. Tang, W.C. Chan, The effect of nanoparticle size, shape, and surface chemistry on biological systems, Annual review of biomedical engineering, 14 (2012) 1-16.

[87] Z. Cheng, A. Al Zaki, J.Z. Hui, V.R. Muzykantov, A. Tsourkas, Multifunctional nanoparticles: cost versus benefit of adding targeting and imaging capabilities, Science, 338 (2012) 903-910.

[88] R.K. Jain, J.D. Martin, T. Stylianopoulos, The role of mechanical forces in tumor growth and therapy, Annual review of biomedical engineering, 16 (2014) 321-346.

[89] R. Hoekstra, F.A. Eskens, J. Verweij, Matrix metalloproteinase inhibitors: current developments and future perspectives, The oncologist, 6 (2001) 415-427.

[90] C. Pisano, I. Vlodavsky, N. Ilan, F. Zunino, The potential of heparanase as a therapeutic target in cancer, Biochemical pharmacology, 89 (2014) 12-19.

[91] J. Liu, S. Liao, B. Diop-Frimpong, W. Chen, S. Goel, K. Naxerova, M. Ancukiewicz, Y. Boucher, R.K. Jain, L. Xu, TGF-beta blockade improves the distribution and efficacy of therapeutics in breast carcinoma by normalizing the tumor stroma, Proceedings of the National Academy of Sciences of the United States of America, 109 (2012) 16618-16623.

[92] H. Meng, Y. Zhao, J. Dong, M. Xue, Y.S. Lin, Z. Ji, W.X. Mai, H. Zhang, C.H. Chang, C.J. Brinker, J.I. Zink, A.E. Nel, Two-wave nanotherapy to target the stroma and optimize gemcitabine delivery to a human pancreatic cancer model in mice, ACS nano, 7 (2013) 10048-10065.

[93] T. Stylianopoulos, R.K. Jain, Combining two strategies to improve perfusion and drug delivery in solid tumors, Proceedings of the National Academy of Sciences of the United States of America, 110 (2013) 18632-18637.

[94] M. Dellian, F. Yuan, V.S. Trubetskoy, V.P. Torchilin, R.K. Jain, Vascular permeability in a human tumour xenograft: molecular charge dependence, British journal of cancer, 82 (2000) 1513-1518.

[95] P.A. Netti, D.A. Berk, M.A. Swartz, A.J. Grodzinsky, R.K. Jain, Role of extracellular matrix assembly in interstitial transport in solid tumors, Cancer research, 60 (2000) 2497-2503.

[96] S. Ramanujan, A. Pluen, T.D. McKee, E.B. Brown, Y. Boucher, R.K. Jain, Diffusion and convection in collagen gels: implications for transport in the tumor interstitium, Biophysical journal, 83 (2002) 1650-1660.

[97] T.D. McKee, P. Grandi, W. Mok, G. Alexandrakis, N. Insin, J.P. Zimmer, M.G. Bawendi, Y. Boucher, X.O. Breakefield, R.K. Jain, Degradation of fibrillar collagen in a human melanoma xenograft improves the efficacy of an oncolytic herpes simplex virus vector, Cancer research, 66 (2006) 2509-2513.

[98] M. Kato, Y. Hattori, M. Kubo, Y. Maitani, Collagenase-1 injection improved tumor distribution and gene expression of cationic lipoplex, International journal of pharmaceutics, 423 (2012) 428-434.

[99] E. Brown, T. McKee, E. diTomaso, A. Pluen, B. Seed, Y. Boucher, R.K. Jain, Dynamic imaging of collagen and its modulation in tumors in vivo using second-harmonic generation, Nature medicine, 9 (2003) 796-800.

[100] E.N. Unemori, E.P. Amento, Relaxin modulates synthesis and secretion of procollagenase and collagen by human dermal fibroblasts, J Biol Chem, 265 (1990) 10681-10685.

[101] X.L. Qiu, L.V. Brown, S. Parameswaran, V.W. Marek, G.S. Ibbott, S.J. Lai-Fook, Effect of hyaluronidase on albumin diffusion in lung interstitium, Lung, 177 (1999) 273-288.

[102] H.T. Pham, N.L. Block, V.B. Lokeshwar, Tumor-derived hyaluronidase: a diagnostic urine marker for high-grade bladder cancer, Cancer research, 57 (1997) 778-783.

[103] K. Beckenlehner, S. Bannke, T. Spruss, G. Bernhardt, H. Schonenberg, W. Schiess, Hyaluronidase enhances the activity of adriamycin in breast cancer models in vitro and in vivo, Journal of cancer research and clinical oncology, 118 (1992) 591-596.

[104] C. Brekken, C. de Lange Davies, Hyaluronidase reduces the interstitial fluid pressure in solid tumours in a non-linear concentration-dependent manner, Cancer letters, 131 (1998) 65-70.

[105] B. Diop-Frimpong, V.P. Chauhan, S. Krane, Y. Boucher, R.K. Jain, Losartan inhibits collagen I synthesis and improves the distribution and efficacy of nanotherapeutics in tumors, Proceedings of the National Academy of Sciences of the United States of America, 108 (2011) 2909-2914.

[106] T.T. Goodman, P.L. Olive, S.H. Pun, Increased nanoparticle penetration in collagenase-treated multicellular spheroids, International journal of nanomedicine, 2 (2007) 265-274.

[107] A. Parodi, S.G. Haddix, N. Taghipour, S. Scaria, F. Taraballi, A. Cevenini, I.K. Yazdi, C. Corbo, R. Palomba, S.Z. Khaled, J.O. Martinez, B.S. Brown, L. Isenhart, E. Tasciotti, Bromelain surface modification increases the diffusion of silica nanoparticles in the tumor extracellular matrix, ACS Nano, 8 (2014) 9874-9883.

[108] S.G. Murty, T. Qiao, P. Tabtieng, T. Higbee, E. Zaki, A. Pure, E. Tsourkas, A., Nanoparticles functionalized with collagenase exhibit improved tumor accumulation in a murine xenograft model, Particle & Particle Systems Characterization, 31 (2014) 6.

[109] M. Loeffler, J.A. Kruger, A.G. Niethammer, R.A. Reisfeld, Targeting tumor-associated fibroblasts improves cancer chemotherapy by increasing intratumoral drug uptake, The Journal of clinical investigation, 116 (2006) 1955-1962.

[110] A.M. LeBeau, W.N. Brennen, S. Aggarwal, S.R. Denmeade, Targeting the cancer stroma with a fibroblast activation protein-activated promelittin protoxin, Molecular cancer therapeutics, 8 (2009) 1378-1386.

[111] P. Baum, D. Muller, R. Ruger, R.E. Kontermann, Single-chain Fv immunoliposomes for the targeting of fibroblast activation protein-expressing tumor stromal cells, Journal of drug targeting, 15 (2007) 399-406.

[112] B.C. Ozdemir, T. Pentcheva-Hoang, J.L. Carstens, X. Zheng, C.C. Wu, T.R. Simpson, H. Laklai, H. Sugimoto, C. Kahlert, S.V. Novitskiy, A. De Jesus-Acosta, P. Sharma, P. Heidari, U. Mahmood, L. Chin, H.L. Moses, V.M. Weaver, A. Maitra, J.P. Allison, V.S. LeBleu, R. Kalluri, Depletion of carcinoma-associated fibroblasts and fibrosis induces immunosuppression and accelerates pancreas cancer with reduced survival, Cancer cell, 25 (2014) 719-734.

[113] C. Capparelli, C. Guido, D. Whitaker-Menezes, G. Bonuccelli, R. Balliet, T.G. Pestell, A.F. Goldberg, R.G. Pestell, A. Howell, S. Sneddon, R. Birbe, A. Tsirigos, U. Martinez-Outschoorn, F. Sotgia, M.P. Lisanti, Autophagy and senescence in cancer-associated fibroblasts metabolically supports tumor growth and metastasis via glycolysis and ketone production, Cell Cycle, 11 (2012) 2285-2302.

[114] M.V. Apte, R.C. Pirola, J.S. Wilson, Pancreatic stellate cells: a starring role in normal and diseased pancreas, Frontiers in physiology, 3 (2012) 344.

[115] C. Feig, A. Gopinathan, A. Neesse, D.S. Chan, N. Cook, D.A. Tuveson, The pancreas cancer microenvironment, Clinical cancer research : an official journal of the American Association for Cancer Research, 18 (2012) 4266-4276.

[116] C. Guido, D. Whitaker-Menezes, C. Capparelli, R. Balliet, Z. Lin, R.G. Pestell, A. Howell, S. Aquila, S. Ando, U. Martinez-Outschoorn, F. Sotgia, M.P. Lisanti, Metabolic reprogramming of cancer-associated fibroblasts by TGF-beta drives tumor growth: connecting TGF-beta signaling with "Warburg-like" cancer metabolism and L-lactate production, Cell Cycle, 11 (2012) 3019-3035.

[117] M.H. Sherman, R.T. Yu, D.D. Engle, N. Ding, A.R. Atkins, H. Tiriac, E.A. Collisson, F. Connor, T. Van Dyke, S. Kozlov, P. Martin, T.W. Tseng, D.W. Dawson, T.R. Donahue, A. Masamune, T. Shimosegawa, M.V. Apte, J.S. Wilson, B. Ng, S.L. Lau, J.E. Gunton, G.M. Wahl, T. Hunter, J.A. Drebin, P.J. O'Dwyer, C. Liddle, D.A. Tuveson, M. Downes, R.M. Evans, Vitamin D receptor-mediated stromal reprogramming suppresses pancreatitis and enhances pancreatic cancer therapy, Cell, 159 (2014) 80-93.

[118] A. Masamune, T. Shimosegawa, Signal transduction in pancreatic stellate cells, Journal of gastroenterology, 44 (2009) 249-260.

[119] W. Bild, L. Hritcu, C. Stefanescu, A. Ciobica, Inhibition of central angiotensin II enhances memory function and reduces oxidative stress status in rat hippocampus, Progress in neuro-psychopharmacology & biological psychiatry, 43 (2013) 79-88.

[120] R. Feng, S.C. Desbordes, H. Xie, E.S. Tillo, F. Pixley, E.R. Stanley, T. Graf, PU.1 and

C/EBPalpha/beta convert fibroblasts into macrophage-like cells, Proceedings of the National Academy of Sciences of the United States of America, 105 (2008) 6057-6062.

[121] Z. Ge, S. Liu, Functional block copolymer assemblies responsive to tumor and intracellular microenvironments for site-specific drug delivery and enhanced imaging performance, Chemical Society reviews, 42 (2013) 7289-7325.

[122] Z. Poon, D. Chang, X. Zhao, P.T. Hammond, Layer-by-layer nanoparticles with a pH-sheddable layer for in vivo targeting of tumor hypoxia, ACS Nano, 5 (2011) 4284-4292.

[123] E. Fleige, M.A. Quadir, R. Haag, Stimuli-responsive polymeric nanocarriers for the controlled transport of active compounds: concepts and applications, Advanced drug delivery reviews, 64 (2012) 866-884.

[124] M.B. Yatvin, J.N. Weinstein, W.H. Dennis, R. Blumenthal, Design of liposomes for enhanced local release of drugs by hyperthermia, Science, 202 (1978) 1290-1293.

[125] T. Yahara, T. Koga, S. Yoshida, S. Nakagawa, H. Deguchi, K. Shirouzu, Relationship between microvessel density and thermographic hot areas in breast cancer, Surgery today, 33 (2003) 243-248.

[126] E. Gateff, T. Loffler, J. Wismar, A temperature-sensitive brain tumor suppressor mutation of Drosophila melanogaster: developmental studies and molecular localization of the gene, Mechanisms of development, 41 (1993) 15-31.

[127] D. Parry, G. Peters, Temperature-sensitive mutants of p16CDKN2 associated with familial melanoma, Molecular and cellular biology, 16 (1996) 3844-3852.

[128] R.L. Elstrom, D.E. Bauer, M. Buzzai, R. Karnauskas, M.H. Harris, D.R. Plas, H. Zhuang, R.M. Cinalli, A. Alavi, C.M. Rudin, C.B. Thompson, Akt stimulates aerobic glycolysis in cancer cells, Cancer research, 64 (2004) 3892-3899.

[129] Z.S. Al-Ahmady, W.T. Al-Jamal, J.V. Bossche, T.T. Bui, A.F. Drake, A.J. Mason, K. Kostarelos, Lipid-peptide vesicle nanoscale hybrids for triggered drug release by mild hyperthermia in vitro and in vivo, ACS Nano, 6 (2012) 9335-9346.

[130] R.A. Gatenby, R.J. Gillies, Why do cancers have high aerobic glycolysis?, Nat Rev Cancer, 4 (2004) 891-899.

[131] L.E. Gerweck, K. Seetharaman, Cellular pH gradient in tumor versus normal tissue: potential exploitation for the treatment of cancer, Cancer research, 56 (1996) 1194-1198.

[132] Y. Wang, K. Zhou, G. Huang, C. Hensley, X. Huang, X. Ma, T. Zhao, B.D. Sumer, R.J. DeBerardinis, J. Gao, A nanoparticle-based strategy for the imaging of a broad range of tumours by nonlinear amplification of microenvironment signals, Nature materials, 13 (2014) 204-212.

[133] K. Zhou, Y. Wang, X. Huang, K. Luby-Phelps, B.D. Sumer, J. Gao, Tunable, ultrasensitive pH-responsive nanoparticles targeting specific endocytic organelles in living cells, Angew Chem Int Ed Engl, 50 (2011) 6109-6114.

[134] M. Bae, S. Cho, J. Song, G.Y. Lee, K. Kim, J. Yang, K. Cho, S.Y. Kim, Y. Byun, Metalloprotease-specific poly(ethylene glycol) methyl ether-peptide-doxorubicin conjugate for

targeting anticancer drug delivery based on angiogenesis, Drugs under experimental and clinical research, 29 (2003) 15-23.

[135] G.Y. Lee, K. Park, S.Y. Kim, Y. Byun, MMPs-specific PEGylated peptide-DOX conjugate micelles that can contain free doxorubicin, Eur J Pharm Biopharm, 67 (2007) 646-654.

[136] J.R. Tauro, R.A. Gemeinhart, Matrix metalloprotease triggered delivery of cancer chemotherapeutics from hydrogel matrixes, Bioconjugate chemistry, 16 (2005) 1133-1139.

[137] J.K. Kim, J. Anderson, H.W. Jun, M.A. Repka, S. Jo, Self-assembling peptide amphiphile-based nanofiber gel for bioresponsive cisplatin delivery, Molecular pharmaceutics, 6 (2009) 978-985.

[138] L. Miao, L. Huang, Exploring the Tumor Microenvironment with Nanoparticles, in: C.A. Mirkin, T.J. Meade, S.H. Petrosko, A.H. Stegh (Eds.) Nanotechnology-Based Precision Tools for the Detection and Treatment of Cancer, Springer International Publishing, 2015, pp. 193-226.

[139] A. Swami, M.R. Reagan, P. Basto, Y. Mishima, N. Kamaly, S. Glavey, S. Zhang, M. Moschetta, D. Seevaratnam, Y. Zhang, J. Liu, M. Memarzadeh, J. Wu, S. Manier, J. Shi, N. Bertrand, Z.N. Lu, K. Nagano, R. Baron, A. Sacco, A.M. Roccaro, O.C. Farokhzad, I.M. Ghobrial, Engineered nanomedicine for myeloma and bone microenvironment targeting, Proceedings of the National Academy of Sciences of the United States of America, 111 (2014) 10287-10292.

[140] H. Peinado, M. Aleckovic, S. Lavotshkin, I. Matei, B. Costa-Silva, G. Moreno-Bueno, M. Hergueta-Redondo, C. Williams, G. Garcia-Santos, C. Ghajar, A. Nitadori-Hoshino, C. Hoffman, K. Badal, B.A. Garcia, M.K. Callahan, J. Yuan, V.R. Martins, J. Skog, R.N. Kaplan, M.S. Brady, J.D. Wolchok, P.B. Chapman, Y. Kang, J. Bromberg, D. Lyden, Melanoma exosomes educate bone marrow progenitor cells toward a pro-metastatic phenotype through MET, Nature medicine, 18 (2012) 883-891.

[141] F.Y. Xu, T Luo, Y, Synthesis and Micellization of Thermosensitive PNIPAAm-b-PLA Amphiphilic Block Copolymers Based on a Bifunctional Initiator, Macromolecular Research, 19 (2011) 9.

[142] Y.Y. Li, H. Cheng, Z.G. Zhang, C. Wang, J.L. Zhu, Y. Liang, K.L. Zhang, S.X. Cheng, X.Z. Zhang, R.X. Zhuo, Cellular internalization and in vivo tracking of thermosensitive luminescent micelles based on luminescent lanthanide chelate, ACS Nano, 2 (2008) 125-133.

[143] C.W. Quan, D Chang, C Zhang, G Cheng, S Zhang, X Zhuo, R, Synthesis of Thermo-Sensitive Micellar Aggregates Self-Assembled from Biotinylated PNAS-b-PNIPAAm-b-PCL Triblock Copolymers for Tumor Targeting, J. Phys. Chem. C, 113 (2009) 6.

[144] N.S. Rejinold, M. Muthunarayanan, V.V. Divyarani, P.R. Sreerekha, K.P. Chennazhi, S.V. Nair, H. Tamura, R. Jayakumar, Curcumin-loaded biocompatible thermoresponsive polymeric nanoparticles for cancer drug delivery, Journal of colloid and interface science, 360 (2011) 39-51.

[145] N.S. Rejinold, P.R. Sreerekha, K.P. Chennazhi, S.V. Nair, R. Jayakumar, Biocompatible, biodegradable and thermo-sensitive chitosan-g-poly (N-isopropylacrylamide) nanocarrier for curcumin drug delivery, International journal of biological macromolecules, 49 (2011) 161-172.

[146] I. Levacheva, O. Samsonova, E. Tazina, M. Beck-Broichsitter, S. Levachev, B. Strehlow, M. Baryshnikova, N. Oborotova, A. Baryshnikov, U. Bakowsky, Optimized thermosensitive liposomes

for selective doxorubicin delivery: formulation development, quality analysis and bioactivity proof, Colloids and surfaces. B, Biointerfaces, 121 (2014) 248-256.

[147] Z.S. Al-Ahmady, O. Chaloin, K. Kostarelos, Monoclonal antibody-targeted, temperature-sensitive liposomes: in vivo tumor chemotherapeutics in combination with mild hyperthermia, Journal of controlled release : official journal of the Controlled Release Society, 196 (2014) 332-343.

[148] B.M. Dicheva, T.L. ten Hagen, D. Schipper, A.L. Seynhaeve, G.C. van Rhoon, A.M. Eggermont, G.A. Koning, Targeted and heat-triggered doxorubicin delivery to tumors by dual targeted cationic thermosensitive liposomes, Journal of controlled release : official journal of the Controlled Release Society, 195 (2014) 37-48.

[149] Z.S. Al-Ahmady, C.L. Scudamore, K. Kostarelos, Triggered doxorubicin release in solid tumors from thermosensitive liposome-peptide hybrids: Critical parameters and therapeutic efficacy, International journal of cancer. Journal international du cancer, 137 (2015) 731-743.

[150] E.R. Wright, V.P. Conticello, Self-assembly of block copolymers derived from elastin-mimetic polypeptide sequences, Advanced drug delivery reviews, 54 (2002) 1057-1073.

[151] G.H. Gao, Y. Li, D.S. Lee, Environmental pH-sensitive polymeric micelles for cancer diagnosis and targeted therapy, Journal of controlled release : official journal of the Controlled Release Society, 169 (2013) 180-184.

[152] E.S. Lee, Z. Gao, D. Kim, K. Park, I.C. Kwon, Y.H. Bae, Super pH-sensitive multifunctional polymeric micelle for tumor pH(e) specific TAT exposure and multidrug resistance, Journal of controlled release : official journal of the Controlled Release Society, 129 (2008) 228-236.

[153] F. Meng, Y. Zhong, R. Cheng, C. Deng, Z. Zhong, pH-sensitive polymeric nanoparticles for tumor-targeting doxorubicin delivery: concept and recent advances, Nanomedicine (Lond), 9 (2014) 487-499.

[154] C.Y. Zhang, Y.Q. Yang, T.X. Huang, B. Zhao, X.D. Guo, J.F. Wang, L.J. Zhang, Self-assembled pH-responsive MPEG-b-(PLA-co-PAE) block copolymer micelles for anticancer drug delivery, Biomaterials, 33 (2012) 6273-6283.

[155] A. Potineni, D.M. Lynn, R. Langer, M.M. Amiji, Poly(ethylene oxide)-modified poly(beta-amino ester) nanoparticles as a pH-sensitive biodegradable system for paclitaxel delivery, Journal of controlled release : official journal of the Controlled Release Society, 86 (2003) 223-234.

[156] K. Zhou, H. Liu, S. Zhang, X. Huang, Y. Wang, G. Huang, B.D. Sumer, J. Gao, Multicolored pH-tunable and activatable fluorescence nanoplatform responsive to physiologic pH stimuli, Journal of the American Chemical Society, 134 (2012) 7803-7811.

[157] V.A. Sethuraman, K. Na, Y.H. Bae, pH-responsive sulfonamide/PEI system for tumor specific gene delivery: an in vitro study, Biomacromolecules, 7 (2006) 64-70.

[158] Z. Deng, Z. Zhen, X. Hu, S. Wu, Z. Xu, P.K. Chu, Hollow chitosan-silica nanospheres as pH-sensitive targeted delivery carriers in breast cancer therapy, Biomaterials, 32 (2011) 4976-4986.

[159] S. Zhu, M. Niu, H. O'Mary, Z. Cui, Targeting of tumor-associated macrophages made possible by PEG-sheddable, mannose-modified nanoparticles, Molecular pharmaceutics, 10 (2013) 3525-

3530.

[160] S. Ruan, Q. He, H. Gao, Matrix metalloproteinase triggered size-shrinkable gelatin-gold fabricated nanoparticles for tumor microenvironment sensitive penetration and diagnosis of glioma, Nanoscale, 7 (2015) 9487-9496.

[161] M. Juweid, R. Neumann, C. Paik, M.J. Perez-Bacete, J. Sato, W. van Osdol, J.N. Weinstein, Micropharmacology of monoclonal antibodies in solid tumors: direct experimental evidence for a binding site barrier, Cancer research, 52 (1992) 5144-5153.

[162] J.N. Weinstein, W. van Osdol, Early intervention in cancer using monoclonal antibodies and other biological ligands: micropharmacology and the "binding site barrier", Cancer research, 52 (1992) 2747s-2751s.

[163] H. Nishihara, Human pathological basis of blood vessels and stromal tissue for nanotechnology, Advanced drug delivery reviews, 74 (2014) 19-27.

[164] R. Navab, D. Strumpf, B. Bandarchi, C.Q. Zhu, M. Pintilie, V.R. Ramnarine, E. Ibrahimov, N. Radulovich, L. Leung, M. Barczyk, D. Panchal, C. To, J.J. Yun, S. Der, F.A. Shepherd, I. Jurisica, M.S. Tsao, Prognostic gene-expression signature of carcinoma-associated fibroblasts in non-small cell lung cancer, Proceedings of the National Academy of Sciences of the United States of America, 108 (2011) 7160-7165.

[165] M. Yamashita, T. Ogawa, X. Zhang, N. Hanamura, Y. Kashikura, M. Takamura, M. Yoneda, T. Shiraishi, Role of stromal myofibroblasts in invasive breast cancer: stromal expression of alpha-smooth muscle actin correlates with worse clinical outcome, Breast cancer, 19 (2012) 170-176.

[166] L. Cheng, R. Montironi, D.D. Davidson, A. Lopez-Beltran, Staging and reporting of urothelial carcinoma of the urinary bladder, Modern pathology : an official journal of the United States and Canadian Academy of Pathology, Inc, 22 Suppl 2 (2009) S70-95.

[167] R. Kalluri, M. Zeisberg, Fibroblasts in cancer, Nature reviews. Cancer, 6 (2006) 392-401.

[168] J. Gore, M. Korc, Pancreatic cancer stroma: friend or foe?, Cancer cell, 25 (2014) 711-712.

[169] L. Miao, Y. Wang, C.M. Lin, Y. Xiong, N. Chen, L. Zhang, W.Y. Kim, L. Huang, Nanoparticle modulation of the tumor microenvironment enhances therapeutic efficacy of cisplatin, Journal of controlled release : official journal of the Controlled Release Society, 217 (2015) 27-41.

[170] Y. Zhang, N.M. Schwerbrock, A.B. Rogers, W.Y. Kim, L. Huang, Codelivery of VEGF siRNA and gemcitabine monophosphate in a single nanoparticle formulation for effective treatment of NSCLC, Molecular therapy : the journal of the American Society of Gene Therapy, 21 (2013) 1559-1569.

[171] Y. Hu, M.T. Haynes, Y. Wang, F. Liu, L. Huang, A highly efficient synthetic vector: nonhydrodynamic delivery of DNA to hepatocyte nuclei in vivo, ACS nano, 7 (2013) 5376-5384.

[172] Y.C. Tseng, Z. Xu, K. Guley, H. Yuan, L. Huang, Lipid-calcium phosphate nanoparticles for delivery to the lymphatic system and SPECT/CT imaging of lymph node metastases, Biomaterials, 35 (2014) 4688-4698.

[173] R. Banerjee, P. Tyagi, S. Li, L. Huang, Anisamide-targeted stealth liposomes: a potent carrier for targeting doxorubicin to human prostate cancer cells, International journal of cancer. Journal international du cancer, 112 (2004) 693-700.

[174] M.T. Leffler, R. Adams, Aminophenyl-2-oxazolines as local anesthetics, Journal of the American Chemical Society, 59 (1937) 2252-2258.

[175] H. Lee, B. Hoang, H. Fonge, R.M. Reilly, C. Allen, In vivo distribution of polymeric nanoparticles at the whole-body, tumor, and cellular levels, Pharmaceutical research, 27 (2010) 2343-2355.

[176] T. Marsh, K. Pietras, S.S. McAllister, Fibroblasts as architects of cancer pathogenesis, Bba-Mol Basis Dis, 1832 (2013) 1070-1078.

[177] S. Guo, Y. Wang, L. Miao, Z. Xu, C.M. Lin, Y. Zhang, L. Huang, Lipid-coated Cisplatin nanoparticles induce neighboring effect and exhibit enhanced anticancer efficacy, ACS nano, 7 (2013) 9896-9904.

[178] C. He, Y. Hu, L. Yin, C. Tang, C. Yin, Effects of particle size and surface charge on cellular uptake and biodistribution of polymeric nanoparticles, Biomaterials, 31 (2010) 3657-3666.

[179] H. Gao, W. Shi, L.B. Freund, Mechanics of receptor-mediated endocytosis, Proceedings of the National Academy of Sciences of the United States of America, 102 (2005) 9469-9474.

[180] S.K. Lai, Y.Y. Wang, K. Hida, R. Cone, J. Hanes, Nanoparticles reveal that human cervicovaginal mucus is riddled with pores larger than viruses, Proceedings of the National Academy of Sciences of the United States of America, 107 (2010) 598-603.

[181] A. Chen, S.A. McKinley, S. Wang, F. Shi, P.J. Mucha, M.G. Forest, S.K. Lai, Transient antibody-mucin interactions produce a dynamic molecular shield against viral invasion, Biophysical journal, 106 (2014) 2028-2036.

[182] A. van Waarde, A.A. Rybczynska, N.K. Ramakrishnan, K. Ishiwata, P.H. Elsinga, R.A. Dierckx, Potential applications for sigma receptor ligands in cancer diagnosis and therapy, Biochimica et biophysica acta, 1848 (2015) 2703-2714.

[183] N. Parker, M.J. Turk, E. Westrick, J.D. Lewis, P.S. Low, C.P. Leamon, Folate receptor expression in carcinomas and normal tissues determined by a quantitative radioligand binding assay, Analytical biochemistry, 338 (2005) 284-293.

[184] M. Prutki, M. Poljak-Blazi, M. Jakopovic, D. Tomas, I. Stipancic, N. Zarkovic, Altered iron metabolism, transferrin receptor 1 and ferritin in patients with colon cancer, Cancer letters, 238 (2006) 188-196.

[185] S.D. Li, L. Huang, Stealth nanoparticles: high density but sheddable PEG is a key for tumor targeting, Journal of controlled release : official journal of the Controlled Release Society, 145 (2010) 178-181.

[186] A. Pluen, Y. Boucher, S. Ramanujan, T.D. McKee, T. Gohongi, E. di Tomaso, E.B. Brown, Y. Izumi, R.B. Campbell, D.A. Berk, R.K. Jain, Role of tumor-host interactions in interstitial diffusion of macromolecules: cranial vs. subcutaneous tumors, Proceedings of the National Academy of

Sciences of the United States of America, 98 (2001) 4628-4633.

[187] T. Stylianopoulos, E.A. Economides, J.W. Baish, D. Fukumura, R.K. Jain, Towards Optimal Design of Cancer Nanomedicines: Multi-stage Nanoparticles for the Treatment of Solid Tumors, Annals of biomedical engineering, 43 (2015) 2291-2300.

[188] R.M. Drayton, J.W. Catto, Molecular mechanisms of cisplatin resistance in bladder cancer, Expert review of anticancer therapy, 12 (2012) 271-281.

[189] X. Yao, K. Panichpisal, N. Kurtzman, K. Nugent, Cisplatin nephrotoxicity: a review, The American journal of the medical sciences, 334 (2007) 115-124.

[190] D.S. Alberts, J.K. Noel, Cisplatin-associated neurotoxicity: can it be prevented?, Anti-cancer drugs, 6 (1995) 369-383.

[191] M.P. Kai, A.W. Keeler, J.L. Perry, K.G. Reuter, J.C. Luft, S.K. O'Neal, W.C. Zamboni, J.M. DeSimone, Evaluation of drug loading, pharmacokinetic behavior, and toxicity of a cisplatin-containing hydrogel nanoparticle, Journal of controlled release : official journal of the Controlled Release Society, 204 (2015) 70-77.

[192] S. Dhar, F.X. Gu, R. Langer, O.C. Farokhzad, S.J. Lippard, Targeted delivery of cisplatin to prostate cancer cells by aptamer functionalized Pt(IV) prodrug-PLGA-PEG nanoparticles, Proceedings of the National Academy of Sciences of the United States of America, 105 (2008) 17356-17361.

[193] A. Paraskar, S. Soni, S. Basu, C.J. Amarasiriwardena, N. Lupoli, S. Srivats, R.S. Roy, S. Sengupta, Rationally engineered polymeric cisplatin nanoparticles for improved antitumor efficacy, Nanotechnology, 22 (2011) 265101.

[194] S. Guo, L. Miao, Y. Wang, L. Huang, Unmodified drug used as a material to construct nanoparticles: delivery of cisplatin for enhanced anti-cancer therapy, Journal of controlled release : official journal of the Controlled Release Society, 174 (2014) 137-142.

[195] L. Miao, S. Guo, J. Zhang, W.Y. Kim, L. Huang, Nanoparticles with Precise Ratiometric Co-Loading and Co-Delivery of Gemcitabine Monophosphate and Cisplatin for Treatment of Bladder Cancer, Advanced functional materials, 24 (2014) 6601-6611.

[196] X. Xu, K. Xie, X.Q. Zhang, E.M. Pridgen, G.Y. Park, D.S. Cui, J. Shi, J. Wu, P.W. Kantoff, S.J. Lippard, R. Langer, G.C. Walker, O.C. Farokhzad, Enhancing tumor cell response to chemotherapy through nanoparticle-mediated codelivery of siRNA and cisplatin prodrug, Proceedings of the National Academy of Sciences of the United States of America, 110 (2013) 18638-18643.

[197] X.J. Liang, H. Meng, Y. Wang, H. He, J. Meng, J. Lu, P.C. Wang, Y. Zhao, X. Gao, B. Sun, C. Chen, G. Xing, D. Shen, M.M. Gottesman, Y. Wu, J.J. Yin, L. Jia, Metallofullerene nanoparticles circumvent tumor resistance to cisplatin by reactivating endocytosis, Proceedings of the National Academy of Sciences of the United States of America, 107 (2010) 7449-7454.

[198] A. Babu, Q. Wang, R. Muralidharan, M. Shanker, A. Munshi, R. Ramesh, Chitosan coated polylactic acid nanoparticle-mediated combinatorial delivery of cisplatin and siRNA/Plasmid DNA chemosensitizes cisplatin-resistant human ovarian cancer cells, Molecular pharmaceutics, 11 (2014) 2720-2733.

[199] O. Tredan, C.M. Galmarini, K. Patel, I.F. Tannock, Drug resistance and the solid tumor microenvironment, Journal of the National Cancer Institute, 99 (2007) 1441-1454.

[200] A.L. Correia, M.J. Bissell, The tumor microenvironment is a dominant force in multidrug resistance, Drug Resist Update, 15 (2012) 39-49.

[201] R. Straussman, T. Morikawa, K. Shee, M. Barzily-Rokni, Z.R. Qian, J. Du, A. Davis, M.M. Mongare, J. Gould, D.T. Frederick, Z.A. Cooper, P.B. Chapman, D.B. Solit, A. Ribas, R.S. Lo, K.T. Flaherty, S. Ogino, J.A. Wargo, T.R. Golub, Tumour micro-environment elicits innate resistance to RAF inhibitors through HGF secretion, Nature, 487 (2012) 500-504.

[202] L.A. Gilbert, M.T. Hemann, DNA damage-mediated induction of a chemoresistant niche, Cell, 143 (2010) 355-366.

[203] C.H. Ries, M.A. Cannarile, S. Hoves, J. Benz, K. Wartha, V. Runza, F. Rey-Giraud, L.P. Pradel, F. Feuerhake, I. Klaman, T. Jones, U. Jucknischke, S. Scheiblich, K. Kaluza, I.H. Gorr, A. Walz, K. Abiraj, P.A. Cassier, A. Sica, C. Gomez-Roca, K.E. de Visser, A. Italiano, C. Le Tourneau, J.P. Delord, H. Levitsky, J.Y. Blay, D. Ruttinger, Targeting tumor-associated macrophages with anti-CSF-1R antibody reveals a strategy for cancer therapy, Cancer cell, 25 (2014) 846-859.

[204] B. Tavora, L.E. Reynolds, S. Batista, F. Demircioglu, I. Fernandez, T. Lechertier, D.M. Lees, P.P. Wong, A. Alexopoulou, G. Elia, A. Clear, A. Ledoux, J. Hunter, N. Perkins, J.G. Gribben, K.M. Hodivala-Dilke, Endothelial-cell FAK targeting sensitizes tumours to DNA-damaging therapy, Nature, (2014).

[205] N. Wajapeyee, R.W. Serra, X. Zhu, M. Mahalingam, M.R. Green, Oncogenic BRAF induces senescence and apoptosis through pathways mediated by the secreted protein IGFBP7, Cell, 132 (2008) 363-374.

[206] R. Binet, D. Ythier, A.I. Robles, M. Collado, D. Larrieu, C. Fonti, E. Brambilla, C. Brambilla, M. Serrano, C.C. Harris, R. Pedeux, WNT16B is a new marker of cellular senescence that regulates p53 activity and the phosphoinositide 3-kinase/AKT pathway, Cancer research, 69 (2009) 9183-9191.

[207] C. Bavik, I. Coleman, J.P. Dean, B. Knudsen, S. Plymate, P.S. Nelson, The gene expression program of prostate fibroblast senescence modulates neoplastic epithelial cell proliferation through paracrine mechanisms, Cancer research, 66 (2006) 794-802.

[208] J.P. Coppe, C.K. Patil, F. Rodier, Y. Sun, D.P. Munoz, J. Goldstein, P.S. Nelson, P.Y. Desprez, J. Campisi, Senescence-associated secretory phenotypes reveal cell-nonautonomous functions of oncogenic RAS and the p53 tumor suppressor, PLoS biology, 6 (2008) 2853-2868.

[209] J.P. Coppe, K. Kauser, J. Campisi, C.M. Beausejour, Secretion of vascular endothelial growth factor by primary human fibroblasts at senescence, The Journal of biological chemistry, 281 (2006) 29568-29574.

[210] C. Niehrs, S.P. Acebron, Mitotic and mitogenic Wnt signalling, The EMBO journal, 31 (2012) 2705-2713.

[211] R. Fodde, T. Brabletz, Wnt/beta-catenin signaling in cancer stemness and malignant behavior, Current opinion in cell biology, 19 (2007) 150-158.

[212] B. He, R.N. Barg, L. You, Z. Xu, N. Reguart, I. Mikami, S. Batra, R. Rosell, D.M. Jablons, Wnt signaling in stem cells and non-small-cell lung cancer, Clinical lung cancer, 7 (2005) 54-60.

[213] J. Cui, W. Jiang, S. Wang, L. Wang, K. Xie, Role of Wnt/beta-catenin signaling in drug resistance of pancreatic cancer, Current pharmaceutical design, 18 (2012) 2464-2471.

[214] N. Takebe, P.J. Harris, R.Q. Warren, S.P. Ivy, Targeting cancer stem cells by inhibiting Wnt, Notch, and Hedgehog pathways, Nature reviews. Clinical oncology, 8 (2011) 97-106.

[215] D.R. Camidge, Y.J. Bang, E.L. Kwak, A.J. Iafrate, M. Varella-Garcia, S.B. Fox, G.J. Riely, B. Solomon, S.H. Ou, D.W. Kim, R. Salgia, P. Fidias, J.A. Engelman, L. Gandhi, P.A. Janne, D.B. Costa, G.I. Shapiro, P. Lorusso, K. Ruffner, P. Stephenson, Y. Tang, K. Wilner, J.W. Clark, A.T. Shaw, Activity and safety of crizotinib in patients with ALK-positive non-small-cell lung cancer: updated results from a phase 1 study, The Lancet. Oncology, 13 (2012) 1011-1019.

[216] F.R. Brennan, L.D. Morton, S. Spindeldreher, A. Kiessling, R. Allenspach, A. Hey, P.Y. Muller, W. Frings, J. Sims, Safety and immunotoxicity assessment of immunomodulatory monoclonal antibodies, mAbs, 2 (2010) 233-255.

[217] Y. Wang, Z. Xu, S. Guo, L. Zhang, A. Sharma, G.P. Robertson, L. Huang, Intravenous delivery of siRNA targeting CD47 effectively inhibits melanoma tumor growth and lung metastasis, Molecular therapy : the journal of the American Society of Gene Therapy, 21 (2013) 1919-1929.

[218] T. Umezu, K. Ohyashiki, M. Kuroda, J.H. Ohyashiki, Leukemia cell to endothelial cell communication via exosomal miRNAs, Oncogene, 32 (2013) 2747-2755.

[219] L. Fu, C. Zhang, L.Y. Zhang, S.S. Dong, L.H. Lu, J. Chen, Y. Dai, Y. Li, K.L. Kong, D.L. Kwong, X.Y. Guan, Wnt2 secreted by tumour fibroblasts promotes tumour progression in oesophageal cancer by activation of the Wnt/beta-catenin signalling pathway, Gut, 60 (2011) 1635-1643.

[220] C.C. Liang, A.Y. Park, J.L. Guan, In vitro scratch assay: a convenient and inexpensive method for analysis of cell migration in vitro, Nature protocols, 2 (2007) 329-333.

[221] G. Viticchie, A.M. Lena, A. Latina, A. Formosa, L.H. Gregersen, A.H. Lund, S. Bernardini, A. Mauriello, R. Miano, L.G. Spagnoli, R.A. Knight, E. Candi, G. Melino, MiR-203 controls proliferation, migration and invasive potential of prostate cancer cell lines, Cell cycle, 10 (2011) 1121-1131.

[222] L. Vermeulen, E.M.F. De Sousa, M. van der Heijden, K. Cameron, J.H. de Jong, T. Borovski, J.B. Tuynman, M. Todaro, C. Merz, H. Rodermond, M.R. Sprick, K. Kemper, D.J. Richel, G. Stassi, J.P. Medema, Wnt activity defines colon cancer stem cells and is regulated by the microenvironment, Nature cell biology, 12 (2010) 468-476.

[223] R.A. Benndorf, E. Schwedhelm, A. Gnann, R. Taheri, G. Kom, M. Didie, A. Steenpass, S. Ergun, R.H. Boger, Isoprostanes inhibit vascular endothelial growth factor-induced endothelial cell migration, tube formation, and cardiac vessel sprouting in vitro, as well as angiogenesis in vivo via activation of the thromboxane A(2) receptor: a potential link between oxidative stress and impaired angiogenesis, Circulation research, 103 (2008) 1037-1046.

[224] I. Arnaoutova, H.K. Kleinman, In vitro angiogenesis: endothelial cell tube formation on gelled

basement membrane extract, Nature protocols, 5 (2010) 628-635.

[225] W. Choi, S. Porten, S. Kim, D. Willis, E.R. Plimack, J. Hoffman-Censits, B. Roth, T. Cheng, M. Tran, I.L. Lee, J. Melquist, J. Bondaruk, T. Majewski, S. Zhang, S. Pretzsch, K. Baggerly, A. Siefker-Radtke, B. Czerniak, C.P. Dinney, D.J. McConkey, Identification of distinct basal and luminal subtypes of muscle-invasive bladder cancer with different sensitivities to frontline chemotherapy, Cancer cell, 25 (2014) 152-165.

[226] J.P. Volkmer, D. Sahoo, R.K. Chin, P.L. Ho, C. Tang, A.V. Kurtova, S.B. Willingham, S.K. Pazhanisamy, H. Contreras-Trujillo, T.A. Storm, Y. Lotan, A.H. Beck, B.I. Chung, A.A. Alizadeh, G. Godoy, S.P. Lerner, M. van de Rijn, L.D. Shortliffe, I.L. Weissman, K.S. Chan, Three differentiation states risk-stratify bladder cancer into distinct subtypes, Proceedings of the National Academy of Sciences of the United States of America, 109 (2012) 2078-2083.

[227] P.M. Corrigan, E. Dobbin, R.W. Freeburn, H. Wheadon, Patterns of Wnt/Fzd/LRP gene expression during embryonic hematopoiesis, Stem cells and development, 18 (2009) 759-772.

[228] N. Fujii, L. You, Z. Xu, K. Uematsu, J. Shan, B. He, I. Mikami, L.R. Edmondson, G. Neale, J. Zheng, R.K. Guy, D.M. Jablons, An antagonist of dishevelled protein-protein interaction suppresses beta-catenin-dependent tumor cell growth, Cancer research, 67 (2007) 573-579.

[229] O. Tetsu, F. McCormick, Beta-catenin regulates expression of cyclin D1 in colon carcinoma cells, Nature, 398 (1999) 422-426.

[230] J. Juan, T. Muraguchi, G. Iezza, R.C. Sears, M. McMahon, Diminished WNT -> beta-catenin -> c-MYC signaling is a barrier for malignant progression of BRAFV600E-induced lung tumors, Genes & development, 28 (2014) 561-575.

[231] T. Arumugam, V. Ramachandran, K.F. Fournier, H. Wang, L. Marquis, J.L. Abbruzzese, G.E. Gallick, C.D. Logsdon, D.J. McConkey, W. Choi, Epithelial to mesenchymal transition contributes to drug resistance in pancreatic cancer, Cancer research, 69 (2009) 5820-5828.

[232] S.P. De Langhe, F.G. Sala, P.M. Del Moral, T.J. Fairbanks, K.M. Yamada, D. Warburton, R.C. Burns, S. Bellusci, Dickkopf-1 (DKK1) reveals that fibronectin is a major target of Wnt signaling in branching morphogenesis of the mouse embryonic lung, Developmental biology, 277 (2005) 316-331.

[233] S.H. Shin, W.J. Kim, M.J. Choi, J.M. Park, H.R. Jin, G.N. Yin, J.K. Ryu, J.K. Suh, Aberrant expression of Wnt family contributes to the pathogenesis of diabetes-induced erectile dysfunction, Andrology, 2 (2014) 107-116.

[234] E.J. Yeo, L. Cassetta, B.Z. Qian, I. Lewkowich, J.F. Li, J.A. Stefater, 3rd, A.N. Smith, L.S. Wiechmann, Y. Wang, J.W. Pollard, R.A. Lang, Myeloid WNT7b mediates the angiogenic switch and metastasis in breast cancer, Cancer research, 74 (2014) 2962-2973.

[235] J.M. Stenman, J. Rajagopal, T.J. Carroll, M. Ishibashi, J. McMahon, A.P. McMahon, Canonical Wnt Signaling Regulates Organ-Specific Assembly and Differentiation of CNS Vasculature, Science, 322 (2008) 1247-1250.

[236] N. Sepp, P. Fritsch, T.A. Luger, Endothelial cells and angiogenesis, Experimental dermatology, 6 (1997) 272-273.

[237] P. Micke, A. Ostman, Tumour-stroma interaction: cancer-associated fibroblasts as novel targets in anti-cancer therapy?, Lung Cancer, 45 Suppl 2 (2004) S163-175.

[238] E. Klotzsch, M.L. Smith, K.E. Kubow, S. Muntwyler, W.C. Little, F. Beyeler, D. Gourdon, B.J. Nelson, V. Vogel, Fibronectin forms the most extensible biological fibers displaying switchable force-exposed cryptic binding sites, Proceedings of the National Academy of Sciences of the United States of America, 106 (2009) 18267-18272.

[239] M.J. Ernsting, B. Hoang, I. Lohse, E. Undzys, P. Cao, T. Do, B. Gill, M. Pintilie, D. Hedley, S.D. Li, Targeting of metastasis-promoting tumor-associated fibroblasts and modulation of pancreatic tumor-associated stroma with a carboxymethylcellulose-docetaxel nanoparticle, Journal of controlled release : official journal of the Controlled Release Society, 206 (2015) 122-130.

[240] M.A. Miller, Y.R. Zheng, S. Gadde, C. Pfirschke, H. Zope, C. Engblom, R.H. Kohler, Y. Iwamoto, K.S. Yang, B. Askevold, N. Kolishetti, M. Pittet, S.J. Lippard, O.C. Farokhzad, R. Weissleder, Tumour-associated macrophages act as a slow-release reservoir of nano-therapeutic Pt(IV) pro-drug, Nature communications, 6 (2015) 8692.

[241] L. Miao, C.M. Lin, L. Huang, Stromal barriers and strategies for the delivery of nanomedicine to desmoplastic tumors, Journal of controlled release : official journal of the Controlled Release Society, 219 (2015) 192-204.

[242] L.E. Roode, H. Brighton, T. Bo, J.L. Perry, M.C. Parrott, F. Kersey, J.C. Luft, J.E. Bear, J.M. DeSimone, I.J. Davis, Subtumoral analysis of PRINT nanoparticle distribution reveals targeting variation based on cellular and particle properties, Nanomedicine : nanotechnology, biology, and medicine, (2016).

[243] R. Shakya, T. Gonda, M. Quante, M. Salas, S. Kim, J. Brooks, S. Hirsch, J. Davies, A. Cullo, K. Olive, T.C. Wang, M. Szabolcs, B. Tycko, T. Ludwig, Hypomethylating therapy in an aggressive stroma-rich model of pancreatic carcinoma, Cancer research, 73 (2013) 885-896.

[244] M.V. Apte, J.S. Wilson, A. Lugea, S.J. Pandol, A starring role for stellate cells in the pancreatic cancer microenvironment, Gastroenterology, 144 (2013) 1210-1219.

[245] N.R. Smith, D. Baker, M. Farren, A. Pommier, R. Swann, X. Wang, S. Mistry, K. McDaid, J. Kendrew, C. Womack, S.R. Wedge, S.T. Barry, Tumor Stromal Architecture Can Define the Intrinsic Tumor Response to VEGF-Targeted Therapy, Clinical Cancer Research, 19 (2013) 6943-6956.

[246] M. Murakami, M.J. Ernsting, E. Undzys, N. Holwell, W.D. Foltz, S.D. Li, Docetaxel Conjugate Nanoparticles That Target alpha-Smooth Muscle Actin-Expressing Stromal Cells Suppress Breast Cancer Metastasis, Cancer research, 73 (2013) 4862-4871.

[247] M. De Palma, C.E. Lewis, Macrophage regulation of tumor responses to anticancer therapies, Cancer cell, 23 (2013) 277-286.

[248] J. Yoo, S. Choi, K.S. Hwang, W.K. Cho, C.R. Jung, S.T. Kwon, D.S. Im, Adeno-associated virus-mediated gene transfer of a secreted form of TRAIL inhibits tumor growth and occurrence in an experimental tumor model, The journal of gene medicine, 8 (2006) 163-174.

[249] X. Zhang, J.P. Edwards, D.M. Mosser, The expression of exogenous genes in macrophages: obstacles and opportunities, Methods in molecular biology, 531 (2009) 123-143.

[250] J. Voortman, T.P. Resende, M.A. Abou El Hassan, G. Giaccone, F.A. Kruyt, TRAIL therapy in non-small cell lung cancer cells: sensitization to death receptor-mediated apoptosis by proteasome inhibitor bortezomib, Molecular cancer therapeutics, 6 (2007) 2103-2112.

[251] L. O'Leary, A.M. van der Sloot, C.R. Reis, S. Deegan, A.E. Ryan, S.P. Dhami, L.S. Murillo, R.H. Cool, P.C. de Sampaio, K. Thompson, G. Murphy, W.J. Quax, L. Serrano, A. Samali, E. Szegezdi, Decoy receptors block TRAIL sensitivity at a supracellular level: the role of stromal cells in controlling tumour TRAIL sensitivity, Oncogene, (2015).

[252] K. Shah, C.H. Tung, K. Yang, R. Weissleder, X.O. Breakefield, Inducible release of TRAIL fusion proteins from a proapoptotic form for tumor therapy, Cancer research, 64 (2004) 3236-3242.

[253] S. Hingtgen, X.H. Ren, E. Terwilliger, M. Masson, R. Weissleder, K. Shah, Targeting multiple pathways in gliomas with stem cell and viral delivered S-TRAIL and Temozolomide, Molecular cancer therapeutics, 7 (2008) 3575-3585.

[254] K. Shah, C.H. Tung, K. Yang, R. Weissleder, X.O. Breakefield, Inducible release of TRAIL fusion proteins from a proapoptotic form for tumor therapy, Cancer research, 64 (2004) 3236-3242.

[255] S. Chono, S.D. Li, C.C. Conwell, L. Huang, An efficient and low immunostimulatory nanoparticle formulation for systemic siRNA delivery to the tumor, Journal of controlled release : official journal of the Controlled Release Society, 131 (2008) 64-69.

[256] J. Incio, P. Suboj, S.M. Chin, T. Vardam-Kaur, H. Liu, T. Hato, S. Babykutty, I. Chen, V. Deshpande, R.K. Jain, D. Fukumura, Metformin Reduces Desmoplasia in Pancreatic Cancer by Reprogramming Stellate Cells and Tumor-Associated Macrophages, PloS one, 10 (2015) e0141392.

[257] H. Ungefroren, M.L. Kruse, A. Trauzold, S. Roeschmann, C. Roeder, A. Arlt, D. Henne-Bruns, H. Kalthoff, FAP-1 in pancreatic cancer cells: functional and mechanistic studies on its inhibitory role in CD95-mediated apoptosis, Journal of cell science, 114 (2001) 2735-2746.

[258] M. Novak, M.K. Leonard, X.H. Yang, A. Kowluru, A.M. Belkin, D.M. Kaetzel, Metastasis suppressor NME1 regulates melanoma cell morphology, self-adhesion and motility via induction of fibronectin expression, Experimental dermatology, 24 (2015) 455-461.

[259] L.J. Hawinkels, M. Paauwe, H.W. Verspaget, E. Wiercinska, J.M. van der Zon, K. van der Ploeg, P.J. Koelink, J.H. Lindeman, W. Mesker, P. ten Dijke, C.F. Sier, Interaction with colon cancer cells hyperactivates TGF-beta signaling in cancer-associated fibroblasts, Oncogene, 33 (2014) 97-107.

[260] Y. Zhu, W.L. Yin, Y.F. Ba, L. Tian, Z.Q. Gu, M.S. Zhang, C.N. Zhong, Transforming growth factor-1 promotes the transcriptional activation of plasminogen activator inhibitor type 1 in carcinoma-associated fibroblasts, Molecular medicine reports, 6 (2012) 1001-1005.

[261] H. Matsuzaki, B.M. Schmied, A. Ulrich, J. Standop, M.B. Schneider, S.K. Batra, K.S. Picha, P.M. Pour, Combination of tumor necrosis factor-related apoptosis-inducing ligand (TRAIL) and actinomycin D induces apoptosis even in TRAIL-resistant human pancreatic cancer cells, Clinical cancer research : an official journal of the American Association for Cancer Research, 7 (2001) 407-414.

[262] E. De Vlieghere, L. Verset, P. Demetter, M. Bracke, O. De Wever, Cancer-associated fibroblasts

as target and tool in cancer therapeutics and diagnostics, Virchows Archiv : an international journal of pathology, 467 (2015) 367-382.

[263] P. Cirri, P. Chiarugi, Cancer-associated-fibroblasts and tumour cells: a diabolic liaison driving cancer progression, Cancer metastasis reviews, 31 (2012) 195-208.

[264] S.M. Kim, J.Y. Lim, S.I. Park, C.H. Jeong, J.H. Oh, M. Jeong, W. Oh, S.H. Park, Y.C. Sung, S.S. Jeun, Gene Therapy Using TRAIL-Secreting Human Umbilical Cord Blood-Derived Mesenchymal Stem Cells against Intracranial Glioma, Cancer research, 68 (2008) 9614-9623.

[265] S.S. Islam, R.B. Mokhtari, Y. El Hout, M.A. Azadi, M. Alauddin, H. Yeger, W.A. Farhat, TGF-beta1 induces EMT reprogramming of porcine bladder urothelial cells into collagen producing fibroblasts-like cells in a Smad2/Smad3-dependent manner, Journal of cell communication and signaling, 8 (2014) 39-58.

[266] M.J. Bissell, W.C. Hines, Why don't we get more cancer? A proposed role of the microenvironment in restraining cancer progression, Nat Med, 17 (2011) 320-329.

[267] F. Greco, M.J. Vicent, Combination therapy: opportunities and challenges for polymer-drug conjugates as anticancer nanomedicines, Adv. Drug Deliv. Rev., 61 (2009) 1203-1213.

[268] H.J. Broxterman, N.H. Georgopapadakou, Anticancer therapeutics: "Addictive" targets, multi-targeted drugs, new drug combinations, Drug Resist. Updat., 8 (2005) 183-197.

[269] L.D. Mayer, A.S. Janoff, Optimizing combination chemotherapy by controlling drug ratios, Mol. Interv., 7 (2007) 216-223.

[270] L.D. Mayer, T.O. Harasym, P.G. Tardi, N.L. Harasym, C.R. Shew, S.A. Johnstone, E.C. Ramsay, M.B. Bally, A.S. Janoff, Ratiometric dosing of anticancer drug combinations: controlling drug ratios after systemic administration regulates therapeutic activity in tumor-bearing mice, Mol. Cancer Ther., 5 (2006) 1854-1863.

[271] P.G. Tardi, N. Dos Santos, T.O. Harasym, S.A. Johnstone, N. Zisman, A.W. Tsang, D.G. Bermudes, L.D. Mayer, Drug ratio-dependent antitumor activity of irinotecan and cisplatin combinations in vitro and in vivo, Mol. Cancer Ther., 8 (2009) 2266-2275.

[272] N. Kolishetti, S. Dhar, P.M. Valencia, L.Q. Lin, R. Karnik, S.J. Lippard, R. Langer, O.C. Farokhzad, Engineering of self-assembled nanoparticle platform for precisely controlled combination drug therapy, Proc. Natl. Acad. Sci. USA, 107 (2010) 17939-17944.

[273] J. Park, S.H. Wrzesinski, E. Stern, M. Look, J. Criscione, R. Ragheb, S.M. Jay, S.L. Demento, A. Agawu, P. Licona Limon, A.F. Ferrandino, D. Gonzalez, A. Habermann, R.A. Flavell, T.M. Fahmy, Combination delivery of TGF-beta inhibitor and IL-2 by nanoscale liposomal polymeric gels enhances tumour immunotherapy, Nat. Mater., 11 (2012) 895-905.

[274] C.E. Ashley, E.C. Carnes, G.K. Phillips, D. Padilla, P.N. Durfee, P.A. Brown, T.N. Hanna, J. Liu, B. Phillips, M.B. Carter, N.J. Carroll, X. Jiang, D.R. Dunphy, C.L. Willman, D.N. Petsev, D.G. Evans, A.N. Parikh, B. Chackerian, W. Wharton, D.S. Peabody, C.J. Brinker, The targeted delivery of multicomponent cargos to cancer cells by nanoporous particle-supported lipid bilayers, Nat. Mater., 10 (2011) 389-397.

[275] C. Wang, Z. Li, D. Cao, Y.L. Zhao, J.W. Gaines, O.A. Bozdemir, M.W. Ambrogio, M. Frasconi, Y.Y. Botros, J.I. Zink, J.F. Stoddart, Stimulated release of size-selected cargos in succession from mesoporous silica nanoparticles, Angew Chem. Int. Ed. Engl., 51 (2012) 5460-5465.

[276] H. Wang, Y. Wu, R. Zhao, G. Nie, Engineering the assemblies of biomaterial nanocarriers for delivery of multiple theranostic agents with enhanced antitumor efficacy, Adv. Mater., 25 (2013) 1616-1622.

[277] S. Aryal, C.M. Hu, L. Zhang, Polymeric nanoparticles with precise ratiometric control over drug loading for combination therapy, Mol. Pharm., 8 (2011) 1401-1407.

[278] C.M. Hu, L. Zhang, Nanoparticle-based combination therapy toward overcoming drug resistance in cancer, Biochem. Pharmacol., 83 (2012) 1104-1111.

[279] S.H. Hu, X. Gao, Nanocomposites with spatially separated functionalities for combined imaging and magnetolytic therapy, J. Am. Chem. Soc., 132 (2010) 7234-7237.

[280] X.W. Chen, K.B. Sneed, S.Y. Pan, C. Cao, J.R. Kanwar, H. Chew, S.F. Zhou, Herb-drug interactions and mechanistic and clinical considerations, Current drug metabolism, 13 (2012) 640-651.

[281] J. Valle, H. Wasan, D.H. Palmer, D. Cunningham, A. Anthoney, A. Maraveyas, S. Madhusudan, T. Iveson, S. Hughes, S.P. Pereira, M. Roughton, J. Bridgewater, Cisplatin plus gemcitabine versus gemcitabine for biliary tract cancer, N. Engl. J. Med., 362 (2010) 1273-1281.

[282] S.M. Lee, T.V. O'Halloran, S.T. Nguyen, Polymer-caged nanobins for synergistic cisplatin-doxorubicin combination chemotherapy, Journal of the American Chemical Society, 132 (2010) 17130-17138.

[283] J.R. Mackey, R.S. Mani, M. Selner, D. Mowles, J.D. Young, J.A. Belt, C.R. Crawford, C.E. Cass, Functional nucleoside transporters are required for gemcitabine influx and manifestation of toxicity in cancer cell lines, Cancer research, 58 (1998) 4349-4357.

[284] W. Plunkett, P. Huang, V. Gandhi, Preclinical characteristics of gemcitabine, Anti-cancer drugs, 6 Suppl 6 (1995) 7-13.

[285] M.A. Moufarij, D.R. Phillips, C. Cullinane, Gemcitabine potentiates cisplatin cytotoxicity and inhibits repair of cisplatin-DNA damage in ovarian cancer cell lines, Mol. Pharmacol., 63 (2003) 862-869.

[286] O.G. Besancon, G.A. Tytgat, R. Meinsma, R. Leen, J. Hoebink, G.V. Kalayda, U. Jaehde, H.N. Caron, A.B. van Kuilenburg, Synergistic interaction between cisplatin and gemcitabine in neuroblastoma cell lines and multicellular tumor spheroids, Cancer Lett., 319 (2012) 23-30.

[287] Y. Zhang, W.Y. Kim, L. Huang, Systemic delivery of gemcitabine triphosphate via LCP nanoparticles for NSCLC and pancreatic cancer therapy, Biomaterials, 34 (2013) 3447-3458.

[288] S. Guo, L. Miao, Y. Wang, L. Huang, Unmodified drug used as a material to construct nanoparticles: delivery of cisplatin for enhanced anti-cancer therapy, J. Control. Release, 174 (2014) 137-142.

[289] J. Zhang, L. Miao, S. Guo, Y. Zhang, L. Zhang, A. Satterlee, W.Y. Kim, L. Huang, Synergistic anti-tumor effects of combined gemcitabine and cisplatin nanoparticles in a stroma-rich bladder carcinoma model, J. Control. Release, DOI 10.1016/j.jconrel.2014.1003.1016.

[290] T.C. Chou, P. Talalay, Quantitative analysis of dose-effect relationships: the combined effects of multiple drugs or enzyme inhibitors, Adv. Enzyme Regul., 22 (1984) 27-55.

[291] Y. Han, Z. He, A. Schulz, T.K. Bronich, R. Jordan, R. Luxenhofer, A.V. Kabanov, Synergistic Combinations of Multiple Chemotherapeutic Agents in High Capacity Poly(2-oxazoline) Micelles, Mol. Pharm., 9 (2012) 2302-2313.

[292] J.L. Vivero-Escoto, K.M. Taylor-Pashow, R.C. Huxford, J. Della Rocca, C. Okoruwa, H. An, W. Lin, W. Lin, Multifunctional mesoporous silica nanospheres with cleavable Gd(III) chelates as MRI contrast agents: synthesis, characterization, target-specificity, and renal clearance, Small, 7 (2011) 3519-3528.

[293] O. Nakagawa, X. Ming, L. Huang, R.L. Juliano, Targeted intracellular delivery of antisense oligonucleotides via conjugation with small-molecule ligands, J. Am. Chem. Soc., 132 (2010) 8848-8849.

[294] K. Avgoustakis, A. Beletsi, Z. Panagi, P. Klepetsanis, A.G. Karydas, D.S. Ithakissios, PLGA-mPEG nanoparticles of cisplatin: in vitro nanoparticle degradation, in vitro drug release and in vivo drug residence in blood properties, J. Control. Release, 79 (2002) 123-135.

[295] S. Aggarwal, S. Yadav, S. Gupta, EGFR targeted PLGA nanoparticles using gemcitabine for treatment of pancreatic cancer, J. Biomed. Nanotechnol., 7 (2011) 137-138.

[296] P. Pantazis, K. Dimas, J.H. Wyche, S. Anant, C.W. Houchen, J. Panyam, R.P. Ramanujam, Preparation of siRNA-encapsulated PLGA nanoparticles for sustained release of siRNA and evaluation of encapsulation efficiency, Methods Mol. Biol., 906 (2012) 311-319.

[297] L. Martin-Banderas, E. Saez-Fernandez, M.A. Holgado, M.M. Duran-Lobato, J.C. Prados, C. Melguizo, J.L. Arias, Biocompatible gemcitabine-based nanomedicine engineered by Flow Focusing for efficient antitumor activity, Int. J. Pharm., 443 (2013) 103-109.

[298] S. Guo, C.M. Lin, Z. Xu, L. Miao, Y. Wang, L. Huang, Co-delivery of Cisplatin and Rapamycin for Enhanced Anticancer Therapy through Synergistic Effects and Microenvironment Modulation, ACS nano, (2014).

[299] H.P. CJA van Moorsel, G Veerman, AM Bergman, CM Kuiper, JB Vermorken, WJF van der Vijgh, Mechanisms of synergism between cisplatin and gemcitabine in ovarian and non-small-cell lung cancer cell lines, Br. J. Cancer, 80 (1999) 10.

[300] B. Liedert, D. Pluim, J. Schellens, J. Thomale, Adduct-specific monoclonal antibodies for the measurement of cisplatin-induced DNA lesions in individual cell nuclei, Nucleic Acids Res., 34 (2006) e47.

[301] Y. Zhang, L. Peng, R.J. Mumper, L. Huang, Combinational delivery of c-myc siRNA and nucleoside analogs in a single, synthetic nanocarrier for targeted cancer therapy, Biomaterials, 34 (2013) 8459-8468.

[302] M.A. Engel, M.F. Neurath, Anticancer properties of the IL-12 family--focus on colorectal cancer, Current medicinal chemistry, 17 (2010) 3303-3308.

[303] R.A. Lake, B.W. Robinson, Immunotherapy and chemotherapy--a practical partnership, Nature reviews. Cancer, 5 (2005) 397-405.